

Optical properties and mechanical stress state in cubic boron nitride and diamond

Rudolph Marthinus Erasmus

A thesis submitted to the Faculty of Science, University of the Witwatersrand, Johannesburg, in fulfilment of the requirements for the degree of Doctor of Philosophy

Johannesburg, 2012

DECLARATION

I declare that this Thesis is my own, unaided work. It is being submitted for the Degree of Doctor of Philosophy at the University of the Witwatersrand, Johannesburg. It has not been submitted before for any degree or examination at any other University.

A handwritten signature in black ink, appearing to read 'R.M. Erasmus'.

(Signature of candidate)

__20th__ day of _September_ 2012 ___ in Johannesburg__

Hy dra sy duif in 'n karton,
sy duif met spikkels op sy vlerke
en oë wat 'n reënboog blink;
blindelings na die spruit waar hy sal wag
tot die son opkom terwyl hy binne
sterf van angs. Want sy duif moet los,
sy duif moet vlieg uit die donker boks
waar hy rondtrap om weg te kom na die son.
Sal hy ooit die grond verlaat,
sal sy vlerke hom bo alles uit kan dra
na die lug waar sy vlerkslag
hom bo bossies en klip en water sal lig
tot die vryheid hom vat
soos 'n werwelwind en hom laat styg
tot niks hom raak?
Sal hy sy hok vergeet, uit vreugde na al die
horisonne sweef waar niks hom hou
tot hy iewers in die onbekende
gaan sit want hy het gevlieg,
gevlieg soos hy wou?

(from "nag op 'n kaal plein" by Dolf van Niekerk, Human & Rousseau, 2006)

Acknowledgements

I would like to thank the following people sincerely for their invaluable contribution towards the completion of this study:

- My supervisor, Prof. J.D. Comins, for his enthusiasm for physics, his interest, support and guidance.
- Pamela Murphy, who first ran the Raman and Luminescence Laboratory, and Michél Nieuwoudt, who “succeeded” her, for without fail being willing to offer advice and assistance and generally keeping the equipment in excellent running condition.
- The National Research Foundation of South Africa for their financial assistance during part of this study.
- The De Beers Diamond Research Laboratory, for financial assistance, samples and use of experimental equipment. Mike Fish found time in a very busy schedule to keep in touch and offer invaluable advice and guidance.
- Dr. Jill Brookes and Rob Daniel in Hull – an almost chance meeting became a very fruitful and enjoyable collaboration. Thank you for the excellent samples and hospitality when I visited.
- The staff of the School of Physics of the University of the Witwatersrand, Johannesburg, for their willingness to help, their interest and encouragement.
- My parents, Theuns and Barbara Erasmus, and siblings Anna-Barbara and Barend, and their spouses, for their unfailing support, interest and encouragement, especially during the time when the bulk of this thesis was written.
- My uncle and aunt, Koos and Hannie Engelbrecht, who treated me like a son and provided a much appreciated home from home.
- Friends (especially the wine crowd!), for being there and believing in me, as well as providing for evenings out which contributed much to keeping me approximately sane.
- My fellow students, and especially Paul, Jonathan, Alistair and Robert, for making sure I never took life (and physics) too seriously.

Abstract

Raman and photoluminescence (PL) spectroscopy techniques were used to investigate the mechanical properties of diamond and cubic boron nitride (cBN) by optical means. Both these materials have extreme mechanical properties that make them the material of choice for many industrial applications, ranging from cutting and grinding to wire-drawing dies. The results obtained on single crystal diamond, polycrystalline diamond (PCD) and cBN are summarised below.

Micro-Raman and photoluminescence (PL) spectroscopy were used to map the three-dimensional (3D) stress and deformation distributions surrounding a plastic impression made in a synthetic, type Ib single crystal diamond. Using data from the Raman peak position, a 3D map of the stress contours surrounding the impression was generated, while the Raman width data yielded a map of the plastic deformation volume. The stress contours compare favorably with the resolved shear stress contours calculated for diamond. PL intensity maps of the zero phonon line (ZPL) associated with the $[N-V]^-$ defect centre at 1.945eV provide images of the extent of vacancy formation and movement during the impression process. Data concerning the position and width of the ZPL correspond well with the Raman results.

Polycrystalline diamond (PCD) tools commonly consist of a PCD layer sintered onto a cobalt-tungsten carbide (Co-WC) substrate. These tools are used in diverse applications and both the magnitude and distribution of the stresses in the PCD layer affect tool behavior. These stresses in sample drillbits were investigated by means of micro-Raman spectroscopy. Cyclic annealing of a sample drillbit to 600 °C shows that the tool properties are retained after 5 cycles, while similar cycling to 800 °C resulted in a permanent decrease of the average surface compressive stress. This implies a reduction in the drillbit's ability to resist crack formation and propagation and is thus a degradation of the tool properties.

The method of Raman mapping of stress and deformation in diamond was also applied to single crystals of cBN. Indentations on cubic boron nitride (cBN) crystals and polycrystalline cubic boron nitride (PcBN) composites were mapped and the shifts of the cBN Raman lines from their unstressed positions used to quantify the residual stresses in the boron nitride due to the deformation brought about by the indentation. These were found to be of the order of 1 GPa.

These measurements illustrated for the first time the use of Raman spectroscopy to study residual stresses in boron nitride.

Defects in cBN were studied using photoluminescence spectroscopy at low temperature (< 10 K) of two types of cBN irradiated at ambient temperature with 1.9 MeV electrons. All the samples were small (< 1 mm diameter) single crystals of cBN. Three defect centres (with narrow lines at 2.28 eV, 2.15 eV and 1.98 eV) were introduced in both the amber-coloured and black-brown coloured samples by the irradiation. The amber coloured sample also showed a defect centre (at 1.65 eV) that is present before and after irradiation. Line shape analysis of the zero phonon lines of all three irradiation-induced centres showed that the lines are predominantly Gaussian in character, suggesting that linetype defects such as dislocations are a prevalent characteristic of these crystals.

Raman spectroscopy of cBN single crystals as a function of temperature was performed over a wide temperature range from 4 K to 1373 K. The low temperature measurements extended the data previously reported in literature, as this data ranged from room temperature upwards. It was concluded from the shift of Raman peak position with temperature that both linear expansion and anharmonic effects were required to adequately account for the observed data. This is in agreement with previously published findings. Both 3- and 4-phonon processes were required to account for the observed linewidths as a function of temperature, again in agreement with literature.

The results presented here and in the associated journal publications illustrate clearly how optical spectroscopy techniques can serve as non-destructive characterisation tools for the mechanical properties of ultra-hard materials.

Contents

List of Figures	x
List of Tables	xiv
Chapter 1: Introduction	1
Chapter 2: Properties of diamond and cubic boron nitride.....	3
2.1 <i>Diamond</i>	3
2.1.1 Crystal structure	
2.1.2 Lattice defects	
2.1.2.1 Point defects	
2.1.2.2 Inclusions and dislocations	
2.1.2.3 Nitrogen and nitrogen-containing defects	
2.1.3 Synthetic diamond	
2.1.4 Optical properties	
2.1.4.1 Raman spectrum	
2.1.4.2 Luminescence	
2.1.5 Nitrogen-vacancy defect centres of interest	
2.1.5.1 The H3 centre	
2.1.5.2 The 575 nm centre	
2.1.5.3 The 1.945 eV centre	
2.1.6 Mechanical properties	
2.1.6.1 Hardness	
2.1.6.2 Plastic deformation	
2.2 <i>Cubic boron nitride</i>	28
2.2.1 Crystal structure	
2.2.2 Synthesis of cBN	
2.2.3 Physical properties	
2.2.3.1 Indentation hardness	
2.2.4 Lattice defects	
2.2.5 Optical properties	
2.2.5.1 Raman spectrum	
2.2.5.2 Luminescence	
Chapter 3: Vibrational spectroscopy.....	49
3.1 <i>The Raman effect</i>	49
3.1.1 Introduction	
3.1.2 A simple quantum mechanical approach	
3.1.3 A simple classical approach	
3.1.4 The width of the Raman line	

3.1.5	The effect of stress on the Raman line	
3.1.5.1	The hydrostatic piezo-Raman coefficient α	
3.1.5.2	Uniaxial stress	
3.1.5.3	Biaxial stress	
3.1.6	The effect of temperature on the Raman line position	
3.2	<i>Photoluminescence</i>	65
3.2.1	Lineshape and line width	
3.2.2	The Voigt profile	
	Chapter 4: Experimental details	72
4.1	<i>The Raman spectrometer</i>	72
4.1.1	The macro chamber	
4.1.2	The microscope attachment	
4.1.3	Light dispersion options	
4.1.4	Detectors	
4.2	<i>Laser sources</i>	76
4.3	<i>Calibration</i>	77
4.4	<i>Data acquisition</i>	77
4.4.1	Normalisation of spectra	
4.5	<i>Cryostats</i>	78
4.5.1	Comment on low temperatures for PL measurements	
4.6	<i>High Temperature Furnaces</i>	81
4.7	<i>Soft Impressor Technique</i>	85
4.7.1	Procedures for acquiring maps of spectral features	
4.7.1.1	2D maps	
4.7.1.2	3D maps	
4.8	<i>Samples</i>	89
	Chapter 5: Results – investigation of diamond	90
5.1	<i>Impressions in single crystal synthetic diamond</i>	90
5.1.1	2D Raman maps	
5.1.2	3D Raman maps	
5.1.2.1	(100) slice and (110) slice	
5.1.2.2	($\bar{1}$ 10) slice	
5.1.2.3	Comparison of calculated resolved shear stresses and experiment	
5.1.3	2D PL maps	
5.2	<i>Summary of results for single crystal diamond</i>	121

Chapter 6: Results – investigation of PCD.....	123
6.1 <i>Investigation of surface stress state of PCD.....</i>	123
6.1.1 Sample description	
6.1.2 Methodology	
6.1.3 Results	
6.1.3.1 Surface stress state as a function of surface finish	
6.1.3.2 Surface stress state as a function of temperature	
6.1.3.3 Surface stress state as a function of cycling and temperature	
6.2 <i>Summary of results for PCD.....</i>	133
Chapter 7: Results – investigation of cBN and PCBN.....	134
7.1 <i>Indentations in single crystal cBN.....</i>	134
7.1.1 Sample detail	
7.1.2 Raman mapping of indentations	
7.1.3 PL of indentations	
7.2 <i>Indentations in PCBN samples.....</i>	140
7.2.1 Raman mapping	
7.2.2 PL mapping	
7.3 <i>PL spectroscopy of electron-irradiated cBN.....</i>	143
7.3.1 Experimental details for PL spectroscopy of electron-irradiated cBN	
7.3.2 Results for PL spectroscopy of electron-irradiated cBN	
7.4 <i>Raman spectroscopy of cBN as a function of temperature.....</i>	147
7.4.1 TO- and LO-mode position shifts	
7.4.2 TO- and LO-mode linewidths	
7.5 <i>Summary of results for cBN and PCBN.....</i>	155
Chapter 8: Conclusions and further work.....	156
8.1 <i>Diamond-based materials.....</i>	156
8.1.1 Possible further work on diamond-based materials	
8.2 <i>cBN-based materials.....</i>	158
8.2.1 Possible further work on cBN-based materials	
References.....	160
Appendix: Copies of published papers.....	169

List of Figures

- 2.1 Tetrahedral arrangement of carbon atoms in the diamond lattice
- 2.2 Arrangement of carbon atoms in the diamond unit cell
- 2.3 IR spectra of (a) type Ib diamond, (b) type IaA, (c) type IaB (with platelet peak B') and (d) type IaB (without platelets)
- 2.4 A diagram of the Hall Belt apparatus for HPHT diamond synthesis
- 2.5 Carbon phase diagram highlighting P-T conditions for diamond synthesis
- 2.6 Schematic diagram of capsule for growth of diamonds by HPHT reconstitution method
- 2.7 Typical Raman spectra for single crystal and polycrystalline diamond (PCD)
- 2.8 Schematic diagram illustrating the effect of temperature and pressure on the deformation of diamond
- 2.9 Crystal structure of cBN, showing the cubic arrangement of the boron and nitrogen atoms
- 2.10 Phase diagram of BN, showing the hBN \leftrightarrow cBN equilibrium curves as suggested by (1) Bundy *et al.* (1963) and (2) Solozhenko (1988, 1995)
- 2.11 Typical Raman spectra showing the peaks observed for (a) single crystals of cBN, and (b) for polycrystalline cBN
- 3.1 Schematic energy level diagram illustrating the (a) Stokes and (b) anti-Stokes transitions that can occur during the Raman process. (c) is the case for Rayleigh scattering
- 3.2 In crystals with the diamond structure (a) and with the zinc blende structure (b) the TO modes at $\mathbf{q} = 0$ (indicated by arrows) are Raman active
- 3.3 Configuration-coordinate diagram illustrating the transitions relevant to photoluminescence processes
- 4.1 Light path diagram of the Jobin-Yvon T64000 spectrograph
- 4.2 Schematic diagram of the light path in a confocal microscope
- 4.3 Diagrammatic representation of the Oxford Instruments Microstat^{He} microscope cryostat used for some of the low temperature measurements
- 4.4 Diagrammatic representation of the Oxford Instruments CF1204 continuous flow exchange gas cryostat
- 4.5 cBN PL spectra of irradiated cBN at 25 K and 5 K, showing the effect of temperature on the shape of the zero phonon line of the RC1 defect

- 4.6 Diagram of custom-built high temperature furnace used for measurements on PCD toolbits
- 4.7 Schematic diagram of the Linkam TS1500 microscope furnace stage
- 4.8 Schematic representation of the deformation of a sample using the soft impressor technique
- 4.9 Schematic diagram of the high-temperature, high vacuum equipment used in the soft impressor technique
- 5.1 Map of diamond showing location of two impressions discussed in text
- 5.2 Optical micrograph of the proper impression as seen under the Raman microscope
- 5.3 Interferogram of an indent similar to that of figure 5.2
- 5.4 (a) 2D contour map of surface stress associated with the impression, calculated from the Raman peak position of diamond. (b) An example of the diamond Raman spectra relevant to the contour maps in figure 5.4(a) and figure 5.5.
- 5.5 2D contour map of the FWHM of the diamond Raman peak across the impression
- 5.6 Optical micrograph of the “skew” impression in figure 5.1
- 5.7 2D contour map of the surface stress associated with the impression shown in figure 5.6, calculated from the Raman peak position of diamond
- 5.8 2D contour map of the FWHM of the diamond Raman peak across the impression in figure 5.6
- 5.9 (a) Stress contour map of the slice mapped into the diamond along the [100] direction. (b) Stress contour map of the slice mapped into the diamond along the [110] direction. (c) Width contour map of the slice mapped into the diamond along the [100] direction. (d) Width contour map of the slice mapped into the diamond along the [110] direction
- 5.10 (a) Stress contour map of the slice mapped into the diamond along the $[\bar{1}10]$ direction. (b) Stress contour map of the slice mapped into the diamond along the [110] direction. (c) Width contour map of the slice mapped into the diamond along the $[\bar{1}10]$ direction. (d) Width contour map of the slice mapped into the diamond along the [110] direction.
- 5.11 Comparison of calculated resolved shear stresses and experimental stress and deformation contours for a section normal to the surface and along [100]. (a) Measured stress contour map, (b) Measured linewidth contour map, (c) Modelled contours (broken lines) of resolved shear stress on the most stressed slip systems for contact on the (001) surface
- 5.12 Comparison of calculated resolved shear stresses and experimental stress and deformation contours for a section normal to the surface and along [110]. (a) Measured stress contour map, (b) Measured linewidth contour map, (c) Modelled contours (broken lines) of resolved shear stress on the most stressed slip systems for contact on the (001) surface

- 5.13 Roberts model of a (110) plane or “slice” showing the area of dislocation initiation and the subsequent limit of dislocation loop expansion
- 5.14 Roberts model of a (110) plane or “slice” showing the likely resultant dislocation structure of an impression before the onset of reverse plasticity
- 5.15 Roberts model for a (110) plane or “slice” showing the likely resultant dislocation structure of an impression just after the onset of rosette formation
- 5.16 (a) Normalised intensity map of ZPL of the 1.945 eV defect. (b) Example spectra of the ZPL of the 1.945 eV defect after background subtraction.
- 5.17 Map of the position of the ZPL of the 1.945 eV defect
- 5.18 Voigt linewidth of the 1.945 eV ZPL
- 5.19 Gaussian component of the width of the 1.945 eV ZPL
- 5.20 Normalised intensity distribution of the ZPL of the 575 nm defect
- 5.21 Map of the position of the ZPL of the 575 nm defect
- 5.22 Voigt linewidth of the 575 nm ZPL
- 5.23 Gaussian component of the width of the 575 nm ZPL
- 6.1 Schematic diagram of a PCD drillbit
- 6.2 Diagram illustrating different mountings of PCD drillbits in diamond drill heads
- 6.3 Compressive surface stress as a function of surface finish across the diameter of three different samples
- 6.4 Change of average surface compressive stress with temperature for two roughly lapped samples
- 6.5 Change of average surface compressive stress with temperature for a different type of PCD drillbit
- 6.6 Surface stress state for the PCD layer of a drillbit as measured at room temperature after each of 5 cycles to 600 °C and 5 cycles to 800 °C
- 6.7 FWHM of the PCD layer of a drillbit as measured at room temperature after each of 5 cycles to 600 °C and 5 cycles to 800 °C
- 7.1 Micrograph of an indent in a cBN crystal made at 30 N maximum load (estimated pressure 3.8 GPa)
- 7.2 Typical Raman spectrum of cBN crystal shown in figure 7.1
- 7.3 Contour plot of the stress derived from the TO Raman peak position across the indent in figure 7.1
- 7.4 Contour map of FWHM of the TO Raman line across the indent in figure 7.1

- 7.5 Normalised PL intensities, measured at 5 K, of a spot in the middle of the indentation (figure 7.1) and a reference spot measured well away from the indentation
- 7.6 Micrograph of an indent in PCBN, made at 2600 N maximum load (estimated pressure ~ 20 GPa)
- 7.7 Stress contour map derived from the position of the Raman TO peak for the indent in figure 7.6
- 7.8 Contour map of FWHM of Raman TO peak for the indent in figure 7.6
- 7.9 PL spectra of PCBN at 5 K. The reference spot is on the PCBN surface well removed from any indents. “Centre of indent” refers to figure 7.6
- 7.10 PL spectra of unirradiated and irradiated black cBN crystals, acquired at 5 K
- 7.11 PL spectra of unirradiated and irradiated amber cBN crystals, acquired at 5 K
- 7.12 cBN crystal as mounted in the Linkam TS1500 microscope furnace and imaged under the Raman microscope; (a) before heating and (b) after heating to 1373 K
- 7.13 Typical Raman spectra of cBN at different temperatures
- 7.14 cBN Raman TO peak position as a function of temperature
- 7.15 cBN Raman LO peak position as a function of temperature
- 7.16 Variation of the anharmonic component of the Raman shift with temperature for the TO and LO modes of cBN
- 7.17 Width (FWHM) of TO Raman peak as a function of temperature
- 7.18 Width (FWHM) of LO Raman peak as a function of temperature

List of Tables

- 2.1 Physical properties of diamond
- 2.2 Classification of diamonds into different types according to nitrogen content
- 2.3 Examples of nitrogen-vacancy defects in the diamond lattice
- 2.4 Physical properties of cBN
- 3.1 Values of the hydrostatic piezo-Raman coefficient α reported in literature
- 3.2 Values for the piezo-Raman coefficient α under uniaxial stress
- 3.3 Values for the piezo-Raman coefficient α in the biaxial stress model
- 5.1 Dimensional characteristics of the two impressions shown in figure 5.1
- 7.1 ZPL peak parameters for the RC defects in the black cBN crystals
- 7.2 ZPL peak parameters for the RC defects in the amber cBN crystals
- 7.3 Fit parameters relevant to solid curves in figure 7.14 and 7.15

Chapter 1: Introduction

Diamond has long been revered for its status as a rare and valuable gemstone. It was, and still is, worn by all manner of people to display their wealth and status in society. Apart from its classification as the hardest natural material known to man, there exists no wide awareness of its myriad of unique physical and chemical properties and their applications. It is mostly in the latter guise, as e.g. an anvil in a Gem Anvil Cell, a high-temperature semiconductor or as the abrasive component in a cutting wheel, that diamond is of interest to physicists and material scientists (Field 1992a).

Relatively few people are aware of the existence of cubic boron nitride. In many respects it bears close resemblance to the physical and chemical properties of diamond (Vel *et al.* 1991) and thus has similar applications. It is wholly synthetic, first having been synthesised by Wentorf *et al.* (1957), and is currently the second hardest material after diamond.

In this body of work, both diamond and cubic boron nitride were studied by means of optical spectroscopy. The initial, somewhat unfocused, question underlying the work can probably be phrased as, “What can be learnt of the properties of these materials useful to their industrial applications?”. Obviously this question holds multiple possibilities and answers, since there is a large diversity of spectroscopic techniques and samples to choose from. The chief property of both diamond and cubic boron nitride that is most relevant to industrial applications, is hardness. The concept of hardness is not as intuitive as it might seem, but initially it will be appropriate to stay with a somewhat unphysical formulation and “define” hardness as that property that makes a material useful with which to fashion other materials.

The marketing of synthetic hard materials for industrial abrasive purposes commonly use qualities related to hardness such as the “friability index” or “toughness index” of a product to characterise its hardness. Use is also made of diagrams illustrating the resistance to abrasion of particular products under typical working conditions to aid the buyers of these products in choosing a product for a particular application[†].

[†] Website of Element Six (Pty) Ltd., www.e6.com, accessed January 2007

The above concepts are based on destructive tests of products. Optical spectroscopy has several advantages as a means to study synthetic ultra hard materials. On an application level, it offers the opportunity to study and possibly characterise these materials in a non-destructive manner. On a more fundamental level it offers the opportunity to investigate the relation between crystal properties and hardness. This knowledge is essential in the pursuit of manufacturing specified products for target applications.

Raman and photoluminescence spectroscopies were the main spectroscopic techniques that were employed in the present work. In the above context, Raman spectroscopy can be applied to identify compounds and to provide information on the phases of compounds present. It can also detect the presence of stress / strain in a material and can semi-qualitatively give an indication of the perfection of the crystal lattice. Photoluminescence provides information on certain defects, both intrinsic and extrinsic, in the crystal lattice. In particular, the line shape of the photoluminescence zero-phonon lines is related to the stress field around the defect in the crystal lattice (Stoneham 1969).

Diamond, as both natural and synthetic crystals of relatively large size, has been available to researchers for several decades. A large body of publications and knowledge, also on optical properties, has been accumulated in this time. Cubic boron nitride, on the other hand, has relatively speaking received less attention and thus has a smaller associated body of knowledge.

It is the aim of this dissertation to add some detailed insights into the relation between crystal properties and hardness in the case of diamond and to broaden the knowledge base available on cubic boron nitride, with an emphasis on mechanical and optical properties.

In chapter 2, the properties of diamond and cubic boron nitride (cBN) relevant to the above-mentioned aim are reviewed. Chapter 3 is a description of Raman and photoluminescence spectroscopies, while chapter 4 describes the equipment used and gives details regarding the experimental procedures followed. The results on single crystal diamond are presented and discussed in chapter 5 and the work on polycrystalline diamond (PCD) follows in chapter 6. Chapter 7 presents the results and discussion of the work on cBN and PcBN and conclusions are drawn and possible further work highlighted in chapter 8.

Chapter 2: Properties of diamond and cubic boron nitride

The properties of a material encompass a very wide scope of science, traversing the domains of physics, chemistry and engineering. This chapter serves as an introduction to the basic properties of diamond and cubic boron nitride, with particular emphasis on those optical and mechanical properties relevant to this thesis.

2.1 Diamond

As alluded to in the introductory chapter, diamond has been imbued with a special aura for many years, especially as a gemstone. It was only in the 19th century that it was discovered that diamond and graphite are both allotropes of carbon. The class of compounds known collectively as fullerenes is yet another allotrope of pure carbon. Some of the properties of diamond, such as the high refractive index, transparency to the optical spectrum, extreme hardness and resistance to many forms of chemical attack have been known for many decades and are easily established in a qualitative manner. Research in the past century, and especially since the advent of the high pressure – high temperature (HPHT) synthesis process, has quantified many of these attributes and has shown diamond to have several other unique properties, e.g. a very high thermal conductivity (Field 1992a) (about five times that of copper at room temperature) and a large bandgap (5.48 eV at 77 K; Field 1991) which makes applications possible as either an electrical insulator or a semiconductor (with appropriate doping).

Diamond is also extremely inert chemically and is not affected at all by any acids or indeed other chemicals, except those that act as oxidising agents at high temperatures (Field 1992a). In an oxygen atmosphere diamond starts to be oxidised at ≈ 900 K and molten sodium nitrate will attack diamond at temperatures as low as ≈ 700 K. Two groups of metals also attack diamond chemically. At high temperatures the group of avid carbide formers that include tungsten, tantalum, titanium and zirconium will react with diamond to form their respective carbides. The second group of metals includes iron, cobalt, manganese, nickel and chromium and

these metals are true solvents for carbon in their molten state, thus literally dissolving diamond at temperatures above their melting points.

2.1.1 Crystal structure

Many of the above mentioned unique properties arise from the fact that diamond has an extremely rigid lattice. In an ideal crystal, the diamond lattice is a network of exclusively tetrahedrally bonded carbon atoms, where the four orbitals of each carbon atom are sp^3 hybridised and the bonds completely covalent. The carbon atom is relatively small; thus the bond angle is very close to the theoretical value of 109.5° in the lattice and the bond length of 0.154 nm is optimised as shown in figure 2.1). This arrangement leads to the rigidity of the diamond lattice. There are two crystallographic forms of diamond, namely cubic (most natural and synthetic diamond) and hexagonal (shock diamond). This work is concerned with the cubic form, which has the space group O_h^7 . The point group of the lattice is O_h and the point group of an individual atom lattice site is T_d . The lattice of carbon atoms can be thought of as two interpenetrating face centred cubic (f.c.c.) lattices, where the origin of the one is offset with respect to the origin of the other along the cube diagonal by $[\frac{1}{4}a, \frac{1}{4}a, \frac{1}{4}a]$, where $a = 0.357$ nm is the lattice parameter as shown in figure 2.2.

Several of the physical properties of diamond are tabulated in Table 2.1 and will be referred to in subsequent paragraphs.

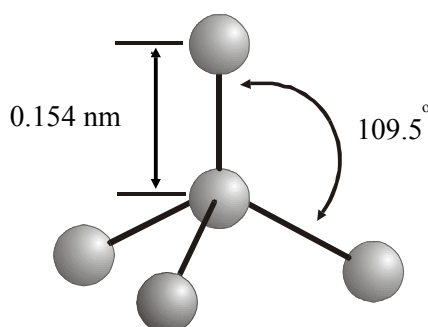


Figure 2.1: Tetrahedral arrangement of carbon atoms in the diamond lattice.

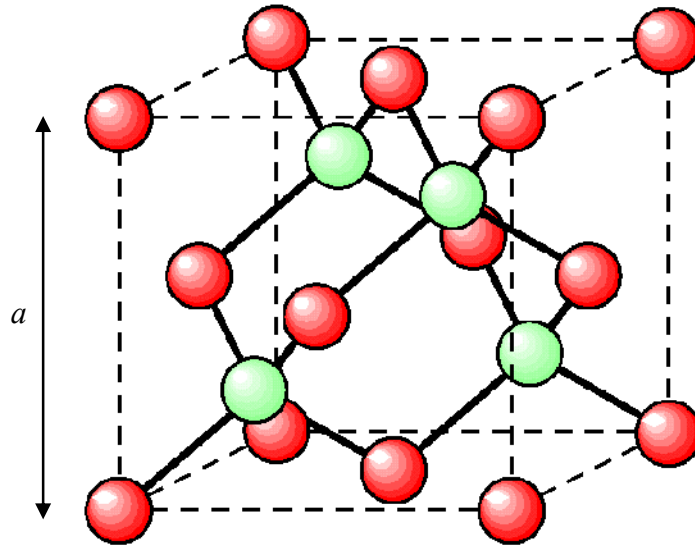


Figure 2.2: Arrangement of carbon atoms in the diamond unit cell. The atoms on each of the two fcc “sub-lattices” have been drawn in green and red to clarify the diagram, but are in fact identical. a is the lattice parameter.

Table 2.1: Physical properties of diamond (Field 1992a).

Property	Symbol	Value
Density	ρ	$3.52 \times 10^3 \text{ kg.m}^{-3}$
Refractive Index	μ	2.417 (at 589.29 nm)
Young's Modulus	E	$11.41 \times 10^{11} \text{ N.m}^{-2}$
Shear Modulus	G	$5.53 \times 10^{11} \text{ N.m}^{-2}$
Bulk Modulus (isotropic)	K	$4.42 \times 10^{11} \text{ N.m}^{-2}$
Tensile Strength	σ	$\approx 300 \text{ kg.mm}^{-2}$
Compressive Strength	S	$\approx 1000 \text{ kg.mm}^{-2}$ (synthetic grit)
Poisson's Ratio (isotropic)	ν	0.07
{111} Cleavage Energy	γ	$5.5 \pm 0.15 \text{ J.m}^{-2}$
Stress Intensity Factor	K_{Ic}	$3.5 - 5.0 \text{ MN.m}^{-3/2}$
BDTT (Brittle-Ductile Transition Temperature)		1100° C (type IIa) 950° C (type Ia) 770° C (type Ib)
Thermal Conductivity (at 293 K)		600 – 1000 $\text{W.m}^{-1}.\text{K}^{-1}$ (type Ia) 2000 – 2200 $\text{W.m}^{-1}.\text{K}^{-1}$ (type IIa)
Thermal Expansion (at 293 K)		$0.8 \pm 0.1 \times 10^{-6} \text{ K}^{-1}$
Electrical Resistivity		$> 10^{14} \text{ }\Omega.\text{m}$ (type Ia; most IIa) 0.1 – 10 $\Omega.\text{m}$ (natural type IIb)

2.1.2 Lattice Defects

An ideal crystal is a useful abstraction, but in practice all crystals contain defects of some description to a greater or lesser degree. The phrase “lattice defects” usually refers to inclusions, stacking faults, dislocations and point defects. On a microscopic level, point defects concern the perturbation of the lattice at a single lattice point. These point defects can interact or aggregate to form new, more complex defects. On a larger scale there are inclusions, which can be viewed as voids in the lattice filled with foreign matter. Inclusions can occur on size scales from nanometres to millimetres, depending on the nature of the inclusion and the size of the host crystal. Imperfections in the crystal lattice such as dislocations form another category of defects. The presence of these defects in the crystal lattice influences the properties of the host lattice to a certain degree. Their influence can be detrimental or advantageous, but in either case often affords the researcher the means by which the lattice properties can be studied.

2.1.2.1 Point defects

Point defects may be divided into two main categories, namely intrinsic and extrinsic types. Intrinsic defects are those only involving the host lattice; in the case of diamond, these include the vacancy, the carbon interstitial and their respective aggregates. Extrinsic defects involve impurity atoms, either in substitutional or interstitial positions in the host lattice.

There are a very large number of optically active point defects in diamond (Field 1992a and Zaitsev 2001), and only those relevant to the present work will be discussed in any detail.

The **vacancy** is a fundamental lattice defect and a constituent of several optically active defects in diamond. In addition to those vacancies that form in the lattice during the crystal growth processes, vacancies can be introduced in the lattice in various ways. Irradiation (with electrons or ions) is frequently used to generate a high concentration of vacancies. The optical centre resulting from radiation damage and leading to the GR1 band with a Zero-Phonon Line (ZPL) = 1.673 eV is attributed to the neutral vacancy (Walker 1979). The temperature at which the carbon interstitials produced during irradiation become mobile depends on the irradiation conditions and irradiation temperature (Newton *et al.* 2002). For low temperature irradiation the interstitials are mobile at temperatures above 50 K (Davies *et al.* 1992) and remove some of the vacancies formed through recombination. Prins *et al.* (1986) state “Large-scale diffusion of interstitial atoms during ion implantation seems to occur above about 50° C”. The vacancy becomes mobile at ~ 550° C (Collins 1993). At temperatures above this it can be trapped at various defects such as substitutional nitrogen, or precipitate at internal surfaces such as

dislocations, or at external surfaces. In synthetic diamond with its abundance of substitutional nitrogen which can act as an electron donor, the preferred form of the vacancy is negatively charged with its optical centre ND1 having a ZPL = 3.510 eV. It has been shown that only the neutral form of the vacancy is mobile and that the activation energy for its migration is 2.3 ± 0.3 eV (Davies *et al.* 1993).

Irradiation is not the only mechanism whereby vacancies may be produced. Simple (negative) climb of an edge dislocation may involve the production of vacancies, which, at elevated temperatures, can diffuse away from the vicinity of the dislocation line. The non-conservative dragging of a jog by a gliding dislocation can cause the evolution of vacancies, as discussed by Nabarro (1967). Jogs are produced in profusion by the cutting interactions of dislocations moving on intersecting slip systems (Read 1953). The numbers involved become appreciable in the case of diamond sintered at high pressure and temperature, as for example in the manufacture of sintered polycrystalline diamond products (Davey *et al.* 1984, Evans *et al.* 1984). The photoluminescence due to vacancy-related optical centres was observed by these authors to increase as a function of increasing temperature and pressure, and decreasing size of the diamond grains involved. This observation was explained as resulting from an increased volume fraction of plastically deformed diamond being formed in the sintering process. The number of vacancies created by sintering was calculated at approximately 10^{15} cm⁻³ (Dodge 1986).

The probability of a given lattice site to be unoccupied, in other words for a vacancy to exist, is proportional to a Boltzmann factor containing the energy of formation of a vacancy. Thus the number of vacancies in a lattice is a function of temperature (Dekker 1970). In the case of diamond the calculated neutral vacancy formation energy is 7.2 eV (Bernholc *et al.* 1992). As diamond graphitises above 900 K in the presence of oxygen or other active agents and from 1800 K in an inert atmosphere (Field 1992a), thermal generation of vacancies only plays a minor role as $\exp[-7.2/kT] \approx 7 \times 10^{-21}$ for T = 1800 K.

Numerous impurities occur in diamond; indeed about 58 different elements have been detected using nuclear probe techniques (Sellschop 1992). Important amongst these are hydrogen, nitrogen, oxygen and sulphur. These elements are relatively common in both natural and synthetic diamond. Elements such as boron, magnesium, aluminium, silicon, calcium, silver, barium, nickel, cobalt and iron occur in smaller quantities and their presence and concentration is often heavily dependent on the geographical origin for natural stones or the synthesis process for synthetic samples.

Nitrogen is the most important impurity in that it determines most of the optical properties and also plays a major part in influencing thermal, electrical and mechanical properties. Early work by Kaiser *et al.* (1959) identified nitrogen as the major impurity in type I diamonds. A classification system shown in Table 2.2 based on the nitrogen content is widely used (Field 1992a). The forms of nitrogen and nitrogen-containing defects are discussed in detail in section 2.1.2.3. to follow.

Table 2.2: Classification of diamonds into different types according to nitrogen content.

Type	Form of nitrogen	Abundance
Ia	A and B aggregates and platelets	98% of natural diamonds
Ib	Single substitutional (C centres)	0.1% of natural, most of synthetic diamonds
IIa	Virtually no nitrogen	2% of natural diamonds
IIb	Virtually no nitrogen, but contains boron (semiconducting)	Rare for natural diamonds
(IaA)	Predominantly A aggregates	Subgroup of Ia
(IaB)	Predominantly B aggregates	Subgroup of Ia

2.1.2.2 Inclusions and dislocations

Inclusions in both natural and synthetic diamond are well-known. In natural diamond, they serve to identify the geological origin as well as the physical conditions that existed during growth (Harris 1992). Synthetic diamond contains varying amounts of inclusions depending on the quality of the product. The inclusions are usually comprised of graphite or amorphous carbon that has not undergone the phase transition to diamond or combinations of carbon and the metal solvent / catalyst that was trapped during growth.

In general, the visible inclusions in synthetic diamond are of two types: large inclusions of up to several tenths of a millimetre in size which may occur at any point within the crystal, and microscopic inclusions distributed either as narrow lines radially directed from the central part of the crystal to its apices or broader bands radially directed from the central part of the crystal to its edges (Wakatsuki 1984).

The most basic line defect is the dislocation. Although diamond is considered to be an almost perfectly brittle material, i.e. having no dislocation mobility at room temperature, dislocations are observed in both natural and synthetic diamond. Diamond exhibits the same number of grown in dislocations as any other covalently bonded crystal, with the exception of natural type IIa diamonds, which tend to have a dense, polygonised dislocation structure.

Stacking faults and strain-producing growth sector boundaries are only common in synthetic diamonds. Dislocation bundles are often associated with the macroscopic seeds used in HPHT reconstituted diamond growth. Natural diamonds usually comprise only {111} growth sectors, while synthetics also contain {100} and, less frequently, {110} and {113} growth sectors, each of which has a different tendency to contain impurity atoms. This gives rise to slight differences in lattice constant in the different growth sectors, and hence to strain (Lang *et al.* 1992).

Dislocations introduced via deformation processes are described in the section on mechanical properties.

2.1.2.3 Nitrogen and nitrogen-containing defects

Nitrogen is present in the diamond lattice in three different forms: as single substitutional nitrogen (Dyer *et al.* 1965, Field 1992a and Kiflawi *et al.* 1994), the A centre (Field 1992a, Davies 1976a and Boyd *et al.* 1994) and the B centre (Field 1992a, Collins 1999 and Boyd *et al.* 1995). The single substitutional nitrogen defect is also known as the C centre. Each centre has a characteristic infrared absorption spectrum from which the concentration of the centre can be found.

Figure 2.3 shows the characteristic infrared (IR) absorption spectra of nitrogen defects in the diamond lattice. Spectrum (a) gives the characteristic (IR) absorption signature of the C centre, with a sharp peak at 1344 cm^{-1} and a broader feature at 1130 cm^{-1} . Spectrum (b) is the IR absorption spectrum of the A-centre, with a characteristic peak at 1282 cm^{-1} . Spectrum (c) shows the characteristic IR absorption spectrum of the B-centre, with a sharp peak at 1332 cm^{-1} and a broader feature at 1175 cm^{-1} and including the platelet peak B' at $\sim 1365\text{ cm}^{-1}$. Spectrum (d) is the absorption spectrum of the B-centre without any platelets. Platelets are extended {001} planar defects in diamond; the current models of platelets are discussed in detail below.

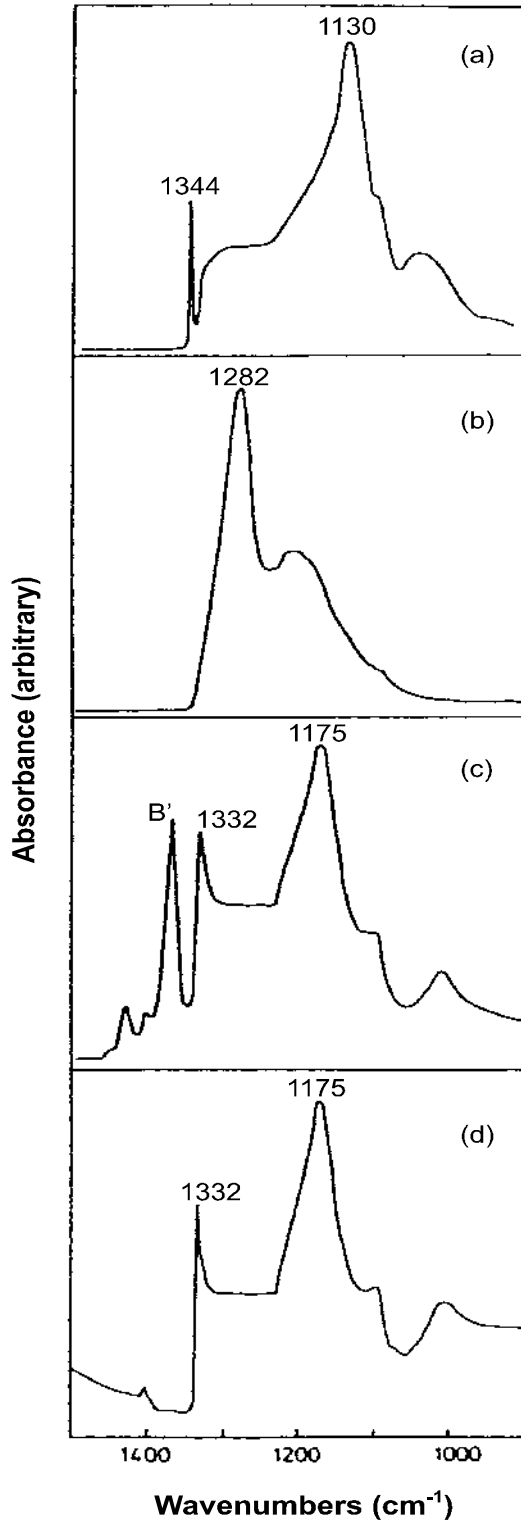


Figure 2.3: IR spectra of (a) type Ib diamond, (b) type IaA, (c) type IaB (with platelet peak B') and (d) type IaB (without platelets) (Collins 1993). These characteristic absorption systems are the basis for the classification of diamond as indicated in Table 2.2.

Synthetic diamond is yellow in colour due to the presence of single substitutional nitrogen (Chrenko *et al.* 1971). This form of nitrogen has a characteristic EPR signal and an absorption in the one-phonon region of the infrared spectrum. It is the absorption in the UV spectrum with a tail into the blue part of the visible spectrum due to the electron transitions between the nitrogen donor and the conduction band which gives rise to the typical yellow colouration mentioned above. The concentration of single substitutional nitrogen varies for different growth sectors in synthetic diamond in the sequence $\{111\} > \{100\} \gg \{113\} > \{110\}$, with $\{111\}$ sectors having about twice as much nitrogen as $\{100\}$ sectors (Woods *et al.* 1975, Burns *et al.* 1990). There is some evidence that for diamonds grown at low temperature the situation is slightly different, with $\{100\}$ sectors having the highest nitrogen concentration (Satoh *et al.* 1990). It should be noted that the growth sector dependence above for nitrogen will affect any other point defects formed with single substitutional nitrogen as constituent. For example, the C-centre-vacancy defect with a ZPL at 1.945 eV was shown in photoluminescence tomography measurements to occur at a much higher concentration in the $\{111\}$ growth zones than in the $\{100\}$ and $\{113\}$ sectors, as expected from the concentration of nitrogen as a function of growth sector (Van Enkevort *et al.* 1988). Photoluminescence of synthetic diamond crystals with morphologies ranging from cubic through cubo-octahedral to almost octahedral was reported by Fish (1995) and Fish *et al.* (1999). Results indicated a more defective crystal lattice and higher concentration of substitutional nitrogen associated with the more cubic crystals, consistent with a higher growth rate associated with the cubic morphology.

The A centre, which is the most common nitrogen centre in natural diamonds, is considered to be two nitrogen atoms on adjacent lattice sites in a $\{111\}$ plane (Davies 1976a). It is possible to aggregate single substitutional nitrogen into A centres by subjecting the crystal to ~ 5.5 GPa pressure and a temperature of 1900°C (Chrenko *et al.* 1977, Satoh *et al.* 1990). The aggregation rate is enhanced by the presence of vacancies, produced by 2 MeV electron bombardment. Following irradiation, a lower temperature is needed for aggregation and the rate is increased (Collins 1980).

The B centre is considered to consist of four nitrogen atoms, on lattice sites, grouped tetrahedrally around a vacancy (Loubser *et al.* 1981). IR absorption spectra (Fig. 2.3c) showing the B centre absorption peak usually display another absorption peak as shown in fig. 2.3.(c). This is known as the B' peak and found to correspond to platelets (Sobolev *et al.* 1968). Platelets are microscopic planar defects (sizes ranging from 10 nm to $\sim 3\ \mu\text{m}$), seen in electron microscopy, which are oriented along $\{100\}$ planes. It has been suggested that platelets contain nitrogen

(Evans *et al.* 1962 and 1981), but more recent work suggest a combination of carbon interstitials and nitrogen (Baker 1998), or mainly carbon (Goss *et al.* 2000 and Goss *et al.* 2003).

Nitrogen forms several defect centres with vacancies. Examples are given in table 2.3.

Table 2.3: Examples of nitrogen-vacancy defects in the diamond lattice.

Origin	Defect centre
A centre + vacancy	H3 centre (N-V-N)
C centre + vacancy	1.945 eV centre [N-V] ⁻
C centre + vacancy	575 nm centre [N-V] ⁰
B centre + vacancy	H4 centre
Three nitrogen atoms + vacancy	N3

Of the examples in table 2.3, the H3 centre, 1.945 eV centre and the 575 nm centre are important to the work in this thesis and the properties of these centres are discussed in a separate section.

It is appropriate to comment on the names of the defect centres at this point. No systematic naming convention exists for optically active point defects in diamond, despite attempts at introducing a systematic approach. For vibronic centres, the zero phonon line (ZPL) tends to be named, often by the energy or wavelength at which it occurs, but sometimes by a letter followed by a number (e.g. the scheme discussed by Walker (1979)). Further confusion is often introduced by the adoption of a different name for the same centre when observed by ESR. The convention adopted here is the one used by Collins (1992) as well as Fish (1995), where the most frequently used name is chosen. No attempt is made to adhere to a single naming scheme or energy unit.

2.1.3 Synthetic diamond

The laboratory synthesis of diamond was first reported in 1955 by a team from General Electric in the U.S.A. (see e.g. Nassau *et al.* 1979, Strong 1989), followed shortly thereafter by commercial production. Volume manufacturing of synthetic diamond was started in South Africa in 1960 by the De Beers company. The early successful attempts at diamond synthesis were all achieved by High Pressure, High Temperature (HPHT) synthesis where a carbon source (graphite), in the presence of a metallic solvent / catalyst, is subjected to pressures and temperatures in the diamond stable region of the carbon phase diagram. The HPHT equipment is usually referred to as the belt apparatus (Hall 1960). A schematic of the so-called ‘‘Hall belt’’ is given in figure 2.4. The belt utilised the Bridgman concepts of massive support and non-extruding gasket made of pyrophyllite, a hydrous aluminium silicate (Bridgman 1950). By using strongly

tapered pistons (A and B in figure 2.4), a large piston motion becomes possible without squeezing the pyrophyllite gasket too thin. This arrangement permits a large sample volume S.

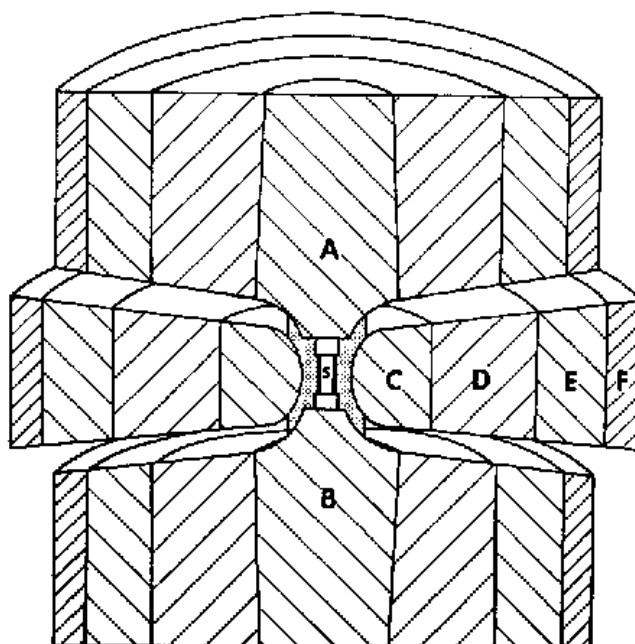


Figure 2.4: A diagram of the Hall Belt apparatus for HPHT diamond synthesis. A and B are strongly tapered pistons and C, D, E and F are separate “belts” to help contain the pressure in the sample volume S (Nassau *et al.* 1979).

The separate “belt” C also supports the outside of the sample volume and interacts with the two tapered pistons to complete the arrangement. Both the pistons A and B and the belt C were made of cobalt-cemented tungsten carbide and supported by several rings of special steel (D, E and F). The sample S is contained in a small graphite tube which bridges the gap between the two anvils A and B. Since the pyrophyllite is an insulator, an electric current passed from one anvil to the other passes through the graphite tube and heats the sample inside it.

This approach still forms the basis of the synthetic diamond abrasives industry today, with graphite (usually in the form of discs and powders) as the carbon source, and alloys of cobalt, iron and nickel and manganese as the most frequently used solvent / catalyst. Other materials used as solvent / catalysts include chromium and tantalum as well as various carbides, carbonates, sulphates and hydroxides (Burns *et al.* 1992). Diamonds of up to 1 mm diameter are typically grown by this HPHT graphite conversion process. Figure 2.5 shows a section of the carbon phase diagram relevant to diamond synthesis. The Berman-Simon line forms the boundary between the graphite stable and diamond stable P-T regions. It can be seen that catalytic synthesis

takes place between ~5 and 10 GPa pressure and 1300 K and 2200 K of temperature. It is clear that significantly higher pressure and temperature conditions are necessary to synthesise diamond in the absence of a catalyst / solvent.

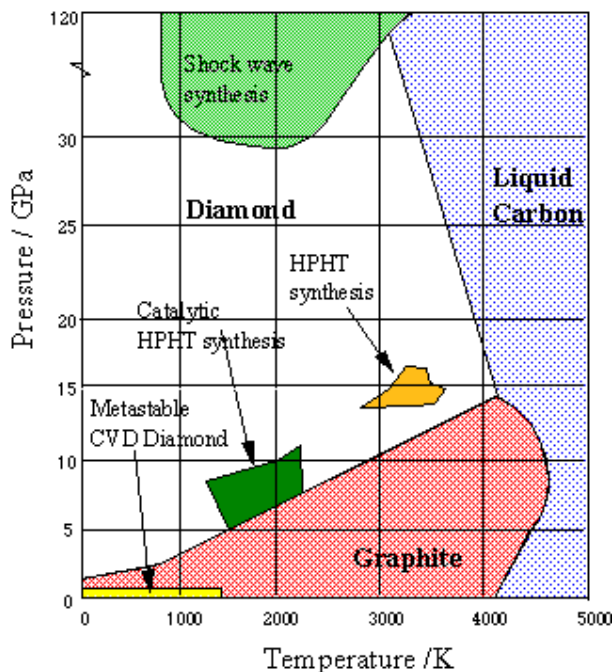


Figure 2.5: Carbon phase diagram highlighting P-T conditions for diamond synthesis (Bundy 1980).

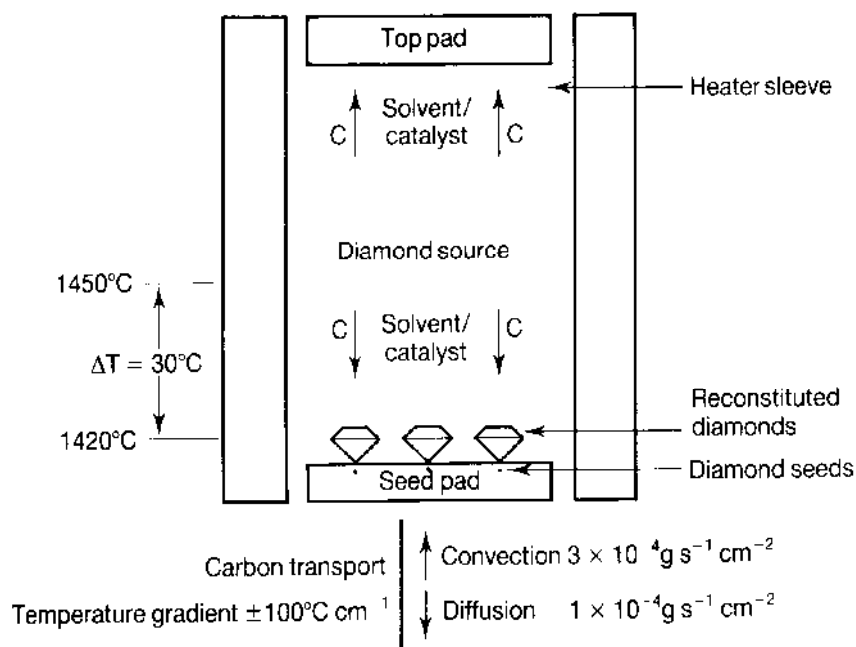


Figure 2.6: Schematic diagram of capsule for growth of diamonds by the HPHT reconstitution method (Burns *et al.* 1992).

A variation of this approach is to replace the graphite in the above scheme with diamond powder and a schematic drawing of the capsule used in this case is given in figure 2.6 (Burns *et al.* 1992). In this arrangement, the source carbon is separated from the growing crystals by a solvent / catalyst metal bath. This approach is known as the HPHT reconstitution technique of diamond growth. Reconstitution is facilitated by using a temperature gradient inside the capsule and by providing the precipitating diamond with nucleation sites, in the form of seed crystals within the capsule. Diamond powder is the preferred carbon source, as it does not produce a volume change in the capsule upon conversion. This technique is favoured for the growth of large synthetic crystals and diamonds grown by this method are used for applications such as single point turning tools, microtome knives, surgical blades, wire drawing dies and heat sinks.

The morphology of synthetic (HPHT) diamond is similar to natural diamond in that it is dependent on the conditions of growth, but favours a cubo-octahedral habit rather than an octo-dodecahedral habit. The detailed reason for this is still being researched but the cubic nature of HPHT diamonds make them particularly useful for monolithic industrial purposes, as they require little processing. The relationship between the cubic {001} growth and octahedral {111} growth depends on various factors such as the choice of solvent metal catalyst, the synthesis temperature and the nitrogen content. In general, the higher the nitrogen content, the more dominant the cubic growth. As diamond growth proceeds from the seed crystal (figure 2.6) in the capsule it offers five {001} faces on which to grow (the sixth is attached to the seed pad). In between each of these {001} sectors there is an interconnecting sector, usually of {111} or {110} habit but {113} sectors have been reported. No two sectors of the same habit touch; there is always a layer with different habit in between, although it is sometimes very small. The three dimensional nature of the growth, together with the competitive growth of the {001} and {111} sectors, result in diamonds where the growth sectoring can be very complicated. As the stone grows away from the seed the sectoring becomes simpler as certain sectors are overgrown and annihilated. After synthesis the diamonds are removed from the capsule, cleaned and the seeds removed. If enough of the earlier reconstituted diamond adjacent to the seed is removed in the process, the result is a crystal that consists, almost exclusively, of {111} and {001} sectors. If the synthesis conditions are appropriately chosen, it is possible to produce stones that are almost exclusively {001} growth sectors.

Polycrystalline diamond (PCD), an extended diamond structure consisting of randomly oriented crystallites with direct diamond-diamond bonding, was developed to reduce the

undesirable effects caused by the anisotropy of single crystal diamond in abrasive applications. This prevents uneven wear due to the varying hardness as a function of direction (see e.g. Brookes 1992a). PCD in general has a greater toughness than single crystal diamond and offers properties that are more homogeneous. This leads to better wear and fracture resistance in abrasive applications. PCD toolbits are manufactured in a belt-type HPHT apparatus by placing diamond powder (optionally mixed with 10 to 20 weight % Co powder) on a cobalt-cemented tungsten carbide substrate and applying a pressure of between 5 and 10 GPa. The high pressures produced locally at diamond inter-particle contact points lead to fracture of the powder and an ensuing reduction in grain size. Subsequently a sintering temperature of 1300° C to 1800° C is applied for times of the order of minutes to several hours. As the temperature reaches the sintering temperature, the cobalt melts and a carbon-cobalt eutectic mixture results. Control of the pressure and temperature of this liquid phase sintering process causes carbon to dissolve into the eutectic and to re-precipitate as diamond, resulting in the formation and growth of “necks” or “bridges” between the particles (see e.g. Notsu *et al.* 1977 and Akaishi *et al.* 1982). This leads to an extended diamond structure with direct diamond-diamond bonding with cobalt at the grain boundaries.

An alternative method of synthesising diamond from a carbon source under physical conditions well outside of the diamond stable region of the carbon phase diagram, is chemical vapour deposition (CVD) of diamond. Here synthesis takes place under low pressures where graphite is the stable form of carbon. Carbon based gases such as methane and acetylene mixed with hydrogen act as the carbon source for diamond growth. This gas mixture enters a reaction chamber at pressures below atmospheric and the carbon based gases are dissociated by means such as electric discharge (plasmas), microwave heating or a glowing tungsten wire. Diamond is deposited onto a substrate, which is often heated and can be of materials such as single crystal diamond, silicon or metal alloys. The hydrogen plays an important role in the microscopic kinetics of the diamond process to ensure that diamond and not graphite is deposited.

The single crystal diamonds used in the present work were all large synthetic crystals grown by the HPHT reconstitution method.

2.1.4 Optical properties

Fundamental to the optical properties of diamond is its large bandgap, 5.48 eV at 77 K (Field 1991). Infrared photons have energies appropriate to the excitation of lattice vibrations, while the wavelength of visible light is too short to excite vibrations and too long to excite valence

electrons from the valence band to the conduction band, i.e. diamond is transparent to visible light. Type I diamond is transparent from approximately 340 nm to 2.5 μm , and then again above 10 μm (Field 1992a), so it should appear colourless in the visible region (400 to 700 nm). Any colouration of diamond is due to absorption bands (impurity levels in the band gap) in the visible region. As mentioned the yellow colouration of type Ib diamonds results from the tail of the ultraviolet absorption associated with the substitutional nitrogen impurity.

Absorption of infrared (IR) photons occurs as a result of the excitation of vibrational modes in the lattice. The diamond structure has no intrinsic electric moment associated with it, and hence the absorption of light by a phonon is forbidden. There are, however, two ways in which absorption of light by pure vibrational means can occur, namely multi-phonon processes and defect induced one-phonon absorption.

In the case of multi-phonon absorption, one vibrational mode induces a temporary electric moment. Absorption of light can cause further vibration of these electric moments. This process is known as two-phonon absorption. Two and three-phonon absorption provide the only intrinsic vibrational absorption processes that occur in diamond. They are thus characteristic of the diamond lattice and hence common to all diamond types.

In a monatomic crystal, one-phonon absorption is generally due to substitutional impurity atoms of a mass greater than that of the host atoms, bonded to the host atoms with strengths comparable with those of the interatomic bonds of the latter. Such an impurity atom gives rise to an electric moment, allowing coupling of one-phonon vibrational modes to radiation. In diamond, there are several defects involving nitrogen that cause one-phonon absorption, which comprises a continuous band of frequencies up to 1332 cm^{-1} , the Raman frequency (the maximum frequency with which phonons can propagate in the diamond crystal). In figure 2.3 and table 2.2 the classification of diamond on the basis of the one-phonon absorption spectra of the different nitrogen defects has already been discussed.

2.1.4.1 Raman spectrum

Numerous authors have studied the Raman effect in diamond (see e.g. Solin *et al.* 1970, Borer *et al.* 1971, Parsons 1977). The $\mathbf{k} = 0$ optical phonons in diamond are triply degenerate due to the cubic symmetry of the crystal (F_{2g} mode). The position of the Raman band is $1332.5 \pm 0.5\text{ cm}^{-1}$ and the halfwidth is $1.65 \pm 0.02\text{ cm}^{-1}$ at 300 K according to Solin *et al.* (1970). Borer *et al.* (1971) report the position of the Raman peak position to be in the range 1332.1 cm^{-1} to 1332.6 cm^{-1} and the half width to be around 1.8 cm^{-1} at 300 K.

A more detailed treatment of the Raman effect is presented in chapter 3, in which the effect of stress on the position of the Raman peak position is also considered.

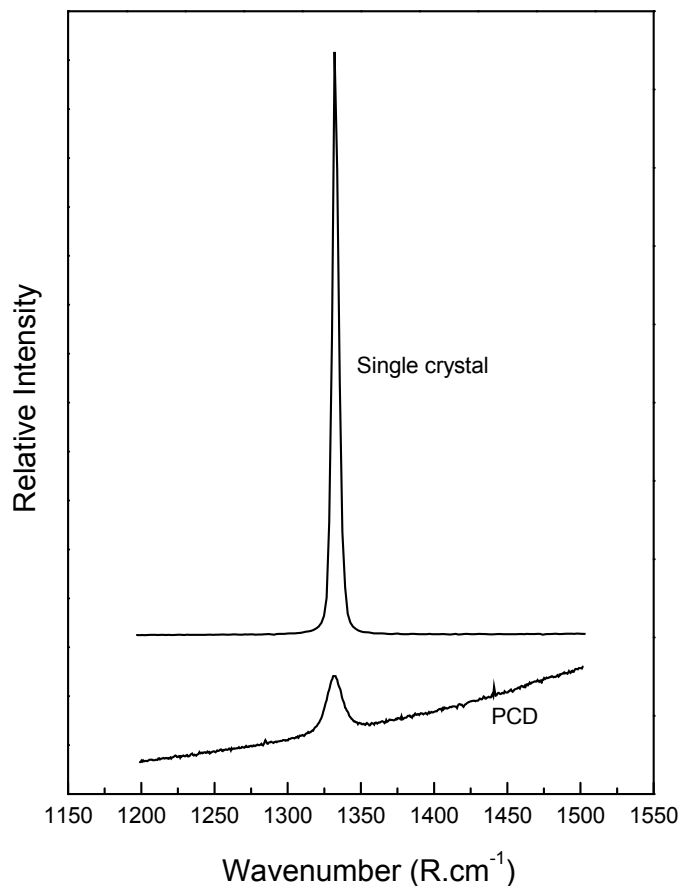


Figure 2.7: Typical Raman spectra for single crystal and polycrystalline diamond (PCD) (data measured by the author).

2.1.4.2 Luminescence

An incident photon may be absorbed by a defect in the diamond lattice by the excitation of an electron from the ground electronic state to an excited electronic state. The effect of the electronic excitation is to create a new spatial distribution of the electrons of the defect. The nuclei surrounding the defect now have to move to new equilibrium positions to accommodate the new electron distribution. In this case an electronic transition results in atomic vibration, so that the process cannot be considered a purely electronic phenomenon, but rather a vibronic phenomenon. The vibronic processes are treated in more detail in chapter 3.

In diamond, cathodoluminescence (luminescence excited by energetic electrons; CL) and photoluminescence (luminescence excited by photons; PL) are widely used in the study of

optically active defect centres. A large number of optically active centres are found in diamond, and a comprehensive listing is given by Field (1979, 1992a) and Zaitsev (2001).

Of the photoluminescent centres, this work is principally concerned with three nitrogen-vacancy defect centres, namely the H3 centre, the 575 nm centre and the 1.945 eV centre. The information contained in the position, width, intensity and line shape of the zero phonon line (ZPL) is discussed in chapter 3. The necessity of normalising the intensity of the spectra is discussed in chapter 4.4.1.

In cathodoluminescence the incident high-energy electrons produce electron-hole pairs. After excitation an electron and hole can capture each other to form a short-lived centre called an exciton. In diamond containing defects the excitons may be captured by optical centres which themselves become excited and then decay and produce characteristic luminescence. Due to the small penetration depth of electrons into the lattice, CL is a surface effect. Not all defect centres that are visible in PL, are active in CL, e.g. the H3 and 575 nm centres are observable in CL, but not the 1.945 eV centre. CL has extensively been used to study the detailed structure of diamond crystals, e.g. growth sectors by Burns *et al.* (1990) and Frank *et al.* (1990), indentations by Brookes *et al.* (1993) and experimental synthetic diamonds by Ponahlo (1992).

2.1.5 Nitrogen–vacancy defect centres of interest

As mentioned, there are three PL active defect centres involving nitrogen and a vacancy that are relevant to the work in this thesis. In this section, the relevant properties of each of these centres are summarised.

2.1.5.1 The H3 centre

The H3 centre with a ZPL at 2.463 eV (503.2 nm) is generally accepted to be a defect where a pair of nitrogen atoms in next nearest neighbour substitutional sites is separated by a vacancy, thus giving an N-V-N defect (Clark *et al.* 1992, Loubser *et al.* 1981). Davies *et al.* (1976b) have shown that this centre is due to a $\langle 110 \rangle$ electric dipole transition at a rhombic I centre. A rhombic I centre in diamond has C_{2v} point group with C_2 along the $\langle 100 \rangle$ axes. The H3 centre is created in the lattice during synthesis and is preferentially incorporated on $\{100\}$ planes, with the defect oriented along $[110]$ or $[\bar{1}\bar{1}0]$ directions. Dodge (1986) and Beard (1987) have suggested when nitrogen atoms form next nearest neighbour pairs orientated along either $[\bar{1}\bar{1}0]$ or $[110]$ on (001) growth surfaces, further diamond growth envelopes the pairs and may leave a vacant lattice site surmounting each pair to form N-V-N defects. The H3 centre is thus widely found in

synthetic diamonds. Annealing studies have shown that H3 increases in concentration up to 1800° C (Evans *et al.* 1984).

Piezo-spectroscopy experiments were undertaken by Davies *et al.* (1976b) to investigate the response of the H3 centre to uniaxial stress. Data was recorded both in absorption and emission (PL). Uniaxial stress was applied up to 3 GPa along $\langle 001 \rangle$, $\langle 111 \rangle$ and $\langle 110 \rangle$ axes at liquid nitrogen temperatures. In PL, the H3 ZPL splits into components with the same rate of frequency change with stress as observed in absorption. The relative intensities of the components were found to be independent of the magnitude of the applied stress, being different from absorption measurements, where such dependence was observed.

The H3 centre is observable in absorption, CL and PL spectroscopy, provided that in the latter case illumination takes place with a sufficiently intense source with a wavelength shorter than 503.2 nm. Typically the 488 nm line of an argon ion laser is used. In luminescence the H3 centre emits a bright green light.

This defect is also observed after annealing radiation damage in diamond containing A centres (Davies 1972). It is also found in unirradiated diamond, associated with slip lines, dislocations and platelets (Hanley *et al.* 1977) and plastically deformed diamond (Brookes *et al.* 1993), as well as as-grown synthetics (Collins 1991).

The origin of the H3 centre in natural diamond requires a different mechanism from that for synthetic diamonds. In natural diamonds, the defect arises from the trapping of radiation products (vacancies) by A centres together with simultaneous formation of the H4 defect centre from B centres by the same mechanism (Davies 1972).

As A centres are rare in synthetic diamond (unless deliberately aggregated or grown in), the presence of the H3 centre indicates either the presence of A centres and vacancies or the HPHT origin of the diamond. As vacancies may arise from irradiation or plastic deformation, the presence of H3 centres in unirradiated natural diamond is quoted as evidence of plastic deformation.

2.1.5.2 The 575 nm centre

It is generally accepted that this defect centre with a ZPL at 2.156 eV involves a nitrogen atom and a vacancy (Walker 1979). In a more detailed model by Zaitsev *et al.* (1991) it was suggested to be a vacancy bonded with a nearest single nitrogen atom in a tetrahedral internode in the direction $\langle 100 \rangle$ having symmetry C_{2v} . Evidence for this suggestion was provided by natural

diamonds where the defect centres were generated by ion-implantation and the splitting of the CL lines by bending of thin diamond plates was subsequently studied.

Subsequently it was suggested that the 575 nm defect centre is the neutral charge state of the [N-V] centre, being a single substitutional nitrogen and a vacancy (Mita 1996, Iakoubovskii *et al.* 2000a). Mita (1996) based this suggestion on observations of the defect centre after irradiating type Ia and Ib diamond with high doses of neutrons, followed by annealing. Iakoubovskii *et al.* (2000a) based their suggestion on spectrally resolved measurements of photochromism of the 2.156 eV and 1.945 eV centres in CVD diamond. According to Zaitsev (2001) the [N-V]⁰ designation is the currently accepted structure of the 575 nm defect.

The 575 nm defect centres are known to decorate slip lines in diamond (Brookes *et al.* 1993, Collins *et al.* 1985) They can be created in all diamonds by electron irradiation followed by annealing (above 550° C and typically at 800° C) (Collins 1979, Walker 1979, Clark *et al.* 1992) or as a result of plastic deformation (Collins *et al.* 1985, Davey *et al.* 1984). Brookes *et al.* (1990, 1993) have established an association between the formation of the 575 nm defect and the presence of slip as seen in cathodoluminescence images of type Ib diamond indented with a soft indenter.

The 575 nm defect centre is readily observed in CL, but not as strongly in PL.

2.1.5.3 The 1.945 eV centre

This defect centre, with a ZPL at 1.945 eV (637.3 nm), is associated with an electronic transition at a centre with trigonal symmetry (C_{3v} point group) from an A₁ ground state to an E excited state. The centre was shown to be the negative charge state of the [N-V] defect (Davies *et al.* 1976c, Loubser *et al.* 1977). It is only observable in absorption and photoluminescence and there is no evidence for the presence of the Jahn-Teller effect (Walker 1979).

The 1.945 eV centre is most commonly observed in synthetic diamond after irradiation with electrons and subsequent annealing above 550° C; it has also been observed in as-synthesised diamond, but very weakly (Collins 1979). The centre is stable at 1500 °C (Collins 1980). In support of the model discussed above, Von Enckevort *et al.* (1988) have shown a correlation between the dispersed nitrogen concentration and the 1.945 eV centre concentration. Furthermore the most intense luminescence from this centre occurred where the highest concentration of single substitutional nitrogen is found, namely in the {111} growth sectors.

2.1.6 Mechanical properties

It has already been mentioned that many of diamond's unique properties can be traced back to the detailed structure of the crystal lattice (§ 2.1.1). The arrangement of carbon atoms produces a lattice in which the bonds are very stiff and difficult to break, which in turn means that the elastic modulus is very high and dislocation movement very difficult. The extreme hardness and stiffness produced in diamond means that this atomic structure is very brittle. The energy to produce a crack is equal to the energy needed to create the two new surfaces, i.e. there is little or no energy lost to plastic behaviour. The periodicity of the diamond lattice means that fracture in diamond is anisotropic, with cleavage occurring predominantly on the {111} plane. A list of relevant mechanical properties is given in table 2.1.

2.1.6.1 Hardness

The concept of hardness as a material property can be defined in various ways, as it depends on the type of test and the conditions of testing as to which results are obtained. The Mohs scale of hardness is a useful relative scale based on a simple scratch test. It ranks materials according to their "scratch resistance" from softest (1) to hardest (10, diamond). It is not quantitative in any sense.

The definition of hardness mentioned in the Introduction can physically be described simply in terms of the resistance of a material to local indentation. A shaped indenter is forced into a flat surface under the action of a known normal load to form a permanent indentation in the surface. If a load W is applied and A is the area of the permanent indentation, the hardness is conveniently defined as $H = W/A$. Using this definition, the hardness is essentially a measure of the plastic properties of the material and it quantifies the ability of the material to withstand plastic deformation. In practice, this indentation hardness is difficult to measure. There are several different types of indenter, each a specific material with a specific geometry. The indentation tests work on the basic premise of measuring the critical dimensions of an indentation left by a specifically dimensioned and loaded indenter. The crystallographic plane on which the indentation is made as well as the orientation of the indenter geometry with respect to the crystallographic directions on the plane influence the outcome of the test. Two well-known hardness tests are briefly mentioned as examples.

The Vickers hardness test makes use of a diamond in the form of a square-based pyramid with included angle of 136° as the indenter. The Vickers hardness is calculated from the force applied and the average length of the diagonal of the indentation left by the indenter. This test is

often easier to use than other hardness tests since the required calculations are independent of the size of the indenter. It can be used for a wide range of materials and has one of the widest scales among hardness tests.

The Knoop hardness test is a microhardness test, i.e. a test for mechanical hardness used particularly for very brittle materials or thin sheets. A pyramidal diamond point is pressed into the polished surface of the test material with a known force, for a specified dwell time and the resulting indentation is measured using a microscope. The geometry of this indenter is an extended pyramid with the length to width ratio being 7:1 and respective face angles are 172° for the long edge and 130° for the short edge. The Knoop hardness is calculated from the length of the indentation along its long axis and the applied load.

Other than geometric factors, it has also been found that, under otherwise identical experimental conditions, the measured indentation hardness of diamond increases as the applied normal load decreases. This phenomenon is known as the indentation size effect (Brookes 1979, 1992a). It is of most importance at loads below 20 N and will be exacerbated where low loads are used to minimise the effect of cracking in brittle behaviour. It is thus very important to control the normal load for accurate and reproducible hardness measurements in very hard materials such as diamond.

A concept that is tied very closely to that of hardness, is that of strength, especially compressive strength. Strength measurements are usually related to the testing of small diamond crystals, as their dimensions make it very difficult to use indentation methods. Field (1992b) and references therein give a very good general overview of the methods involved and their respective advantages and disadvantages. These methods usually make use of a crushing technique where the grit is crushed between rollers or individual particles are compressed between anvils. The strength of the batch of crystals being tested can be expressed in a variety of ways. For the grit crushed by rollers, a qualitative ranking for different batches of grit can be made by comparing the fraction of uncrushed grit remaining after a pass through the rollers. For the crushing between anvils, the strength may be plotted as a compressive fracture strength distribution graph (Webb *et al.* 1995). In the literature there is a wide variation in the reported experimental values for the strength of diamond. This illustrates not only the difficulties in working with an ultra-hard material such as diamond, but also that the strength of individual diamonds are significantly affected by defects, inclusions and impurities within each crystal.

At elevated temperatures, it has been shown (e.g. Brookes 1979) that the measured hardness of diamond using indentation methods decreases monotonically with increasing

temperature. Initially the decrease is approximately linear with temperature, while at about 1500 °C the decrease in rate begins to diminish, i.e. the unit decrease in measured hardness per unit temperature increase reduces. This trend is explained as an initial increase in dislocation activity due to the increase in temperature, which aids the lattice to flow during an indentation. This leads to a larger indentation area for a given load and thus a lower measured hardness. For diamond, significant plastic deformation has only been observed at temperatures above 750° C (Brookes *et al.* 1990). The flattening out of the trend is explained as a work hardening effect due to the dislocations interacting with one another to retard the dislocation movement.

The effect of nitrogen on the room temperature hardness of diamond is still somewhat uncertain, but Knoop hardness experiments indicate that the nature of the nitrogen impurity plays a definite role. Knoop hardness values for type II diamond are higher than those for type I diamond for a variety of crystal planes and crystallographic orientations (Brookes 1979 and Brookes 1992a). The effect of nitrogen on the plasticity of diamond has been researched in more detail, and this is treated in the next section.

2.1.6.2 Plastic deformation

In discussing the plastic behaviour of diamond, it is first necessary to define the concepts of Brittle-Ductile Transition Temperature (BDTT) and Critical Resolved Shear Stress (CRSS). The definitions below follow the treatment of Daniel (2000).

The **BDTT** is that transition temperature at which a material, under load, ceases brittle behaviour and becomes ductile / plastic. In a single crystal, this temperature is only the temperature at which dislocation activity is possible. The identification of the BDTT depends on the definition of the point at which brittle behaviour ceases and plasticity begins and in turn this depends on the experimental conditions. A crystal can thus fail in a brittle manner but still show signs of plasticity. From an engineer's point of view the BDTT can be seen as the point at which dislocations affect the properties of the material, while a physicist would view the BDTT as that point when the very first signs of dislocation activity are observed.

Observing a well-prepared crystalline surface, the clearest evidence of plastic deformation will be that of slip lines or bands. This type of plasticity is known as translational slip and is where one part of a crystal lattice has moved with respect to another under an applied shear force. There is thus no net change in the crystal order.

The long-range order of crystals means that slip is generally confined to certain planes and directions, called slip systems. This anisotropy in slip is directly related to the order in which

the atoms are laid down in the crystal lattice. The direction most easily sheared is generally the one where the distance between the neighbouring atoms is the shortest and the most easily sheared plane of atoms is the one with the densest packing. In diamond, with an f.c.c. structure, the slip direction is $\langle 110 \rangle$ and the plane $\{111\}$ and the slip system is usually written as $\{111\}\langle 110 \rangle$. The symmetry of crystals means that for a given crystal and direction of force, there is often not just one active slip plane but several, all from within the same family of slip planes.

The point of greatest shear stress should also be the point where slip initiates, although with crystals this point may not correspond with the slip plane and direction of the crystal. Therefore, the point where slip initiates may not be the point that has the greatest magnitude of shear but rather the point at which the shear force exceeds the critical value for initiation of slip in that slip plane. It follows that the critical resolved shear stress (**CRSS**) is defined as that level of stress acting over the active slip plane and in the slip direction which is just sufficient to initiate plastic flow. As a rule of thumb, the CRSS for covalent crystals is $10^{-2} G$ where G is the shear modulus (table 2.1).

Diamond is accepted as the material with the greatest resistance to plastic flow. It is thus of interest to accurately determine the conditions under which such flow is possible. In natural diamonds dislocations have been associated with a brown colour (Harris 1992). Dislocations in natural diamond have been observed with TEM and have been associated with blue cathodoluminescence (Sumida *et al.* 1981). Evans *et al.* (1967) have shown that bulk plastic flow can be induced in thin plates of natural diamond loaded in three-point bending at temperatures in excess of 1900 K.

The issue of dislocation motion in diamond at room temperature is more controversial. Brookes *et al.* (2001) state that experimental evidence points to the conclusion that dislocation motion is not possible except at high temperature.

The CRSS for diamond is higher than the stress necessary for cleavage fracture. In much of the literature using conventional indentation techniques (e.g. Knoop test), it is likely that some degree of brittle fracture took place before any dislocation movement could be initiated. This relieves much of the stress and makes it unlikely that any remaining stresses would be sufficient to initiate dislocation movement. The soft indenter technique pioneered by Brookes (Brookes 1979, 1992a and references therein) inhibits stress concentrations that cause brittle failure and promotes plastic behaviour by allowing the necessary shear stresses to be set up in the material for dislocation formation and movement to take place.

One of the seminal papers illustrating the application of the soft impressor method to measure the indentation hardness of diamond at high temperature (1100° C), is that by Brookes *et al.* (1990). It was shown that it is possible to induce multiple intersecting slip in type Ia, synthetic type Ib and type IIa diamond at relatively low homologous temperatures, i.e. $\sim 0.35 T_m$ (where T_m is the melting temperature in Kelvin). Generally temperatures of approximately $0.5 T_m$ are taken as the point of onset of plastic deformation (BDTT). It was also shown that the ease and extent of dislocation movement decreases in the order: synthetic type Ib, natural type Ia, natural type IIa.

The above work was extended with topographic and spectroscopic cathodoluminescence work on indentations in different types of diamond (Brookes *et al.* 1993). Indentations were made at 1400° C on near- $\{001\}$ polished faces using conical cubic boron nitride indentors. It was shown that the patterns of slip in the different regions surrounding the indentation pits are active in cathodoluminescence. In synthetic type Ib diamond, the dominant visual decoration of the slip traces was by the species responsible for the 575 nm luminescence centre. Some band A luminescence was also detected spectroscopically. In type IaA diamond the decorating species was the well-known H3 centre, and for type IaB diamond it was the 491 nm centre. In the latter two cases it was found that the emission spectra were severely broadened by lattice strain. For the type IIa diamond, slip patterns were absent from the regions surrounding the indentations.

The above observations were explained as follows: Vacancies were generated during the dislocation movement that was responsible for the slip patterns. These vacancies were mobile at the measurement temperatures and diffused through the lattice, becoming trapped at nitrogen centres in the diamond lattice to form the observed optically active vacancy-nitrogen defect centres. The 575 nm defect centre is associated with a single substitutional nitrogen-vacancy pairing and the H3 centre has been shown to be a N-V-N defect centre (see the discussion and references in section 2.1.5). Photoluminescence also showed the presence of the 1.945 eV defect centre (a N-V defect) for the type Ib diamond. The band A luminescence is associated with dislocations (Yamamoto *et al.* 1984), its presence being consistent with the above explanation.

Photoluminescence studies of polycrystalline sintered diamond compacts were reported by Evans *et al.* (1984) and Davey *et al.* (1984). Complementary cathodoluminescence studies were undertaken by Collins *et al.* (1985). The sintering temperature was $> 1300^\circ \text{C}$, i.e. well above the temperature at which vacancies become mobile in the lattice. With natural diamond compacts, an increase in the intensity of the H3 defect centre with increasing temperature was reported using PL and CL. For synthetic diamond compacts, the 1.945 eV and 575 nm defect centres were observed to increase in intensity to about 1500°C , after which their intensity

decreased. The intensity of the H3 centre increased up to the maximum temperature of 1800° C, by which stage the 1.945 eV and 575 nm centres had disappeared. The authors explained the results in terms of the creation of vacancies by plastic deformation during the sintering process, these becoming trapped by nitrogen centres. The nitrogen centres depended on the type of diamond involved (C centres for synthetic type Ib diamond, and A centres for natural diamond). At temperatures above 1300° C, the single substitutional nitrogen in synthetic diamond was considered to diffuse by the vacancy enhanced mechanism (i.e. as N-V pairs) and to combine with other nitrogen atoms to form H3 defects.

Measurements of the strain broadening of the emission spectra showed that the diamond crystals in the compacts were under considerable strain whose magnitude depended on the grain size: the smaller the grain size, the larger the strain. The luminescence intensity was also found to depend on the grain size, with a higher intensity reported for smaller grain size. This was interpreted as the amount of plastic deformation being larger for compacts of smaller grain size.

From the literature quoted above, it is clear that it is widely accepted that plastic deformation of diamond is possible at elevated temperature. Brookes (1992b) developed a schematic diagram to represent the effect of temperature and pressure on the deformation of diamond and this was slightly modified by Daniel (2000) (figure 2.8).

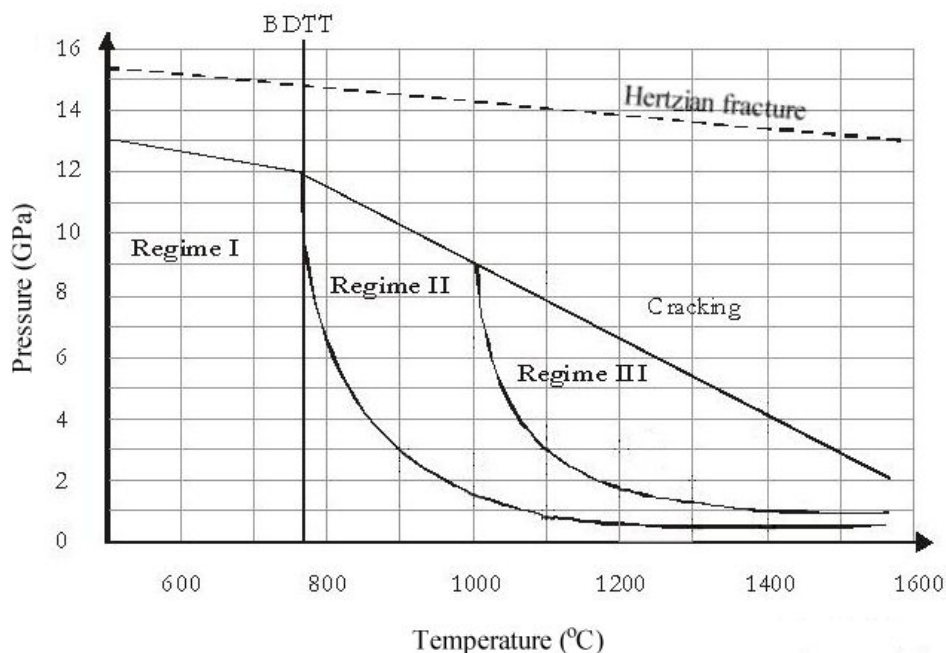


Figure 2.8: Schematic diagram illustrating the effect of temperature and pressure on the deformation of diamond (Daniel 2000).

It can be seen from this diagram that there are three distinct regions of deformation. Regime I is distinguished by the purely elastic response to applied load up to a certain maximum pressure, beyond which the fracture stress is exceeded and Hertzian {111} ring cracks are produced. Regime II begins at the BDTT, and is a region where both elastic and plastic responses are found but the pressure to produce plastic deformation reduces in a parabolic manner with increasing temperature. If cracks are produced in this region, they tend to lie on {110} planes and are considered to be produced by dislocation interactions. The onset of regime III is where the plasticity level becomes relatively insensitive to temperature.

Brookes (1992b) also showed that while the shape of figure 2.8 is the same for all types of diamond, the BDTT is dependent on the type of diamond, with the BDTT at 770° C, 950° C and 1100° C for types Ib, Ia and IIa, respectively. Since the classification of diamond depends on its nitrogen content, it implies that the BDTT is a function of nitrogen content.

More recently Daniel (2000) has reported on the effect of nitrogen concentration on the BDTT in synthetic type Ib diamond. With reference to figure 2.8, at lower experimental temperatures ($\approx 750^{\circ}\text{C} - 1300^{\circ}\text{C}$), reducing the nitrogen content increases the temperature needed to produce plastic deformation, i.e. the BDTT. At higher temperatures ($> 1300^{\circ}\text{C}$) the opposite is observed. Reducing the nitrogen content at these temperatures increases the extent of plastic deformation, i.e. a response equivalent to reducing the BDTT.

Daniel (2000) also showed that the region II/III boundary is not a straight line as suggested by Brookes (1992b), but has a slope similar to that of the region I/II boundary, with an onset above 1000° C. Reducing nitrogen concentration has the effect of lowering the region II/III boundary.

2.2 Cubic boron nitride

Unlike the almost universal knowledge of diamond, albeit as a gemstone, cubic boron nitride (cBN) is a material only known to those utilising it for its specific physical and chemical properties. In many ways these properties are similar to those of diamond, but cBN has a unique subset of properties making it attractive for industrial use in grinding, cutting and polishing applications.

This section will give a brief overview of the properties of cBN, with a focus on those relevant to the work in this thesis. Topical reviews of the synthesis, physico-chemical properties and applications of cBN are given by Vel *et al.* (1991) and Demazeau (1993).

2.2.1 Crystal structure

The elements boron and nitrogen lie on either side of carbon in the periodic table, making the compound boron nitride (BN) iso-electronic with carbon. As with carbon, it occurs in several phases. Hexagonal boron nitride (hBN) (also called gBN or α BN in some papers) has a graphite-like structure. It is a white, soft solid that is used as a refractory and lubricant. The hBN lattice consists of a stacking arrangement along the c axis of planar layers of hexagonal rings, boron and nitrogen alternately occupying the corners. The layers sequence in hBN is ABAB... (boron and nitrogen atoms also being alternate along the c axis). The intralayer B–N bonds are strongly covalent (sp^2), whereas the interlayer bonds are weak, being of the van der Waals type.

A second form of BN isotopic with hexagonal diamond is BN in a wurtzite-type structure (wBN). This lattice can be imagined as a perturbation of the above hexagonal arrangement with the hexagons deformed so that the hybridization changes from sp^2 to sp^3 . Each (001) planar layer of the lattice splits into two planes: one contains boron atoms and the other nitrogen atoms along the c axis. The stacking sequence ABAB... (where each plane contained boron and nitrogen) is replaced by the stacking sequence abab... (where alternating planes now consists entirely of boron or nitrogen). The wBN phase is not considered thermodynamically stable (see the discussion of the BN phase diagram in the section on synthesis).

Rhombohedral BN (rBN) is also a variation on the hBN lattice, where the stacking sequence is ABCABC, i.e. a different stacking arrangement along the c axis. This phase of BN does not have an analogous carbon structure.

The phase of BN of interest here is the cubic form cBN, also called zBN (for zincblende) or sphalerite or β BN. It has a zincblende structure with tetrahedral symmetry (space group T_d^2 , 2 atoms per unit cell), and thus has a cubic structure without an inversion centre. The boron and nitrogen bonds are sp^3 hybridised. The B–N bond is highly covalent, although some charge transfer does take place, i.e. there is some ionic character. cBN thus has the same structure as that of the diamond lattice, with its associated extreme rigidity. It is the second hardest material after diamond and has the second highest thermal conductivity. The physical properties of cBN are discussed in § 2.2.3 and a listing is given in Table 2.4.

The crystal habit of synthesised cBN crystals varies from irregular block-like forms without definite habit to regular {111} first order tetrahedra. The cBN lattice has six {110} cleavage planes.

Unlike diamond, all the phases of BN are synthetic, i.e. they do not occur in nature.

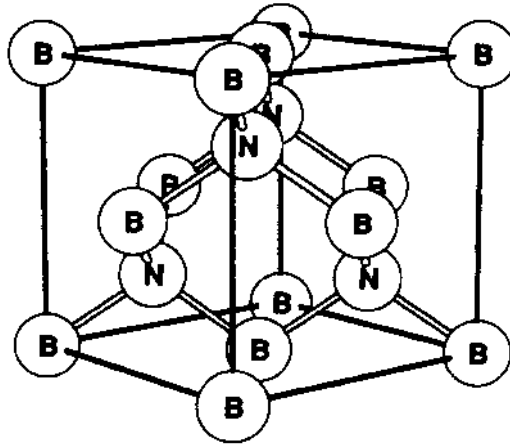


Figure 2.9: Crystal structure of cBN, showing the cubic arrangement of the boron and nitrogen atoms.

2.2.2 Synthesis of cBN

In the same way diamond is synthesised from graphite at high pressure and temperature, so cBN is synthesised from hBN under such conditions in very similar equipment. The cBN may be obtained either through direct conversion, or with the aid of a flux precursor to decrease the high activation energy for the direct transformation through a dissolution–re-precipitation process.

The first synthesis of cBN was reported by Wentorf (1957), while the earliest BN phase diagram was suggested by Bundy *et al.* (1963). The phase diagram drew on the experimental work by Wentorf (1959, 1961) and estimations of the positions for the cBN melting curve and the BN triple point based on the analogous behaviour of the carbon phase diagram at high pressure and temperature. The hBN \leftrightarrow cBN equilibrium curve was extrapolated to the low pressure region of the phase diagram by Corrigan *et al.* (1975) based on the similarity of the BN and carbon phase diagrams at high pressure. This extrapolation suggested, in analogy with carbon, that the denser modification of BN (cBN) is metastable over the entire temperature range. The equilibrium line as modified by Tani *et al.* (1975) can be expressed as follows

$$P(\text{GPa}) = 0.0030T(\text{K}) - 1.03, \quad (2.1)$$

where the pressure P is in GPa and the temperature T is in Kelvin.

However, thermodynamic calculations by Solozhenko (1988, 1995) showed that the low temperature region of the BN phase diagram is fundamentally different from the corresponding region in the carbon phase diagram. Whereas the graphite \leftrightarrow diamond equilibrium line intersects the pressure axis at $P = 1.35$ GPa, making diamond the metastable phase under normal

conditions, the hBN \leftrightarrow cBN equilibrium curve intersects the temperature axis at $T \sim 1570$ K, making cBN the stable phase under normal conditions (figure 2.10). This is drastically different from the earlier accepted notions regarding the thermodynamic stability regions for BN and carbon. Calculations of the equilibrium curves for the four different modifications of BN (Solozhenko 1995) showed that there were no regions of thermodynamic stability for the wBN and rBN phases within the studied pressure-temperature space (0 – 4000 K, ≤ 10 GPa). It was estimated that the thermodynamic stability region for wBN would occur at pressures in excess of 30 GPa.

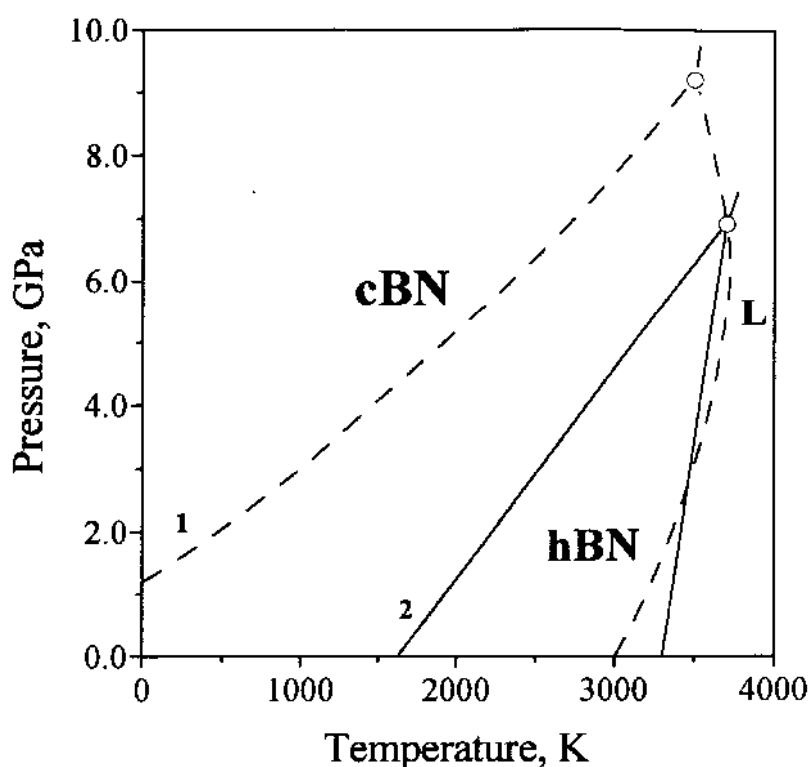


Figure 2.10: Phase diagram of BN, showing the hBN \leftrightarrow cBN equilibrium curves as suggested by (1) Bundy *et al.* (1963) and (2) Solozhenko (1988, 1995).

The first direct conversion of hBN to cBN was reported by Bundy *et al.* (1963), using a belt-type apparatus. In this and subsequent work (Wakatsuki *et al.* 1972), it was found that the hBN to cBN direct conversion depends on several factors. The particle size and crystallinity of the precursor material was very important, as well as the purity of the starting materials. It was found that under optimum conditions a full conversion of hBN to cBN could be achieved at a pressure of 6.0 GPa and a temperature of 1420 K – 1720 K. The resulting cBN material was

usually in the form of polycrystalline aggregates. Under non-optimum conditions, higher pressures (11 – 12 GPa) and higher temperatures (≥ 2000 K) were required to achieve a direct conversion. Poorly crystallised hBN (i.e. with broadened X-ray diffraction lines) was found to yield only cBN. Well-crystallised hBN yielded wBN in addition to cBN. The presence of B_2O_3 (Corrigan *et al.* 1975) and water (H_2O) in the precursor hBN material was also found to influence the conversion conditions. Water acted as a catalyst (Susa *et al.* 1974), i.e. lowered the pressure and temperature required for synthesis, while B_2O_3 had the opposite effect.

A technologically simpler solution is to convert hBN to cBN with a catalysed process. This is the main method used on an industrial scale for the production of cBN. In this process, compounds are added to hBN to decrease the high activation barrier for conversion that involves the breaking and reforming of atomic bonds. These compounds that are added are not strictly speaking catalysts, but rather flux precursors, giving a eutectic with hBN. At high pressure and temperature, cBN crystals are spontaneously nucleated in the cBN stable part of the phase diagram. There are a large number of compounds and their derivatives that can act as flux precursors for the hBN \rightarrow cBN conversion. The most widely used are lithium, magnesium and calcium, as well as the nitrides of these alkaline and alkaline earth metals. With the metals, brown to black crystals are produced and the colour is explained by the presence of a high concentration of B in the lattice. With the nitrides, no free boron is present and the cBN crystals are yellow to transparent in colour. Other possible flux precursors include fluoro-nitrides, water, inorganic fluorides, silicon, silicon nitride and aluminium nitride and are reviewed by Vel *et al.* (1991). Crystals obtained are generally small in size (submicron to ~ 0.5 mm) and have predominant tetrahedral or octahedral shapes, the latter usually truncated. As with diamond, the crystals often contain flux precursor residues as inclusions.

Solozhenko *et al.* (1990) have reported on the impurities found in cBN crystals as analysed via mass spectrometry and X-ray microanalysis. The elements carbon, oxygen, magnesium and silicon were present in concentrations of more than 0.05 mass %, while sodium, aluminium, phosphorus, chlorine, potassium, calcium, iron and copper were present in trace amounts. The authors point out that crystals synthesised by other groups may possibly have a very different impurity content to that determined for their crystals. It was also reported that the impurities were likely to be in the form of micro-inclusions rather than being incorporated directly in the lattice.

The HPHT reconstitution method (temperature difference method) for diamond synthesis described in § 2.1.3, can also be applied to the synthesis of cBN (Mishima 1990). The flux

precursors used are generally those based on the alkaline and alkaline earth metals and their compounds mentioned earlier in this section. As with diamond, much longer synthesis times are required to grow larger crystals. Yazu *et al.* (1986) have patented a pressure cell for this synthesis, and Mishima *et al.* (1987) have reported on techniques to obtain the desired temperature differential. It appears that cBN is not produced as an industrial commercial product using the HPHT reconstitution method.

The samples used in this thesis were all synthesised using the standard catalysed hBN → cBN conversion process, but for completeness it must be mentioned that cBN may also be synthesised using dynamic shock methods (Sawaoka *et al.* 1984) and methods based on synthesis of cBN from gas phase precursors, analogous with diamond CVD processes. In the case of cBN the gas phase methods can be CVD-based (e.g. Demazeau 1993, Ichiki *et al.* (1994) and Zhang *et al.* (2001)) or physical vapour deposition (PVD) processes (e.g. Hofsäss *et al.* (1995)), and generally consist of the degrading of a BN precursor with a hot filament, plasma or laser. The reactive chemical species are then deposited on a substrate, which may have a negative electrical bias, and can be made of materials such as ceramics, glass and TiN. Solozhenko (1994) has also shown that cBN may be synthesised at low pressures in conventional systems in the presence of supercritical fluids. Growth of cBN on the octahedral faces of diamond single crystal seed crystals in the hBN–Li₃N–NH₃ system took place at a temperature of $T \sim 1200$ K and atmospheric pressure.

The phase diagram of BN is dependent on the different equilibrium lines for the different BN phase modifications. As all the phase transformations in both direct conversion and catalytic processes take place under non-equilibrium conditions, it is important to take note of the decisive role of kinetic factors in determining which conversions are observed. The kinetics depend strongly on factors such as the grain size of the starting materials, their defect content and purity. Sachdev *et al.* (1997) investigated the phase transformation of cBN to hBN at normal pressure. The work showed that cBN is the stable modification of BN at standard conditions in agreement with the thermodynamic calculations by Solozhenko (1988, 1995). The onset temperature for the conversion was found to depend strongly on the grain size and impurities present in the starting materials, with the lowest temperature of 900° C observed for micron sized cBN. Evidence was presented that both a solid state and a gas phase mechanism have to be considered when accounting for the phase conversion.

As in the case of diamond, polycrystalline derivatives of cBN also exist. PcBN materials are manufactured at very high temperatures and ultra-high pressures to maintain the stable, cubic

form of boron nitride (cBN), forming a tough, coherent, high strength and chemically stable aggregated material. Grains of cBN, with an average diameter of 10 μm , are sintered in the presence of a metal, usually aluminium. During sintering, cBN grains form a skeletal structure, with little evidence of crystal regrowth. Within the voids of the skeleton, the aluminium binder reacts with the cBN, producing a mixture of aluminium nitride (AlN) and aluminium diboride (AlB₂). AlN encloses the exposed cBN grains whilst the AlB₂ forms a rigid, chemically inert binder. PcBN materials are also manufactured through the addition of titanium with the aluminium, which at high volume fractions (>20%) forms a titanium carbide binder phase. High cBN content PcBN material (~90 wt% cBN) is usually in solid form, whereas materials with TiC are brazed onto a WC/Co substrate for support.

2.2.3 Physical properties

Table 2.4 is a listing of physical properties of cBN. The previous sections have mentioned the similarities between diamond and cBN, largely based on the correspondence of their crystal structures. The similar properties of the two ultra-hard materials lead to matching applications in industry. There are, however, a few important differences in the properties of diamond and cBN, which yield certain advantages of cBN as a commercial product.

Table 2.4: Physical properties of cBN (Vel *et al.* 1991).

Property	Symbol	Value
Density	ρ	$3.48 \times 10^3 \text{ kg.m}^{-3}$
Refractive index	n	2.117 (at 589 nm)
Lattice parameter	a	$0.3615 \pm 0.0002 \text{ nm}$
Young's Modulus	E	$8.33 \times 10^{11} \text{ N.m}^{-2}$
Shear Modulus (calculated)	G	$4.22 \times 10^{11} \text{ N.m}^{-2}$
Bulk Modulus (experimental)	K	$3.67 - 4.00 \times 10^{11} \text{ N.m}^{-2}$
Mechanical hardness	H	9 – 10 (Mohs scale) 40 – 90 GPa (Knoop scale) 60 – 75 GPa (Vickers microscale)
Compressive Strength	S	4.15 – 5.33 GPa
Poisson's Ratio	ν	0.316
Debye Temperature		~ 1700 K
Thermal Conductivity (at 293 K)		200 – 900 $\text{W.m}^{-1}.\text{K}^{-1}$
Thermal Expansion (at 700 K)		$4.80 \times 10^{-6} \text{ K}^{-1}$
Indirect bandgap (measured, 293 K)		$6.4 \pm 0.5 \text{ eV}$ (UV absorption)
Electrical Resistivity (298 K)		$10^{10} \text{ }\Omega.\text{m}$ (undoped) $10^2 - 10^4 \text{ }\Omega.\text{m}$ (p-type) $10^3 - 10^7 \text{ }\Omega.\text{m}$ (n-type)

As mentioned previously, diamond is extremely inert to chemical attack except by those chemicals that act as oxidising agents at high temperature. cBN is also chemically highly inert, but has a higher resistance to degradation under oxidising conditions. While diamond reacts with metals such as iron, cobalt, manganese and nickel, which in the molten state are true solvents for carbon, cBN has a low chemical reactivity with the iron group of metals, and is thus particularly suited to machining hardened steels, chilled cast iron, carbides and nickel or cobalt-based superalloys.

Comparing tables 2.1 and 2.4, it can be seen that cBN ranks second after diamond in terms of its thermal conductivity. This property also makes it very suitable for engineering applications such as those mentioned in the previous paragraph, as the heat generated at the tool / workpiece interface is rapidly conducted away.

cBN is also a III-V semiconductor with a very large bandgap. It is an indirect bandgap material with a bandgap of 6.36 ± 0.03 eV (Evans *et al* 2008). It can be doped either n-type (B, S, Si) or p-type (Be), which makes it possible to manufacture p-n diodes and other electronic devices (Era *et al.* 1990, Mishima 1990).

2.2.3.1 Indentation hardness

One of the important figures of merit when considering the hardness of a material, is the value of its bulk modulus (K). Experimental work in the past decade has done a great deal to eliminate much of the uncertainty regarding the value for cBN, after initial speculation that cBN may have a larger value than that of diamond. Experimental work in a diamond anvil cell at room temperature, along with supporting theoretical calculations by Knittle *et al.* (1989), returned the value of $K = 369 \pm 14$ GPa. This value was also confirmed via shock wave experiments in the same paper. Measurements of the elastic constants of cBN via Brillouin spectroscopy by Grimsditch *et al.* (1994) gave $K = 400 \pm 20$ GPa. Local density approximation (LDA) calculations have been carried out for cBN and have resulted in values of $K = 390$ GPa (Van Camp *et al.* 1989) and $K = 398$ GPa (Kern 1998 and Kern *et al.* 1999). Molecular dynamics simulations using a Tersoff potential gave $K = 365.3$ GPa (Sekkal *et al.* 1998). Datchi *et al.* (2007) found $K = 395 \pm 2$ GPa by fitting high-pressure XRD data to various Equation of State (EOS) models. It is clear that earlier estimates of the bulk modulus as 465 ± 50 GPa (Sanjurjo *et al.* 1983) based on empirical correlations for elastic constants were too high.

Standard indentation hardness measurements via the Knoop indenter and Vickers indenter methods have been reported for cBN (see table 2.4). Brookes *et al.* (1983) have reported

Knoop hardness measurements on cBN. They have found that measured values for cBN depend on the face being tested as well as on the direction of testing on a particular face, being similar to the anisotropy found for diamond. This is not surprising since cBN has a similar crystal structure to diamond and has the same slip system, namely $\{111\}\langle 110\rangle$.

With regard to the plastic deformation of cBN, relatively little work has been done in comparison with diamond. Novikov *et al.* (1985) have reported that plastic deformation of cBN is possible at room temperature, in contrast to diamond. In their work, the plastic deformation of cBN was studied at various pressures, temperatures and holding times via the broadening of the (220) and (331) X-ray diffraction peaks. It was found that cBN readily underwent plastic deformation at high pressure and temperature (8.5 GPa, 2100° C). Plastic deformation of cBN crystals under loading conditions approximating hydrostatic pressure and room temperature also showed evidence of plastic deformation. In sintered polycrystals, two stages were observed during compression. An initial stage of broadening of the XRD lines was observed, attributed to a compaction stage where a large degree of plastic deformation and associated dislocation motion took place, followed by a decrease in the width of the lines, attributed to the annealing of defects and / or the decrease in dislocation density.

As far as it is known, no indentation work using soft indenter based techniques has been attempted yet, very likely due to the problems of crystal size and quality. Flow stress measurements have been carried out on commercial polycrystalline (PCBN) samples (Harris 1997), but these results do not yield the same information as would be given by single crystal work.

2.2.4 Lattice defects

The theory of lattice defects in cBN is very similar to that of diamond, with the difference that cBN consists of two elements rather than one. This leads to more possible permutations for intrinsic defects than for diamond. Self-interstitials can be either boron or nitrogen, and antisite defects are also possible, i.e. a boron atom on a nitrogen lattice site and vice versa. There are also two types of vacancy, one for each sublattice, i.e. a boron vacancy (V_B) and a nitrogen vacancy (V_N). In terms of extrinsic defects and inclusions in the lattice, the situation is very similar to that for diamond.

A vast literature relating to the study of the defects in diamond has been assembled over the past few decades. Similar work on cBN, both regarding theoretical modelling and experimental work, has been reported only recently. A summary is given here of the theoretical

work, which focuses on the electronic properties of cBN and the influence of lattice defects on them. In a later paragraph, experimental work is discussed with emphasis on the luminescence properties of cBN.

Using a 64 atom supercell, Gubanov *et al.* (1996a) investigated the electronic structure of boron and nitrogen vacancies in cBN using several calculation methods. In their model, lattice relaxation around the vacancies was not considered, i.e. the atoms surrounding the vacancies remained in ideal positions for the purposes of the calculations. Both boron and nitrogen defect states appear to form well-defined narrow bands in the forbidden gap of cBN. The boron related vacancy band has a width of 0.4 eV, lies 0.6 eV above the valence band and is partially occupied. When the valence electrons are thermally excited to this band, p-type doping behaviour is observed in cBN. A nitrogen vacancy gives rise to two narrow bands, one completely occupied band near the valence band, and one partially occupied band near the conduction band edge. This band can thus act as a donor and increase the *n*-type conductivity of the crystal.

Howard (1996) investigated the stability of interstitials in the cBN lattice using *ab initio* Hartree-Fock calculations on clusters. These simulated the local environment of an interstitial in two types of cavities of T_d symmetry in the cBN lattice. In the $B_{14}N_4H_{28}$ cluster the central cavity has nitrogen atoms as the four nearest neighbours while in $B_4N_{14}H_{28}$ cluster, boron atoms play this role. The neutral interstitials Li, Be, excess B, C, O, Si and S were considered. Relaxation of the first and second nearest neighbour shells of atoms around the interstitial was allowed. It was found that all interstitials were less stable when the nearest neighbours were nitrogen rather than boron. The model predicted stability only for Li and Be in a B-coordinated cavity. This finding was qualified by mentioning that the relaxation of the breathing type of lattice dilation assumed in the study was not necessarily appropriate for atoms like Si, with a larger radius than the native lattice atoms.

Castineira *et al.* (1998) carried out self-consistent calculations on the electronic structure of vacancies, and substitutional and interstitial Be in cBN. It was found that Be substituting for boron gave a shallow acceptor level just above the top of the valence band, producing a p-type semiconductor. This accounts for the observed p-type behaviour in Be doped cBN. Be replacing nitrogen lead to energy levels in the middle gap region; this dopant placement produced a semiconductor with amphoteric character. Be at tetrahedral interstitial sites produced deep levels in the bandgap. Calculations also showed that the nitrogen vacancy (V_N) is a possible shallow donor centre, in agreement with Gubanov *et al.* (1996a).

Detailed calculations of the electronic properties of carbon and silicon substitutional impurities in N and B sublattices as a function of pressure and the consequences of such doping were carried out by Gubanov *et al.* (1996b).

Mosuang *et al.* (2002a and 2002b) have studied the relative stability of cubic and different hexagonal forms of boron nitride as well as the influence of neutral defects on the h-BN to c-BN phase transformation using *ab initio* pseudopotential total-energy calculations. Their results show that there are small energy differences between certain h-BN structures, suggesting that the exact nature of the h-BN precursor will significantly influence the h-BN to c-BN phase transformation during synthesis. Calculations also predict that C, N and O interstitial defects have low formation energies and furthermore can considerably influence the energy difference between the h-BN and c-BN structures and thus affect the pressure at which the phase transition would occur. O is shown to have the lowest formation energies suggesting it is a promising candidate to influence h-BN to c-BN phase transformations.

2.2.5 Optical properties

Eremets *et al.* (1995) reported on Raman, absorption and reflection spectra studied in the spectral range 400 – 50000 cm^{-1} . One-phonon and multi-phonon absorption peaks were measured, as well as the dispersion of the refractive index. IR spectra showed an intrinsic peak at 1818 cm^{-1} . The static dielectric constant ($\epsilon_0 = 6.80$) and high frequency dielectric constant ($\epsilon_\infty = 4.46$) were measured and from these the effective charges were calculated. The authors conclude that cBN is a very ionic compound. This statement appears incongruous, given cBN's very high bulk modulus and the general acceptance that materials exhibiting directional, covalent bonding in a high-symmetry, 3-dimensional lattice have the highest bulk moduli (Haines *et al.* 2001). Both earlier work (Gielisse *et al.* 1967) and more recent work (Petrescu 2004) indicate a 20-22% ionic character for the bonds in cBN.

2.2.5.1 Raman spectrum

The hBN and cBN phases of boron nitride both have characteristic Raman signatures. hBN displays two Raman peaks, at 51.8 cm^{-1} and 1366.2 cm^{-1} (Nemanich *et al.* 1981). The high wavenumber line is associated with non-polar intralayer vibrations, and the low frequency line with the rigid layer shear mode. The low wavenumber peak is not normally observed, as it is too close to the exciting laser line to resolve with ease, but specialised spectrometers will readily be able to separate the line. Nemanich *et al.* (1981) showed that the high frequency line shifts to

higher frequencies and broadens markedly with decreasing crystallite size in hBN. Crystallite sizes were in the range 4 – 30 nm.

Brafman *et al.* (1968) reported on the measurement of Raman and IR spectra of small transparent cBN polycrystals. It was found that the transverse optical (TO) phonon peak is at $\omega_{\text{TO}} = 1056 \text{ cm}^{-1}$ and the longitudinal optical (LO) phonon peak is at $\omega_{\text{LO}} = 1304 \text{ cm}^{-1}$. It was observed that cBN conformed to the tendency for III-V compounds to have the TO peak at a higher intensity than the LO peak.

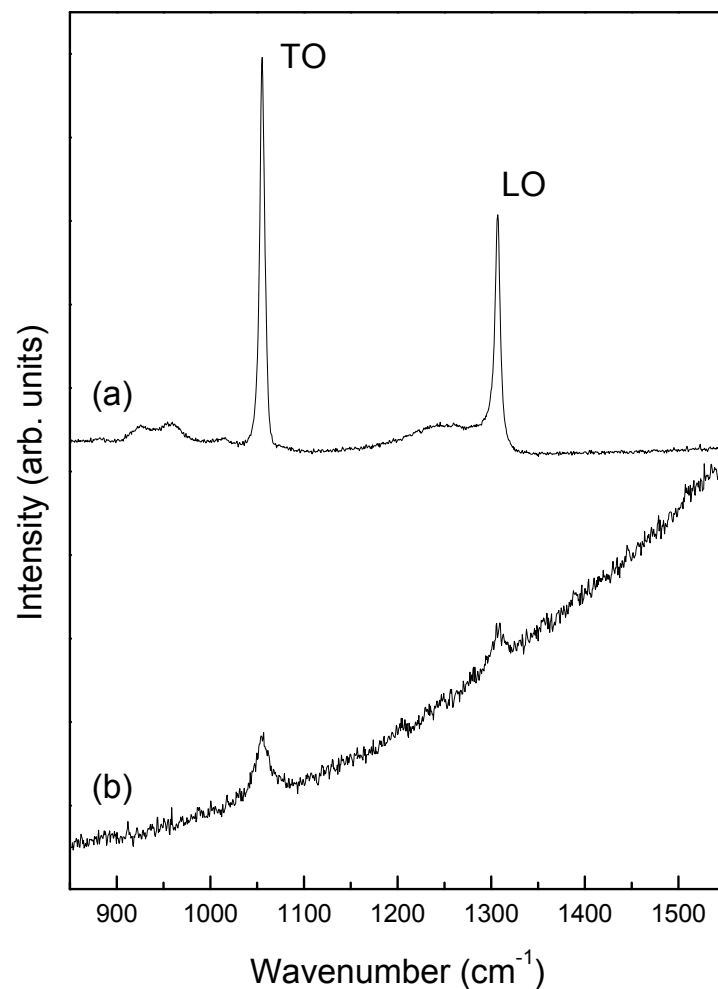


Figure 2.11: Typical Raman spectra showing the peaks observed for (a) single crystals of cBN, and (b) for polycrystalline cBN (data measured by the author).

Lukomskii *et al.* (1987) reported on the Raman spectrum of cBN synthesised with excess nitrogen. Small, transparent single crystals and powders were investigated. The Raman lines for

the single crystals were measured to be at $\omega_{\text{TO}} = 1055.6 \pm 0.5 \text{ cm}^{-1}$ and $\omega_{\text{LO}} = 1305.9 \pm 0.5 \text{ cm}^{-1}$. The width of the lines was 3.7 cm^{-1} . The positions of the Raman lines for the powder sample was found to be identical to those of the single crystals. No comment was made on the width of the Raman lines for the powder sample.

Werninghaus *et al.* (1997a) have reported on the Raman spectrum of cBN crystals with different diameters. It was found that the Raman line shape became increasingly asymmetric towards lower frequency shifts and broader and weaker with decreasing crystal diameter. Crystals with diameters of 1 mm, 100 μm , 1 μm and 0.1 μm were investigated. For the largest diameter single crystal, the Raman spectrum displayed $\omega_{\text{TO}} = 1057 \text{ cm}^{-1}$ and $\omega_{\text{LO}} = 1309 \text{ cm}^{-1}$, as well as a broad, very weak feature centred at approximately 1260 cm^{-1} . The measured Raman lines were shifted relative to the bulk modes mentioned earlier in this paragraph, which was attributed to the presence of residual compressive stress of about 1 GPa in the crystal. The broad, weak feature was attributed to nano-crystalline or amorphous BN in the crystallites. The spatial correlation model (mentioned in chapter 3) was used to fit the observed asymmetry and shift in the peaks with decreasing crystal diameter. The main parameter extracted from these fits is the correlation length (“mean free path”) S of the relevant phonon. Physically S corresponds to the average diameter of undisturbed regions in the crystal rather than the diameter of the crystallite itself. Correlation lengths were in the nm range, i.e. several orders of magnitude below the actual crystallite size, indicating a high defect density. For the 1 mm diameter crystal, it was found that $S = 50 \text{ nm}$ and for the 0.1 μm diameter crystallite $S = 17 \text{ nm}$. For amorphous cBN, i.e. where $S \approx a$ and a is the lattice parameter, a peak at a frequency position of about 1260 cm^{-1} is obtained, which justifies the assignment of the broad weak feature in the observed spectra of single crystals to nano-crystalline or amorphous cBN in the crystals.

Sanjurjo *et al.* (1983) reported on the pressure dependence of the Raman lines of several III-V semiconductors at room temperature, using a diamond anvil cell. For cBN the results show, within experimental error, a linear dependence of the position of the TO and LO peaks on pressure in the measurement range (0 – 8.2 GPa). This dependence can be expressed as follows:

$$\omega_{\text{LO}} = (1305 \pm 1) + (3.45 \pm 0.07)p \quad (2.2)$$

$$\omega_{\text{TO}} = (1054.7 \pm 0.6) + (3.39 \pm 0.08)p \quad (2.3)$$

with ω_{TO} and ω_{LO} in cm^{-1} and p in GPa.

The mode Grüneisen parameters γ_i are defined as

$$\gamma_i = -\frac{\partial \ln \omega_i}{\partial \ln V} = \frac{B_0}{\omega_i} \frac{d\omega_i}{dp}, \quad (2.4)$$

where the ω_i are the given phonon modes and B_0 is the zero pressure bulk modulus. As mentioned in § 2.2.3.1, the value of the bulk modulus used by Sanjurjo *et al.* (1983) is clearly too high in the light of subsequent work. When the γ_i are recalculated using the value of B_0 as measured by Knittle *et al.* (1989) (369 GPa), the values $\gamma_{\text{TO}} = 1.19$ and $\gamma_{\text{LO}} = 0.98$ are obtained. These values are in good agreement with calculations by Kern (1998) and Kern *et al.* (1999), where $\gamma_{\text{TO}} = 1.2$ and $\gamma_{\text{LO}} = 0.9$ were reported. The effects of strain on the zone-centre TO phonon frequencies of cBN (and thus the positions of the IR absorption peaks) have been calculated by Fahy (1995, 1996) using a first-principles total-energy-band-structure method. The calculated phonon wave number for unstrained material (at 1063 cm^{-1}) was in excellent agreement with the experimental value for bulk cBN. The calculated line shift was found to be -36 cm^{-1} per 1% isotropic strain, and for uniaxial strain the values were -29 cm^{-1} and -13 cm^{-1} per 1% strain for phonon polarisations parallel and perpendicular to the strain axis, respectively. The Poisson ratio of cBN was calculated to be 0.316. Cardona *et al.* (1996) discussed the above paper, and highlighted some inconsistencies in the interpretation of the results. This work also gave a calculated mode Grüneisen parameter for the TO phonon of $\gamma_{\text{TO}} = 1.13$, which is in good agreement with the values given above. These results of Cardona *et al.* (1996) were applied by Fahy *et al.* (1997) to the study of shifts of IR absorption peaks in cBN thin films. A model was developed to relate the observed shifts to the growth mechanism rather than intrinsic strain in the thin films due to the deposition process.

The temperature dependence of the Raman lines of cBN has been investigated by Alvarenga *et al.* (1992) and Herchen *et al.* (1993). Alvarenga *et al.* (1992) studied cBN powders to temperatures of 1600 K and reported a linear decrease in frequency position with increase in temperature for both the LO and TO modes. Herchen *et al.* (1993) investigated single crystal cBN in the temperature range 300 K to 1830 K. The positions of the Raman lines shifted to lower frequencies with increasing temperature and showed a quadratic dependence. The Raman linewidths broadened with increasing temperature and it was found that three- and four-phonon processes were required to adequately model the linewidth variation with temperature.

2.2.5.2 Luminescence

The first reported study on the cathodoluminescence of cBN was by Pipkin (1980). Black crystals of predominantly octahedral habit having eight $\{111\}$ faces were examined. Only four faces were observed in CL, producing luminescence with a deep purple-blue colour. The four-fold symmetry of these faces was interpreted as the CL reflecting the symmetry of the crystal structure although the crystal habit did not. The CL was thus related to an atomic arrangement unique to the lattice symmetry of cBN. This observation of a particular defect occurring on a specific crystal face has an analogy in diamond with the H3 defect centre that is grown in for the $\{100\}$ faces in synthetic diamond. Recent theoretical investigation into the detailed surface structure and energetics of the (111) and $(\bar{1}\bar{1}\bar{1})$ faces of cBN (Kádas *et al.* 1998), have highlighted the differences in the reconstructions and stoichiometries that give stable configurations for the two faces. It is possible that these differences also play a role in generating the luminescence pattern observed.

Detailed spectroscopic studies of the CL of as-grown cBN were first presented by Tkachev *et al.* (1985a, 1985b). The samples were parallelepipeds of polycrystalline cBN with polished facets. The main feature was a broad band with a maximum around 3.1 eV (~ 400 nm), accompanied by a weaker broad band with maximum at around 2.2 eV (~ 560 nm). The vibronic spectra of three defects were also observed. These defects were labelled GC1 (ZPL = 1.76 eV, ~ 704 nm), GC2 (ZPL = 1.63 eV, ~ 760 nm) and GC3 (ZPL = 1.55 eV, ~ 800 nm). The GC1 defect was observed in nearly all the samples, with the intensity of the ZPL dependent on the synthesis method. GC2 and GC3 were observed only in some samples, usually when the GC1 peak was strong. In some cases the GC2 peak was observed to be a doublet (Zaitsev *et al.* 1986a, Shipilo *et al.* 1990). A fourth band, labelled GC4 (ZPL = 1.44 eV) was reported by Shipilo *et al.* (1988a). The thermal softness, defined by Zaitsev *et al.* (1987) as the degree of broadening of an optical line with temperature, of GC1 and GC2 was compared to the GR1 defect (neutral vacancy) in diamond and the suggestion was made that GC1 was a vacancy related defect and GC2 a vacancy complex. It was also observed that the half-width of the ZPL of GC1 was dependent on the depth of excitation of the CL, i.e. dependent on the energy of the incident electrons. This was taken as evidence of a high degree of crystal inhomogeneity with depth.

CL studies of the annealing of unirradiated polycrystalline and single crystal cBN was reported by Zaitsev *et al.* (1986a). GC1 and GC2 defects were found to be stable up to the maximum annealing temperature of 1900 K. This is far higher than expected for an isolated vacancy, and further strengthens the suggestion that these defect centres involve vacancy-impurity complexes. It was found that cBN synthesised with excess boron gave a strong GC1

intensity and cBN synthesised with excess nitrogen gave a strong GC2 intensity. It was thus proposed that the suggested vacancy-impurity centres of GC1 and GC2 are associated with the nitrogen vacancy (V_N) and boron vacancy (V_B), respectively.

The half-widths of GC1 and GC2 ZPLs were found to vary for different polycrystalline samples, indicating a range of defective structures and mechanical strains. Annealing of polycrystalline cBN in the range 870 K to 1100 K resulted in the half-widths of the ZPLs of the GC1 and GC2 defects decreasing, and the intensity increasing. This was explained as a reduction in strain broadening with annealing and associated improvement in structural perfection. Annealing above 1500 K caused the intensity to decrease and the width to increase. This was speculated to be due to the onset of the cBN to hBN phase conversion.

CL of electron irradiated cBN was reported by Zaitsev *et al.* (1986b). The samples were irradiated with 4.5 MeV electrons with a dose up to $2 \times 10^{17} \text{ cm}^{-2}$. Three strong vibronic systems were introduced by the irradiation and the defects were labelled RC1 (ZPL = 2.27 eV, ~546 nm), RC2 (ZPL = 2.15 eV, ~577 nm) and RC3 (ZPL = 1.99 eV, ~623 nm). The presence of these three centres in all samples after irradiation pointed to an intrinsic nature for these defect centres. A high thermal softness for all three defect centres pointed to the likelihood that they contain vacancies. The RC defect series annealed out in temperature range 970 K – 1020 K. Simultaneous annealing of all three defect centres suggest a common component in their annealing behaviour. Spectral broadening with temperature increase was also observed. The RC defect series was concluded to be primarily intrinsic vacancy-type defects.

Further studies on the effect of ion implantation on the CL spectrum of single crystal cBN were undertaken by Zaitsev *et al.* (1987). H^+ , He^+ , B^+ , S^+ , Ne^+ , and Se^+ were implanted with energies in the range 60 – 700 keV and doses up to $5 \times 10^{14} \text{ cm}^{-2}$. It was found that all the ions introduced the RC defect series upon implantation. All three ZPLs were observed to be doublets, this feature being assigned to the Jahn-Teller effect. The widths of the ZPLs varied from sample to sample and depended on the irradiation conditions, showing their sensitivity to inhomogeneous distributions of elastic stresses in the samples. Since implantations by a large range of ions all introduced the RC series of defects, this points to the actual ions not being part of the defect centres, but rather that they are intrinsic in nature, in agreement with the conclusions based on electron radiation work. All three ZPLs were observed to anneal out sharply at 973 K. A depth profile of the intensity of the RC defects with sputtering revealed that the ZPL intensity decreased with depth.

The thermal softness of the RC defects introduced by H⁺ implantation in cBN was compared to that of the same defects introduced by electron irradiation. A reduced thermal softness was observed in the case of the H⁺ implanted samples. This observation did not conflict with the conclusion that the RC defects contained nitrogen, which is discussed later, since the damage by the ions reduces the electron-phonon interaction which gives rise to the broadening, thus explaining the observation.

The effect of pressure on the CL spectra of cBN polycrystals was investigated by Shipilo *et al.* (1988a, 1988b). Initial samples showed three broad bands, labelled A (centred on 2.2 eV, ~560 nm), B (2.45 eV, 506 nm) and C (1.55 – 1.85 eV, 800 nm – 670 nm). Pressure treatment comprised the application of load up to a fixed pressure at a rate of 3 MPa/sec and holding the pressure for 1 hour. The pressure was then removed within 30 seconds. The maximum pressure applied was 9.5 GPa. This process led to drastic changes in the ambient pressure intensities of the A, B and C bands, as well as introducing RC1, RC2 and a new set of centres, labelled PC1 (ZPL = 2.84 eV, ~437 nm), PC2 (ZPL = 2.325 eV, 533.3 nm) and PC3 (ZPL = 1.79 eV, 693 nm). The most pronounced change of band intensities and widths occurred at 3.5 GPa, at which point plastic deformation can take place at room temperature (Novikov *et al.* 1985). The authors present arguments that the A and B bands can be associated with electronic states in the bandgap due to multivacancy complexes based on V_N and V_B and band C is associated with plastic deformation of cBN. The PC series of defects are speculated to be of possible interstitial origin.

Investigation of the effect of pressure on the CL spectra of single crystals of cBN was reported by Shipilo *et al.* (1990). The pressure treatment procedure was similar to that for the polycrystals discussed above. Untreated samples showed the broad bands A and B to be present, with A dominant in intensity, as well as the ZPL of the GC2 centre. Some crystals also showed new ZPLs with positions at 2.56 eV (~484 nm) and 1.89 eV (~656 nm). Differences were also observed for the CL spectra of (111) and ($\bar{1}\bar{1}\bar{1}$) faces, with the GC2 defect dominating for the ($\bar{1}\bar{1}\bar{1}$) face, and the A band dominating for the (111) face. With the application of high pressure the CL lines of both faces show common trends. Up to 3.5 GPa the ZPL lines narrow and the luminescence intensities decrease. Above 3.5 GPa those lines broaden with pressure to a degree dependent on the orientation of the crystallographic face being measured. The high pressure application also introduces some of the RC and PC optical centres mentioned previously, as well as new ZPLs at 2.10 eV (~590 nm) and 1.816 eV (682.8 nm). The RC2, RC3 and PC2 ZPLs are present up to 3.5 GPa, above which the RC lines disappear and the PC3 ZPL appears, but split into a multiplet of lines. Above 5.0 GPa the PC3 line vanishes, with a ZPL at 1.89 eV remaining.

It is suggested that the RC2 and RC3 defect centres represent Frenkel pairs based on nitrogen vacancies, while the PC2 centre defect structure contains nitrogen vacancies. The PC3 defect is suggested to be related to the presence of a transition metal in the crystal structure. The centre with a ZPL at 1.89 eV is suggested to relate to interstitial-type defects. The onset of broadening of the ZPLs above 3.5 GPa is cited as evidence for the onset of plastic strain at this pressure level.

Shishonok *et al.* (1989) have investigated the PC3 defect in detail and concluded that it is associated with a transition-metal impurity, possibly chromium (Cr^{3+}), in the cBN lattice.

The use of CL, and specifically that of the RC2 defect, to study and model the effect of high energy ion beam modification of cBN, have been reported by Burenkov *et al.* (1989) and Zaitsev (1992). Burenkov *et al.* (1989) focus on the depth distribution of the radiation-induced defects after implantation with high-energy (59 to 130 MeV) N, C, B, Ni, Co, Cu and Xe ions. Experimental results are compared with theoretical calculations, and both show that the spatial distribution of the defect formation is mainly determined by the distribution of the elastic energy deposition. Zaitsev (1992) focuses on high energy ion implantation as an ion beam modification tool for the manufacture of doped structures in superhard materials such as diamond and cBN. The opportunities offered by the tracks of high energy ions for controlled doping of very small areas is highlighted, as well as the localised regions of high pressure associated with the tracks that may offer the possibility of small volumes of different phases.

In the unpublished thesis by Bourne (1989), the optical properties of cBN were investigated by means of Raman spectroscopy, photoluminescence and thermoluminescence. The effect of electron irradiation and subsequent annealing was also investigated. A variety of samples was used, either polycrystalline single grains or fine powders. The results are discussed in the following paragraphs.

The Raman spectrum was studied as a function of electron dose and annealing temperature. The positions of the Raman lines were found not to be affected by irradiation and annealing. The Full Width at Half Maximum (FWHM) of the Raman lines gave variations of the order of the experimental error in FWHM with increasing electron dose for powders. The Raman width of the single grain samples showed variations of ~40% with increasing electron dose but this was not the same for all samples. During annealing of irradiated samples, a reduction in the FWHM was observed between 400° C and 800° C and attributed to a possible decrease in lattice strain. Both the 351.1 nm and the 488 nm lines of an argon ion laser were used. The UV line gave a ~30% larger FWHM than the 488 nm line. This effect was not understood, but speculated to be due to charge carrier redistribution occurring during illumination with the UV light.

PL investigations of as-grown cBN synthesised with various catalysts were conducted. Broad emission bands, with maxima at 15800 cm^{-1} ($\sim 633\text{ nm}$, 1.96 eV) and 16800 cm^{-1} ($\sim 595\text{ nm}$, 2.08 eV), labelled A and B, were observed in nearly all spectra. Band B appeared to be a superposition of two or more emission bands. The relative intensities of A and B varied from sample to sample, which implies there are probably different centres giving rise to these emission bands. It was determined that these broad bands were not due to hBN. Their presence in all samples led to the conclusion that they were intrinsic of origin and possibly associated with stable neutral complexes.

Several sharp lines were observed in two types of single grain samples. In one type, the RC series of defects was reported for the first time in as-grown material. It was speculated that the nitrogen vacancy was a constituent of these centres. A new line, possibly associated with the boron vacancy, was reported at 14321 cm^{-1} (698.27 nm , 1.776 eV). In another type of sample, doped with phosphorus, a new set of vibronic centres was observed and it was suggested that P is a likely component of these centres.

Electron irradiation (2 MeV) introduced several intrinsic defects. Both the 351.1 nm line and the 488 nm line of an argon-ion laser were used, but only the results obtained with the 488 nm line are summarised here. Electrons were found to introduce sharp lines, previously observed in CL and labelled RC1, RC2 and RC3. Only RC1 was introduced in all samples, in contrast to the findings of Zaitsev *et al.* (1986b). The RC2 defect centre was observed in all samples but one. High electron doses ($> 5 \times 10^{17}\text{ cm}^{-2}$) introduced the R7 defect. The emergence of R7 coincided with the disappearance of RC2, pointing to the possibility that the two defects are linked. RC3 was seen in about 50% of the samples.

The annealing behaviour of RC1, RC2 and RC3 introduced by electrons was investigated by Zaitsev *et al.* (1986b). No mention was made in this work of the difficulty encountered by Bourne (1989) to separate the first phonon peak of the RC1 defect and the RC2 ZPL.

It was observed that the presence of RC3 in the PL spectrum appeared to affect the annealing behaviour of RC1. When RC3 was not present, the RC1 anneal curve displayed a maximum at 500° C and 700° C . With RC3 present, various anneal curves were obtained for RC1. It is possible that other centres (including RC3) alter the charge carrier distribution at RC1, which influence its annealing curves.

The RC1 defect commenced annealing at 800° C in all samples. This points to an important change in the defect structure of cBN in the temperature range 800° C to 1000° C . When the RC1 and RC2 defects annealed out, the broad band luminescence was altered. It is

possible that one defect is mobile in this range of temperatures, combining with the observed centres.

It was suggested by Zaitsev *et al.* (1986b and 1987) and Shipilo *et al.* (1987) that the RC1, RC2 and RC3 centres contain the nitrogen vacancy, V_N . In Bourne's irradiation work, only the RC1 was introduced in all samples, giving strong evidence of its intrinsic nature. It was proposed by Bourne that RC1 is an isolated nitrogen vacancy, V_N .

In one type of cBN sample, synthesised in the presence of Mg_3N_2 , the RC1, RC2 and RC3 defects were observed in the as-grown state. This is the only type of sample where these three defects were observed in this situation; in other types of sample these centres were introduced by irradiation. This implies that vacancies need to be introduced during growth. As all materials studied by Bourne were synthesised using similar procedures, an additional variable is necessary to account for the observed introduction of nitrogen vacancies during growth. As the as-grown sample displaying the RC defects was the only such material synthesised using Mg_3N_2 , it is suggested that if Mg_3N_2 is incorporated into the cBN lattice, with Mg on boron sites, there would be one nitrogen atom short; thus a vacancy is introduced. It is not known how Mg is distributed in the lattice, i.e. evenly or as clumps.

Shishonok *et al.* (2002) report on the electron irradiation of single crystal cBN in a transmission electron microscope at various accelerating voltages. Low temperature PL studies at several different excitation wavelengths lead to an estimate for the displacement threshold in cBN, the discovery of a new interstitial-related optical centre and results on new characteristics of previously reported damage-induced optical centres. Room temperature electron irradiation at energies between 150 keV and 300 keV to a dose of approximately 2×10^{20} electrons.cm⁻² introduces the well-known RC series of radiation damage centres in light grey translucent boron-rich crystals, synthesised using MgB_2 . Yellow, nitrogen-rich crystals, synthesised using Li_3N , showed no radiation-induced, sharp optical features in the low temperature (7 K) PL spectra. It was noted that higher energy (4.5 MeV) electrons introduce the RC series of defects in all cBN samples, irrespective of their origin and quality.

UV PL of the light grey crystals using 325 nm excitation also revealed a new centre (labelled BN1) with ZPL at 376.5 nm (3.29 eV). This defect was compared to the 3.188 eV defect centre in electron-irradiated diamond due to similarities in their luminescence spectra. It was suggested that the BN1 centre involves interstitial atoms. It was observed that the radiation-induced centres were not confined to the irradiated areas only, but extended outside it. Such behaviour was typified as characteristic of high dose near-threshold irradiation with the same

phenomenon previously observed in diamond and SiC. The RC centre ZPLs were also observed with 514.5 nm excitation, showing different intensity distributions as compared with the results for UV excitation. RC2 and RC3 intensities were weak in the irradiated area, with RC2 stronger on the periphery and RC3 extended further away from the irradiated area with enhanced intensity. It was noted that the presence of the irradiation-induced defects was dependent on the area of a crystal chosen for irradiation, with the BN1 ZPL being absent from some locations. No detailed model for the atomic structure of the RC defects is advanced, except to note that results are consistent with previous claims that these centres are related to nitrogen vacancies associated with nitrogen interstitials in different lattice positions. Peak splitting of the RC centre ZPLs was encountered frequently, with these splittings associated particularly with locations close to coarse, linear growth steps visible in the crystal. There was no clear pattern for the splitting of the different ZPLs, with only one ZPL sometimes split, while on other occasions only two or all three ZPLs would exhibit splitting. The splitting is likely to be stress-induced, with residual stresses apparently retained in the cBN crystal at the already mentioned coarse ledge structures during synthesis.

Shishonok *et al.* (2004) made a detailed PL study of the RC centres introduced by near-threshold electron irradiation of cBN. The experimental procedure is very similar to that mentioned above for Shishonok *et al.* (2002), except that 488 nm excitation was used. It was found that the energy of the irradiating electrons affects the energy of the ZPLs of the RC series of defects, as well as their fine structure. Deconvolution of the fine structure leads to the proposal that the vacancy-related defect structure of the RC1 defect has orthorhombic symmetry with the defect axis along $\langle 110 \rangle$, while the RC2 defect has tetragonal symmetry along $\langle 100 \rangle$ and the RC3 defect has trigonal symmetry with the defect axis along $\langle 111 \rangle$. Annealing of the irradiated samples at temperatures of 650° C to 800° C causes relaxation of the defect structure. The fine structure of the RC3 defect was reported to be less sensitive to incident electron energy and relaxed more easily during annealing compared to the fine structure of the RC1 and RC2 ZPLs.

Chapter 3: Vibrational spectroscopy

One of the avenues of investigation open to an experimentalist to study the detailed structure of matter, is the study of the interaction of light (photons) and matter (gases, solids and liquids). Broadly speaking, this interaction can result in the absorption, emission or scattering of the incident electromagnetic radiation. These phenomena are intimately related to transitions between the energy levels in the matter, be it in the form of atoms, molecules or crystals. Transitions between rotational energy levels are associated with electromagnetic radiation in the microwave region of the spectrum, vibrational energy levels with infrared wavelengths and transitions between electronic levels with optical and ultraviolet wavelengths. A transition from a lower level to a higher level with transfer of energy from the radiation field to the host matter is called absorption. A transition from a higher to a lower level is called emission if energy is transferred to the radiation field or non-radiative decay if no radiation is emitted, e.g. decay via phonons in a crystal lattice. Scattering (or redirection) of light due to interaction with matter may or may not occur with transfer of energy, i.e. the scattered radiation has respectively a slightly different wavelength or the same wavelength. In this work, we are chiefly concerned with two specific processes; the **Raman effect**, which is a scattering process, and **photoluminescence**, which is an emission process.

This chapter gives a short overview of the theory behind the Raman effect and the photoluminescence process. A discussion on the influence of stress / strain on the Raman process is also given.

3.1 The Raman effect

In the writing of this section, various texts were consulted. Principal use was made of Brüesch (1986). The reader is also referred to Griffith (1975), Thorne (1988), Klein (1990) and Keresztury (2002) for general overviews and the book by Marcuse (1980) for a comprehensive quantum electronic description of the Raman effect.

3.1.1 Introduction

The possible existence of the Raman effect was predicted in 1923 by Adolf Smekal, and in 1928 Sir Chandrasekhara V. Raman, using sunlight filtered through a prism and toluene as the scattering medium, demonstrated the phenomenon to which his name was subsequently given (Raman 1928 and Raman *et al.* 1928). It is sometimes referred to as the Smekal–Raman effect by continental writers. Independently, and only a month later, Landsberg and Mandelstam (1928a and 1928b) observed the phenomenon using mercury radiation on quartz and so were the first to observe the Raman spectrum of a mineral.

In the following, the discussion focuses primarily on solids, as these are the materials dealt with in this thesis. When matter is irradiated by non-resonance monochromatic radiation of frequency ν , a certain fraction of the radiation is scattered. Light scattering arises from three main factors, named after their discoverers, namely Tyndall, Rayleigh and Raman. Tyndall scattering is caused by the presence of very small but macromolecular particles in the substance under illumination and does not involve a change in the frequency of the scattered light. Both Rayleigh and Raman scattering derive from the interaction of the radiation with the crystal lattice of the sample. The Rayleigh effect, where the light is scattered elastically (the direction of the incident photons is changed, but not their wavelength), accounts for the majority of the scattered light and also does not involve a change in the frequency of the scattered light. The intensity of the Raman light is five to six orders of magnitude less than that of the Rayleigh scattered light and does involve a change in the frequency of the scattered light due to the light being scattered inelastically. The Raman spectrum of a specific sample shows a number of discrete scattered frequencies both higher and lower than that of the exciting radiation (ν). Such new frequencies in the scattered light are the so-called Raman bands and each has an associated Raman shift ($\Delta\nu$) relative to the exciting radiation frequency ν . Those bands of lower frequency than the exciting radiation are called Stokes lines, and are usually stronger than those bands of higher frequency than the exciting radiation, the anti-Stokes lines. In first-order scattering only one phonon is involved; this corresponds to the terms linear in the normal coordinates Q_s (equation 3.17). In second-order scattering two phonons are involved, corresponding to the terms proportional to $Q_s Q_s$ in equation 3.17 or to anharmonic coupling of a phonon which is active in first-order Raman scattering with two other phonons.

The literature on Raman scattering is huge and bewildering because of the many different ways in which the effect can be described. A rigorous semi-classical treatment of the Raman effect requires third order perturbation theory while its quantum-mechanical description as a two-

photon process requires second order perturbation theory (Marcuse 1980). In solids it is necessary to explicitly describe the vibrational waves which are excited by the Raman process, so that third order perturbation theory is again necessary.

In the following paragraphs, both a simple classical and quantum mechanical treatment of the Raman process is given that suffices to describe the observed features of a Raman spectrum and facilitates the understanding of the Raman process on a microscopic level.

3.1.2 A simple quantum mechanical approach

This subsection gives an introductory qualitative discussion in terms of discrete energy levels and of photons. The quantum-mechanical model is the two-photon process shown schematically in figure 3.1. Let (ω_L, \mathbf{k}_L) be the incident photon of the laser with frequency ω_L and wavevector \mathbf{k}_L , $(\omega_{sc}, \mathbf{k}_{sc})$ the scattered photon and (ω_j, \mathbf{q}) the optical phonon $s = (\mathbf{q}, j)$ involved in the scattering process. Energy and momentum are conserved between initial and final states of the system. For Rayleigh scattering we have $\omega_L = \omega_{sc}$ and $\mathbf{k}_L = \mathbf{k}_{sc}$. For Raman scattering the conservation of energy and momentum are $\omega_L = \omega_{sc} \pm \omega_j(\mathbf{q})$ and $\mathbf{k}_L = \mathbf{k}_{sc} \pm \mathbf{q}$, respectively. Since $\omega_L \gg \omega_s = \omega_j(\mathbf{q})$ it follows from energy conservation that $\omega_L \cong \omega_{sc}$. Experiments are usually carried out at frequencies where there is essentially no dispersion of the refractive index n , i.e. the transparent region of the crystal. Since \mathbf{k}_L and \mathbf{k}_{sc} are the wave vectors within the crystal, we have $k_L = 2\pi/\lambda_L$, $k_{sc} = 2\pi/\lambda_{sc}$, where $\lambda_L = \lambda_v / n(\omega_L)$ and $\lambda_{sc} = \lambda_v / n(\omega_{sc})$, with λ_v the wavelength in vacuum. From $c = v\lambda_v$ we obtain $k_L = n(\omega_L) \omega_L / c$, $k_{sc} = n(\omega_{sc}) \omega_{sc} / c$ and since $\omega_L \cong \omega_{sc}$ it follows that $k_L \cong k_{sc}$. In addition λ_L and λ_{sc} are much larger than the lattice parameter a , and hence k_L and k_{sc} are much smaller than π/a , the magnitude of the wavevector at the zone boundary. Thus from momentum conservation it follows that $q \ll \pi/a$, i.e. in first order Raman scattering only $\mathbf{q} \cong 0$ optical modes can be excited.

With reference to figure 3.1, suppose that we denote some vibrational state of a crystal as $|a\rangle$. This need not necessarily be an excited state. An incident photon of energy $\hbar\omega_L$ is absorbed, raising the system to some intermediate or virtual state. Insofar as this is energetically distant from a real level (large δE), the uncertainty principle, $\delta E \delta t \sim \hbar$, allows the virtual state a vanishingly small lifetime (of the order of 10^{-14} seconds). The system immediately makes a Stokes transition, emitting a (scattered) photon of energy $\hbar\omega_{sc} < \hbar\omega_L$. In conserving energy, the difference $\hbar\omega_L - \hbar\omega_{sc} = \hbar\omega_{ba}$ goes into exciting the crystal to a higher vibrational energy level

$|b\rangle$. It is possible that electronic or rotational excitation results as well. Alternatively, if the initial state is an excited one, the crystal, after absorbing and emitting a photon, may drop back to an even lower state $|a\rangle$, thereby making an anti-Stokes transition. In this instance $\hbar\omega_{sc} > \hbar\omega_L$, which means that some vibrational energy of the crystal ($\hbar\omega_{sc} - \hbar\omega_L = \hbar\omega_{ba}$) has been converted to radiant energy. In either case the resulting differences between ω_{sc} and ω_L correspond to specific energy level differences for the substance under study and as such yield insights into crystal structure.

It is important to note that the “absorption” of the photon $\hbar\omega_L$ and the emission of the photon $\hbar\omega_{sc}$ are truly simultaneous events and cannot be separated in time from one another. The apparent time sequence of events in the above description is merely part of the process of explanation.

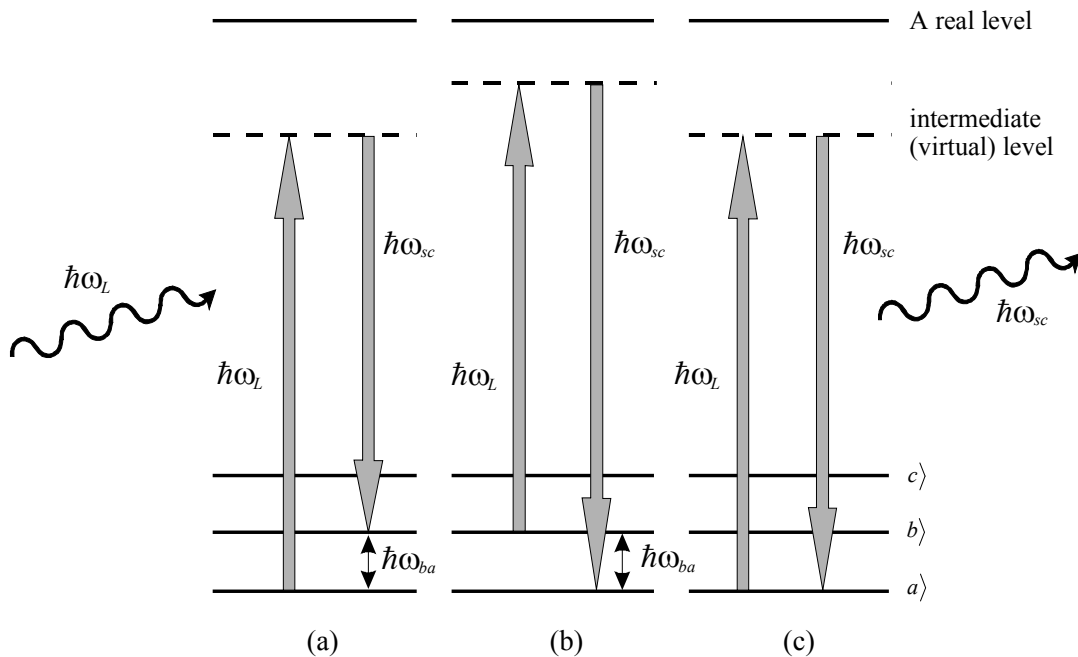


Figure 3.1: Schematic energy level diagram illustrating the (a) Stokes and (b) anti-Stokes transitions that can occur during the Raman process. (c) is the case for Rayleigh scattering.

This description of the Raman effect accounts for the observed difference in the intensities of the Stokes and anti-Stokes bands, since the population of the ground vibrational level (figure 3.1a) is much greater, for optical phonons and not too high temperatures, than the population of excited vibrational levels (figure 3.1b). Thus the chance the incident photon finds the system in an excited vibrational level is much smaller than for the ground state. Since the

ratio of the two populations, according to Bose-Einstein statistics, is proportional to $\exp[\hbar\omega_s / k_B T]$, the ratio of the intensities of a Stokes line to a corresponding anti-Stokes line is expected to be proportional to $\left(\frac{\omega_L - \omega_s}{\omega_L + \omega_s}\right)^4 \exp\left(\frac{\hbar\omega_s}{k_B T}\right)$ and this ratio is considerably larger than unity.

3.1.3 A simple classical approach

For this discussion, we consider a single molecule, but it is equally applicable to an inter-atomic bond in a solid. When electromagnetic radiation impinges on such a sample, the electric field \mathbf{E} induces an atomic dipole, the nuclei of the solid in the vicinity of the \mathbf{E} field being displaced towards the negative end of the dipole and the electron cloud to the positive part. Let $\mathbf{E} = \mathbf{E}_0 \cos\omega_L t$ be the electric vector of the incident light. Since ω_L is much larger than the vibrational frequencies of the atoms, only the electrons but not the atoms can respond to the light field \mathbf{E} . For a dipole moment \mathbf{M} induced by \mathbf{E} we write

$$\mathbf{M} = \alpha\mathbf{E} + \frac{1}{2}\beta\mathbf{E}^2 + \dots \quad (3.1)$$

where α is the electronic polarizability of the sample matter and can be thought of as being related to the ease with which the electron cloud may be deformed. Both \mathbf{M} and \mathbf{E} are vectors, α is a second-order tensor and β is a third-order tensor known as the hyperpolarizability, which gives rise to the Hyper-Raman Effect. This effect will not be discussed here.

In general, the direction of \mathbf{M} does not coincide with the direction of \mathbf{E} , i.e. α is a second-order tensor with components α_{ij} . For the present discussion, it is assumed that \mathbf{M} is parallel to \mathbf{E} (this is the case for isotropic systems or if \mathbf{E} is parallel to the direction of one of the axes of high symmetry of the system). The electronic polarizability α depends on the electric charge distribution of the system. If the atomic configuration changes during a vibration, the charge distribution and hence α will also change. Expanding α in a Taylor series gives

$$\alpha = \alpha_0 + \left(\frac{\partial\alpha}{\partial Q}\right)_0 Q + \frac{1}{2}\left(\frac{\partial^2\alpha}{\partial Q^2}\right)_0 Q^2 + \dots, \quad (3.2)$$

with Q a normal coordinate and α_0 the polarizability of the molecule when it is not vibrating. The first-order Raman effect is determined by the term linear in Q , the second-order Raman effect by the term quadratic in Q , etc. In the following, only first-order Raman scattering is considered. If a particular bond in the molecule vibrates with the frequency ω_s , then $Q = Q_0 \cos\omega_s t$ and

$$\alpha(t) = \alpha_0 + \left(\frac{\partial \alpha}{\partial Q} \right)_0 Q_0 \cos \omega_s t. \quad (3.3)$$

Substituting equation 3.3 into equation 3.1 gives

$$\mathbf{M}(t) = \alpha_0 \mathbf{E}_0 \cos \omega_L t + \left(\frac{\partial \alpha}{\partial Q} \right)_0 Q_0 \mathbf{E}_0 \cos \omega_L t \cos \omega_s t \quad (3.4)$$

On expansion this gives

$$\mathbf{M}(t) = \mathbf{a} \cos \omega_L t + \mathbf{b} [\cos(\omega_L - \omega_s)t + \cos(\omega_L + \omega_s)t] \quad (3.5)$$

where

$$\mathbf{a} = \alpha_0 \mathbf{E}_0; \quad \mathbf{b} = \frac{1}{2} \left(\frac{\partial \alpha}{\partial Q} \right)_0 Q_0 \mathbf{E}_0 \quad (3.6)$$

Equation 3.5 shows that the induced dipole moment \mathbf{M} vibrates not only with the frequency ω_L of the incident light, but also with the frequencies $\omega_L \pm \omega_s$. Thus we have three frequency components. The first term of equation 3.5 is the classical expression of Rayleigh scattering since an oscillating dipole will itself emit radiation of frequency ω_L and the intensity of the radiation is proportional to the mean square of $\ddot{\mathbf{M}}(t)$. The second and third terms give the Stokes and anti-Stokes Raman components respectively.

An important consequence of equation 3.5 is that it also gives the basic selection rules for the activity of a Raman vibration. If the rate of change of polarizability with the bond vibration ω_s is zero, then that vibration will be Raman inactive and there will be Rayleigh scattering only. Thus for a vibration to be Raman active a change of polarizability must be involved.

From classical radiation theory of an oscillating dipole, the intensity of the emitted radiation by the dipole moment $\mathbf{M}(t)$ into the solid angle $d\Omega = \sin \vartheta d\vartheta d\phi$ is given by (Crawford 1968 and Brüesch 1986)

$$dI(t) = \frac{d\Omega}{4\pi c^3} \sin^2 \vartheta |\ddot{\mathbf{M}}(t)|^2 \quad (3.7a)$$

and per unit solid angle $d\Omega$ by

$$I(t) = \frac{1}{4\pi c^3} \sin^2 \vartheta |\ddot{\mathbf{M}}(t)|^2 = A |\ddot{\mathbf{M}}(t)|^2 \quad (3.7b)$$

In MKS units the intensity or time-averaged power per unit solid angle radiated by an oscillating electric dipole induced by the electric field of the incident radiation of frequency ω_L along a direction making an angle ϑ with the axis of the dipole is given by

$$I = \frac{\omega_s^4 Q_0^2}{32\pi^2 \epsilon_0 c^3} \sin^2 \vartheta \quad (3.7c)$$

where Q_0^2 is the amplitude of the induced electric dipole with frequency ω_s .

By use of equations 3.5 to 3.7, the intensity of the scattered light per unit solid angle is now given by

$$I(t) = AE_0^2 [k_0^2 \cos^2 \omega_L t + k_1^2 \cos^2(\omega_L - \omega_s)t + k_2^2 \cos^2(\omega_L + \omega_s)t] + \text{cross terms}, \quad (3.8)$$

where

$$k_0^2 = \alpha_0^2 \omega_L^4, \quad (3.9)$$

$$k_1^2 = \frac{1}{4} \left(\frac{\partial \alpha}{\partial Q} \right)_0^2 Q_0^2 (\omega_L - \omega_s)^4, \quad (3.10)$$

$$k_2^2 = \frac{1}{4} \left(\frac{\partial \alpha}{\partial Q} \right)_0^2 Q_0^2 (\omega_L + \omega_s)^4. \quad (3.11)$$

The cross terms in equation 3.8 can be neglected since the power they radiate averages to zero over time intervals of sufficient length. This can easily be verified by calculating the time average

$$I = \lim_{\tau \rightarrow \infty} \frac{1}{\tau} \int_0^\tau I(t) dt = \frac{1}{2} AE_0^2 (k_0^2 + k_1^2 + k_2^2). \quad (3.12)$$

From equation 3.8 we expect that the scattered light will have peaks at the frequencies ω_L and $\omega_L \pm \omega_s$. This can directly be verified by calculating the frequency dependence of the scattered light, the power spectrum, which is obtained by forming the square of the Fourier transform of

$$\mathbf{M}(t), \text{ namely } P(\omega) = A \lim_{\tau \rightarrow \infty} \frac{2}{\tau} \left| \int_{-\tau/2}^{\tau/2} \ddot{\mathbf{M}}(t) \exp(-i\omega t) dt \right|^2 \quad (\text{Brüesch 1986}).$$

The classical theory thus correctly predicts the occurrence of the Stokes and anti-Stokes lines, but leads to an incorrect ratio of their intensities. From equations 3.10 to 3.12 it follows that the ratio of the intensities of the Stokes and anti-Stokes lines should be

$$\frac{I_{Stokes}}{I_{anti-Stokes}} = \frac{(\omega_L - \omega_s)^4}{(\omega_L + \omega_s)^4}, \quad (3.13)$$

which will certainly be less than unity, whereas experimentally it is found that the Stokes lines are more intense than the anti-Stokes lines. This inconsistency is eliminated in the quantum theory of the Raman effect.

At the beginning of this section (§3.1.3) it was pointed out that, in general, the direction of the induced dipole moment \mathbf{M} does not coincide with the direction of the electric field \mathbf{E} . In most cases the polarizability within a molecule will be greater in one direction than in another, so that the induced dipole will tend to align itself with the direction of greatest polarizability in the molecule rather than with \mathbf{E} . In such a case equation 3.1 (neglecting the quadratic term) has the form:

$$\begin{aligned} M_x &= \alpha_{xx}E_x + \alpha_{xy}E_y + \alpha_{xz}E_z \\ M_y &= \alpha_{yx}E_x + \alpha_{yy}E_y + \alpha_{yz}E_z \\ M_z &= \alpha_{zx}E_x + \alpha_{zy}E_y + \alpha_{zz}E_z \end{aligned} \quad (3.14)$$

Considering the energy of the polarised system, it may be shown that α is a symmetrical tensor with

$$\alpha_{xy} = \alpha_{yx}, \alpha_{xz} = \alpha_{zx} \text{ and } \alpha_{yz} = \alpha_{zy}$$

and the α_{ij} components of the polarizability tensor can be described by a real symmetric matrix.

It can also be shown that there exists always a coordinate system with axes (x', y', z') such that the relation between \mathbf{M} and \mathbf{E} , when referred to these axes, assumes the simple form

$$\begin{pmatrix} M'_{x'} \\ M'_{y'} \\ M'_{z'} \end{pmatrix} = \begin{pmatrix} \alpha'_{x'x'} & 0 & 0 \\ 0 & \alpha'_{y'y'} & 0 \\ 0 & 0 & \alpha'_{z'z'} \end{pmatrix} = \begin{pmatrix} E'_{x'} \\ E'_{y'} \\ E'_{z'} \end{pmatrix} \text{ or } \mathbf{M}' = \alpha' \mathbf{E}', \quad (3.15)$$

where α' is a diagonal matrix. Such axes are called principal axes of polarizability and are easy to find for a symmetrical system (molecule or crystal), since they must coincide with the symmetry axes present and be perpendicular to any plane of symmetry.

It is convenient to define the system (x, y, z) in such a way that it coincides with the principal axes of the equilibrium configuration of the molecule or crystal. For the equilibrium configuration the components of α are

$$\alpha_{ij} = \delta_{ij} \alpha_{ij}^{(0)} \quad (3.16a)$$

or written differently

$$\alpha = \begin{pmatrix} \alpha_{xx}^{(0)} & 0 & 0 \\ 0 & \alpha_{yy}^{(0)} & 0 \\ 0 & 0 & \alpha_{zz}^{(0)} \end{pmatrix}. \quad (3.16b)$$

If as a result of thermal fluctuation the system is in a distorted configuration there will be a new principal-axes system, the system (x', y', z') , which in general will not coincide with (x, y, z) . The polarizability will again be diagonal if referred to (x', y', z') but not necessarily if referred to

(x, y, z) . In the latter case each component α_{ij} can be expanded in terms of the normal coordinates Q_s (as for equation 3.2) to give

$$\alpha_{ij} = \alpha_{ij}^{(0)} + \sum_s \alpha_{ij,s} Q_s + \frac{1}{2} \sum_{s's''} \alpha_{ij,s's''} Q_s' Q_{s''} + \dots \quad (3.17)$$

For a given normal coordinate Q_s we may define changes in the polarizability components

$$\Delta \alpha_{ij,s} = \alpha_{ij,s} Q_s = \left(\frac{\partial \alpha_{ij}}{\partial Q_s} \right)_0 Q_s \quad (3.18)$$

and a matrix with elements

$$\alpha_{ij,s} = \left(\frac{\partial \alpha_{ij}}{\partial Q_s} \right)_0, \quad (3.19)$$

namely

$$\delta \alpha^{(s)} = \begin{pmatrix} \alpha_{xx,s} & \alpha_{xy,s} & \alpha_{xz,s} \\ \alpha_{yx,s} & \alpha_{yy,s} & \alpha_{yz,s} \\ \alpha_{zx,s} & \alpha_{zy,s} & \alpha_{zz,s} \end{pmatrix}. \quad (3.20)$$

Substituting equation 3.17 into equation 3.14 and using

$$E_j = E_{0j} \cos \omega_L t \quad (3.21a)$$

$$Q_s = Q_0 \cos \omega_s t \quad (3.21b)$$

we obtain

$$M_i(t) = a_i \cos \omega_L t + \sum_s b_{si} [\cos(\omega_L - \omega_s)t + \cos(\omega_L + \omega_s)t] \quad (3.22)$$

where

$$a_i = \sum_j \alpha_{ij}^{(0)} E_{0j} \quad (3.23a)$$

$$b_{si} = \frac{1}{2} Q_{s0} \sum_j \alpha_{ij,s} E_{0j} \quad (3.23b)$$

Equation 3.22 is a generalisation of the corresponding equation 3.5 for diatomic molecules. The first term in equation 3.22 is responsible for Rayleigh scattering while the other terms give rise to Raman scattering. We therefore expect Raman lines at the frequencies $\omega_L \pm \omega_s$. From equation 3.23b it is evident that the normal mode Q_s will appear in the Raman spectrum only if at least one of the six components $\alpha_{ij,s}$ of the matrix $\delta \alpha^{(s)}$ is different from zero. If this is the case, the normal mode Q_s is Raman active. Whether or not a normal mode is Raman active depends on the symmetry of the equilibrium configuration and of the symmetry of the normal modes Q_s . This can

be determined by consulting group character tables for the relevant point group. The tables are also useful to establish which crystal orientations for a single crystal will produce Raman activity for a given mode.

Figure 3.2 visualises the vibrational modes that are Raman active for diamond and cubic boron nitride. As mentioned in chapter 2, the diamond structure (figure 3.2a) is composed of two fcc lattices displaced from each other by one-quarter of a body diagonal. The structure possesses a centre of inversion symmetry i which is, however, not located at the atoms, but at the mid-point of each line connecting nearest-neighbour atoms. The triply degenerate $q = 0$ TO mode is shown by arrows and can be pictured as a relative motion of the two interpenetrating fcc lattices against each other (figure 2.6). The TO mode resembles the normal oscillation of a homonuclear diatomic molecule and is Raman active but not infrared active.

The cBN structure (figure 3.2b) does not have inversion symmetry and the arrows indicate the optical mode at $q = 0$; it resembles the normal oscillation of a heteronuclear diatomic molecule and is thus expected to be Raman active. Since cBN has some polarity to the bonds, the macroscopic electric field associated with the vibration removes the degeneracy of the optical mode yielding a doubly degenerate TO mode and a LO mode (figure 2.10).

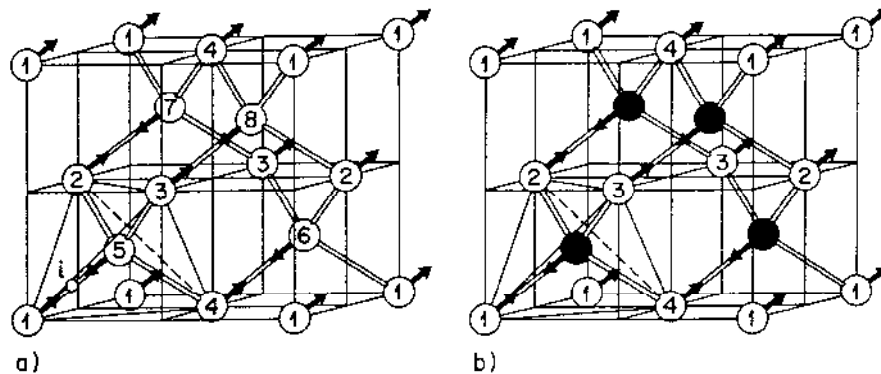


Figure 3.2: In crystals with the diamond structure (a) and with the zinc blende structure (b) the TO modes at $q = 0$ (indicated by arrows) are Raman active (Brüesch 1986).

3.1.4 The width of the Raman line

In addition to information contained in the position of the Raman peak, the relative value of the Full Width at Half Maximum (FWHM) of the Raman peak is also of importance. The Raman linewidth in general can be broadened via several mechanisms. The main mechanisms applicable here are homogeneous (lifetime) broadening (Borer *et al.* 1971) and broadening due to the size effect of the crystal (Nemanich *et al.* 1981, Ager *et al.* 1991). The Raman linewidth of natural

diamond is related to the lifetime of the phonon created in the Raman process. The primary broadening mechanism in a perfect crystal is decay of the optical phonon into two acoustic phonons with opposite wave vectors. However, in imperfect crystals the phonon created in the Raman process can also decay (scatter) at grain boundaries and at defect sites, further reducing the lifetime and broadening the Raman line. The theory of the homogeneous spectral line shape predicts that the linewidth is inversely proportional to the phonon lifetime and that the line shape is symmetric and of a Lorentzian form. The FWHM of a Raman peak can thus be used as a convenient ranking indicator of degree of plastic deformation as the FWHM is sensitive to “crystal disorder” via the homogeneous broadening mechanism.

The other possible mechanism which results in Raman line broadening is phonon confinement in a small domain size. This well-established model, first developed to explain Raman peak shifts and line shapes in semiconductors such as Si and GaAs (Richter *et al.* 1981, Campbell *et al.* 1986), is based on the uncertainty principle, which states that the smaller the domain size, the larger the range of different phonons (with different q vector and different energy) that are allowed to participate in the Raman process. Hence the broadening of the Raman line in this case is due to the spread in phonon energy. According to this model, the linewidth gets broader and the Raman peak shifts to a lower frequency and the line shape becomes asymmetric towards lower frequencies as the domain size decreases.

3.1.5 The effect of stress on the Raman line

In the previous sections it was shown that the Raman effect is due to the interaction of photons with vibrational mode(s) (phonons) in a crystal. Phenomenologically, the effect of applying stress to a crystal that has Raman active vibrational modes may be explained as follows: If no changes are introduced to the unit cell of that crystal except to slightly change the frequency of the vibration, then this will result in a slight change in the position of the observed Raman bands. Such a change as imagined above can be introduced by way of an applied stress to the unit cell. A slight compression will result in a slight change in the force constants of the vibration, thus leading to a change in the frequency of the vibration. The same argument can be applied if the unit cell dilates slightly due to the presence of tensile stresses in the lattice.

If the applied stress is isotropic, then no change takes place with respect to the Raman band except for a change in position since the symmetry of the unit cell is not changed. If uniaxial stress is applied, then the unit cell will deform preferentially in one direction and the symmetry of the cell changes locally. This leads to a directional dependence in position of the Raman band,

i.e. the magnitude of the shift due to stress would depend on the direction in which it is applied and the orientation of the measurement relative to the direction of stress. If the Raman band is degenerate, then the application of uniaxial stress will lead to a lifting of the degeneracy and a consequent splitting of the Raman band.

3.1.5.1 The hydrostatic piezo-Raman coefficient α

The treatment according to Mossbrucker *et al.* (1997) and Anastassakis *et al.* (1970) is followed here. Diamond belongs to the crystal class m3m. Hence, in the absence of any strain the $\mathbf{k} = 0$ optical phonons in diamond are triply degenerate due to the cubic symmetry of the crystal. In the presence of strain, the differential equations for the $\mathbf{k} = 0$ triply degenerate (F_{2g} symmetry) optical phonons in diamond type crystals to terms linear in the strain, have the form

$$\bar{m}\ddot{x}_i = -\int_k D_{ik} x_k = -\left(D_{ii}^{(0)} x_i + \sum_{klm} \frac{\partial}{\partial \varepsilon_{lm}} D_{ik} \varepsilon_{lm} x_k \right) \quad (3.24)$$

where x_i is the i th component of the relative displacement of the two atoms in the unit cell, \bar{m} is the reduced mass of the two atoms, $D_{ii}^{(0)} = \bar{m}\omega_0^2$ is the effective spring constant of the F_{2g} modes in the absence of strain, the change in the spring constant due to applied stress ε_{lm} is defined by

$$\frac{\partial}{\partial \varepsilon_{lm}} D_{ik} \varepsilon_{lm} = D_{iklm}^{(1)} \varepsilon_{lm} = D_{ikml}^{(1)} \varepsilon_{ml} \quad (3.25)$$

and i, k, l and m designate x, y or z . Since diamond belongs to the cubic symmetry group, only three components of the tensor $D^{(1)}$ are independent:

$$\begin{aligned} D_{1111}^{(1)} &= D_{2222}^{(1)} = D_{3333}^{(1)} = \bar{m}p \\ D_{1122}^{(1)} &= D_{2233}^{(1)} = D_{1133}^{(1)} = \bar{m}q \\ D_{1212}^{(1)} &= D_{2323}^{(1)} = D_{1313}^{(1)} = \bar{m}r \end{aligned} \quad (3.26)$$

From the dynamical equation (3.24) and assuming a harmonic solution, one obtains the following secular equation whose solutions yield the frequencies of the optical phonons in the presence of strain:

$$\begin{bmatrix} p\varepsilon_{xx} + q(\varepsilon_{yy} + \varepsilon_{zz}) - \lambda & 2r\varepsilon_{xy} & 2r\varepsilon_{xz} \\ 2r\varepsilon_{xy} & p\varepsilon_{yy} + q(\varepsilon_{xx} + \varepsilon_{zz}) - \lambda & 2r\varepsilon_{yz} \\ 2r\varepsilon_{xz} & 2r\varepsilon_{yz} & p\varepsilon_{zz} + q(\varepsilon_{xx} + \varepsilon_{yy}) - \lambda \end{bmatrix} \equiv 0 \quad (3.27)$$

where $\lambda = \Omega^2 - \omega_0^2$, and $\Omega = \omega_0 + \lambda/(2\omega_0)$ is the strain dependent frequency of the optical phonons. The secular equation is referred to the system of crystallographic axes, $x = [100]$, $y = [010]$ and $z = [001]$. Diagonalisation of the secular matrix yields the set of three eigenvectors of the optical phonons in the presence of strain. The phonon deformation potentials p , q and r are related to changes in spring constants with applied strain and have been measured for many cubic materials, including diamond (Grimsditch *et al.* 1978).

For the hydrostatic case, a piezo-Raman coefficient may be calculated quite easily. Cubic diamond has a single first-order Raman line at $\nu_0 = 1332.5 \text{ cm}^{-1}$ (room temperature), reflecting the frequency of the triply degenerate zone-centre optical phonon. As mentioned, these phonon frequencies are sensitive to lattice deformations caused by mechanical stress. An arbitrary stress tensor can be generally decomposed into a hydrostatic component and a deviator, inducing a volume change of the unit cell and a distortion of the bond angle, respectively. The volume change of the unit cell due to the hydrostatic stress results in a linear shift of the triply degenerate Raman line. The Raman shift $\Delta\nu_H$ relative to the stress-free state is related to the magnitude of the hydrostatic stress σ by (Mitra *et al.* 1969, Mohrbacher *et al.* 1996)

$$\Delta\nu_H = \frac{\nu_0\gamma}{B}\sigma. \quad (3.28)$$

Taking the room temperature values $\gamma = 1.06$ for the diamond Grüneisen parameter (Grimsditch *et al.* 1978) and $B = 442 \text{ GPa}$ for the bulk modulus (Field 1992a), a hydrostatic piezo-Raman coefficient of $-3.20 \text{ cm}^{-1}/\text{GPa}$ is obtained.

Experimentally, this linear dependence of the peak position of the Raman line on the applied stress was confirmed by Grimsditch *et al.* (1978). It was shown that upon applying compressive stress to diamond, the peak position of the Raman line shifts linearly with stress to a higher frequency. The dependence of the Raman shift $\Delta\nu$ on the applied stress σ is

$$\Delta\nu = \nu - \nu_0 = -\alpha\sigma \quad (3.29)$$

where α is the pressure or piezo-Raman coefficient and ν_0 is taken to be the Raman peak position of the natural diamond when no pressure is applied. Conversely, a move of the Raman peak position to lower frequencies is associated with the presence of tensile stress in the diamond.

The value of the coefficient α has been calculated and measured in a diamond anvil cell (DAC) by several authors. Table 3.1 summarises several of the reported values in the literature.

Table 3.1: Values for the hydrostatic piezo-Raman coefficient α reported in literature.

Value of α (cm ⁻¹ /GPa)	Conditions of measurement	Reference
2.8 ± 0.3	Hydrostatic (DAC)	Mitra <i>et al.</i> 1969
2.87 ± 0.1	Hydrostatic (DAC)	Boppart <i>et al.</i> 1985
2.96 ± 0.11	Hydrostatic (DAC)	Whalley <i>et al.</i> 1976
3.20 ± 0.2	Hydrostatic	Grimsditch <i>et al.</i> 1978
3.1	Calculated	Van Camp <i>et al.</i> 1992
1.9	Reported average value for hydrostatic case	Bergman <i>et al.</i> 1995
2.9	Reported as literature hydrostatic value	Ager <i>et al.</i> 1991
2.88 ± 0.17	Average of published hydrostatic measurements in DAC	Catledge <i>et al.</i> 1996
3.6 ± 0.3	Hydrostatic (Tetrahedral cell)	Parsons 1977
2.90 ± 0.05	Hydrostatic (DAC)	Hanfland <i>et al.</i> 1985

3.1.5.2 Uniaxial stress

The triple degeneracy of the zone-centre optical phonon is lifted when deviatoric stress distorts the bond angles and removes the symmetry. Strains and changes in crystal symmetry are expected to alter the vibrational mode frequencies and intensities due to anharmonic effects and changes in selection rules. This causes the splitting of the single Raman line into either three singlets or into a singlet and a doublet. For uniaxial stress applied along either the [001] or the [111] directions, one finds that the threefold degeneracy of the $\mathbf{k} = 0$ optical phonon is split into a singlet with the eigenvector parallel to the stress and a doublet with eigenvectors perpendicular to the stress. Uniaxial stress along the [110] direction is expected to completely remove the threefold degeneracy. There is also a shift in the frequency of the optical phonons to $\Omega_0 = \omega_0 + \Delta\Omega_h$ due to the hydrostatic component of the applied stress (Anastassakis *et al.* 1970). It is found, however, that the centroid position of the split lines does not change under deviatoric stress. In particular cases (pure shear (traceless) stress), the splitting of the singlet is twice that of the doublet and opposite in sign (Grimsditch *et al.* 1978), whereas the doublet splits symmetrically in other cases. The centroid position of the Raman split line is thus entirely determined by the hydrostatic stress. Since the strain-induced changes in the Raman tensor are small it is safe to assume that the scattering is determined by the first order Raman scattering tensor. The relative magnitude of the shift for the two components is dependent of the direction of the stress. The Raman spectra of the two components can be distinguished by polarisation analysis. The linewidth of the two components does not change with increasing uniaxial stress; this is also true

for the single line observed in hydrostatic stress experiments (Mitra *et al.* 1969, Anastassakis *et al.* 1970).

Table 3.2: Values for the piezo-Raman coefficient α under uniaxial stress.

Value of α (cm ⁻¹ /GPa)	Conditions of measurement	Reference
2.2 ± 0.2*	Uniaxial stress along [111]	Grimsditch <i>et al.</i> 1978
0.73 ± 0.1*	Uniaxial stress along [001]	
1.6 [§]	Calculated; strain along [111]	Van Camp <i>et al.</i> 1992
2.0 [§]	Calculated; strain along [110]	
1.6 [§]	Calculated; strain along [100]	
2.37	Value is for singlet; strain direction not specified	Sharma <i>et al.</i> 1985
1.04	Calculated; [110] compression; first peak	Gupta <i>et al.</i> 1989
1.97	Calculated; [110] compression; second peak	
0.67	Calculated; [110] compression; third peak	
1.68 [†]	[100] compression; singlet	Boteler <i>et al.</i> 1993
1.1 [†]	[100] compression; doublet	
0.93 [†]	[110] compression; first peak	Boteler <i>et al.</i> 1993
2.22 [†]	[110] compression; second peak	
0.09 [†]	[110] compression; third peak	

* Note that for these values, it is the relative splitting between the two peak components that is given and not the value of α as defined in equation 3.29.

§ The authors do not state to which of the component(s) of the split peak these values apply.

† These values were estimated from the published figures in this reference.

3.1.5.3 Biaxial stress

In the case of diamond on a substrate, e.g. CVD films on a silicon substrate or polycrystalline layers on a tungsten carbide backing, a so-called biaxial stress model has been invoked to explain the observed features of the Raman spectrum (Ager *et al.* 1993, Catledge *et al.* 1995, Catledge *et al.* 1996, Nugent *et al.* 1998). In this model, it is assumed that the stress in the diamond film can be split into two components, namely an in-plane stress component parallel to the film or layer and a component normal to the film or layer.

For diamond, biaxial compressive stress in either {100} or {111} planes splits the Raman phonon into a singlet and a doublet (wave vector perpendicular and parallel to stress plane, respectively), where the doublet is at higher frequency in diamond (Ager *et al.* 1993). Biaxial stresses along other axes lifts the triple degeneracy completely.

In the case where a biaxial model is suspected to be applicable, but no splitting is observed, it may be that the peak splitting is too small to be resolved by the spectrometer. In this

case a “weighted” shift $\Delta\nu = \frac{1}{3}\Delta\nu_s + \frac{2}{3}\Delta\nu_d$ can be used to calculate the stress ($\sigma = -0.617 \text{ GPa/cm}^{-1} (\nu - \nu_0)$ for the unsplit peak) (Catledge *et al.* 1995).

It is important to note that for a backscattering measurement geometry and for the case of a (100) facet, only the singlet would ever be observed (Ager *et al.* 1993) and such a biaxial stress could never lead to splitting of the peak. If the stress is along some other direction or is uniaxial, this analysis no longer rigorously applies (Nugent *et al.* 1998).

Table 3.3: Values for the piezo-Raman coefficient α in the biaxial stress model.

Value of α (cm ⁻¹ /GPa)	Conditions of measurement	Reference
1.64 2.37	Calculated; for the (100) singlet Calculated; for the (100) doublet	Ager <i>et al.</i> (1993)
0.67 2.86	Calculated; for the (111) singlet Calculated; for the (111) doublet	Ager <i>et al.</i> (1993)
0.90 2.25	Calculated; for the (110) singlet Calculated; for the (110) doublet	Ager <i>et al.</i> (1993)
0.93 2.60	Calculated; polycrystalline diamond, singlet phonon Calculated; polycrystalline diamond, doublet phonon	Ager <i>et al.</i> (1993)
1.62	For unsplit peak; see text	Catledge <i>et al.</i> (1995)

Note that here the plane of the in-plane stress component of the biaxial stress distribution is specified rather than the direction in which the stress is applied, as with the uniaxial stress data.

3.1.6 The effect of temperature on the Raman line position

The lattice dynamics that give rise to the Raman effect are important in determining both thermal properties, such as specific heat and thermal conductivity, and high-temperature stability. Measurements of the temperature-dependent Raman line shifts and widths also allow comparison with predictions of anharmonic crystal theory.

The temperature dependence of the shifts and width can be understood in terms of an oscillator that reacts to the anharmonic potential within which the atoms move. The anharmonicity of the potential manifests itself in the temperature dependence of the Raman line shift, which can be written (in the absence of strain) as a result of two additive effects: the first is the change of vibrational frequencies due to thermal expansion (or volume change) and secondly due to the change in the average vibrational energy at constant volume (a self-energy shift that arises from phonon coupling). The former affects all frequencies while the latter affects the

higher-lying states more than the lower-lying states (Postmus *et al.* 1968). These additive effects can be written as (Herschen *et al.* 1993 and Datchi *et al.* 2004)

$$\Delta\nu = \left(\frac{\partial\nu}{\partial V}\right)_T \Delta V + \left(\frac{\partial\nu}{\partial T}\right)_V \Delta T. \quad (3.30)$$

Any change in temperature will affect these two factors, thereby changing the position of the Raman peak as a function of temperature.

At higher temperatures, the anharmonicity of the potential within which atoms move will lead to increased phonon-phonon interactions that result in scattering and shorter lifetimes of the optical phonons with a concomitant increase in the population of acoustical phonons. Hence the Raman peak width in a single crystal is determined by phonon decay processes and the width of a Raman line will increase with increasing temperature (Brüesch 1982). Elementary theoretical predictions of the change in TO Raman linewidth with temperature depends on the concept that at higher temperatures the phonon occupation number n increases, leading to an increased probability of phonon decay. The process can be a TO-mode phonon decaying either into two longitudinal acoustic phonons of opposite momentum or into three acoustical phonons. If the phonon occupation number is defined as

$$n(\nu, T) = \frac{1}{[\exp(hc\nu/kT) - 1]}, \quad (3.31)$$

and the former decay mechanism is the sole decay mechanism, then for this 2-phonon process the predicted Raman linewidth Γ is (Hart *et al.* 1970)

$$\Gamma(T) = \Gamma(0) [1 + 2n(\nu/2, T)]. \quad (3.32)$$

$\Gamma(0)$ is an adjustable parameter that is fixed by fitting the curve through the lowest-temperature value available.

Equation 3.32 was extended by Balkanski *et al.* (1983) to include the contribution of 3- and 4-phonon processes and for this model the predicted Raman linewidth is

$$\Gamma(T) = A [1 + 2n(\nu/2, T)] + B [1 + 3n(\nu/3, T) + 3n^2(\nu/3, T)], \quad (3.33)$$

where A and B are constants.

3.2 Photoluminescence

The process of photoluminescence is, as the name suggests, a luminescence phenomenon brought about through the action of photons. In the same way, cathodoluminescence involves excitation with electrons and thermoluminescence depends on temperature. The following discussion is modelled on the presentation by Henderson (1972).

In order to understand the physical processes that lead to photoluminescence, a simple model of the absorption and emission of light at a defect centre in a crystal lattice will be discussed. This is usually referred to as the configuration–coordinate model and is a qualitative description of the transition processes that occur when a photon is absorbed at a defect centre in a crystal lattice.

The physical basis for the model is the adiabatic Born-Oppenheimer approximation. In this approximation the eigenstates of a particular electron associated with the defect centre are calculated by considering the movement of the electron under the influence of the neighbouring nuclei and treating the energy of the nuclei as a small perturbation. In view of its small mass the electron responds to the vibrations of the nuclei, whereas the lattice only responds to the average positions of the electrons. The energy of the electron is a function of some configuration–coordinate which specifies the position of the nearest neighbour atoms. The vibrations interacting with the ground and excited states respectively have frequencies ν_g and ν_e which are eigenvalues of an harmonic oscillator. Thus the quantum mechanical eigenvalues for the coupled system are $E_g = (n + \frac{1}{2})\hbar\nu_g$ and $E_e = (m + \frac{1}{2})\hbar\nu_e + E_0$, where n and m are the vibrational quantum numbers and E_0 is the energy separation between the states for which $n = m = 0$. The energy levels are illustrated in figure 3.3, where the shapes of both ground and excited state curves are parabolic (harmonic oscillator). The discrete quantum mechanical nature of the lattice vibrations limits the allowed values for E_g and E_e to those represented by the horizontal lines in figure 3.3 corresponding to the different values of n and m . In contrast to the spectroscopy of atoms, where sharp lines are observed, it is evident that the lattice has introduced a large number of discrete energy levels between which transitions may occur. Thus broad bands are to be expected in the optical spectra of solids. Since the wave function in the excited state is more diffuse than in the ground state, the minimum energy of the excited state occurs at a different nuclear coordinate than in the ground state.

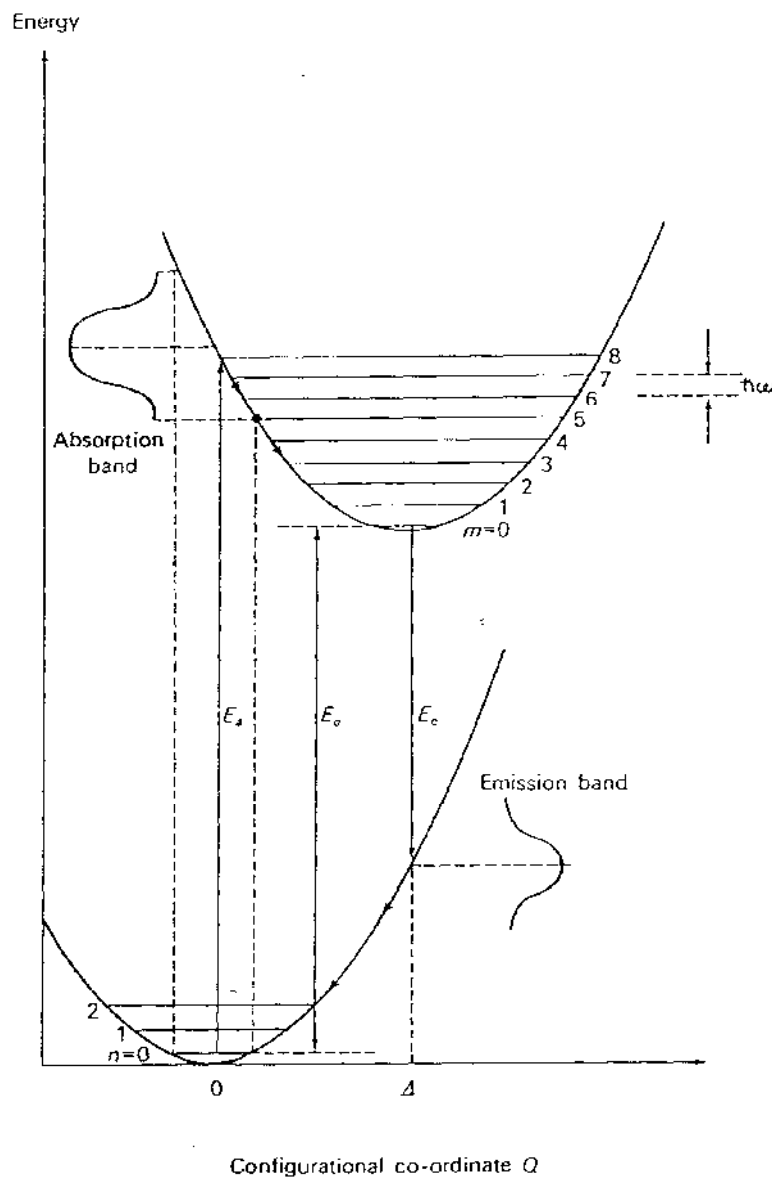


Figure 3.3: Configuration-coordinate diagram illustrating the transitions relevant to photoluminescence processes (from Henderson 1972).

With reference to figure 3.3, consider the case of allowed optical transitions at zero temperature (0 K): since only the $n = 0$ vibrational level is occupied, transitions will occur only from this level. Since the time taken for an electronic transition is short compared with the period of atomic vibrations, the lattice coordinates do not change during the transition. This is the so-called Frank-Condon principle and leads to the transition being represented by vertical lines in figure 3.3. Such transitions occur with varying probability from any position consistent with the spatial extent of the $n = 0$ vibrational wave function. Thus the transition energy varies as the

lattice vibrates between the limits set by the horizontal line representing the vibrational level in the configuration–coordinate diagram. The probability of any transition occurring from a particular value of the configuration–coordinate is proportional to $|\psi_n(Q)|^2$, where ψ_n is the harmonic oscillator wavefunction for the $n = 0$ state. The maximum value of $|\psi_n(Q)|^2$ occurs at the equilibrium position of $Q = 0$ and transitions from this point represent the peak of the absorption band at 0 K. The width of the peak at this temperature is effectively defined by the spatial limit of the line at $n = 0$. As the temperature increases, different vibrational levels become occupied, which have different probability distribution functions. It can be shown that the probability function and consequently the band shape is a Gaussian distribution about $Q = 0$. The width of the Gaussian band changes with temperature according as the statistical population of the vibrational states for which $n > 0$.

Immediately after the excited state configuration has been reached by a transition within the absorption band, the lattice relaxes around the defect to the $m = 0$ vibrational level by emission of an appropriate number of phonons. Physically it can be thought of as the adjustment of the nearest neighbour nuclei to the changed energy state of the electron. Radiative decay from the excited state to the ground state then occurs, the peak position corresponding to the maximum probability in the $m = 0$ state at $Q = \Delta$. Thus since $E_a > E_e$ in figure 3.3, it is apparent that there is a shift in the relative positions of the absorption and emission bands; this is usually referred to as the Stokes shift.

Figure 3.3 indicates that the greater the number of phonons excited in a transition, the larger the Stokes shift will be. A further consequence is that the weaker the coupling (fewer phonons), the greater the amount of overlap between the lowest vibrational states $n = m = 0$. If there is an appreciable overlap of the wavefunctions $\psi_n(Q)$ and $\psi_m(Q)$, then we can excite a transition at energy E_0 , in which the final $m = 0$ state is reached without the emission of phonons. The probability of a transition between any of the levels is given as

$$P_{nm} = f |\langle \psi_m | \psi_n \rangle|^2 \quad (3.34)$$

where f is the oscillator strength of the transition and $\langle \psi_m | \psi_n \rangle$ represents the overlap integral between the two vibrational levels. The result of calculating this integral may be taken from e.g. Watts (1977) so that the general result for a transition involving S phonons being excited at 0 K is

$$P_{0m} = \frac{e^{-S} S^m}{m!} \quad (3.35)$$

This expression defines the optical lineshape. In general when S is small, the probability of observing the zero phonon transition is greatest. Increasing S effectively increases the intensity in the phonon sidebands at the expense of the zero phonon line. When S is very large the shape approaches the Gaussian band, in which the band peak occurs at $S = m$.

Very sharp zero phonon lines have now been observed in many systems and have been useful in investigation of intrinsic defects and impurities in alkali halides, alkaline earth oxides and some semiconductors. The narrowness of the zero phonon line allows use to be made of applied external perturbations to investigate the structure of defects. Such perturbations include externally applied elastic stresses, magnetic fields and electric fields.

3.2.1 Lineshape and line width

In real crystals at low temperatures the PL line shape is determined almost entirely by the crystal strain inhomogeneities. The inhomogeneous broadening is at least 1000 times greater than the homogeneous broadening (Davies 1970), the latter of which occurs when the linewidth is caused by the finite lifetimes of the states between which the transitions occur. In general, the principal mechanism of the inhomogeneous broadening at low temperatures is the strain broadening that arises from the presence of dislocation-type defects and point defects in the crystal (Stoneham 1969). The defects introduce strain fields throughout the crystal that interact with and perturb the optical transitions energies. The statistical distributions and density of the optical centres and defects in the crystal as well as defect type determines the variations in the transition energies of the optical centres and the respective PL line shape.

A comprehensive review of the theory of inhomogeneous strain broadening in crystals was presented by Stoneham (1969). In this review, the calculation of the shapes of resonance lines was presented using the so-called statistical method. This method determines the line shape as a function of the distribution of the defects with respect to the centres studied, the density of the defects and the perturbation fields of the individual defects. In order to be able to apply the main results of the above calculations, it is necessary to take note of the assumptions made in applying the statistical method to inhomogeneous strain broadening. There are three assumptions, namely:

- 1) The transition energy is linear in the local strain, i.e.

$$\hbar\omega = \hbar\omega_0 + \hbar\omega_1\varepsilon, \quad (3.36)$$

where

$$\varepsilon = \sum_{i,j} a_{ij} e_{ij}. \quad (3.37)$$

Here $\hbar\omega_1 a_{ij}$ are coupling coefficients that can be measured in separate experiments in which the transition is observed under an externally applied stress and the e_j represent the strain. The assumption is essentially that of first-order perturbation theory and means that the line shape may be calculated by calculating the distribution of ε .

- 2) The contributions to ε of all the defects which cause broadening simply add linearly.
- 3) The defects which cause broadening are not correlated with each other. This assumption is only good for low defect concentrations.

The main results of the above treatment are:

- For a symmetric lattice, in which the lattice sites accommodate at random the optical centres and defects, the line shape is expected to be symmetric.
- When the strain in the crystal arises solely from uniformly distributed point defects, the luminescence line shape is expected to be Lorentzian.
- When the sources of the strain in the crystal are uniformly distributed dislocations (line-type defects) the line shape is expected to be a Gaussian.
- In the case when both types of defects are present in the crystal, the resulting line is the convoluted line shape of the Gaussian and the Lorentzian; this line shape is known as the Voigt profile. The relative linewidths of the Gaussian component and the Lorentzian component in the Voigt profile reflect which defect is the dominant stress source in the crystal.

The above results of Stoneham assumed an ideal continuous single crystal for which the spatial distribution of the defects and the optical centres were taken to be uniform. Fish (1995) and Fish *et al.* (1997 and 1999) have applied this theory to point defects in synthetic diamonds with different crystal morphology, showing good agreement between the theory's predictions and experimental results.

It is germane to mention here further work done in the above regard by Davies (1971) and Orth *et al.* (1993). In these papers, particular attention is paid to the inhomogeneous broadening of zero phonon line shape by point defect strain fields and it is shown that in the case of high densities of point defects the expected line shape is Gaussian. This is not in contradiction with the findings of Stoneham (1969), since one of his assumptions was that the crystals under investigation have low defect concentrations. It is thus important during data analysis to know what defect densities are involved in order to properly apply the results regarding inhomogeneous broadening of optical line shapes.

3.2.2 The Voigt profile

As mentioned in the previous section, the line shape known as the Voigt profile is of particular significance in photoluminescence studies. The mathematical description of the profile is as follows (Origin 5.0 data analysis and technical graphing software):

$$y = y_0 + A \cdot \frac{2 \ln 2}{\pi^{3/2}} \frac{w_L}{w_G^2} \cdot \int_{-\infty}^{\infty} \frac{e^{-t^2}}{\left(\left(\sqrt{\ln 2} \frac{w_L}{w_G} \right)^2 + \left(4 \sqrt{\ln 2} \frac{x - x_c}{w_G} - t \right)^2 \right)} dt \quad (3.38)$$

where y_0 is the background intensity, A is the area under the Voigt peak, w_L is the Lorentzian linewidth, w_G is the Gaussian linewidth and x_c is the peak position. Using commercial peak fitting computer software (Origin 5.0 from Microcal Software) it is possible to fit this expression to the measured data and so doing extract the unknown variables. The actual width of the Voigt peak, w_V , can be calculated from the following relation (Whiting 1968):

$$w_V = \frac{w_L}{2} + \sqrt{\frac{w_L^2}{4} + w_G^2} \quad (3.39)$$

where w_L and w_G are as above.

Chapter 4: Experimental details

This chapter describes the experimental equipment and samples used in the present research. The first sections deal with the Raman spectrograph and its attachments and operation thereof. Subsequent sections describe the cryostat equipment and the Soft Impressor Technique and give details of the samples studied. Exact measurement conditions for each experiment are detailed in the results chapters.

4.1 The Raman spectrometer

The heart of the experimental setup was the Jobin-Yvon T64000 Raman spectrograph, a sophisticated research instrument with multiple configurations. Figure 4.1 is a schematic diagram showing the light path for the different configurations of the instrument. These are discussed in subsequent paragraphs with reference to figure 4.1.

4.1.1 The macro chamber

A macro chamber suitable for large samples or bulky ancillary equipment, e.g. a furnace or cryostat, was available. Both backscattering and 90 degree configurations for the collection optics were possible.

4.1.2 The microscope attachment

A microscope (Olympus BX40; referred to as a micro-Raman attachment) allowed for measurements to be conducted on small samples. This attachment was primarily used in this work. Several objectives were available, with magnification factors of 20×, 50× (Ultra Long Working Distance) and 100×. Use was mainly made of the 20× objective (N.A. 0.40), which gave a focused laser spot of diameter 1.6 μm on the surface of a sample. The 50× (N.A. 0.55) and 100× (N.A. 0.90) objectives gave focused laser spot diameters of 1.1 μm and 0.7 μm , respectively. In addition to the standard manual microscope stage, a motorised X-Y stage (supplied by Jobin-Yvon and manufactured by Marzhauser) was also available. This latter stage allowed the sample

to be moved in the X and Y directions under computer control with a step size as little as 0.1 μm and was very useful to map the intensity, position or width of a specific spectroscopic feature, e.g. a Raman peak, across the surface of a sample, as discussed in more detail in §4.7.1.1. A transparent sample could also be mapped in the Z-direction (i.e. depth mapping) by either using the manual adjustment of the Z-direction via the microscope focusing knob or via a piezo-electric drive that moved the objective up or down. This is discussed in more detail in §4.7.1.2. Scattered light from the sample could only be collected in the backscattering configuration with the microscope.

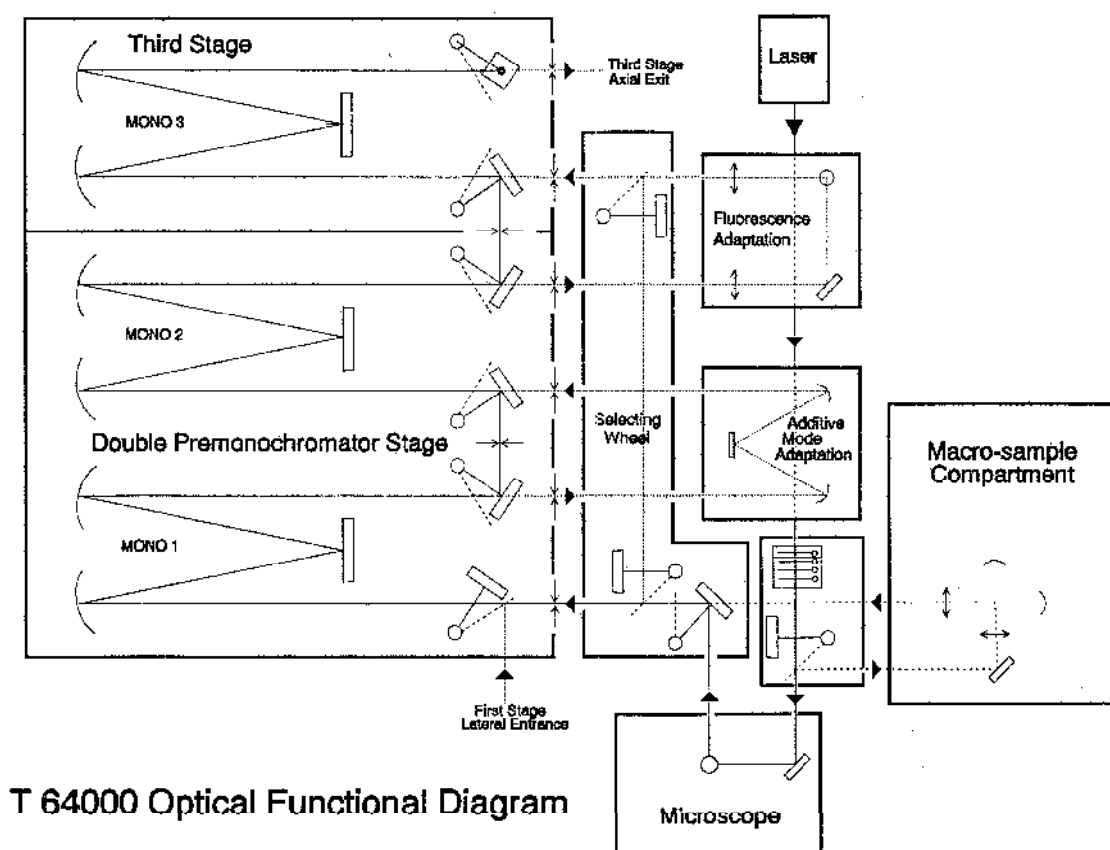


Figure 4.1: Light path diagram of the Jobin-Yvon T64000 spectrograph, illustrating the different light path permutations available to the user (Jobin-Yvon 1992).

The microscope attachment was also equipped to conduct confocal microscopy. This consists of a variable diameter pinhole in the back focal plane of the microscope. By decreasing the aperture of the pinhole, the length of the focal barrel of the objective is shortened, thus increasing the height, or z-dimension, spatial resolution of the measurements (figure 4.2). This is

particularly useful for studying thin transparent films, where no backscattering and thus spectral information from the substrate is desired. It is also convenient when studying small features inside transparent crystals or when mapping spectral features across an x-y plane within a transparent crystal.

The microscope was equipped with a CCD camera attached to a TV monitor for viewing the samples on the stage and placing the laser beam on a specific spot on the sample.

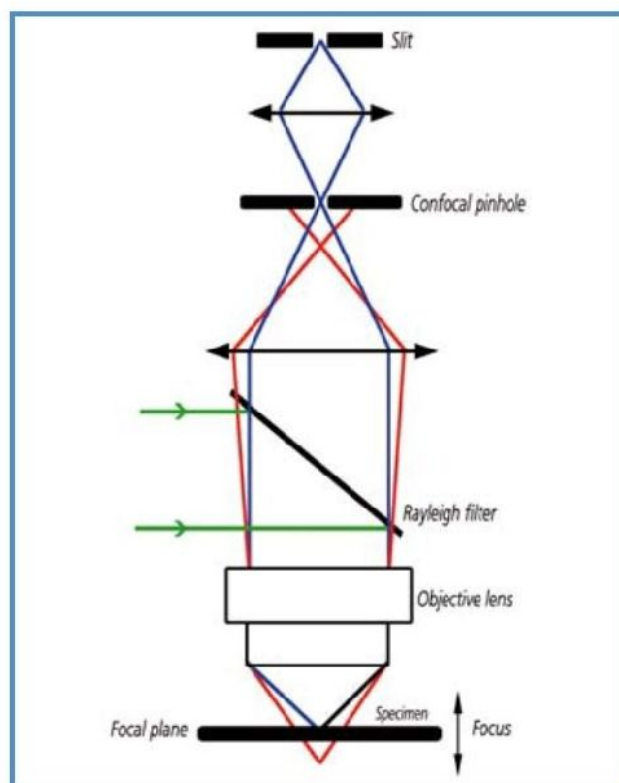


Figure 4.2: Schematic diagram[†] of the light path in a confocal microscope, illustrating the effect of the size of the confocal pinhole in the back focal plane on the sampling size of the focal barrel at the specimen.

4.1.3 Light dispersion options

The light collected from the sample could be dispersed in three possible ways: the single spectrograph mode, triple additive mode or triple subtractive mode. The selecting wheel (figure 4.1) directs the scattered light from either the macro-chamber or the microscope via a series of mirrors to the entrance slit of either the single or triple configuration. In single spectrograph mode, the collected light is dispersed only by the final stage spectrograph (mono 3

[†] From www.jobinyvon.com, accessed October 2005

in figure 4.1), while in the two triple configurations it first passes through a double pre-monochromator (mono 1 and mono 2 in figure 4.1). For the triple additive mode, the light also passes through the “Additive Mode Adaptation”. The advantages of the single spectrograph mode are a high throughput and rapid analysis time, but this is at the expense of spectral resolution and detection of low wavenumber ($<200\text{ cm}^{-1}$) peaks. The triple subtractive mode offers excellent stray light rejection and is thus ideal for analysis of features close to the exciting laser line, but at the cost of low throughput. The triple additive mode offers excellent resolution, but a low throughput. The type of sample under investigation and the interesting features in its associated spectra would thus determine which of the single or triple additive modes would be used.

Two different gratings were available with the single spectrograph stage, a 600 grooves/mm grating and a 1800 grooves/mm grating. Switching between these gratings took place via an automated rotation turret controlled via software (see § 4.4). The triple modes were fitted with only 1800 gr/mm gratings. The 600 gr/mm grating had the advantage of a higher intensity signal and acquisition of a relatively large spectral range at a time. This was at the expense of a lower spectral resolution relative to the 1800 gr/mm grating. In general the 1800 gr/mm grating was used for Raman spectroscopy and the 600 gr/mm grating for photoluminescence spectroscopy.

The stray light rejection in single spectrograph mode is 10^{-5} at 1 nm from the 514.5 nm laser line; thus there is the need to remove the elastically scattered component of the exciting laser line from the backscattered light when using this mode. This is done via a holographic notch filter (Kaiser Optical Systems, Inc.) suited to the particular excitation line wavelength. Such filters at 488.0 nm and 514.5 nm (argon ion laser) and 647.1 nm (krypton ion laser) were available. This implies that any work with excitation lines other than the above three would have to take place via one of the two triple modes. The triple additive mode offers stray light rejection of 10^{-14} at 20 cm^{-1} from 514.5 nm and the triple subtractive mode offers stray light rejection of 10^{-13} under the same conditions.

In the single spectrograph mode, the dispersion of the 600 gr/mm grating at 600 nm is 2.45 nm/mm. With a slit width of $50\text{ }\mu\text{m}$ this translates to a bandpass of 0.1225 nm or 3.4 cm^{-1} at 600 nm. The dispersion of the 1800gr/mm grating at 600 nm is 0.64 nm/mm. A slit width of $50\text{ }\mu\text{m}$ translates to a bandpass of 0.032 nm or 0.9 cm^{-1} at 600 nm. The dispersion of the triple subtractive mode at 600 nm is 0.64 nm/mm, which is the same as that of the 1800gr/mm grating at 600 nm in single spectrograph mode. In triple additive mode, the 1800 gr/mm gratings result in

a dispersion of 0.21 nm/mm at 600 nm. A 50 μm slit width translates to a bandpass of 0.015 nm or 0.3 cm^{-1} at 600 nm.

These data will be referred to when discussing the analyses of data in subsequent chapters.

A “Fluorescence Adapter” option is shown in figure 4.1, but is not an installed option on the instrument used.

4.1.4 Detectors

Two detectors for measuring the signal passed through the dispersive stages were available, namely a charge coupled device (CCD) detector and a photomultiplier tube (PMT). These detectors are not shown in figure 4.1, but are mounted at the exit of the third stage spectrograph. The CCD detector was a large area array detector with 1024×256 pixels in a 27.6×7 mm grid of 27 micron square pixels. The detector chip was kept at 140 K at all times with a liquid nitrogen bath to minimise intrinsic thermal noise. This detector had the advantage of fast acquisition times and rapid acquisition of spectra over a large spectral range, especially with the 600gr/mm grating and was controlled via the “Spectrum One” CCD software (and Labspec 3 software after an upgrade) on the desktop computer. The PMT detector offered much better resolution and a better signal to noise ratio with heavy background fluorescence. The CCD detector was exclusively used in this work, as the triple additive mode provided a more than adequate improvement in resolution where needed.

The resolution of the CCD detector chip depends on the gratings being used and the spectral range being covered. For single spectrograph mode, in the green part of the spectrum the 1800gr/mm grating gives $0.6\text{cm}^{-1}/\text{pixel}$, while the 600gr/mm grating gives $2.0\text{cm}^{-1}/\text{pixel}$ in the green-yellow part of the spectrum.

4.2 Laser sources

The laser source in this work was a Coherent INNOVA Model 308 argon ion laser. The 514.5 nm and 488.0 nm lines were suitable for diamond and cubic boron nitride measurements. Both lines were used for Raman and photoluminescence measurements on diamond, while only the 488.0 nm line was used for measurements on cBN. Werninghaus *et al.* (1997b) investigated several laser lines in the wavelength range 441.6 nm to 647.1 nm and showed that the 482.5 nm line of a Kr^+ laser and the 488.0 nm line of an Ar^+ laser exhibited the best Raman LO and TO

cBN features. Bourne (1989) also illustrated that this wavelength was suitable for PL on cBN in the optical part of the spectrum.

A prism was placed in the beam path directly after the laser aperture to assist in the removal of plasma lines present in the laser beam. This filter did not completely remove the plasma lines and a further narrow bandpass interference filter (Oriel Instruments) could be placed in the beam path to remove these lines. The interference filter considerably reduced the intensity of the laser beam and was thus not used unless necessary, e.g. when a plasma line coincided with a spectral peak. It was also not used at high laser powers due to possible damage to the filter.

A Spectra Physics Model 165 krypton ion laser (647.1 nm) and a Spectra Physics tuneable dye laser were also available, but not utilised in this work.

4.3 Calibration

Several calibration standards were used in calibrating the position of the spectral features of interest. The chief standards were emission lines at 546.07 nm and 579.04 nm of a Hg discharge lamp. The former was used with Raman spectroscopy of diamond when using the 514.5 nm excitation line, since at 1122.60 cm^{-1} it is conveniently close to the diamond Raman line at $\sim 1332\text{ cm}^{-1}$. Both these lines were used in diamond PL spectra.

The Raman spectra of cBN were calibrated via the 1056.94 cm^{-1} plasma line (relative to 488.0 nm) of the argon ion laser, as this line is in close proximity to the Raman lines at 1054 cm^{-1} and 1306 cm^{-1} . After calibration, an interference filter (previously mentioned) was used to remove this plasma line during measurements. The Hg emission lines were also used with the PL spectra of cBN, as well as the 748.69 nm emission line of a Kr discharge lamp for calibrating the higher wavenumber features (around 7000 cm^{-1}) in the PL spectra.

4.4 Data acquisition

The Raman spectrometer configuration and data acquisition procedures were controlled via a desktop computer. Proprietary software from Jobin-Yvon, SpectraMax (v1.0d), was run under MS-DOS (v6.2) and later upgraded to Labspec v3.03 software running under Windows 95. The software controlled the whole acquisition procedure and stored the data in a proprietary format on the computer hard disk drive. Data analysis and printing was possible under the Jobin-Yvon software and this software was principally used for the analysis of 2D and 3D mapping data. Peak fitting analysis of PL data was mainly done by exporting the data to a text file and importing it into and manipulating it with Microcal Origin software (v5.0).

For peak fitting either a linear combination of a Gaussian and a Lorentzian lineshape (offered by the JY software) was used, or the functions available with Origin software (Gaussian, Lorentzian or Voigt).

Mapping procedures are detailed in § 4.7.1, but a note regarding the manipulation of map data is made here. When exporting a map data file from Labspec format to text format, the data for the individual spectra in the map are saved as rows, not as columns. After importing the text file into Origin, it is thus necessary to transpose the worksheet so that the first column contains the x-data common to all the spectra, and subsequent columns contain the y-data for the individual spectra.

4.4.1 Normalisation of spectra

In order to compare the intensities of photoluminescence peaks, it is necessary to normalise the spectra. This is due to the intensity of PL spectra depending on several, often uncontrollable factors such as laser beam penetration depth, excitation volume, collection efficiency and geometry of the experiment. The approach adopted was that followed by Evans *et al.* (1984), and also used by Fish (1995). The luminescence was normalised by dividing the luminescence intensity at specific wavelengths throughout the spectral range by the integrated intensity of the first order Raman peak, measured under identical excitation, collection and geometric conditions. The Raman peak intensity was linearly proportional to the power of the laser and the volume of diamond from which luminescence was being excited, allowing for a reasonable compensation of the uncontrollable factors mentioned above. It is noted that this normalisation must still be considered to be only semi-quantitative.

4.5 Cryostats

An Oxford Instruments Microstat^{He} continuous flow liquid helium microscope cryostat (figure 4.3) was used for both diamond and cBN PL measurements. The cryostat was used in conjunction with an Oxford Instruments GFS 300 liquid cryogen transfer tube, a GF3 diaphragm vacuum pump (for cryogen flow), a VC30 gas flow controller, an Oxford Instruments ITC4 temperature controller and a Pfeiffer-Balzars turbo-molecular pump with rotary backing pump for vacuum pumping duties. The vacuum gauge utilised Balzers Pirani and cold cathode gauges. The temperature sensor of the cryostat was a RhFe thermocouple. A temperature stability of ± 0.1 K is possible with liquid helium, while a stability of ± 0.2 K is quoted in the manual for liquid nitrogen. It is capable of operating from liquid helium temperatures to 500 K.

In the cryostat, the samples were mounted in vacuum on a cold finger attached to a copper heat exchanger block. The mounting was facilitated with Apiezon “L” vacuum grease to keep the samples in position and ensure good thermal contact with the cold finger from the lowest temperature up to room temperature. A base temperature of 4.2 K was readily attainable. Optical access to the samples was via Spectrosil B windows. A vacuum of $< 5 \times 10^{-5}$ Torr was sufficient for trouble-free low temperature operation.

The cryostat was clamped to the motorised X-Y stage via a custom-built attachment, allowing for measurement of several small samples or the mapping of features present in larger samples at low temperature.

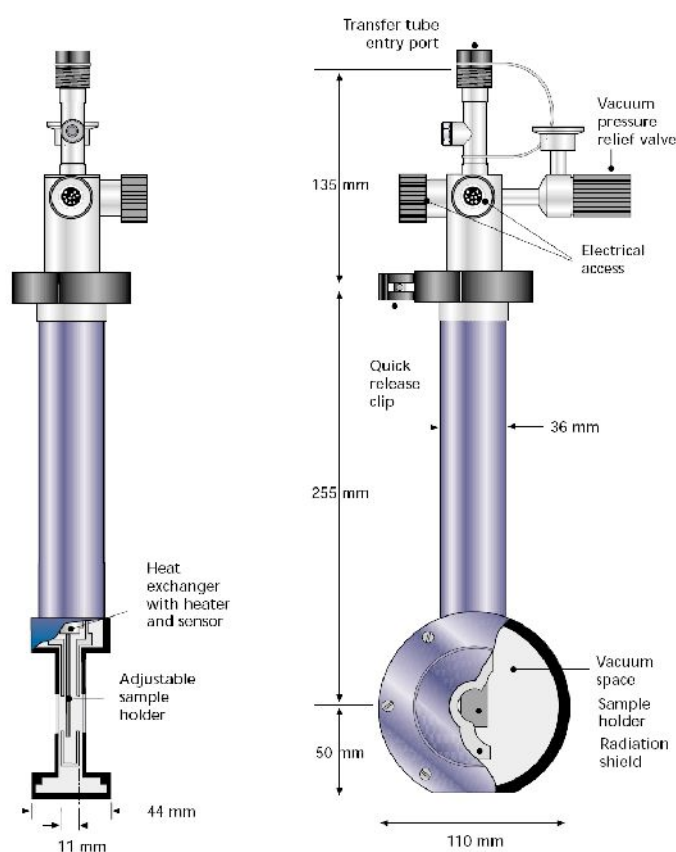


Figure 4.3: Diagrammatic representation of the Oxford Instrument Microstat^{He} microscope cryostat used for some of the low temperature measurements[†].

For the low temperature Raman measurements on cBN it was found necessary to make the measurements in an exchange gas cryostat, i.e. where the sample chamber is filled with

[†] From www.oxinst.com, accessed January 2007

nitrogen or helium. As mentioned in chapter 6, measurements in the exchange gas cryostat gave less scattered results, especially for the cBN Raman peak position data, compared to the vacuum mounting in the Microstat^{He} detailed above.

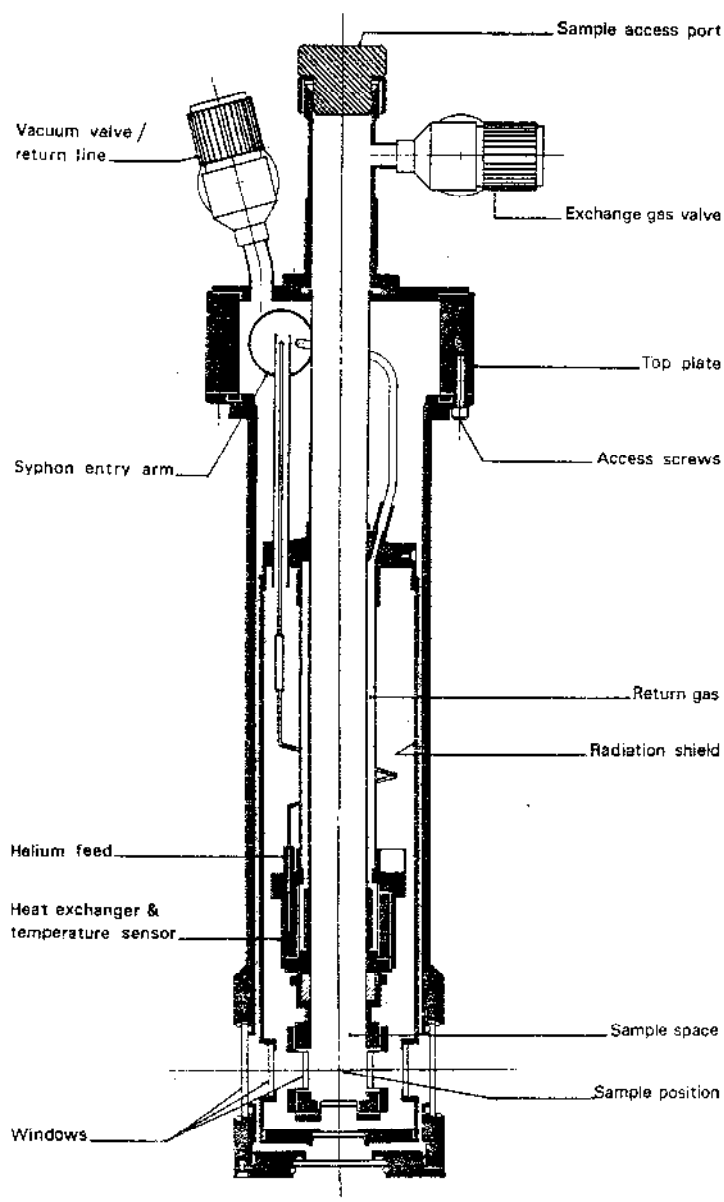


Figure 4.4: Diagrammatic representation of Oxford Instruments CF1204 continuous flow exchange gas cryostat (Oxford Instruments 1988).

The cryostat employed for the low temperature Raman spectroscopy of cBN was an Oxford Instruments CF1204 continuous flow liquid helium cryostat (figure 4.4). The cryostat was used in conjunction with an Oxford Instruments GFS 300 liquid cryogen transfer tube, a GF3

diaphragm vacuum pump (for cryogen flow), a VC30 gas flow controller, an Oxford Instruments ITC4 temperature controller and a Pfeiffer-Balzers turbo-molecular pump with rotary backing pump for vacuum pumping duties. The vacuum gauges comprised Balzers Pirani and cold cathode gauges. The cryostat had two temperature sensors; one connected to the copper heat exchanger block (RhFe thermocouple) and used by the ITC4 controller to control the temperature and a second one (AuFe/Chromel thermocouple using liquid nitrogen as reference) attached directly to the sample holder for a more accurate measurement of the sample temperature. After evacuation by the vacuum pump, the sample chamber was backfilled with helium gas. This ensured good thermal equilibrium between the sample and sample temperature sensor, as well as helping to prevent any possible localised heating of the sample by the laser. A base temperature of 4.2 K was readily attainable and the temperature stability was ± 0.1 K using liquid helium as the cryogen.

4.5.1 Comment on low temperatures for PL measurements

The diamond photoluminescence measurements took place at 77 K, and the cubic boron nitride photoluminescence studies took place at 5 K. It was experimentally determined that this lower temperature was necessary in the case of cBN, since there was an appreciable difference in the zero phonon lines at 25 K and 5 K. This is illustrated in figure 4.5.

4.6 High Temperature Furnaces

Two different high temperature furnaces were used in the course of this body of work. A custom built furnace (Rammutla 2001) capable of ~ 1000 °C and suitable for larger samples was used for the high temperature work on PCD drillbits. In order to hold the latter, the sample holder was a quartz tube with a flared end of a diameter suitable to “cradle” the drillbit in a horizontal position. A Linkam TS1500 microscope furnace was used for the high temperature measurements on the cBN single crystals.

A diagram of the custom-built furnace is given in figure 4.6. The sample is mounted on a quartz tube which can be adjusted vertically to position the sample in front of the quartz window, through which the incoming laser beam is directed and via which the backscattered radiation is collected as well. The vacuum space was evacuated via a diffusion pump with rotary backing pump. The sample was heated via a wound heating element (99.99% pure Molybdenum wire) and the sample temperature was monitored via a Type R thermocouple (Pt/13%Rh vs Pt). A tantalum foil radiation shield was used to help restrict radiative heat losses. The temperature was

controlled via a Eurotherm 818 temperature controller coupled with a Eurotherm 426 thyristor unit. Power to the element was controlled via an autotransformer.

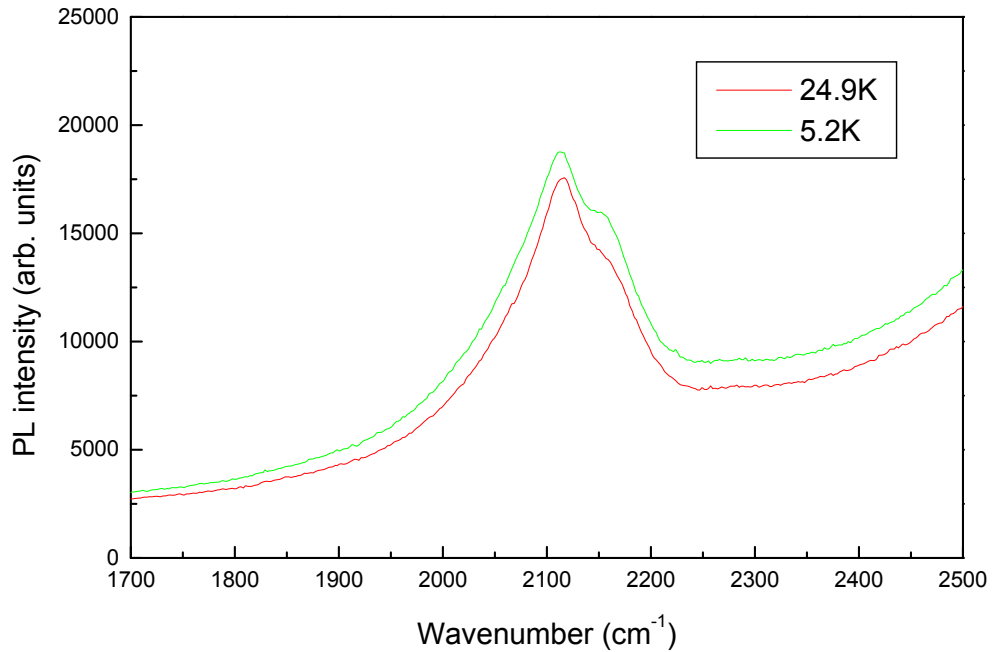


Figure 4.5: PL spectra of irradiated cBN at 25 K and 5 K, showing the effect of temperature on the shape of the zero phonon line of the RC1 defect (see §6.4 for discussion)

The vacuum system was connected in such a way that after evacuation the furnace could be backfilled with UHP (ultra-high purity; 99.999%) argon gas under low pressure (~5 Torr). At lower temperatures (<1000 K) when radiant heating is less efficient, the presence of the argon gas ensures a good thermal equilibrium between the sample, heating element and thermocouple. Above 1000 K the sample space was evacuated as the presence of the gas then placed a heavy load on the outer water-cooling jacket of the furnace.

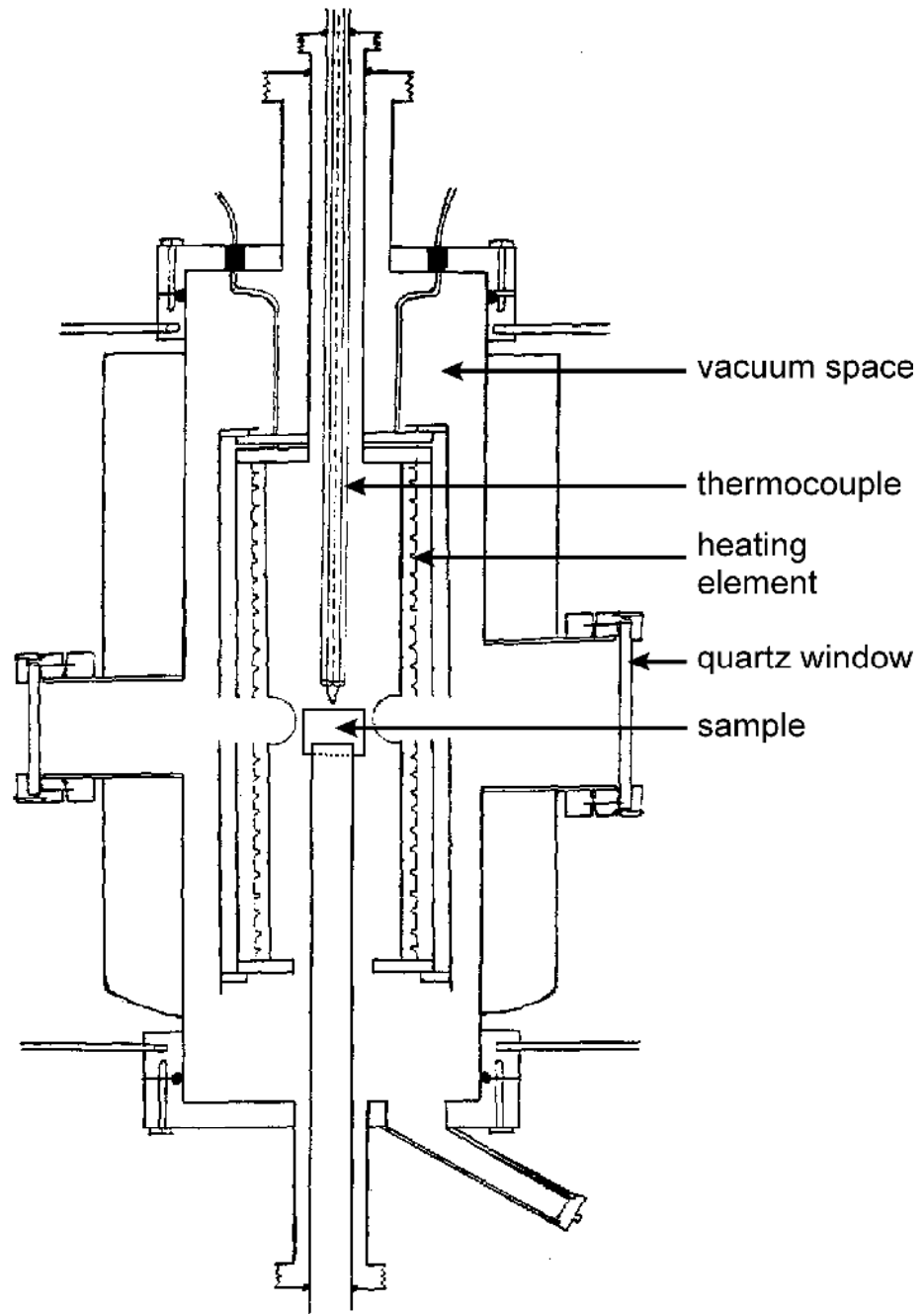


Figure 4.6: Diagram of custom-built high temperature furnace used for measurements on PCD drillbits (from Rammutla 2001).

A diagram of the setup for the Linkam TS1500 microscope furnace is given in figure 4.7. This is a microscope furnace capable of achieving 1500 °C with the sample in an UHP argon atmosphere. The body of the furnace is water-cooled while argon is flushed through at a flow rate

of < 60 ml/min. The sample is placed on a thin sapphire disk (thickness 0.3 mm) inside the ceramic sample cup, which is heated via platinum wire windings around the outside of the cup. The thermocouple for temperature sensing is mounted directly under the sapphire disk, so that only the thickness of the sapphire disk is between the sample and temperature sensor. The good thermal conductivity of sapphire, coupled with the presence of the argon, gives an accurate reading of the sample temperature. An alumina radiation shield with a small hole for viewing the sample is placed on top of the sample cup and optical access to the sample is via a water-cooled quartz window. The whole furnace is conveniently clamped onto the motorised XY stage of the microscope for positioning the sample under the objective. Temperature control is via a programmable Linkam TMS93 unit that heats the sample via DC pulses. Due to the small size of the sample and sample cup, high heating rates of up to 100 °C/min can be achieved, but in the present work a heating rate of 10 °C/min was used.

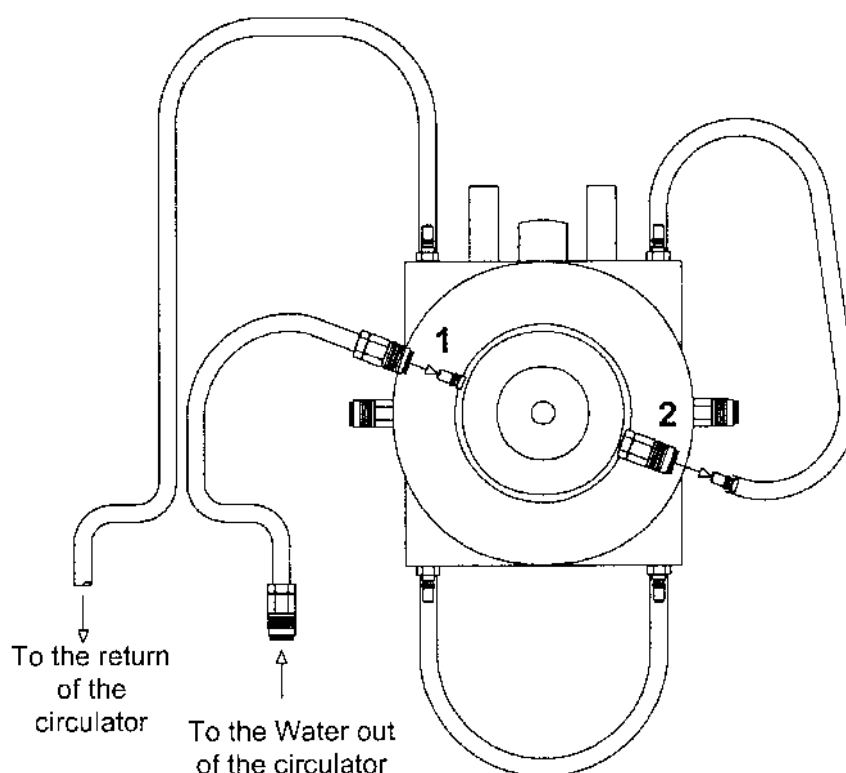


Figure 4.7: Schematic diagram of the Linkam TS1500 microscope furnace stage (Linkam 1997).

4.7 Soft Impressor Technique

The soft impressor technique (Brookes 1992a and references therein) is based on the use of cones made from materials that are considerably softer than the flat specimen surface to be indented. In a simple modification of the indentation method, the impressor material (usually a cone with included angle 120°) deforms when loaded to apply a uniform and controllable mean contact pressure over a circular area (figure 4.8). The cone continues to flatten until the normal applied load is supported quasi-hydrostatically and the degree to which the cone flattens is dependent on the hardness of the cone material and independent of the specimen material. The mean pressure (P_m) applied to the specimen is calculated by $P_m = L/A$ (Pa); where L is the applied load (N) and A (m^2) is the contact area between the cone and the specimen, being the area over which the cone has flattened. The contact pressure applied in this way is much lower than that applied by a conventional rigid indenter such that the representative stress developed beneath the impression may not exceed the fracture stress of the specimen. This reduces the instances of brittle failure.

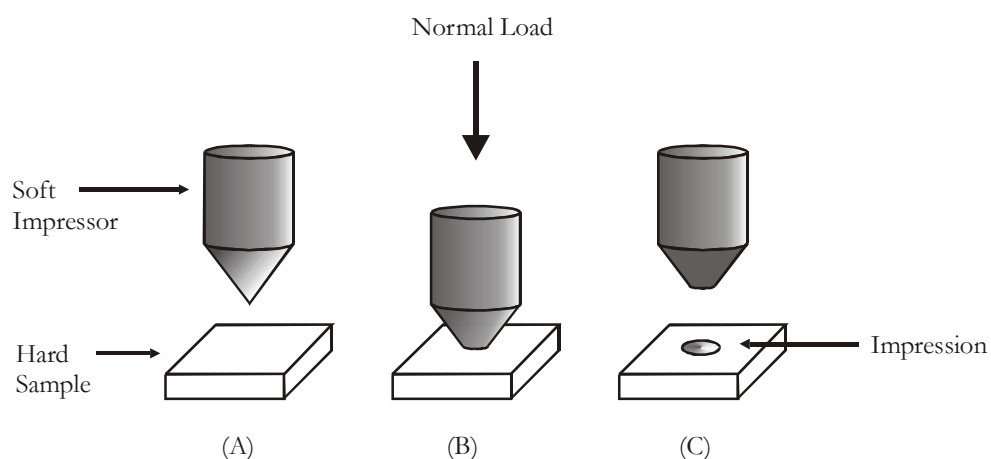


Figure 4.8: Schematic representation of the deformation of a sample using the soft impressor technique. The actions depicted all take place at high temperature ($>700^\circ\text{C}$) under vacuum for diamond (Daniel 2000).

The choice of cone material is important and determined by various factors such as indentation temperature, stability of the cone material at the selected temperature, and the hardness of the sample material. To achieve sufficient pressures to deform diamond the cone material must be extremely hard, and cone materials suitable for this include reaction sintered cBN, silicon nitride (Si_3N_4) and hot pressed titanium diboride (TiB_2). The indentations discussed in subsequent chapters were made using Si_3N_4 .

In the present work the deformations in the diamond samples made via the soft impressor technique are referred to as impressions rather than indentations.

Pressures in excess of 1 GPa and temperatures of 700 °C to 1400 °C were generated in custom-designed and built high temperature, high-vacuum equipment at the University of Hull, UK, by the research group of Dr EJ Brookes. Figure 4.9 shows a schematic diagram of the equipment (not to scale). The standard applied load of the system was in the range 115 N to 130 N, depending on the atmospheric pressure. The procedure would be to place a sample on the graphite susceptor and check that the soft impressor makes contact in the appropriate spot. A vacuum is then created and the sample is heated by induction heating via the R.F. induction coil to the desired temperature. The temperature was monitored via a pyrometer. The desired load was applied for a specified dwell time, after which the load was released and the sample allowed to cool.

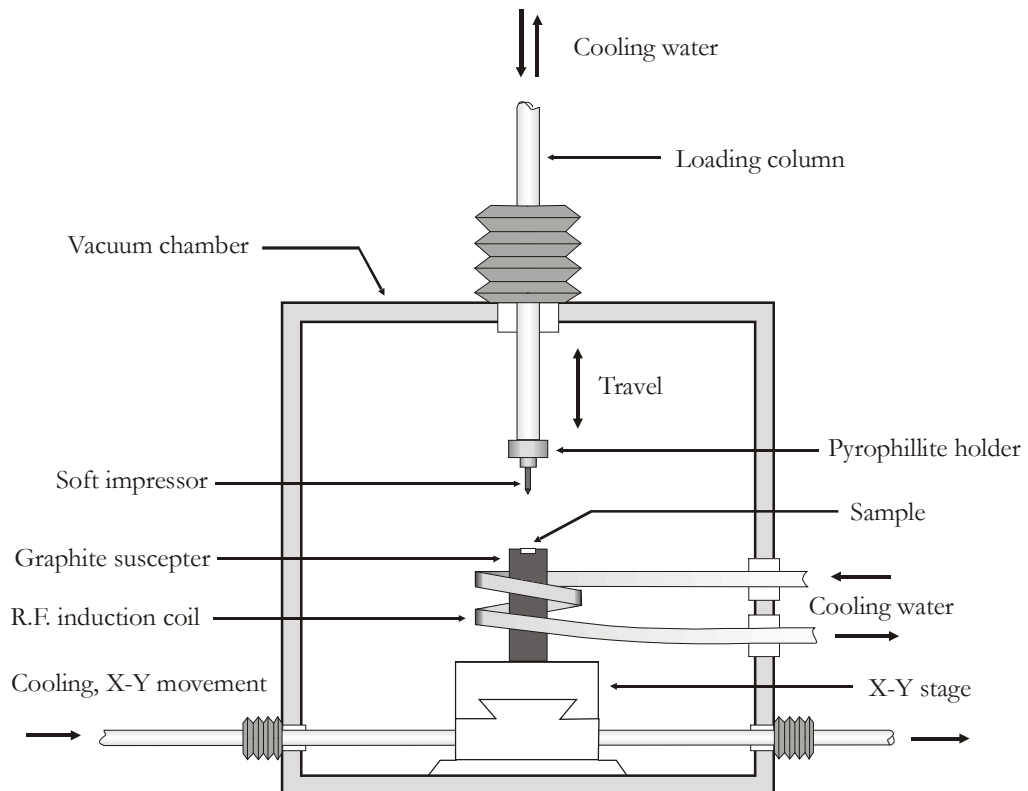


Figure 4.9: Schematic diagram of high-temperature, high vacuum equipment used in the soft impressor technique (Daniel 2000).

4.7.1 Procedures for acquiring maps of spectral features

The procedures for acquiring 2-dimensional (2D) and 3-dimensional (3D) maps of specific spectral features, e.g. a peak intensity or a peak position of either a Raman line or a PL peak, are

described here in general terms. The important parameters that need to be considered are highlighted, but exact values for the experimental work of this thesis are given in the results chapters.

4.7.1.1 2D maps

For 2D maps, the computer-controlled XY stage is used with the Raman microscope. The sample is mounted on the stage such that the laser is centred on the area to be mapped. The XY stage movements are driven by stepper motors, and can involve a slight jerk for small movements. For room temperature measurements, it was found that for small crystals with smooth facets it was best to secure the sample to the microscope slide using a tiny piece of Prestik[†] to prevent the crystal moving slightly on the slide during a mapping procedure.

It was found that square grids result in clear contour maps that are relatively easy to interpret. In using both the Jobin-Yvon and Origin software, rectangular maps tended to display with a distorted aspect ratio, making it difficult to relate mapped contours to the physical sample.

The size of the grid used for a particular map depends on a number of factors. Firstly the size of the feature to be mapped must be considered, as this will dictate the physical size of the grid, i.e. x microns to a side. Secondly the resolution of the grid must be decided, i.e. what is the spatial interval between consecutive grid points. This depends on what scale the feature being mapped is expected to change, i.e. if e.g. the stress changes slowly over several hundred microns, then grid points every 20 or 50 microns would probably suffice, but if the stress changes on scales of tens of microns, then points every 2 or 5 microns (or even finer) would be indicated. The interval between grid points is also influenced by the spectral intensity of the feature being mapped. If it takes 1 second to acquire a good spectrum, many more grid points can reasonably be accommodated than if a longer time (such as 60 seconds) is required to acquire a good spectrum.

The next factor to consider is the combination of objective and confocal pinhole diameter. Generally the higher magnification objectives have larger N.A. (numerical aperture), i.e. they are more efficient at collecting the backscattered light (the intensity of the collected light is proportional to the square of the N.A.). As mentioned previously, the choice of objective also influences the diameter of the laser beam at the sample. The combination of a high magnification objective (typically 50 \times or 100 \times) and a small confocal pinhole diameter (such as 0.2 mm or

[†] Prestik is a rubber-like temporary adhesive marketed in South Africa and manufactured by Bostik (www.bostik.co.za). It is similar to Blu-Tack (www.blu-tack.co.uk or www.blutack.com).

0.1 mm) also gives the shortest focal barrel, which is required when thin slices of transparent materials are being mapped or when background scattering, e.g. from highly reflective samples, needs to be suppressed.

The higher magnification objectives have shallower depths of view, especially the 100× objective. This requires the sample being mapped to be very flat (small surface roughness and everywhere orthogonal to the laser beam) otherwise the focus changes appreciably over the extent of the mapping grid and changes in the intensities of mapped spectral features are due to changes in focus rather than changes in the sample. The 100× objective also has a very short working distance, so there is the danger of the objective touching the sample during the map if the sample is not very flat.

Obviously the choice of objective and pinhole diameter will influence the optimum acquisition time, so that some experimentation with different objective, diameter and time permutations is necessary before an actual map can be acquired.

Additional factors (unrelated to the mapping procedure) to consider, would include laser power at the sample, entrance slit width and choice of spectrometer configuration and grating.

Once the objective, pinhole diameter and total grid size and the size of the increments have been decided, the software will then automatically map the spectral feature of interest by acquiring a spectrum at each point on the defined grid. Total acquisition time for a map thus varies between tens of minutes and hours, depending on the total number of points and the acquisition time for each grid point.

It is noted here that although the software provides for the grid spacing to be defined as either the total grid size plus the number of points (software calculates the increment size) or as the total grid size plus the increment size (software calculates the number of points), it was found that the first option works better. This option has also been recommended as the best to use by a Jobin-Yvon service engineer.

Once a map has been acquired, it can be stored in Jobin-Yvon software format, or exported as a text file to Origin for further analysis. Intensity contour maps of particular spectral features can be derived fairly easily, but it has been found to be more consistent to first do a background subtraction and then to fit a function to all the spectra. From these fitting parameters contour maps of the intensity, position and width can be plotted.

4.7.1.2 3D maps

For 3D maps, the procedure is very similar to that outlined above, except for the addition of a spatial dimension. 3D maps can be acquired using either a “Piezo 100” Z-stage in conjunction with the motorised XY stage, or by manually adjusting the Z-direction and using the motorised XY stage for the X- and Y-dimensions.

The “Piezo 100” Z-stage is a special mounting for a microscope objective where the objective is moved up and down via a piezo-electric drive. The only limitation of this drive is that its maximum z translation is 100 μm . One can thus not map “deeper” than 100 μm into a transparent sample for a fixed position of the objective.

To acquire a 3D map, the grid size and spacing is set up with the same considerations that apply to the 2D maps. The software controls both the XY stage and the piezo Z-drive to acquire the defined 3D map. If the 3D map needs to penetrate deeper than 100 μm into a transparent sample, several 3D maps using the piezo Z-stage can be acquired and manually combined, or the z movement can be completely manual (via the microscope adjustment knob) so that the 3D map is a combination of several 2D maps that have been acquired at different depths into the sample.

4.8 Samples

Both single crystal diamond and polycrystalline diamond samples were studied. The single crystal diamonds were synthetic (HPHT) type Ib crystals with predominantly (001) faces. The crystals were polished and indented by the research group of Dr E J Brookes at the University of Hull. The polycrystalline diamond samples were all Syndrill drillbits, supplied by De Beers Industrial Diamond Division and subsequently Element Six (Pty) Ltd. The samples were used as-received, with no further processing. Further details regarding the diamond-based samples used in this work, are given in the relevant sections of chapters 5 and 6.

For cBN both single crystals and polycrystalline samples were studied. Polycrystalline samples were available in form of small sintered squares, 10 mm to a side, with no backing material. The composition was at least 90% cBN, with the remainder being binder material. Various single crystal samples were available, ranging in diameter from 360 μm to 1 mm and in colour from deep black to almost transparent light amber. The crystallographic morphology of the crystals was generally quite poor, with crystals having a sugary appearance. A more detailed description of the cBN-based samples is given in the relevant sections of chapter 7.

Chapter 5: Results – investigation of diamond

This chapter serves to present and discuss results of a Raman and photoluminescence (PL) characterisation of impressions made in single crystal diamond with the soft impressor technique. In addition, Raman spectroscopy was used to characterise the stresses in the PCD layer of several industrial toolbits and results of this work are reported in chapter 6. A short précis of the soft impressor technique is given in § 4.7 and a description of the method by which the Raman peak features were mapped in a matrix across each impression can be found in § 4.7.1.

The significant results described in the chapter were published in Erasmus *et al.* (2011a).

5.1 Impressions in single crystal synthetic diamond

All the results in this section were measured on impressions in one specific diamond. This diamond was a synthetic single crystal of the “Monodie” type, synthesised via the HPHT method by De Beers Industrial Diamonds (Pty) Ltd[†], with ~500ppm substitutional nitrogen as the major impurity. Two impressions were made on the diamond surface, of which one was useable. This will be referred to as the “proper” impression. The other was too close to the edge of the diamond surface to be useful, but will be briefly discussed below and will be referred to as the “skew” impression for reasons that will become apparent later.

Both impressions were made under the same experimental conditions, which are a Si₃Ni₄ impressor on a {001} crystallographic face, a temperature of 1400 °C in a vacuum furnace, a 300 second dwell time and a 115 N load. Figure 5.1 and Table 5.1 below give the sample map and impression characteristics, respectively.

[†] Currently Element Six (Pty) Ltd.

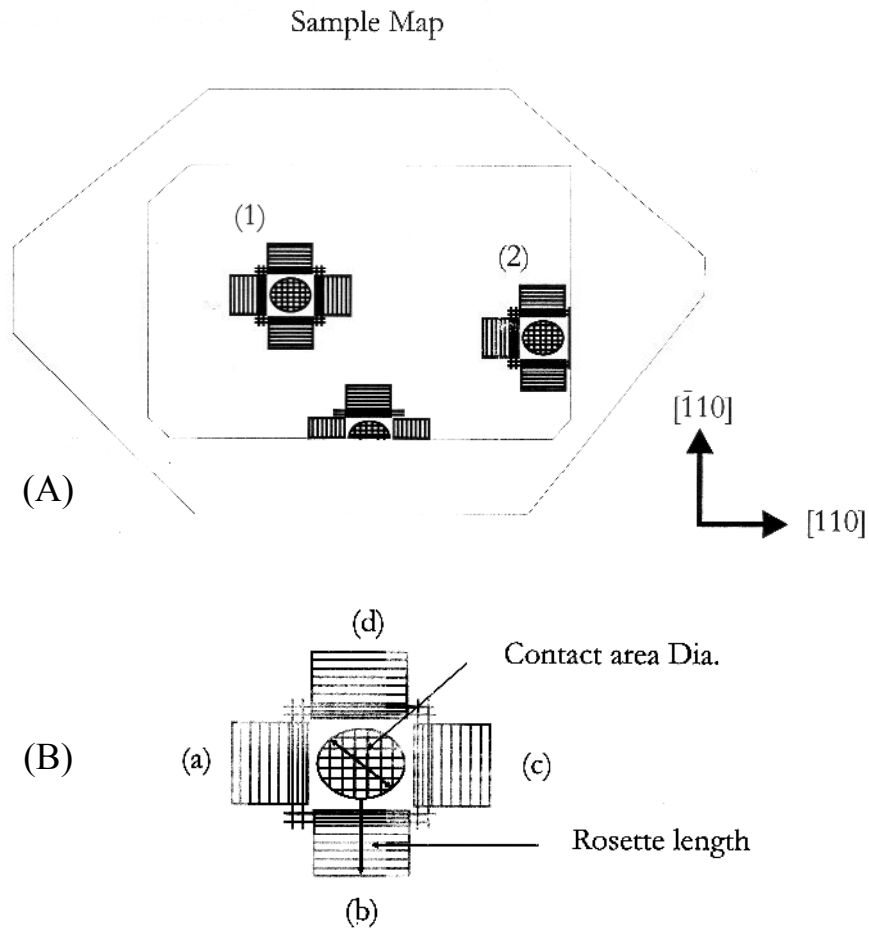


Figure 5.1: (A) Map of the diamond showing location of two impressions discussed in the text. The impression marked (1) is the "proper" impression and the impression marked (2) is the "skew" impression. It is important to note the crystallographic orientation of the impressions on the diamond surface. A third, unsuccessful, impression is located right on the edge below (1) and (2). (B) Diagram of an impression identifying the measurements in Table 5.1.

Table 5.1: Dimensional characteristics of the two impressions shown in figure 5.1.

	Average diameter (μm)	Mean pressure (GPa)	Rosette lengths (μm)			
			(a)	(b)	(c)	(d)
(1)	223	3.07	235	226	270	184
(2)	231	2.86	315	295	/	329

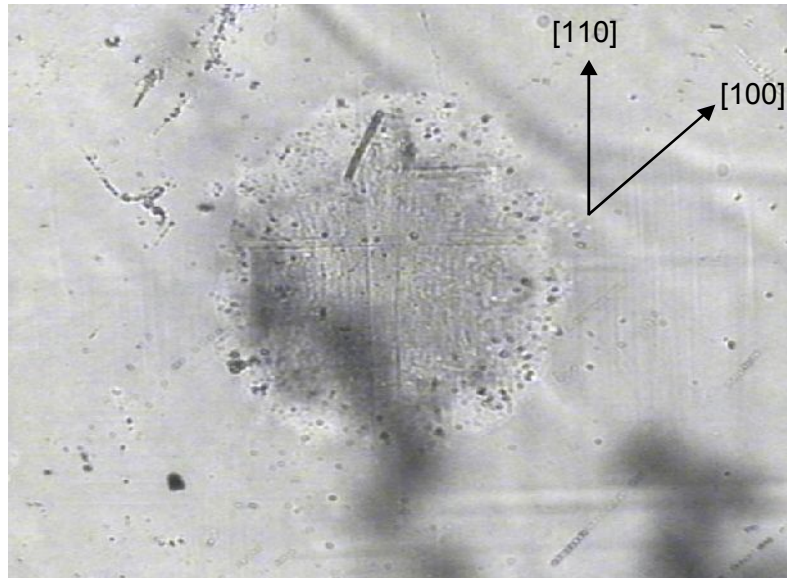


Figure 5.2: Optical micrograph of the proper impression as seen under the Raman microscope. The image was taken in transmitted light and the average diameter of the circular impression area is 223 μm . The intersecting straight lines visible inside the impression and to the right are due to the dislocations running out onto the surface of the diamond during the impression process. An indication of the crystallographic orientation of the impression is given in the figure.

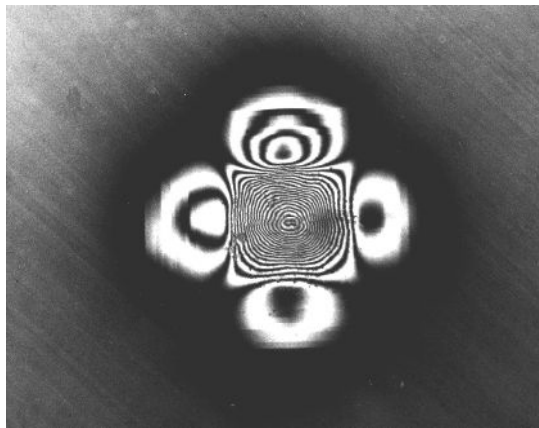


Figure 5.3: Interferogram of an indent similar to that of figure 5.2. It was made under identical experimental conditions with the only difference being that the diamond here has 650 ppm nitrogen as impurity. The interference fringes clearly illustrate that the contact area is a shallow bowl-shaped impression and that there are four lobes of pile-up associated with the impression (image from Daniel (2000)).

It is clear from figure 5.2 that no cracking has taken place either inside or in the vicinity of the impression. The deformation is thus completely plastic. The rosette pattern associated with a high-temperature impression is not very clear in figure 5.2. It is possible to visualise this pattern more clearly by etching the surface with molten KNO_3 (Daniel 2000), but this was not done for the diamond sample in question in case it modified the residual stresses at the surface of the diamond. The interferogram of a similar indent (figure 5.3) visualises the associated rosette pattern very clearly. In the interferogram the diameter of the impression is $\sim 200 \mu\text{m}$, the depth is $\sim 9 \mu\text{m}$ and the “height” of the pile-up is $\sim 2 \mu\text{m}$.

5.1.1 2D Raman maps

Raman spectra were acquired at ambient pressure and temperature using the micro-Raman attachment of a Jobin-Yvon T64000 Raman spectrometer operated in single spectrograph mode. The excitation source was the 514.5 nm line of an argon ion laser and the backscattered light was dispersed onto a liquid-nitrogen cooled CCD detector by an 1800 grooves/mm grating.

A computer-controlled motorised XY stage was used for mapping the diamond Raman line across the surface of the impression. The grid in figures 5.4 and 5.5 below is a 10×10 matrix, measuring $900 \mu\text{m} \times 900 \mu\text{m}$. The confocal pinhole was set so as to sample a $50 \mu\text{m}$ thick section of diamond and the laser beam diameter at the surface was $\sim 1.5 \mu\text{m}$. The position and width of the diamond Raman peak was extracted by fitting a Lorentzian function to the data using Origin 5.0 software. The entrance slitwidth used was $20 \mu\text{m}$, which gave a bandpass of 0.45 cm^{-1} with the grating used. This is substantially smaller than the Raman peak widths measured, indicating that any Gaussian component due to the instrument will only make a small contribution. The stress at any given mapping point was calculated using equation 3.29. The value of α used was $1.9 \text{ cm}^{-1}/\text{GPa}$ (Bergman *et al.* 1995). Orange in figure 5.4 corresponds to a zero (stress-free) value, while red corresponds to tensile stress (positive stress values). The progression of colours from yellow through green to blue corresponds to increasing compressive stress (increasing negative stress values), with the maximum compressive stress of $\sim 200 \text{ MPa}$ in the dark blue shading.

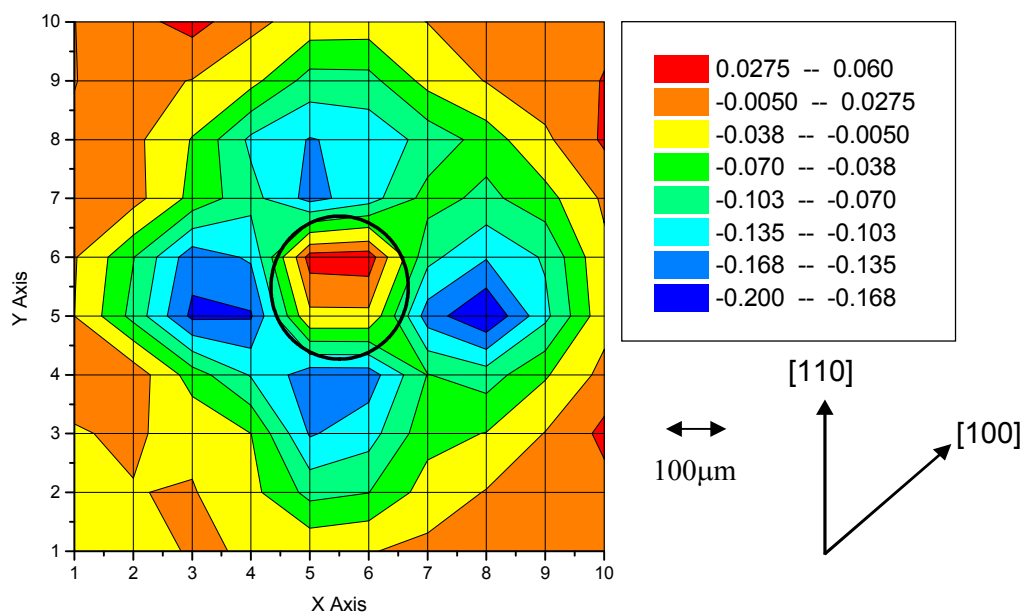


Figure 5.4 (a): 2D contour map of the surface stress associated with the impression, calculated from the Raman peak position of diamond. The black circle corresponds to the physical area of the impression in figure 5.2. The units for the values in the table at the top right are GPa. The orange shading corresponds to an essentially zero (stress-free) value, while red shading corresponds to tensile stress (having positive stress values). The progression of colours from yellow through green to blue corresponds to increasing compressive stress (increasing negative stress values), with the maximum compressive stress of ~ 0.2 GPa in the dark blue shaded regions. A scale bar indicating the size of the grid blocks and an indication of the crystallographic orientation of the contour map is also given.

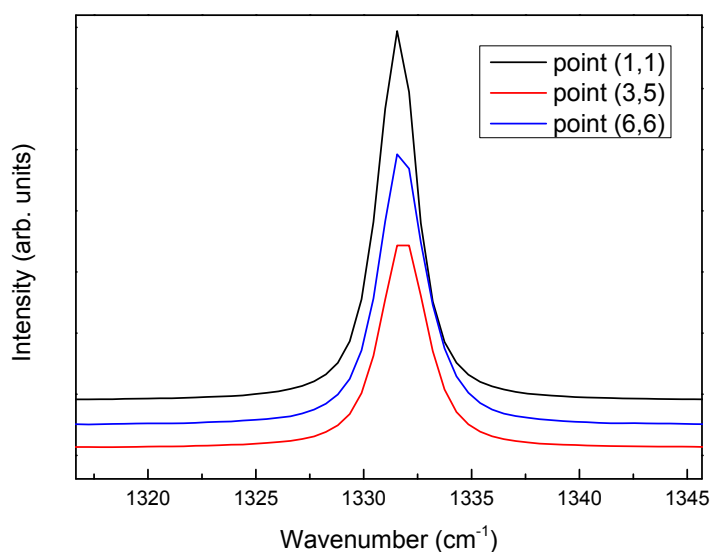


Figure 5.4(b) (at left): An example of the diamond Raman spectra relevant to the contour maps in figure 5.4(a) and figure 5.5. The point coordinates in the legend are (x,y) coordinates referring to the mapping grid in figures 5.4(a) and 5.5.

In the case of figure 5.5, the blue colour corresponds to a “background” value for the FWHM of 2.0 cm^{-1} to 2.1 cm^{-1} and the maximum peak width (red in figure 5.5) corresponds to a peak width of 2.6 cm^{-1} to 2.7 cm^{-1} . The peak width thus increases by $\sim 30\%$ in the centre of the impression. There is a clear radially symmetric pattern associated with the impression on the surface.

The diamond Raman peak for the “skew” impression (figure 5.6) was mapped using exactly the same experimental conditions as for the “proper” impression.

The darker green in figure 5.7 corresponds to a zero (stress-free) value, while red corresponds to tensile stress. The progression of colours from darker green through lighter green to blue corresponds to increasing compressive stress, with the maximum compressive stress of $\sim 170\text{ MPa}$ in the dark blue shading.

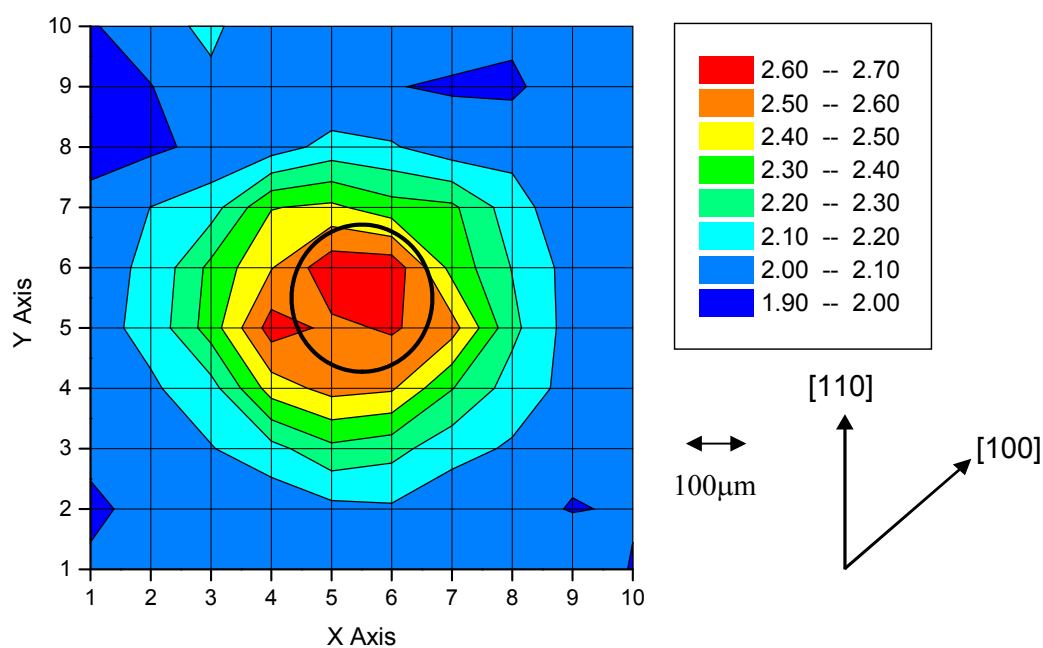


Figure 5.5: 2D contour map of the FWHM of the diamond Raman peak across the impression. The black circle corresponds to the physical area of the impression in figure 5.2. The units for the values in the table at the top right are cm^{-1} . The dominant blue colour corresponds to a “background” value for the FWHM of 2.0 to 2.1 cm^{-1} and the maximum peak width (red) corresponds to 2.6 to 2.7 cm^{-1} . A scale bar indicating the size of the grid blocks and an indication of the crystallographic orientation of the contour map is also given.

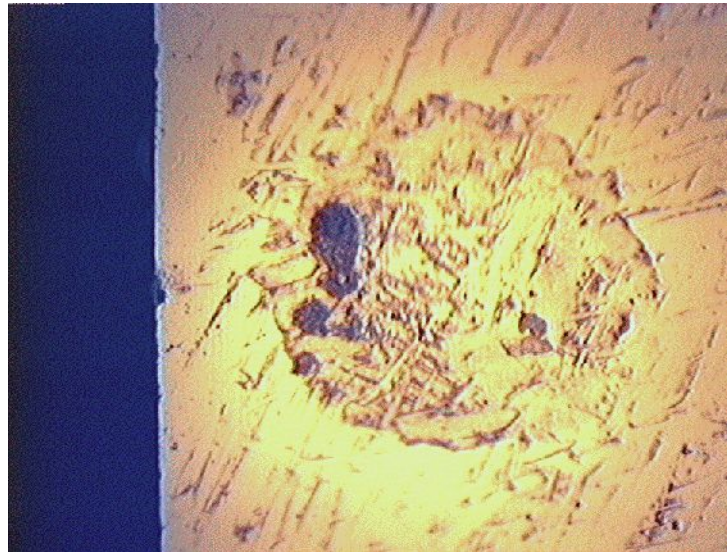


Figure 5.6: Optical micrograph of the “skew” impression in figure 5.1. It can be clearly seen that the impression was made very close to the edge of the diamond surface. The average diameter of the circular physical contact area is 231 μm .

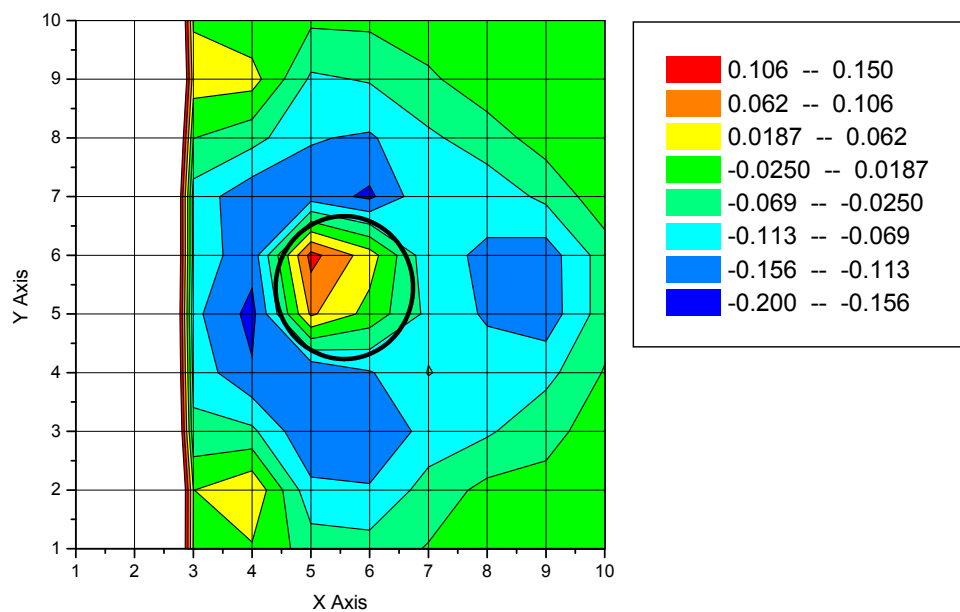


Figure 5.7: 2D contour map of the surface stress associated with the impression shown in figure 5.6, calculated from the Raman peak position of diamond. The black circle corresponds to the physical area of the impression. The units for the values in the table at the top right are GPa. The darker green corresponds to a zero (stress-free) value, while red corresponds to tensile stress. The progression of colours from darker green through lighter green to blue corresponds to increasing compressive stress, with the maximum compressive stress of ~ 0.170 GPa in the dark blue shading.

In the case of figure 5.8, the blue colour corresponds to a “background” value for the FWHM of 2.0cm^{-1} to 2.1cm^{-1} and the maximum peak width (red in figure 5.8) corresponds to a peak width of 2.8cm^{-1} to 2.9cm^{-1} . The peak width thus increases by $\sim 40\%$ in the centre of the impression. The effect of the proximity of the impression to the edge of the diamond can be clearly seen in the deformation map, where the area of maximum plastic deformation has been displaced outside the contact circle of the impression. It is for this reason that this impression was called the “skew” impression.

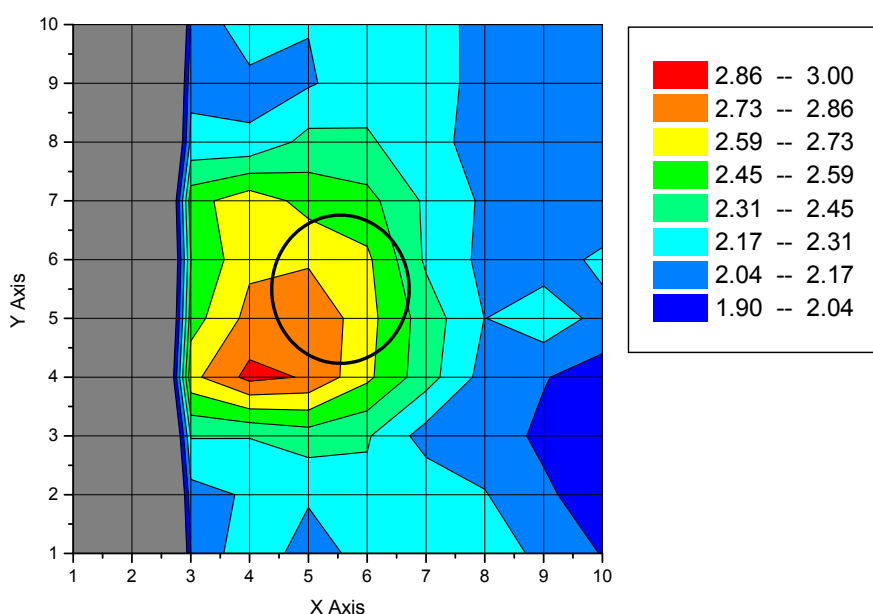


Figure 5.8: 2D contour map of the FWHM of the diamond Raman peak across the impression in figure 5.6. The black circle corresponds to the physical area of the impression. The units for the values in the table at the top right are cm^{-1} . The blue colour corresponds to a “background” value for the FWHM of 2.0 cm^{-1} to 2.1 cm^{-1} and the maximum peak width (red) corresponds to a peak width of 2.8 cm^{-1} to 2.9 cm^{-1} .

5.1.2 3D Raman maps

The general procedure for the measurement of a 3-dimensional (3D) map was given in §4.7.1.2. For the specific maps under discussion here, vertical “slices” were measured along two different crystallographic planes into the diamond using the “proper” impression only. Slices were made along the (100) and (110) planes. The centre of the impression is at the origin of the arrow “a” in the figures in paragraphs 5.1.2.1 and 5.1.2.2. The arrow “a” represents the radius of the circular

impression on the surface of the diamond. Each map is thus of dimension $2a$ on a side. The mapping grid size is 25×25 points, with $10 \mu\text{m}$ intervals. A $50\times$ ultra-long working distance objective was used with a 0.5 mm pinhole, resulting in a $10 \mu\text{m}$ thickness being sampled in the Z-direction. As previously, compressive stress is indicated by negative stress values and its colour range (green, minimum to dark blue, maximum), while tensile stress is indicated by positive stress values and its colour range (yellow, minimum to red, maximum).

5.1.2.1 (100) slice and (110) slice

The stress and deformation maps for these slices are presented in figure 5.9(a) to (d) below. The (100) slice map (figures 5.9(a)&(c)) falls between two arms of the rosette pattern associated with the impression. The largest stress values and the greatest degree of deformation are associated with the volume of diamond immediately below the contact area of the impressor. The magnitude of the tensile stress measured for the (100) (maximum of 0.99 GPa) and (110) (maximum of 0.83 GPa) slices agree very well, and the degree of deformation are also in good agreement (maximum widths of 8.2 cm^{-1} and 9.0 cm^{-1} for (100) and (110) slices, respectively).

The (110) slice stress map very clearly illustrates the presence of the arm of the rosette in the $[110]$ direction. The maximum compressive stress in the arm (-1.49 GPa) is associated with a volume located approximately $50 \mu\text{m}$ below the surface of the diamond. The volume associated with the greatest magnitude of tensile stress is located immediately below the contact area of the impressor, also at a depth of approximately $50 \mu\text{m}$. The degree of deformation mapped in figure 5.9(d) clearly shows that the maximum deformation is associated with the volume immediately below the contact area of the impressor.

It is important to note that the magnitudes of the stresses and degrees of deformation measured in figures 5.4 and 5.5 are different from those reported in this section (§ 5.1.2.1) as different volumes of diamond were sampled in the two cases due to different confocal parameters being used. In the case of the 2D surface maps, the thickness of the slice sampled was $50 \mu\text{m}$, while for the 3D maps within the diamond this value was $10 \mu\text{m}$. For the thicker slice, the stresses and deformation was averaged over a larger volume, thus leading to lower values than for the thinner slice. The importance of the correct confocal parameters to get a clear picture of the relevant contours is clearly illustrated.

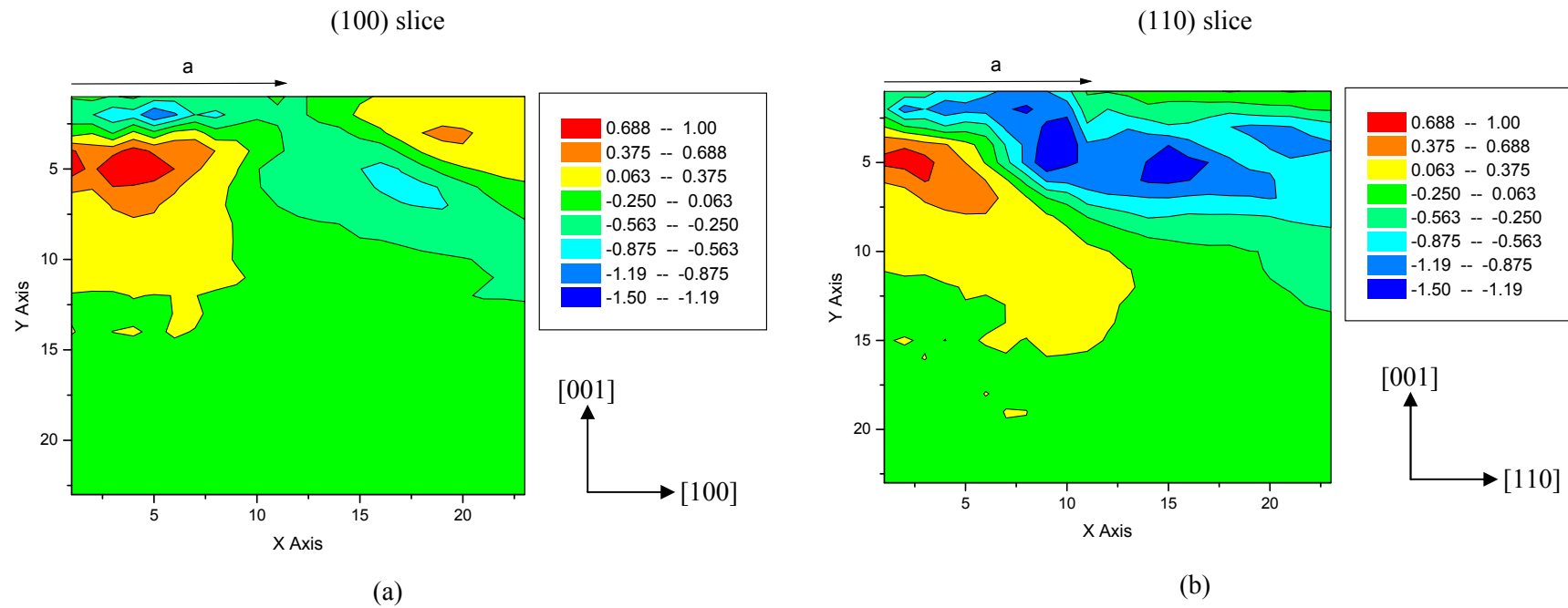


Figure 5.9: (a) Stress contour map of the slice mapped into the diamond along the [100] direction. The centre of the impression is at the top left and the radius of the impression is “ $a = 110\mu\text{m}$ ”. The units of the values in the tables at top right are GPa. Negative values indicate compressive stress and positive values indicate tensile stress, as before. (b) Stress contour map of the slice mapped into the diamond along the [110] direction. Units are the same as for figure (a). Compressive stress is indicated by negative stress values and its colour range (green, minimum to dark blue, maximum), while tensile stress is indicated by positive stress values and its colour range (yellow, minimum to red, maximum).

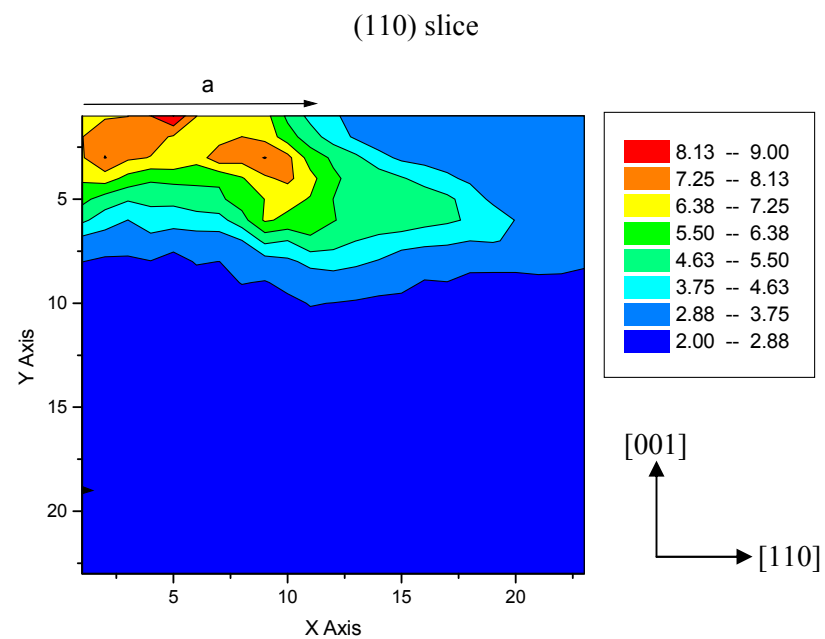
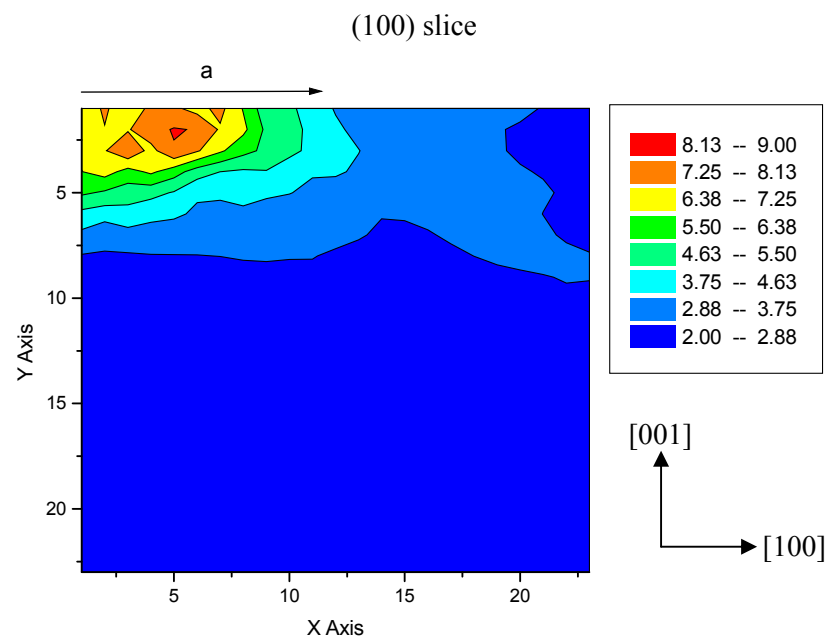


Figure 5.9 (continued): (c) Width contour map of the slice mapped into the diamond along the [100] direction. The centre of the impression is at the top left and the radius of the impression is “ $a = 110\mu\text{m}$ ”. The units of the values in the tables at the top right are cm^{-1} . (d) Width contour map of the slice mapped into the diamond along the [110] direction. Units are the same as for figure (c). The dark blue colour corresponds to a “background” value for the FWHM of 2.00 to 2.88 cm^{-1} and the maximum peak width (red) corresponds to a peak width of 8.13 to 9.00 cm^{-1} .

5.1.2.2 ($\bar{1}10$) slice

Subsequent to the measurements reported on in the paragraphs above, the question arose as to whether the stress and width contours along two arms of the rosette pattern are similar, as different slip systems are operative for two orthogonal arms. Slices into the diamond were mapped along the $[\bar{1}10]$ and $[110]$ directions of impression 1 in figure 5.1. (See the inset in figure 5.12(c) for comparison of the slip systems for the two different directions). Although the same measurement conditions and confocal parameters as in §5.1.2.1 were used, the “slice” along $[110]$ was duplicated to ensure that direct comparisons between the contour maps for the two different directions could be made independent of possible changes in the instrumental setup.

From figure 5.10 it can be seen that the stress and deformation contours for the two crystallographic directions are qualitatively similar. The presence of the compressive stress “arm” of the rosette pattern is clear for both directions. In the case of the ($\bar{1}10$) slice, the maximum tensile stress (red area) is 0.78 GPa while the maximum compressive stress (intermediate blue) in the arm is -0.84 GPa. The maximum tensile stress is achieved in the volume directly beneath the contact area of the impressor. The maximum deformation corresponds to a linewidth of 8.0 cm^{-1} in figure 5.10(c).

In the case of the (110) slice, the maximum tensile stress (red area) is 0.72 GPa while the maximum compressive stress (dark blue) is -1.1 GPa . The maximum tensile stress is also achieved in a volume directly beneath the contact area of the impressor. The maximum deformation corresponds to a linewidth of 7.7 cm^{-1} in figure 5.11(d).

It is noted that the stress and linewidth values for the (110) slice measured here are less than those for the previous measurement of the (110) slice in figure 5.9. The two separate measurements of the (110) slice were separated by ~ 1.5 years in time, so it is possible that a slow relaxation process is taking place, even at room temperature.

The length of the rosette “arm” for the ($\bar{1}10$) slice is less than that for the (110) slice. This is in agreement with the visual measurement of the arm length given in Table 5.1.

It is also noted that whereas the degree of plastic deformation as indicated by the linewidth extends approximately $75 \text{ }\mu\text{m}$ from the surface of the diamond, the tensile stress field extends to approximately $150 \text{ }\mu\text{m}$ from the surface. It thus appears that the extent of the plastic deformation is less than that of the tensile stress field.

These results indicate that deformation along orthogonal rosette arms gives rise to qualitatively very similar residual stress contours and deformation profiles.

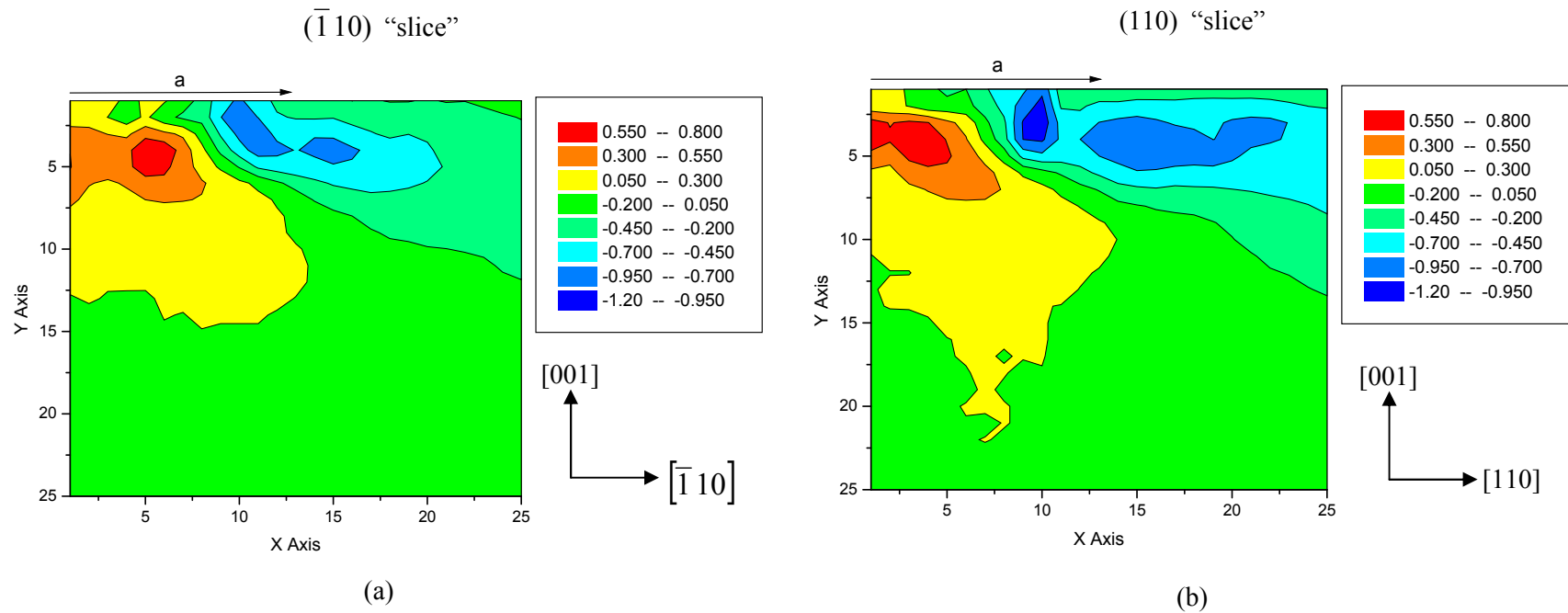


Figure 5.10: (a) Stress contour map of slice mapped into the diamond along the $[\bar{1} 10]$ direction. The centre of the impression is at top left and the radius of the impression is “ $a = 110 \mu\text{m}$ ”. The units of the values in the tables at top right are GPa. Negative values indicate compressive stress and positive values indicate tensile stress, as before. (b) Stress contour map of slice mapped into the diamond along the $[110]$ direction. Units are the same as for figure (a). Compressive stress is indicated by negative stress values and its colour range (green, minimum to dark blue, maximum), while tensile stress is indicated by positive stress values and its colour range (yellow, minimum to red, maximum).

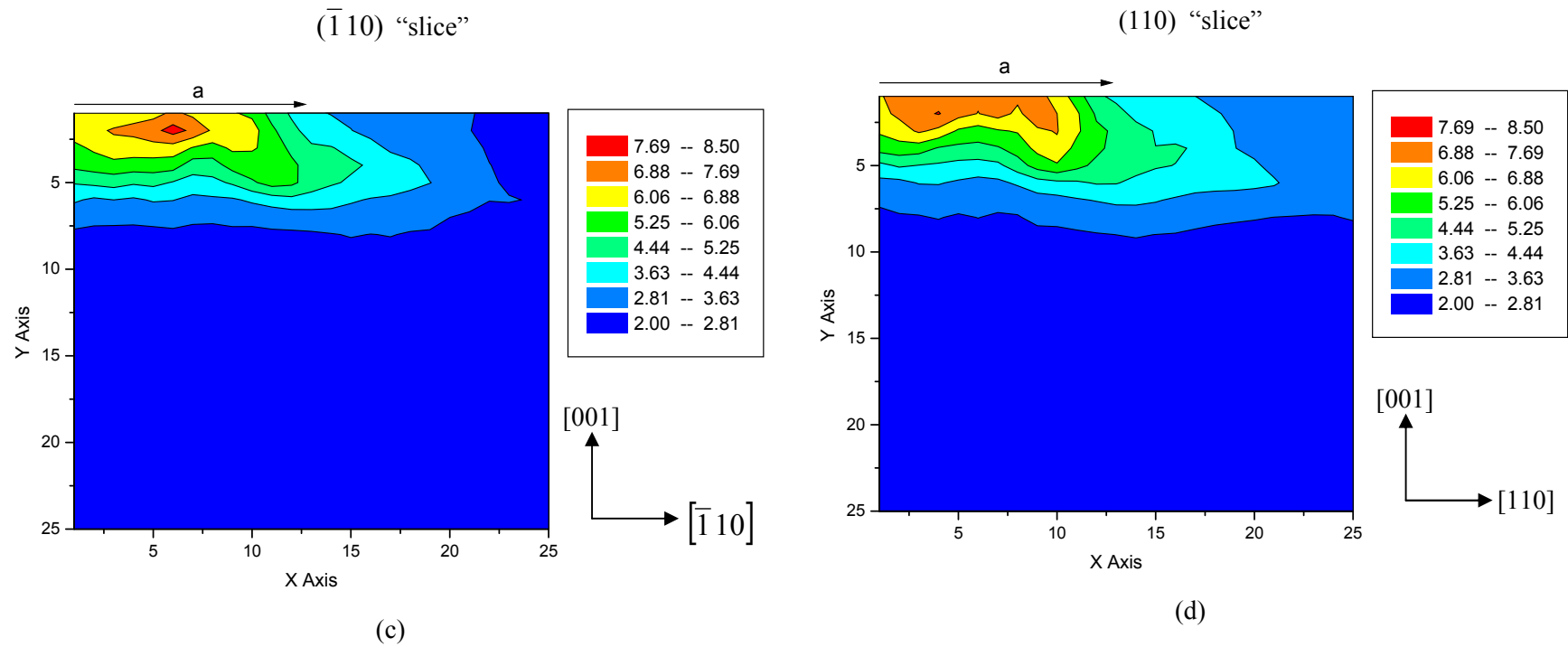


Figure 5.10 (continued): (c) Width contour map of slice mapped into the diamond along the $[\bar{1}10]$ direction. The centre of the impression is at top left and the radius of the impression is " $a = 110 \mu\text{m}$ ". The units of the values in the tables at top right are cm^{-1} . (d) Width contour map of slice mapped into the diamond along the $[110]$ direction. Units are the same as for figure (c). The dark blue colour corresponds to a "background" value for the FWHM of 2.00 to 2.81 cm^{-1} and the maximum peak width (red) corresponds to a peak width of 7.69 to 8.50 cm^{-1} .

5.1.2.3 Comparison of calculated resolved shear stresses and experiment

In this section the calculated resolved shear stresses due to a normally loaded circular contact are compared with the “slice” data presented thus far. Figures 5.11(c) and 5.12(c) and their descriptions are taken from Brookes *et al.* (1990) and Brookes (1992a).

Models for the anisotropy in the indentation hardness of crystals were based on the calculation of an effective shear stress beneath an indenter using the Schmid-Boas resolved shear stress equation, modified by various constraint terms. In these models a number of assumptions are made and they do not account for all observed data. The most suitable model at present is that suggested by Roberts (1988) who modelled the whole of the slip pattern over an area of $2a \times 2a$, where a is the contact area radius. This includes the areas directly beneath and adjacent to the contact point. Roberts used extended stress fields produced by a circular contact in an elastically isotropic material, making use of the approach by Love (1929) to predict the likely slip patterns and the stresses associated with them. This allowed complete 3D patterns of the relevant slip planes to be visualised together with the resolved shear stresses on them.

To model the magnitude of the resolved shear stresses which control plastic deformation in the bulk of a crystal, the crystallographic plane of the indented surface and the active slip systems must be identified. For this discussion, a (001) surface and $\{111\}\langle 110\rangle$ slip systems are considered, where $\{111\}\langle 110\rangle$ refers to applied stress that is resolved onto $\{111\}$ planes in $\langle 110\rangle$ directions. Figures 5.11(c) and 5.12(c) are maps showing the highest resolved shear stresses and the slip systems which are associated with those stresses on a (100) plane and a (110) plane, respectively, where both of these planes represent sections which pass through the centre of a circular contact area and are normal to the indented surface. The 12 possible slip systems in diamond cubic crystals are identified and numbered on the slip plane pyramids shown in which the apices “C” are assumed to be below the indented plane. A further convention used here is that a bar over the slip system number indicates that material under that slip plane is sheared downwards while a number without the bar corresponds to material above the slip plane being sheared downwards; in other words, negative and positive slip, respectively. The actual slip systems subjected to the highest resolved shear stress in various regions beneath the contact area are shown between the full lines.

For figure 5.11(c), i.e. on the (100) section or “slice”, the resolved shear stress (RSS) values immediately below the surface are relatively low. The maximum shear stress is about $0.316P_m$, where P_m is the stress applied by the impressor over a circular contact area of radius a and lies in a region where slip systems 9 and 12 are those most likely to be activated. This region

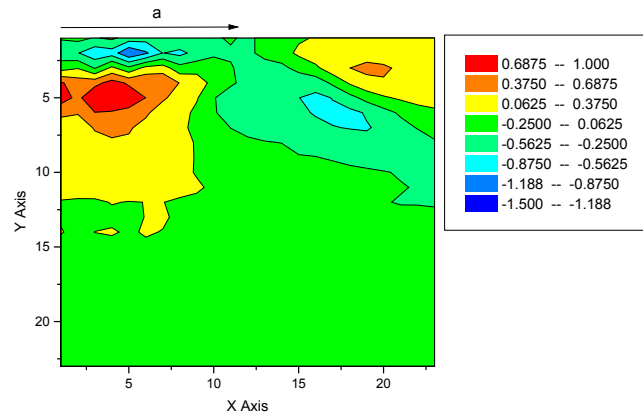
is $\sim 0.58a$ beneath the centre and $\sim 0.54a$ from the centre line of the impression. For figure 5.12(c), i.e. on the (110) section or “slice”, the maximum shear stress is $0.30P_m$ and this region is $\sim 0.52a$ beneath the centre of the impression and $\sim 0.5a$ from the centre line of the impression. Thus the zone of maximum resolved shear stress is roughly toroidal in shape (doughnut-shaped).

In figures 5.11 and 5.12, the volume of maximum tensile stress corresponds fairly closely with the volume of diamond that would experience the maximum resolved shear stress during the impression process (broken line contours of 30% of the mean applied pressure P_m). The volume of maximum tensile stress for the (100) slice also appears to be slightly larger than that for the (110) slice, which corresponds with the 30% contour being larger for the (100) slice. The maps in (a) of figures 5.11 and 5.12 thus shows a close correspondence with the resolved shear stress contours in (c) of the these figures.

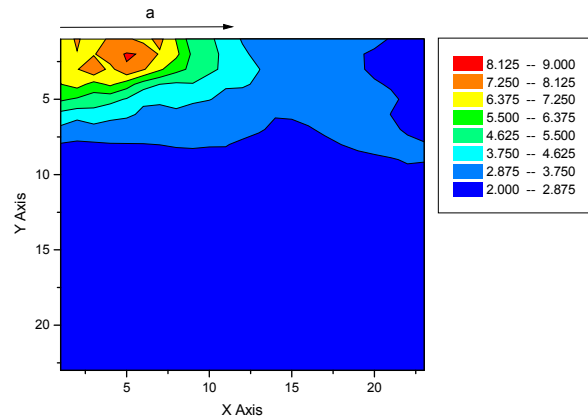
In order to further discuss the relationship(s) between the experimental and model contours in figures 5.11 and 5.12, it is necessary to include a description of the process by which the soft impressor technique creates strain and plastic deformation. Dislocation movement plays an important part. This description is published in Erasmus *et al.* (2011a) and also refers to concepts discussed in § 2.1.6.2.

The deformation process by which a conical soft impressor creates a circular impression in diamond can be split into three parts, the first being the initiation and multiplication of dislocations. The second part is the mechanism by which they fill the highly stressed volume beneath the impressor and the third part involves the mechanism by which further dislocation initiation and subsequent movement manifests itself as the visible rosette formation with accompanying pile-up. These three parts are discussed in the following paragraphs:

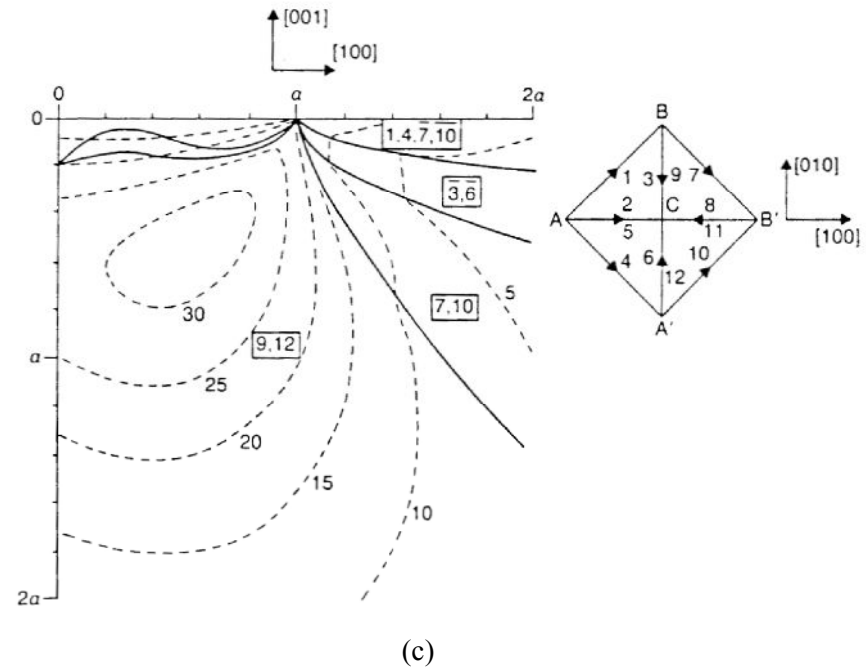
Part 1: When a diamond crystal is subjected to stress, the crystal will slip on the plane most favourably oriented to allow dislocations to move. Thus dislocations are created and begin to move at a fixed level of resolved shear stress, but restricted to certain planes and directions. For diamond the applied stress is resolved onto $\{111\}$ planes in the $\langle 110 \rangle$ directions. The critical resolved shear stress is the resolved stress required to create and move a dislocation onto the surface. During the impression process, one can imagine a dislocation is initiated at a discrete point under the contact area and expands under the applied stress until it reaches the surface. At the same time the dislocation propagates into the bulk until it reaches a point where the resolved shear stress acting on it is insufficient to sustain dislocation movement.



(a)

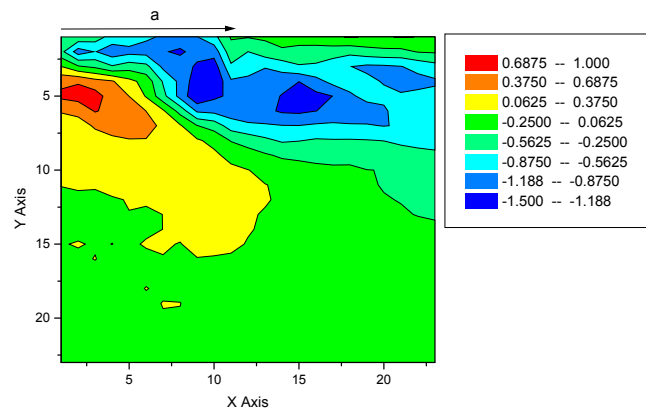


(b)

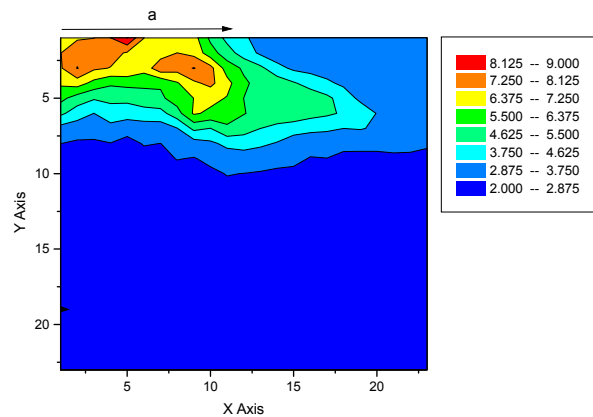


(c)

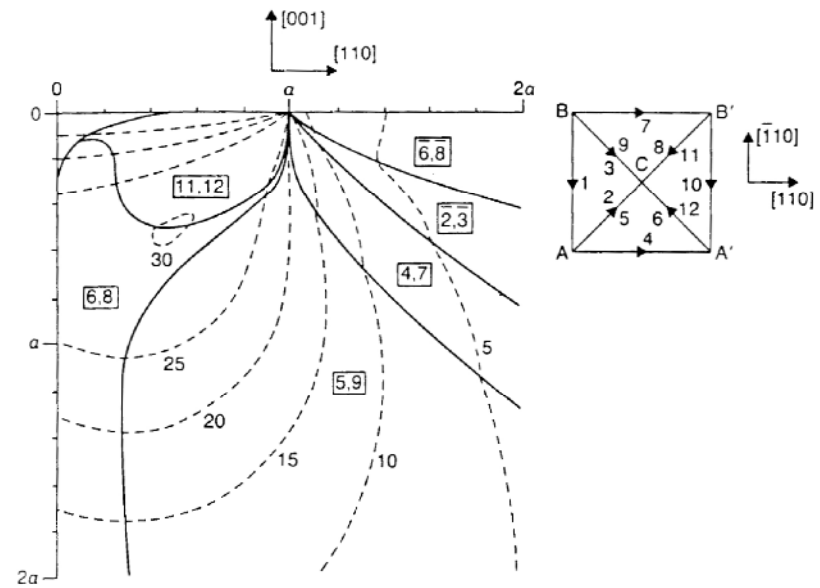
Figure 5.11: Comparison of calculated resolved shear stresses and experimental stress and deformation contours for a section normal to the surface and along $[100]$. (a) Measured stress contour map, units in GPa; (b) Measured linewidth contour map, units in cm^{-1} ; (c) Modelled contours (broken lines) of resolved shear stress on the most stressed slip systems for contact on the (001) surface; values are percentages of the stress P_m applied over a circular contact area of radius a . Solid lines divide regions where different slip systems are the most highly stressed. The slip system labelling is shown in the inserts, where the apices “C” of the pyramids of $\{111\}$ slip planes (viewed from above the contact surface) are below the plane of the paper. The convention for the senses of slip indicated by bars over the numbers is given in the text.



(a)



(b)



(c)

Figure 5.12: Comparison of calculated resolved shear stresses and experimental stress and deformation contours for a section normal to the surface and along $[110]$. (a) Measured stress contour map, units in GPa; (b) Measured linewidth contour map, units in cm^{-1} ; (c) Modelled contours (broken lines) of resolved shear stress on the most stressed slip systems for contact on the (001) surface; values are percentages of the stress P_m applied over a circular contact area of radius a . Solid lines divide regions where different slip systems are the most highly stressed. The slip system labelling is shown in the inserts, where the apices “C” of the pyramids of $\{111\}$ slip planes (viewed from above the contact surface) are below the plane of the paper. The convention for the senses of slip indicated by bars over the numbers is given in the text.

Part 2: Increasing the pressure by a small amount will increase the volume around the initial point of highest shear stress in which the resolved shear stress (RSS) is sufficient to initiate dislocations. This leads to further dislocation production with each able to expand on their respective slip planes under the applied shear stress. Figure 5.13 shows the Roberts model for a (110) cross section, where the dark shading indicates the area in which the RSS is high enough to initiate dislocations. The lighter shading indicates the limit of the area in which the RSS is sufficient to cause dislocation loop expansion.

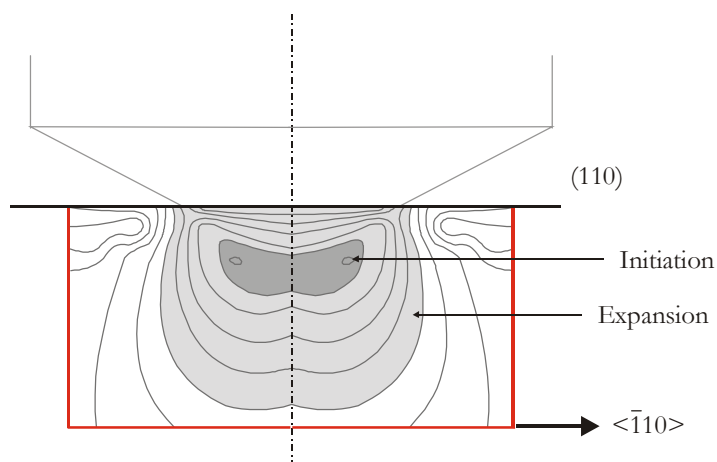


Figure 5.13: Roberts model of a (110) plane or “slice” showing the area of dislocation initiation (dark shading) and the subsequent limit of dislocation loop expansion (light shading).

A dislocated volume is thus created, the level of strain is increased and work hardening is possible. If a cross section were taken of an impression where a significant volume had been allowed to dislocate, then the resultant dislocation structure might look similar to that shown in figure 5.14. As the slip system of diamond creates two points of maximum RSS, the dislocation structure is that of two overlapping structures, each one being roughly identical in shape.

The picture in reality is more complicated, as the initiated dislocations are not confined to those slip systems that intersect the surface or those that are perpendicular to the (110) plane – slip on all of the $\{111\}\langle 110 \rangle$ slip systems is possible. Nevertheless the principle remains the same.

Part 3: In general, rosette patterns are formed at certain higher pressures and temperatures. The critical resolved shear stress at temperatures above 1300 °C (i.e. when it is relatively independent of temperature) is between 0.32 and 1.3 GPa (Brookes 1992b). The impression in question (impression 1 in figure 5.1) was made at 1400 °C and the mean contact

pressure was 3.07 GPa. This implies the critical resolved shear stress for impression 1 was comfortably achieved during its formation (30% of 3.07 GPa = 0.92 GPa). Brookes (1992b) also showed that the resultant resolved shear stresses in the range quoted above were sufficient to initiate dislocations from inside the contact area, but not outside. The dislocations thus form and start to move beneath the contact area. The geometry of the slip plane with respect to the surface means that dislocations emerge outside the contact area. A cross section of an impression at the point where rosette formation just begins is shown in figure 5.15.

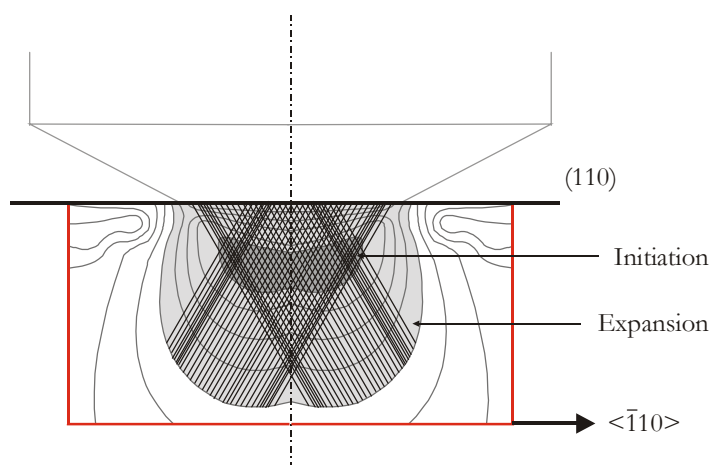


Figure 5.14: Roberts model of a (110) plane or “slice” showing the likely resultant dislocation structure of an impression before the onset of reversed plasticity.

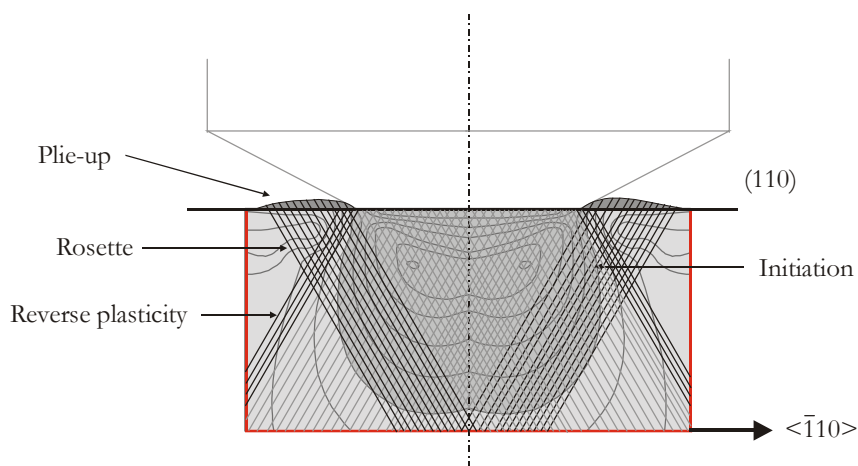


Figure 5.15: Roberts model for a (110) plane or “slice” showing the likely resultant dislocation structure of an impression just after the onset of rosette formation.

It has to be kept in mind that once the first dislocation is produced, the ideal shear stress distribution, as shown by the Roberts model, is altered. As more dislocations are produced, the

volume in which dislocation initiation is possible is increased, as the stress field of each dislocation will distort the elastic stress field. Significant dislocation activity leading to rosette pattern formation further complicates the picture. When all these factors are taken into account, it can be seen that the dislocation structure beneath an impression becomes increasingly chaotic. Ideally the stress field model should be elastic-plastic, including the stresses from effects generated at the surface plus stresses from other defects present within the plastic zone. The basic elastic stress field calculations remain valid, however, when considering the whole of the deformed region as the extent of the deformed volume is similar to that predicted.

From the description given above (narrative surrounding figures 5.13 to 5.15) the process resulting in the measured contours can be visualised. The first dislocation nucleation takes place in the volume of maximum resolved shear stress (30% broken line contour in figures 5.11 and 5.12). As the impression process continues, dislocations multiply and move to fill the volume under indenter contact area. Material is thus “moving away” from the volume where the dislocations movement originates. At the end of the deformation process, this volume is thus “deficient” in material with the result that it is in tension. Although it would be expected that some relaxation of shear stress were to take place due to plastic deformation, the results show that most of the shear stress is “locked in” on cooling. A 0.316 fraction of 3.07 GPa = 0.97 GPa, very close to the measured maximum stress of 0.99 GPa for the (100) “slice” in the vicinity of the 30% contour. A 0.3 fraction of 3.07 GPa = 0.92 GPa, comparable with the measured maximum for the (110) “slice” in an equivalent position of 0.83 GPa. The calculated resolved shear stress contours for the (100) “slice” encompass a larger volume than those for the (110) “slice” and this is reflected to a certain degree in the measured contours as well.

As noted previously, the extent of deformation for both the “slice” directions as measured by the Raman linewidth appears to be shallower than the range of the stress contours. This would be accounted for by the critical resolved shear stress (CRSS) initially being exceeded closer to the surface, whereas deeper into the crystal no dislocation movement took place, but there is a residual stress gradient between the deformed and undeformed volumes. These residual stress gradients are to a certain extent “locked in” by the irreversible nature of the plastic deformation.

It is also observed that the volume of maximum plastic deformation corresponds closely with the volume of maximum tensile stress. The deformation represents that volume of diamond where dislocation movement had produced plastic deformation. Dislocation initiation and movement starts from that volume of diamond where the CRSS is attained first. It is thus to be expected that the largest degree of deformation would correspond with the volume where the

movement initiated. This volume is also “most deficient” of diamond (as per the argument above), resulting in it also being the volume of maximum tensile stress.

It is noted that the very good correspondence of the measured contours and the Roberts model is further reason to use the latter in spite of the breakdown of the original elastic stress field assumptions of the model in reality.

The “extra” material being displaced from under the impression propagates along the slip planes to form pile-up, and due to the slip system of diamond, this extra material ends up in the arms of the rosette and with the arms being in compression. The compressive stress contours associated with the arms of the rosette pattern are not reflected in the calculated resolved shear stress contours of the Roberts model. This is due to the contours being related to the applied pressure from the impressor being projected onto the slip system of diamond, whereas the arms of the rosette pattern are wholly the result of the plastic deformation taking place at high temperature. In this aspect the Roberts model is thus not adequate to predict what is observed in experiment.

5.1.3 2D PL maps

All photoluminescence measurements reported here were carried out at 77 K in the Microstat^{He} microscope cryostat described in §4.5. These 2D PL maps correspond with the Raman maps in §5.1.1. The 514.5 nm line of an argon ion laser was used as the excitation source, and the same 10×10 mapping grid was employed. A 600 grooves/mm grating was used to give a larger spectral range. For each grid point, a Voigt lineshape (§ 3.2.2) was fitted to the zero phonon line of the defect under investigation and the intensity of the peak, the width of the peak and the Gaussian and Lorentzian components of the peak extracted from the fit. The actual (Voigt) width of the peak was calculated from equation 3.39. Care was taken to measure the Raman signal for every point where a PL signal was acquired to enable the normalisation of the ZPL intensity (as per §4.4.1). The data for the 1.945 eV defect and the 575 nm defect are given below. No H3 defect was visible for this diamond and impression when measured with the appropriate laser line (488 nm of an argon ion laser).

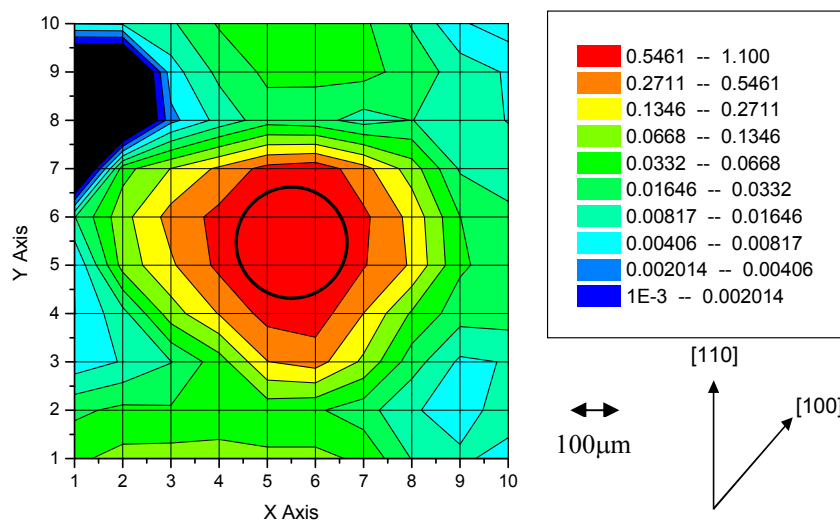


Figure 5.16(a): Normalised intensity map of the ZPL of the 1.945 eV defect. Note that the scale is logarithmic. The black circle represents the contact area of the impressor. The black area represents a surface area where no ZPL was measured. Blue to green colours indicate a very low intensity level, while yellow to red indicate a sharp increase in the intensity.

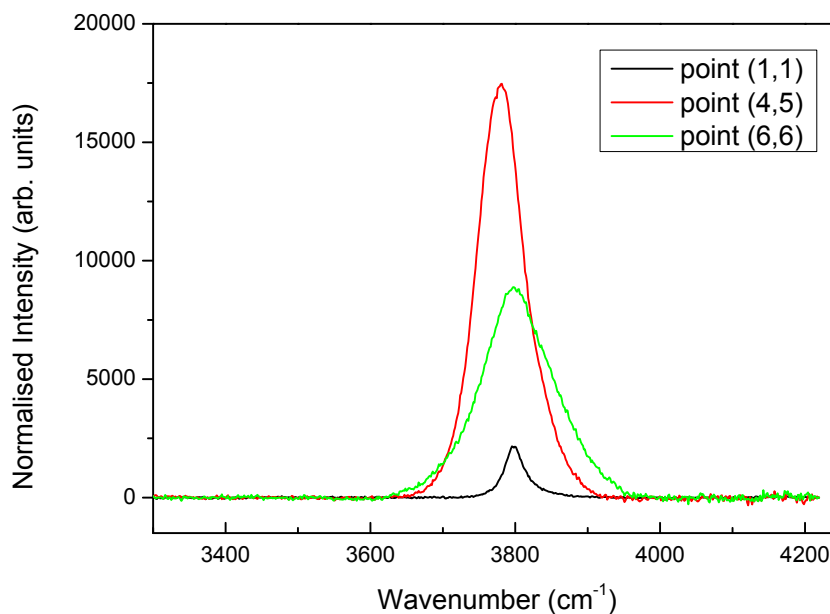


Figure 5.16(b): Example spectra of the ZPL of the 1.945 eV defect after background subtraction. The (x,y) coordinates in the legend refer to the coordinates of the mapping grid in figures 5.16 to 5.19. The changes in normalised intensity, peak width and peak position are clearly illustrated.

The normalised intensity of the 1.945 eV defect is given in figure 5.16. Note that the intensity is plotted on a logarithmic scale to emphasise the very strong growth of the intensity of

the defect over the background level. The black area represents a surface area where no ZPL was measured. This figure illustrates the very clear association of the negative charge state of the [N-V] defect with the impression in the diamond. The impression under discussion was made at 1400 °C, which is substantially above the temperature (~600 °C) where the vacancy in diamond becomes mobile. Non-conservative slip of dislocations during the impression process generates vacancies, which are then free to diffuse and bind with substitutional nitrogen, which is the dominant form of nitrogen in synthetic type Ib diamond. This gives rise to the [N-V]⁻ defect observed here. The intensity gradient highlights the fact that most of the vacancy generation takes place in the immediate vicinity of the impression. Comparison of figures 5.5 and 5.16 show very similar extent of the surface contours for the degree of deformation as mapped via Raman linewidth and the extent of vacancy formation as mapped via the intensity of the 1.945 eV defect. Although these two maps result from different physical mechanisms (Raman line broadening and PL-active defect concentration), they contribute to a consistent picture of the processes that take place during the formation of an impression. The good correlation of the contours implies that most of the plastic deformation is confined to the immediate vicinity of the impression and that vacancies formed during the impression process are quickly trapped after their formation.

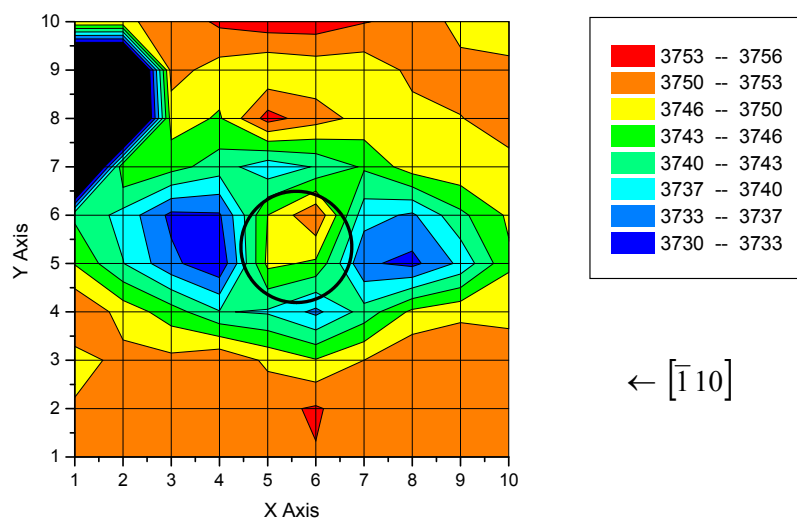


Figure 5.17: Map of the position of the ZPL of the 1.945 eV defect. The units of the scale are relative wavenumbers (relative to the excitation laser at 19435 cm⁻¹ or 514.5 nm). The black circle represents the contact area of the impressor. The dark blue colour represents the smallest values of the peak position, while red represents the largest values of the peak position.

Figure 5.17 maps the position of the ZPL of the 1.945 eV defect across the impression. There are clearly two lobes (left and right of the impression in the figure) as well as a much

weaker two-lobe pattern at right angles to the strong pair. This lobe pattern is a visualisation in PL of the residual stresses associated with the impression in the diamond. In the figure above, the electric field of the incoming laser light is linearly polarised and parallel to the “x-axis”. It is also important to note the direction of the $[\bar{1}10]$ axis as indicated. In figure 5.17 the electric field of the incoming laser light and the stress axis associated with the two left-right lobes are thus parallel. It is this polarisation of the incoming light that gives rise to the asymmetry of the pattern. Davies *et al.* (1976c) investigated the effect of strain on the optical properties of the 1.945 eV defect. Shifting and splitting of the ZPL was reported for various uniaxial stress configurations. The ZPL shift and splitting as a function of applied pressure is reported chiefly for absorption rather than luminescence of the defect. Comparison with the calculations for splitting under uniaxial stress in the case of PL by Mohammed *et al.* (1982) shows that although the intensity ratios of the components differ between absorption and luminescence, the rate of shift of the ZPL components for the case of $[\bar{1}10]$ stress and electric field parallel to this stress (as in figure 5.17) is the same for absorption and luminescence. It is thus possible to use the data of Davies and Hamer (1976c) to calculate the stress in the two left-right lobes in figure 5.17. Although the uniaxial stress data in the paper under discussion shows a split in the ZPL for the stated relative orientation of stress axis and exciting light, there is no clear evidence for peak splitting in the measured PL spectra. The majority of peaks are symmetrical without any sidebands. In the few cases where a shoulder may be present, it is weak and difficult to deconvolute from the major peak. It is suggested that there are two reasons for this observation. For the stress axis – exciting light geometry applicable here, the ZPL splits into a major and minor component, with the major component expected to be ~ 3 times more intense. The confocal parameters are also such that an approximate 50 μm thickness of diamond is being sampled. This averaging effect coupled with the difference in intensity ratios between the components of the peak leads to only a single component of the ZPL in fact being observed. For the two left-right lobes mentioned earlier in this paragraph, the ZPL peak position is shifted downwards by $\sim 20\text{cm}^{-1}$, which converts to an energy difference of $\sim 2\text{ meV}$. According to Davies *et al.* (1976c) this shift is due to a stress of just greater than 0.2 GPa. This value is in very good agreement with that measured via Raman spectroscopy in §5.1.1.

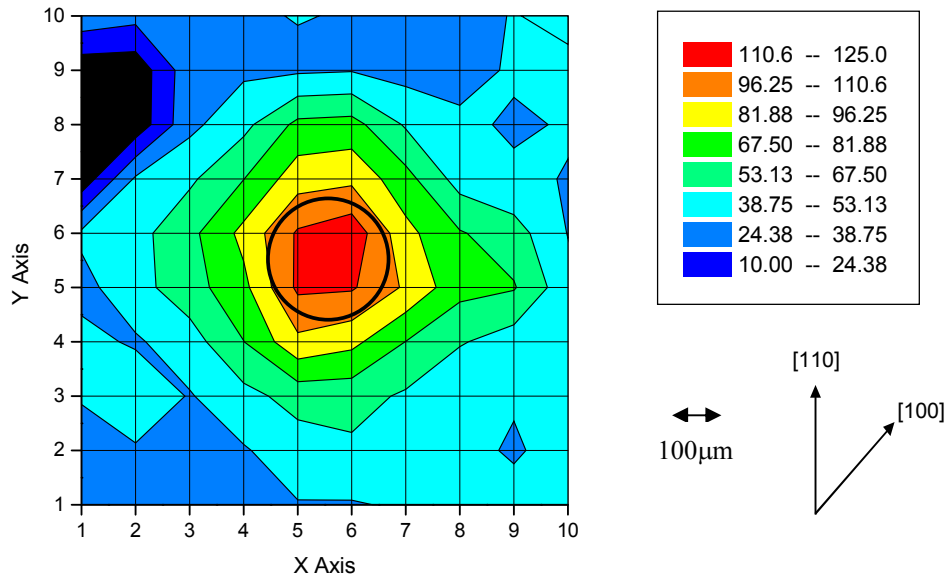


Figure 5.18: Voigt linewidth of the 1.945 eV ZPL. Units in the table at the top right are wavenumbers. The black circle represents the contact area of the impressor. The darker blue colours are associated with the background FWHM values, while the range of light blue, through green, yellow, orange to red represents the increasing values of the Voigt linewidth.

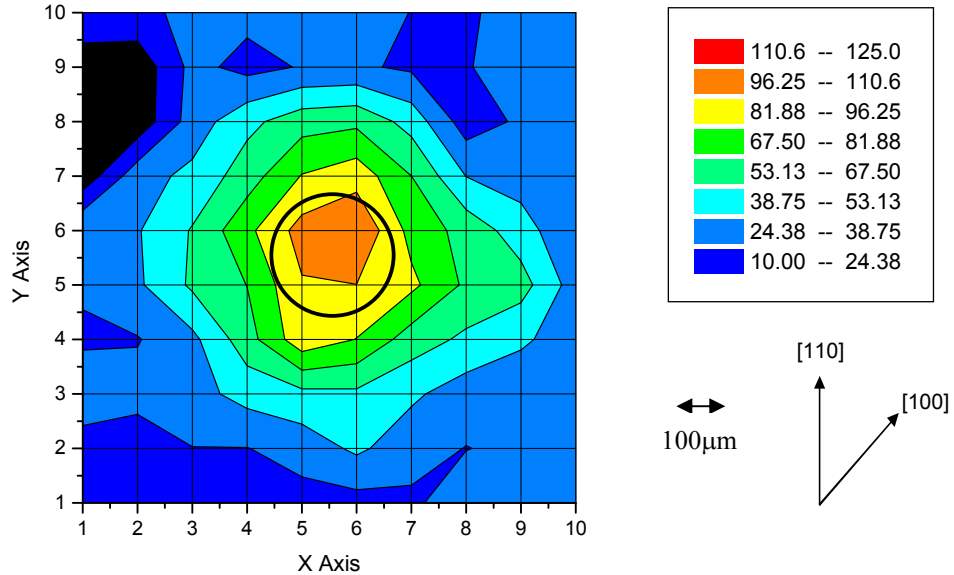


Figure 5.19: Gaussian component of the width of the 1.945 eV ZPL. Units in the table at the top right are wavenumbers. The black circle represents the contact area of the impressor. The darker blue colours are associated with the background FWHM values, while the range of light blue, through green, yellow to orange represents the increasing values of the Gaussian component of the linewidth.

As per the theory pertaining to zero phonon lines in §3.2.1, a larger linewidth is associated with a larger degree of deformation due to inhomogeneous line broadening. The deformation of the diamond due to the impression is clearly mapped via the linewidth of the ZPL in figure 5.18 and is clearly centred on the contact area of the impressor. It corresponds well with the deformation mapped via the Raman linewidth in figure 5.5. Comparison of the change in the values of the width (units in wavenumbers) in figures 5.5 and 5.18 shows that the ZPL width is a more sensitive indicator for local deformation. The Raman linewidth in figure 5.5 changes by approximately a third between the bulk (undeformed) value and the centre of the impression, while the ZPL Voigt width more than doubles when comparing the width of ZPLs from defects present in undeformed diamond with those in the centre of the impression.

In figure 5.19, the Gaussian component of the linewidth is mapped and it is clear that the major contribution to the width is due to this component. As per the theory outlined in §3.2.1, figure 5.19 implies that the majority of defects giving rise to the 1.945 eV luminescence are at or near line-type defects. This is not unexpected, as the dislocation movement during the deformation process is expected to give rise to line-type defects. It must be mentioned here that although the assumption of Stoneham's theory that the defects causing the inhomogeneous strain broadening are not correlated with each other probably does not hold due to the large concentration of defects associated with the impression, the theory appears to be sufficiently robust to explain the observed distribution of the Gaussian component of the linewidth in figure 5.19.

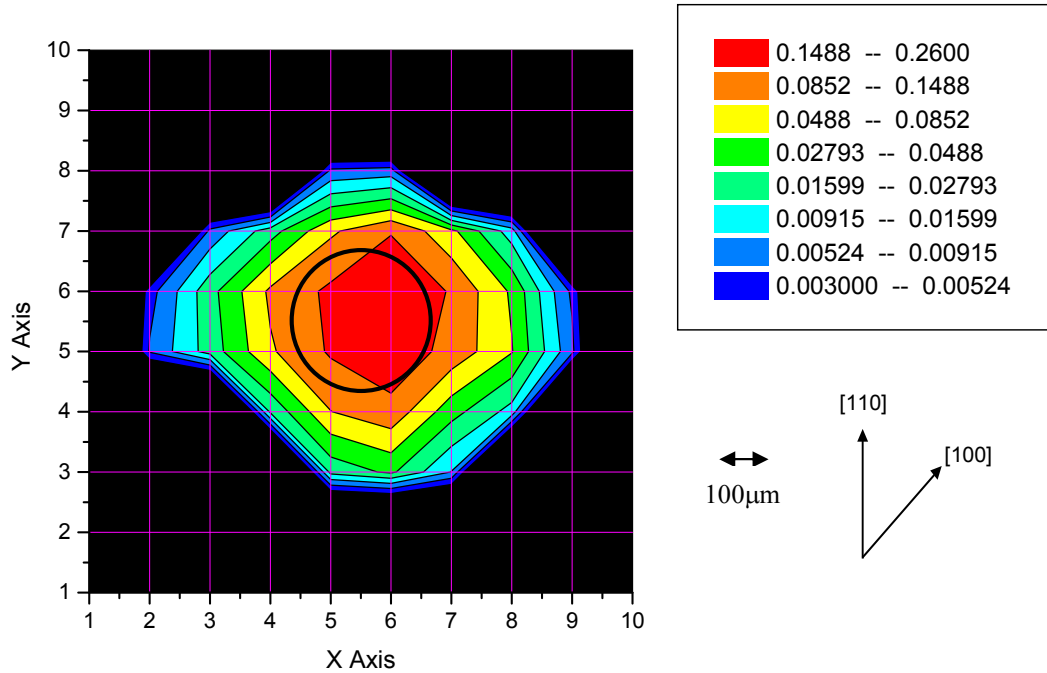


Figure 5.20: Normalised intensity distribution in arbitrary units of the ZPL of the 575 nm defect. Note that the intensity scale is logarithmic. The black circle represents the contact area of the impressor. The black background represents a zero value for the intensity of the ZPL. Blue to green colours indicate a very low intensity level, while yellow to red indicate a sharp increase in the intensity.

The data for the ZPL of the 575 nm defect (neutral charge state of [N-V]) is given in figures 5.20 to 5.23. In figure 5.20 the black background represents a zero value for the intensity of the ZPL. The scale of the intensity is plotted on a logarithmic scale to emphasise the steep increase in the intensity in the immediate vicinity of the impression. The vacancy-related mechanism for the formation of the 1.945 eV defect naturally also leads to the formation of the 575 nm defect. It has been observed that the 575 nm defect is more readily observable with CL than PL, possibly explaining the absence of a background 575 nm ZPL signal where the 1.945 eV defect is present (compare with figure 5.16).

In figure 5.21 the position of the ZPL of the 575 nm defect is mapped across the impression. The measurement conditions and geometry is the same as that for the 1.945 eV ZPL discussed earlier. In contrast with the lobed position distribution mapped for the 1.945 eV ZPL, the 575 nm ZPL shows a maximum shift of about -40 cm^{-1} ($\sim 5 \text{ meV}$) associated with the centre of the impression, surrounded by a relatively undefined horizontal band (green in figure 5.21).

Piezo-spectroscopic measurements, investigating the response in absorption and PL of the 575 nm ZPL to uni-axial stress, have been reported by Davies (1979) and (using CL) by Zaitsev (2001). A clear splitting of the ZPL is observed for stress along $\langle 110 \rangle$ by both authors.

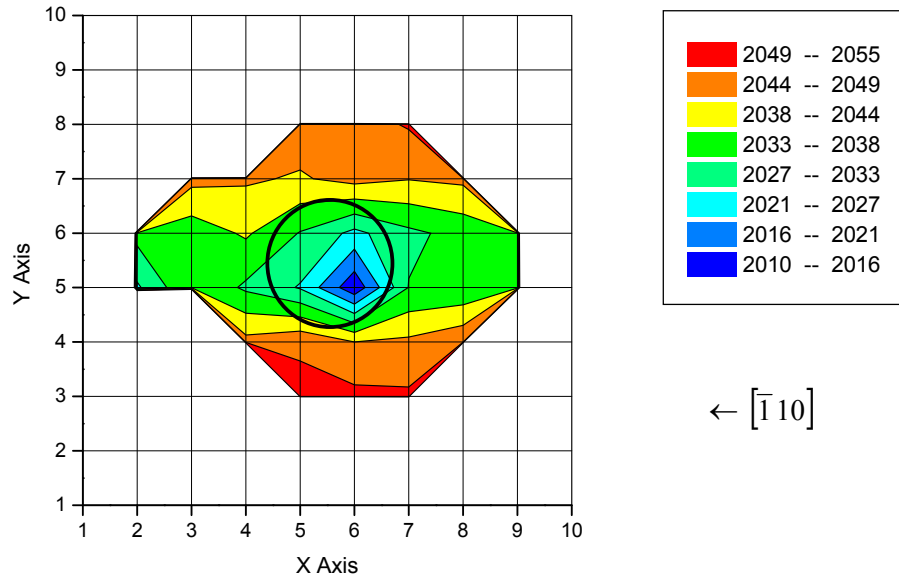


Figure 5.21: Map of the position of the ZPL of the 575 nm defect. The units of the scale are relative wavenumbers (relative to the excitation laser at 19435 cm^{-1} or 514.5 nm). The black circle represents the contact area of the impressor.

Similar to the results of the 1.945 eV ZPL, no splitting is observed in our results. However, in contrast with the 1.945 eV results, there is poor agreement regarding the magnitude of the shift. According to Davies (1979), a shift of -40 cm^{-1} for the geometry concerned corresponds to an applied stress of $\sim 1.8 \text{ GPa}$, which is much more than the 0.2 GPa derived from Raman spectroscopy and the 1.945 eV ZPL data. Zaitsev (2001) gives more detailed data for the splitting of the 575 nm ZPL at stresses below 1 GPa (although measured in CL rather than PL), and this indicates that a stress of 0.2 GPa would correspond to a ZPL shift of less than 1 meV , which corresponds to a shift of less than 8 cm^{-1} . Although the differences between the contours of the ZPL position maps for the 575 nm and 1.945 eV defects and the discrepancies between the calculated stress values are difficult to explain, the large degree of broadening of the 575 nm ZPL (maximum width close to 175 cm^{-1}) may be contributing to swamping the much smaller shifts (8 cm^{-1}) that should be present.

In figures 5.22 and 5.23 the Voigt linewidth and the Gaussian component of the linewidth of the ZPL of the 575 nm defect are mapped in the same manner as for the 1.945 eV defect. The

black background is again associated with the absence of the defect. The Voigt linewidth is clearly broadest in the contact area of the impressor, decreasing approximately radially. This images a maximum degree of plastic deformation associated with the impressor, the degree of deformation decreasing away from the impression. The map for the Gaussian linewidth is very similar to that for the Voigt linewidth, indicating that the Gaussian component dominates the width, and thus indicating that line-type defects dominate the deformation volume associated with the impression. This corresponds with the information obtained from the 1.945 eV defect and conforms to expectations.

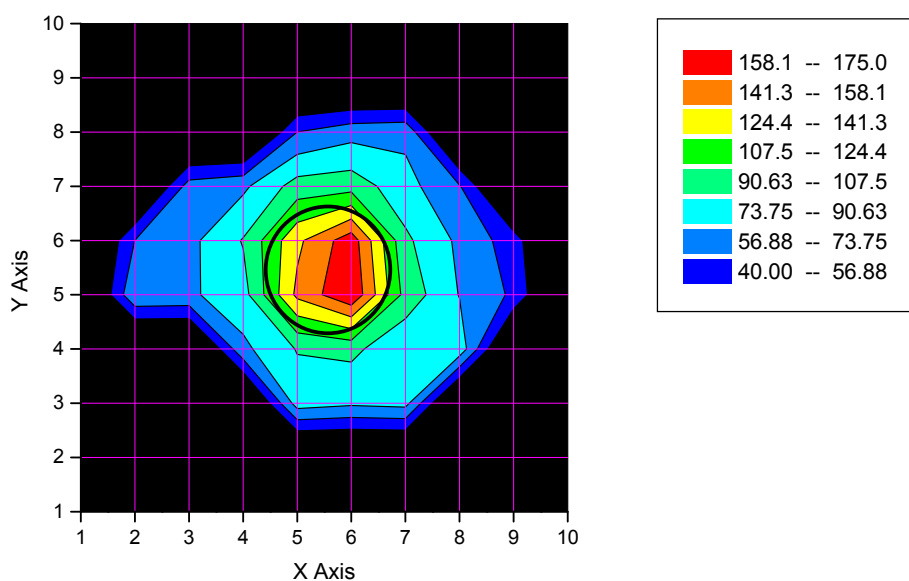


Figure 5.22: Voigt linewidth of the 575 nm ZPL. Units in the table at the top right are wavenumbers. The black circle represents the contact area of the impressor. The darker blue colours are associated with the background FWHM values, while the range of light blue, through green, yellow, orange to red represents the increasing values of the Voigt linewidth.

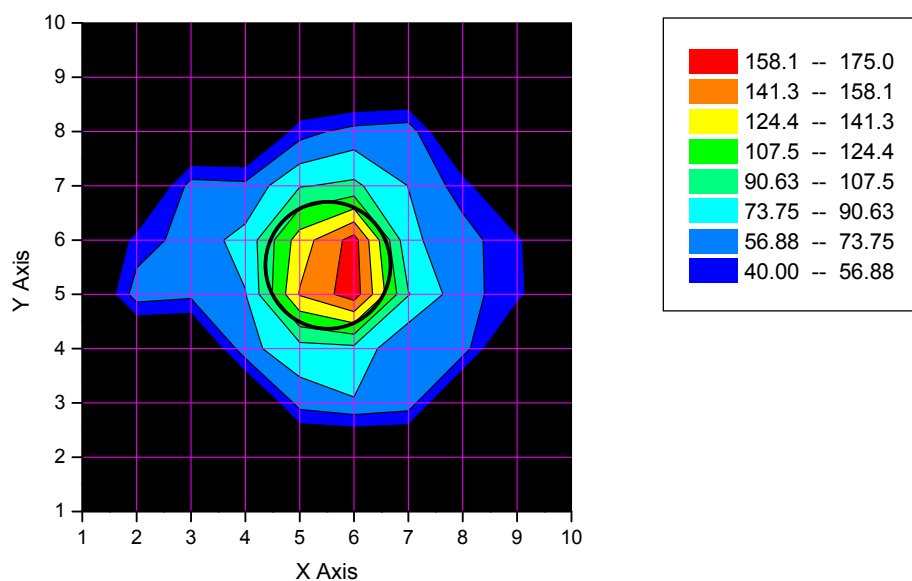


Figure 5.23: Gaussian component of the width of the 575 nm ZPL. Units in the table at the top right are wavenumbers. The black circle represents the contact area of the impressor. The darker blue colours are associated with the background FWHM values, while the range of light blue, through green, yellow, orange to red represents the increasing values of the Gaussian component of the linewidth.

5.2 Summary of results for single crystal diamond

Micro-Raman and PL spectroscopy were used to map the three-dimensional (3D) stress distribution surrounding a plastic impression made in a synthetic, type Ib single crystal diamond. The impression was created on a (100) face of the crystal with a Si_3N_4 impressor at 1400 °C using the so-called Soft Impressor Technique. The diamond Raman peak was mapped at room temperature at the surface and at fixed intervals of 10 μm below the surface using a motorised X-Y stage. The depth (Z)-resolution was limited to 10 μm by means of a confocal pinhole. Using data from the Raman peak position, a 3D map of the stress contours surrounding the impression was generated, while the Raman width data yielded a map of the plastic deformation volume. The surface stress map shows a cross-shaped rosette pattern that corresponds very closely with micrographs imaging the pile-up on the surface due to dislocation movement. The "arms" of the pattern are in compression (~ 1.5 GPa), while the centre of the impression is in tension (~ 1 GPa). The deformation map shows a radially symmetric area of deformation centred on the impression, with the maximum degree of deformation at the centre. These experimental stress contour maps were compared with contours modelled from elastic stress theory. A good correspondence was

found between the results and the predictions from the model, although some disagreements exist which can be attributed to the breakdown of the assumptions associated with the elastic stress fields. PL intensity maps of the zero phonon line (ZPL) associated with the $[\text{N-V}]^-$ defect centre at 1.945 eV provide images of the extent of vacancy formation and movement during the impression process. This data was qualitatively and quantitatively (for stress values) in good agreement with those from the Raman measurements.

Chapter 6: Results – investigation of PCD

In this chapter, Raman spectroscopy was used to characterise the stresses in the PCD layer of several industrial drillbits. The effect of surface finish and temperature on the residual surface stress state is reported and discussed. These results were published in Erasmus *et al.* (2011b).

6.1 Investigation of surface stress state of PCD

In this section, measurements of stress on polycrystalline diamond (PCD) drillbits at room temperature and higher temperatures using Raman spectroscopy are reported. The work was done in various stages, incorporating two student projects under my co-supervision and guidance in which the initial trial measurements were carried out personally (§ 6.1.3.1 and § 6.1.3.2), followed by more extensive annealing experiments which are wholly my own work (§ 6.1.3.3). The results of the initial projects are included in this chapter to give a holistic representation of the results and knowledge on PCD drillbits.

6.1.1 Sample description

Polycrystalline diamond is formed by sintering diamond powder in the presence of a suitable solvent/catalyst (usually cobalt), and has the advantages of effectively isotropic properties and a greater toughness than single crystal diamond while still maintaining a reasonably high thermal conductivity. The diamond used was HPHT-synthesised synthetic grit (type Ib) with nitrogen as substitutional impurity present in excess of 500 ppm. Synthesis conditions for PCD generally involve applied pressures of 5 to 10 GPa, sintering temperatures of 1300 °C to 1800 °C and sintering times of 5 to 60 minutes. The average grain size was 10 µm. During the synthesis process, liquid phase sintering facilitated by molten Co takes place, resulting in an extended diamond structure with considerable direct diamond to diamond bonding and cobalt at the grain boundaries (see e.g. Evans *et al.* 1984 and Uehara *et al.* 1988).

The drillbits (Element Six (Pty) Ltd.) used in these measurements were stubby cylinders of cobalt-cemented tungsten carbide (Co:WC), with a PCD layer sintered onto one flat face. Typical dimensions of such a cylinder are a diameter of 19 mm, height of 17 mm, and a PCD

layer of thickness 0.6 to 1 mm, depending on the processing conditions, as illustrated in figure 6.1.

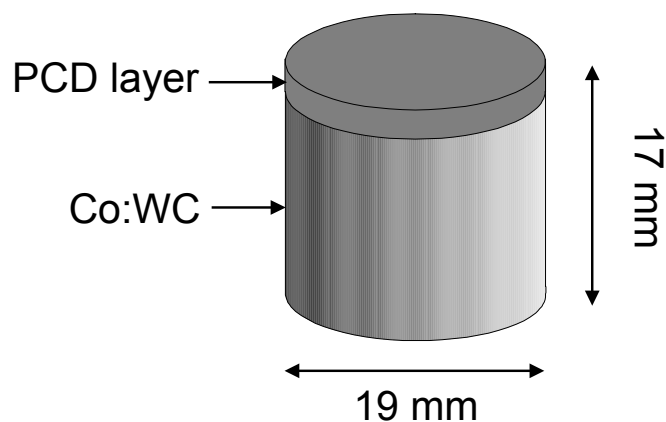


Figure 6.1: Schematic diagram of a PCD drillbit.



Figure 6.2: Diagram illustrating different mountings of PCD drillbits in diamond drill heads (Hughes-Christensen, part of Baker-Hughes Incorporated).

These cylindrical drillbits are usually mounted in arrays within the head of a diamond drill used for drilling into soil and/or rock (examples are given in figure 6.2). In the further text, “drillbits” or “PCD drillbits” refer to the individual drilling elements (figure 6.1) that make up the diamond drillheads illustrated in figure 6.2. The application environment of these drillbits is thus particularly harsh, requiring high strength and high toughness. The strength property is provided by the inter-grown diamond matrix and the toughness is enhanced by the presence of a net surface compressive stress. Such a stress state opposes the formation and propagation of median cracks under impact loads, as well as the propagation of micro-cracks already present in the PCD. A

tensile stress state is conducive to crack formation and propagation. It is thus clear that a net surface compressive stress is desirable.

6.1.2 Methodology

As in the case of single crystal diamond, Raman spectroscopy is particularly suited to measuring the stress state and magnitude in PCD layers, providing a relatively quick, non-destructive and quantitative method of analysis. A typical Raman spectrum for PCD can be seen in chapter 2, figure 2.7. As with single crystal diamond, the peak position conveys information regarding the stress in the diamond volume sampled by the laser, and the peak width contains information regarding the degree of deformation of the diamond. In all cases below, room temperature measurements were done using the confocal micro-Raman configuration (§ 4.1.2), and high-temperature measurements were done in a custom-built furnace (§ 4.6) mounted in the macro-chamber. In all cases a backscattering geometry was used. The laser beam was focused to a $\sim 1.5 \mu\text{m}$ diameter spot in the microscope and a motorised X-Y microscope stage (§ 4.1.2) was used to obtain high spatial resolution measurements. The spot size in the macro-chamber was $\sim 300 \mu\text{m}$ diameter. The PCD layer was quite opaque, thus limiting the penetration depth of the laser to several tens of microns. The 514.5 nm line of an argon ion laser was used as excitation source, with the JY Raman spectrometer operated in the single spectrograph mode with an 1800 grooves/mm grating (§ 4.1.3) and a CCD detector (§ 4.1.4). The position of the diamond Raman peak was carefully calibrated using the 546.074 nm emission line of a mercury lamp. The position of the diamond Raman peak as measured on a natural type IIa diamond was used as the "stress-free" standard (1332.55 cm^{-1}). A Voigt function was fitted to the spectra after background subtraction to extract the peak parameters, and a value of $\alpha = 1.92 \text{ cm}^{-1}/\text{GPa}$ was used to calculate the stress values. This value of α corresponds with the assumption of a bi-axial stress model (§3.1.5.3, Ager III (1993) and Bergman *et al.* (1995)). The furnace is described in more detail in §4.6. For the high temperature measurements, the furnace was evacuated to high vacuum prior to heating, and backfilled with low pressure argon gas to promote a uniform temperature of the sample and good thermal equilibrium between the sample and the thermocouple.

6.1.3 Results

6.1.3.1 Surface stress state as a function of surface finish

These results formed the major component of the work done by Zöe Martin as part of her MA degree in the Department of Materials at the University of Oxford. The main results of this work have been reported in her thesis (Martin 1999) and in Comins *et al.* (2001).

Three sets of drillbit samples from the same manufacturing batch, i.e. with nominally the same PCD structure and properties, but with different surface finishes for each set, were studied. The three surface finishes were classified as roughly lapped, finely lapped and polished. During rough lapping grit sizes of 20 to 40 μm are typically employed and for fine lapping the sizes range from 6 to 15 μm . These are usually suspended in an organic alcohol such as iso-propanol. The final polishing step (3rd batch of samples) took place on a scaife, where the polishing to a mirror finish was done dry on a resin-bonded diamond wheel with air-cooling.

For each sample two linear traverses, separated by 1 mm, were measured along the circular diameter of the PCD layer for a sample from each batch. The points within each traverse were separated by 500 μm . The results of the measurements are given in figure 6.3.

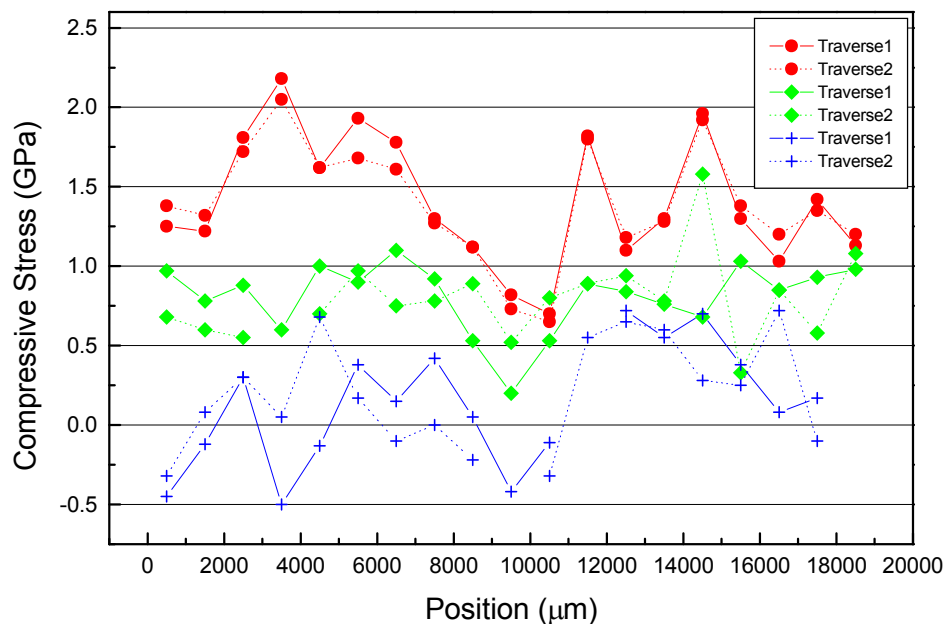


Figure 6.3: Compressive surface stress as a function of surface finish across the diameter of three different samples. Circles (●) correspond to a roughly lapped sample, diamonds (◆) to a finely lapped sample and the crosses (+) correspond to a polished surface.

The traverses are shown for one sample for each of the different surface finishes. Although large variations in stress occur from point to point, there is a definite trend showing a lowering of the average compressive stress with successive surface processing stages. The surface compressive stress averaged over the two traverses for the roughly lapped samples is 1.4 GPa, for the finely lapped samples it is 0.8 GPa and for the polished samples it is 0.1 GPa. Certain samples, especially those with a polished surface, were found to have very weak diamond peaks at certain points. In these cases, or where the peak was not detectable, data points are missing on the graph.

Figure 6.3 shows there are not obvious stress distributions along the diameter of the samples and the variations in the magnitude of the stress are large over relatively short distances. The stress measurements were repeated for the roughly lapped samples with a larger diameter laser spot, i.e. a defocused laser spot in an attempt to “average” over a larger number of grains with a single measurement. These results were very similar to those presented in figure 6.3 and suggest that there is a random distribution of fluctuating stress values across the surface of the sample.

If it is assumed that the PCD layer on the Co:WC substrate can be treated as a thin film, it is reasonable to expect a compressive stress in the diamond layer and a tensile stress in the substrate induced by the differential thermal contraction between the PCD and substrate during cooling from the sintering temperature (Lin *et al.* 1994). If it is further assumed that the stresses are transmitted uniformly through the diamond layer, then the induced compressive stress can be calculated to be between 1.5 GPa and 2.7 GPa. These values are comparable to the actual values measured.

The lapping process is known to introduce a compressive surface layer, primarily due to the plastic deformation of the surface that occurs when chips are formed (Martin 1999). The observed surface compressive stress for the lapped samples is in agreement with this. The polishing process can be considered a combination of chipping and plastic flow taking place on a very small scale. Frictional processes play a large role in the material removal, with the result that local hot spots are formed on the diamond surface. These hot spots allow for the plastic flow of diamond and subsequent decrease in localised residual stresses. If the annealing process is sufficiently localised, it can result in a spot of tensile stress developing.

6.1.3.2 Surface stress state as a function of temperature

This work was done as part of Z e Martin's thesis for an M.A. at the University of Oxford, and was extended by student Victor Mofokeng during vacation work (published in Comins *et al.* 2001). High temperature measurements were only performed on the samples with roughly lapped surfaces, as these samples gave the best signal-to-noise ratios in the spectra. Only a single line of points spaced at 2 mm intervals was measured in the high temperature furnace. The position of the diamond Raman line shifts as a function of temperature (Herschen *et al.* 1991). This shift was compensated for according to this reference before calculating the residual stresses in the PCD during the heating experiments.

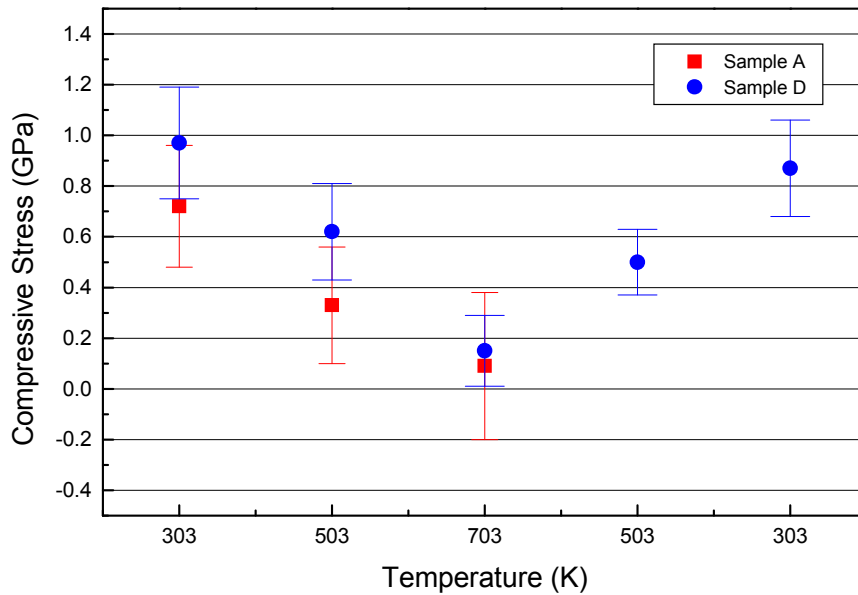


Figure 6.4: Change of average surface compressive stress with temperature for two roughly lapped samples. The error bars correspond to the standard deviation of the variations across the surface.

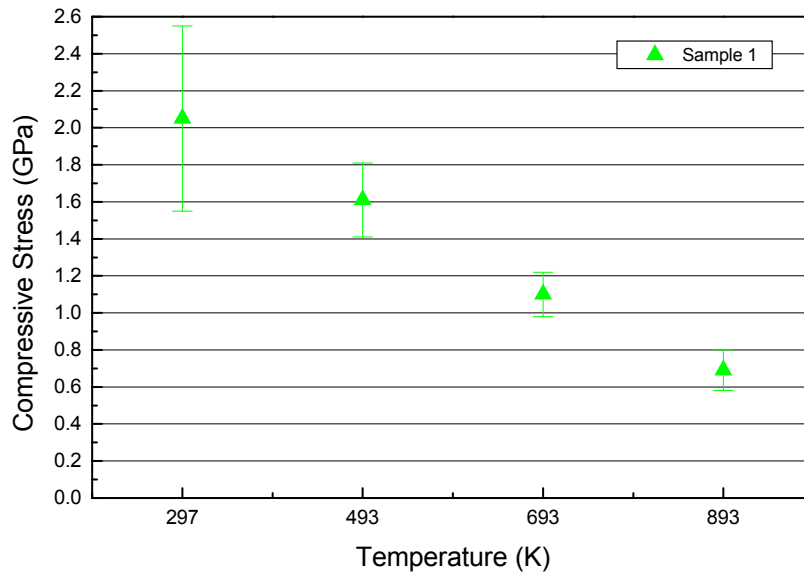


Figure 6.5: Change of average surface compressive stress with temperature for a different type of PCD drillbit. The error bars correspond to the standard deviation of the variations across the surface.

In figure 6.4, the average surface compressive stresses as a function of temperature for two roughly lapped samples (A and D) are shown. The average surface compressive stress decreases linearly with increasing temperature. In the limited number of experiments conducted, it appears that on cooling to room temperature, the surface compressive stress recovers to a value that is slightly less than the room temperature starting value. Although this value is the same within the error bars, the small difference led to the question if cycling to high temperature would have an effect on its properties. This question is addressed in §6.1.3.3.

Figure 6.5 shows results for measurements on a different drillbit to higher temperatures. On heating, the compressive stress values decrease in a similar way to that observed in figure 6.4, i.e. the linear trend observed at first holds for heating to the higher temperatures.

When considering the effect of temperature on compressive stress, it is clear that a reversible mechanism must be considered to account for the largest observed changes, with an irreversible mechanism possibly contributing to a lesser degree. A plausible reversible mechanism is the differential thermal expansion between the PCD layer and the substrate. Upon heating the differential expansion decreases, leading to a relaxation in the measured stress, with increase in stress upon returning to room temperature. The apparent linear relationship between temperature and compressive stress also supports the suggestion that differential thermal

expansion is the dominant mechanism at work during heating and cooling. The temperature data thus also suggests that the assumption that the PCD layer acts as a thin film is valid.

There are several possible mechanisms that will account for the observed decrease in surface compressive stress after annealing, including relaxation due to annealing in the substrate and annealing of the cobalt within the PCD layer. The effect of cycling and cycling temperature is investigated in more detail in the next section.

6.1.3.3 Surface stress state as a function of cycling and temperature

Following the above experiments, the question arose as to what effect repeated cycling to a specific temperature would have on the drillbit properties. To investigate this question, a drillbit was mounted in the atmosphere-controlled furnace in the macro-chamber of the spectrograph in a backscattering configuration (§ 4.6). Several points ($n = 10$ to 11) were measured across the surface of the PCD layer, using the X-Y-Z micrometer-driven mounting stage of the furnace to move the sample. The surface stress state was measured at room temperature ($21\text{ }^{\circ}\text{C}$) prior to annealing and after each annealing cycle for 5 cycles. During each heating cycle, the sample was heated at $15\text{ }^{\circ}\text{C}/\text{min}$ to the set temperature, held at the set temperature for 30 minutes, and then cooled at $15\text{ }^{\circ}\text{C}/\text{min}$ back to room temperature.

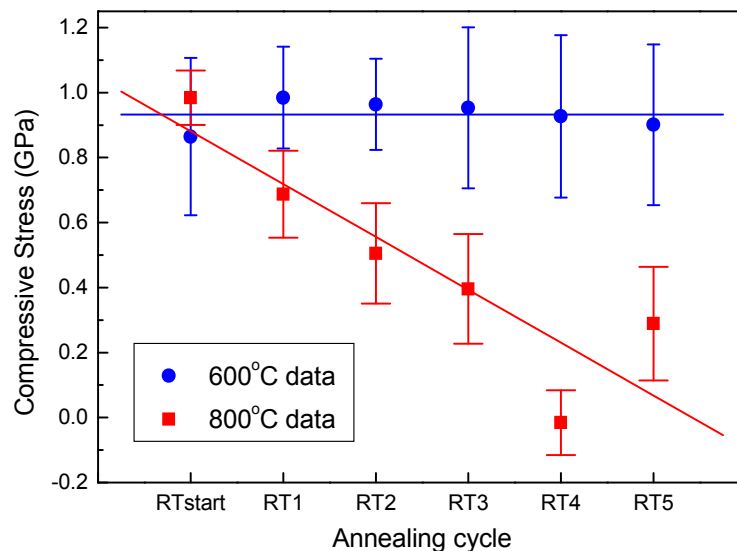


Figure 6.6: Surface stress state for the PCD layer of a drillbit as measured at room temperature after each of 5 cycles to $600\text{ }^{\circ}\text{C}$ and 5 cycles to $800\text{ }^{\circ}\text{C}$. The solid lines are linear fits to the data to illustrate the trends. The data in the figure represent the average stress value across the surface, and the error bars represent one standard deviation in the data.

In practice the furnace cooled at the set rate to $\sim 200\text{ }^{\circ}\text{C}$, below which the cooling rate decreased substantially. This did not affect the results, as the temperatures where changes were expected to happen, were substantially above this temperature.

Results for 5 annealing cycles to $600\text{ }^{\circ}\text{C}$ in an argon atmosphere are plotted in figure 6.6. It is clear that the surface compressive stress as measured at room temperature remains unchanged at approximately 0.9 GPa under these temperature and annealing conditions, indicating that the tool retains its properties. The data for the FWHM of the peak follows a similar trend, i.e. remains unchanged at around 12.5 cm^{-1} with cycling to $600\text{ }^{\circ}\text{C}$ (figure 6.7).

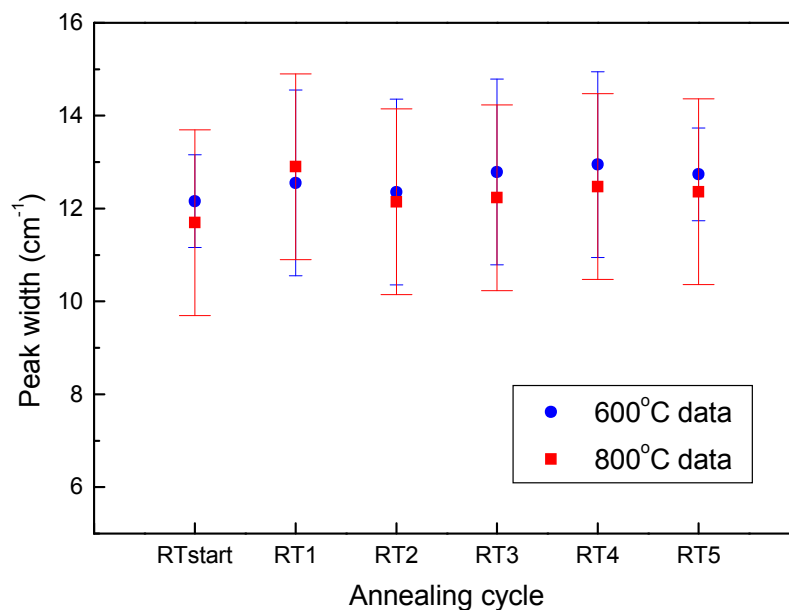


Figure 6.7: FWHM of the PCD layer of a drillbit as measured at room temperature after each of 5 cycles to $600\text{ }^{\circ}\text{C}$ and 5 cycles to $800\text{ }^{\circ}\text{C}$. The data in the figure represent the average width value across the surface, and the error bars represent one standard deviation in the data.

Results for 5 annealing cycles to $800\text{ }^{\circ}\text{C}$ in vacuum of a different drillbit from the same manufacturing batch are plotted in figure 6.6 as well. Here it is clear that the annealing temperature and cycling is affecting the surface compressive stress, with the magnitude of the stress decreasing from 0.9 GPa to considerably lower values with increasing cycling. The drillbit properties are thus being modified permanently. The FWHM in this case remains unchanged at around 12.2 cm^{-1} with cycling (figure 6.7). Although substantially larger than the FWHM for single crystal diamond, these values are consistent with those reported by e.g. Ager III *et al.* (1991) and Bergman *et al.* (1995) for polycrystalline diamond. The large width is ascribed to both

the micro-defects that form due to fracture during the pressure ramp of the synthesis cycle, as well as the plastic deformation that takes place during sintering.

As mentioned earlier, a surface compressive stress state is desirable, as it would act to prevent the formation and slow the propagation of cracks in application, thus effectively acting as a toughening mechanism. It is clear from our results that the higher annealing temperature thus has a negative effect on the drillbit properties.

Several possible mechanisms exist that can account for the observed trends in surface stress state with annealing temperature. The annealing temperatures were chosen to assist in discriminating between mechanisms. Cobalt undergoes a phase transition from hcp to fcc around 420 °C. It is thus anticipated that annealing at 600 °C would indicate any effect that this process has on the surface stress state. The data shows that the surface stress state remains essentially unchanged during annealing to 600 °C, showing that the cobalt phase transition does not affect the surface stress state. Cobalt-catalysed graphitisation of diamond has an onset temperature of around 750 °C at ambient pressure, and thus annealing to 800 °C would show if this mechanism affects the surface stress state. Our data suggests strongly that this mechanism is mainly responsible for the change in surface stress state. It is noted that in other experiments by our group it was found that PCD heated to 1000 °C shows clear evidence of graphitic carbon in the Raman spectra measured on the surface of the PCD.

The results for the FWHM data indicate that no annealing of the diamond material in the PCD layer is taking place, as the FWHM is unchanged with repeated cycling for both temperatures. This suggests that the stress relieving mechanism is not due to a change in the diamond grains, e.g. possible dislocation movement, but due to changes in the diamond-matrix boundaries. This supports the role of a mechanism such as the cobalt-catalysed graphitisation mentioned in the previous paragraph.

The constituent diamond for the PCD layer in the above drillbits is Type Ib. It has been shown that the Brittle-Ductile Transition Temperature (BDTT) for single crystal Type Ib diamond is 750 °C (Brookes *et al.* 1990) and the question arises if this has any bearing on the results for the peak width data in figure 6.7. Due to limited thermal stability of diamond-cobalt materials around 800 °C flow stress data for these materials are inconclusive (TK Harris, personal communication), but flow stress studies on diamond/ β -SiC aggregates have shown that in the range of 800 °C to 1250 °C time dependent plastic deformation does not occur (Harris *et al.* 2001). The indication is thus that for polycrystalline diamond materials the BDTT is at a higher value than for single crystal diamond. The absence of a change in the Raman peak width data

with repeated cycling thus suggests that the BDTT has not been reached yet for the drillbits considered in the present study. Processes in the cobalt matrix and/or graphitisation of the diamond are thus the most likely mechanisms to account for the observed reduction in compressive stress.

6.2 Summary of results for PCD

Polycrystalline diamond (PCD) tools commonly consist of a PCD layer sintered onto a cobalt-tungsten carbide (Co-WC) substrate. These tools are used in diverse applications and both the magnitude and distribution of the stresses in the PCD layer affect tool behaviour. These stresses in sample drillbits were investigated by means of micro-Raman spectroscopy in which the properties of the diamond Raman peak reveal both the nature of the stress present (compressive or tensile) and its magnitude.

As discussed above, prior work in our research group was reviewed first. Here it was found that the surface preparation techniques influenced the average stress present in the PCD surface layer which was in compression in all cases investigated. The largest stresses were encountered in the roughly lapped sample (1.4 GPa) with the stress values decreasing for fine lapping (0.8 GPa) and polishing (0.1 GPa). Small areas with low tensile stresses were found in some polished samples. Measurements of stress as a function of temperature for roughly lapped sample drillbits indicated a linear trend of decreasing stress values with increasing temperature, although the stress remained compressive.

Following on this, the results of this thesis found that cyclic annealing of a sample drillbit to 600 °C shows that the tool properties are retained after 5 cycles, while similar cycling to 800 °C resulted in a permanent decrease of the average surface compressive stress. This implies a reduction in the drillbit's ability to resist crack formation and propagation and is thus a degradation of the tool properties

In conclusion it can be stated that a PCD tool is a complex material, involving several variables in its manufacture and use. The work reported here has provided new information on the surface stress state in the PCD layer drillbits, this being of value to manufacturers and end users of these products. It is suggested that use be made of Finite Element Modelling to investigate stress distributions from a complementary, theoretical point of view.

Chapter 7: Results – investigation of cBN and PCBN

This chapter details the results of Raman and photoluminescence studies on cubic boron nitride samples. The structure, synthesis and properties of cBN were discussed in §2.2. The stress contours centred on room temperature indents in single crystal cBN as well as impressions in PCBN are discussed in the first sections. Photoluminescence studies of these same indents are presented in following sections. This data was published in Erasmus *et al.* (2000). Photoluminescence studies of electron-irradiated cBN crystals are presented in §7.3; this data was published in Erasmus *et al.* (2004). In conclusion measurements of the Raman peak positions of cBN are presented as a function of temperature in the range 4 K to 1373 K.

7.1 Indentations in single crystal cBN

In exactly the same way as with diamond, Raman spectroscopy can be used to map stresses in cBN by measuring the positions of the cBN Raman peaks. The peak widths again give information regarding the degree of plastic deformation present in the sample volume. As was mentioned in §2.2.5.1, cBN has two Raman peaks, a TO peak at 1054 cm^{-1} and an LO peak at 1305 cm^{-1} .

7.1.1 Sample detail

The cubic boron nitride samples studied were in the form of small, faceted single crystals. The crystals varied in size from $\sim 360\text{ }\mu\text{m}$ diameter to $\sim 1\text{ mm}$ diameter and in colour from dark yellow to black. Raman spectra were acquired with the spectrometer operated in single spectrograph mode with an 1800 grooves/mm grating and a CCD detector. Details on the Jobin-Yvon T64000 Raman spectrograph are given in §4.1.3 and the detector is discussed in §4.1.4. The 488 nm line of a Coherent argon ion laser was used as the excitation source (§4.2). The laser spot size was $\sim 1.5\text{ }\mu\text{m}$ in diameter, and a motorised X-Y microscope stage was used to obtain high resolution maps of the samples (§4.1.2 and §4.7.1.1). Indents were made with polycrystalline diamond conical indentors, of which the tip was ground to a fine point and then very lightly sanded down

to a flat of the order of a hundred microns diameter. The indentations were made by lowering the tip at a fixed rate into the sample and then releasing the load when a predetermined value was reached. In order to make a usable indentation, it was necessary to hold a crystal firmly in place during the indentation such that the crystal facet being indented was orthogonal to the indenter. Due to the irregular shape of the crystals the best solution found was to sinter the crystals into a brass matrix such that the crystal facet needed for indentation was co-planar with the surface and the bulk of the crystal was held by the metal matrix. This arrangement held the crystal rigidly enough for the indentation process and was also a convenient “sample holder” for the indented crystal during the Raman mapping process.

As the exact position of the Raman peaks are of importance in determining the nature and magnitude of stresses measured, the spectrograph was carefully calibrated before each set of acquisitions using the 1056.94 cm^{-1} laser plasma line. During acquisition, this laser line was removed by means of an interference filter in order to prevent it distorting the position and shape of the cBN TO Raman peak.

The indentations on the single crystals were technically difficult, since the samples were very small and the indentation could not always be centred on the sample as desired. Figure 7.1 is a micrograph of an indent made in a black cBN crystal at a maximum load of 30 N. The circular indent is clearly visible with cracking around its circumference and 2 cracks radiating away from the indent. The leftmost crack runs to the edge of the crystal.

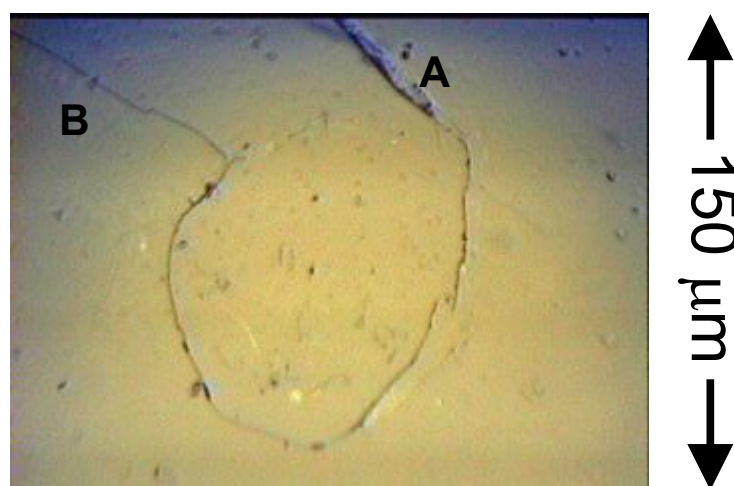


Figure 7.1: Micrograph of an indent in a cBN crystal, made at 30 N maximum load (estimated pressure 3.8 GPa). The indenter tip diameter was $100\text{ }\mu\text{m}$. The labels “A” and “B” refer to the crack features discussed in the text.

7.1.2 Raman mapping of indentations

A typical Raman spectrum of the cBN crystal shown in figure 7.1 is given in figure 7.2. The Raman spectrum of 49 points across the indent (figure 7.1) was obtained in the shape of a 7×7 matrix, with a $25 \mu\text{m}$ step size between the points and the grid centred on the indent. A $\sim 1.1 \mu\text{m}$ diameter laser spot size was used. The peak positions and FWHM of our data are in good agreement with the Raman data on one of the samples of cBN measured by Sachdev *et al.* (1997). The TO peak was used in preference to the LO peak for the mapping data, since the latter was frequently less intense and for some samples there was a broad feature present to the lower frequency side of the peak, which complicated background subtraction and introduced uncertainty with the width measurement of the peak. The TO peak was fitted to a Lorentz line shape, which yielded the position and FWHM of the peak. The Lorentz line shape was a good fit to the experimental data, with no asymmetry visible in the peak. The position of the TO Raman peak and the FWHM of the same peak across the indent are plotted as contour maps in figures 7.3 and 7.4.

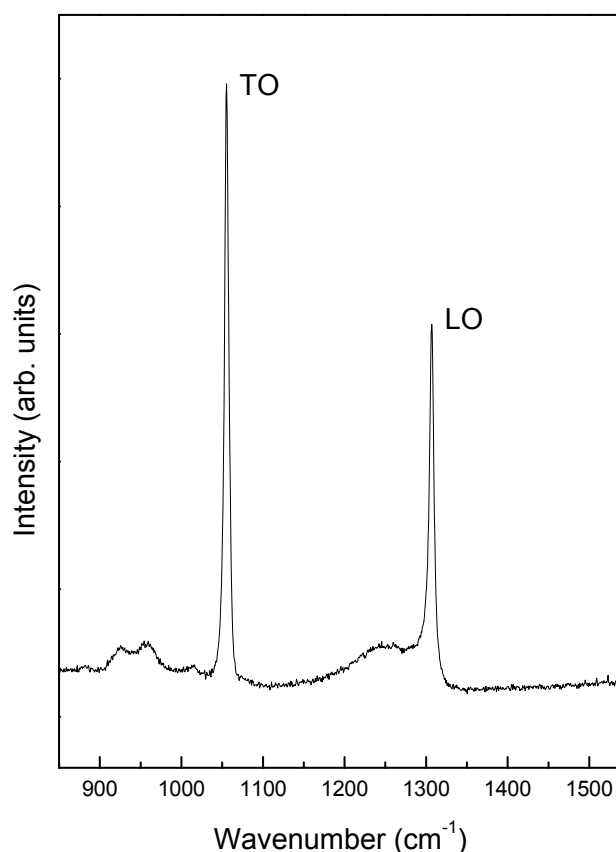


Figure 7.2: Typical Raman spectrum of cBN crystal shown in figure 7.1 (data measured by author).

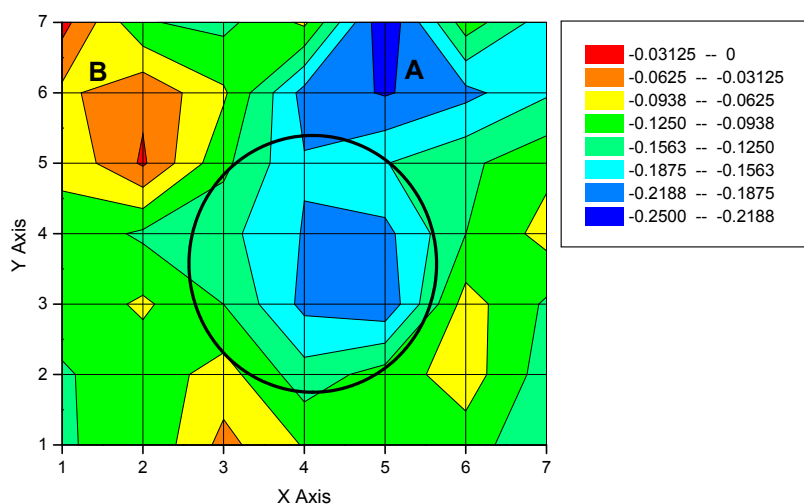


Figure 7.3: Contour plot of the stress derived from the TO Raman peak position across the indent in figure 7.1. The greatest degree of shift of the peak to higher frequencies is indicated by dark blue (~ 0.25 GPa compressive), with smaller shifts progressing through light blue to green, yellow and orange to red, which indicates the smallest shift (~ 0.02 GPa compressive). The biggest shift in peak position is visible in the centre of the plot and towards the top. The units in the table at top right are GPa. The black circle corresponds approximately to the position of the indent in figure 7.1.

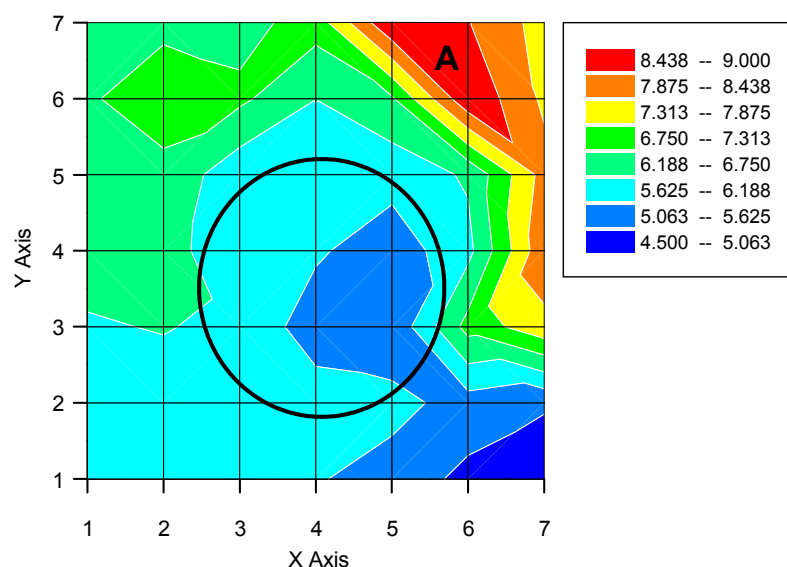


Figure 7.4: Contour map of FWHM of the TO Raman line across the indent in figure 7.1. Red indicates the largest FWHM values (8.3 to 8.7 cm^{-1}) and blue the smallest (~ 5.5 cm^{-1}), with orange, yellow and green indicating intermediate values in order of decreasing magnitude. The units in the table at top right are cm^{-1} .

Stresses were calculated in the same way as for diamond, using the data given in chapter 2, §2.2.5.1. The value used for the coefficient of stress-induced shift was thus $d\omega_{\text{TO}}/dp = 3.39 \pm 0.08 \text{ cm}^{-1}/\text{GPa}$ (equation 2.3, Sanjurjo *et al.* 1983). This stress-induced shift of the TO Raman line is applicable in the case of hydrostatic (isotropic) stresses in the cBN lattice. In the case of diamond thin films and PCD layers sintered on a tungsten carbide backing, a biaxial stress model (Ager *et al.* 1993) is often invoked due to the lattice and thermal mismatch between layer and substrate. In the presence of large stress values, a biaxial stress model gives rise to the splitting of the triply degenerate diamond Raman line into a singlet and a doublet (Ager *et al.* 1993, Catledge *et al.* 1995). For the cBN samples in this study, the application of a biaxial stress model to the results is unnecessary. The single cBN crystal is not constrained by a substrate, nor are the PCBN squares, as these are solid blocks of sintered cBN with no backing. The stress distribution in the cBN samples is thus assumed to be approximately hydrostatic.

It can be seen from figure 7.3 that there are clear contour lines indicating the presence of the indent. The peak position is shifted to higher frequencies near the centre of the indent, as well as in the region of the crack feature (labelled “A”) near the top centre of figure 7.1. At these positions (blue/dark blue in figure 7.3) the stresses are compressive and approximately 0.25 GPa in magnitude. Away from the centre of the indent, the peak has been shifted less, but still to higher frequencies, indicating compressive stresses are present. The lowest value stress is 0.02 GPa (orange/red, top left in figure 7.3). It is noted that these lowest values are associated with a different crack (labelled “B” in figure 7.1) at top left which runs to the edge of the crystal (out of the field of view to the left of the image), indicating the stress relief brought about by this crack. This contour map very clearly illustrates the effect of the indent on the cBN crystal surface.

In figure 7.4 the crack feature labelled “A” near the top centre of figure 7.1 is again clearly visible as the region with the biggest FWHM (8.3 cm^{-1} to 8.7 cm^{-1} ; red colour). The FWHM decreases towards the centre of the contour map, where a clear suggestion of the presence of the indent is visible. The FWHM at the centre varies around 5.5 cm^{-1} (intermediate blue). This is somewhat unexpected, as deformation of the cBN would likely lead to an increase in FWHM. This result is not yet understood.

7.1.3 PL of indentations

Plastic deformation is associated with the creation of vacancies in the lattice via the mechanism of non-conservative slip. As plastic deformation can take place at room temperature in cBN

(Novikov 1985 and discussion in chapter 2), it is expected that these vacancies will give rise to vacancy-related PL active defect systems. In order to study the possibility of PL-active defects introduced via the plastic deformation associated with the indentations, PL spectra of cBN crystals were measured before and after irradiation with electrons (nominal dose of $2 \times 10^{17} \text{ cm}^{-2}$ and energy of 1.9 MeV). Any PL active defects that appear after irradiation are likely to be vacancy related, and can thus be compared with features in the spectra of the plastically deformed crystals. The PL studies of the electron-irradiated samples are discussed in more detail in §7.3.

The experimental conditions for the PL of the indented cBN were the same as those for the Raman spectra mentioned in the previous paragraph, except that the samples were mounted in a continuous flow liquid helium microscope cryostat. All PL spectra were measured at $\sim 5 \text{ K}$, as it was found that this gave the highest resolution of the peaks (see figure 4.3 in chapter 4).

None of the PL spectra of points measured within and without the indent showed any evidence of sharp ZPLs. The luminescence intensity was normalised as was done for diamond PL spectra and discussed in §4.4.1 and is observed to be substantially greater at the centre of the indent. Two broad features are visible, with a shoulder peak centred on 2600 cm^{-1} (17892 cm^{-1}) and a very broad hump centred around 3800 cm^{-1} (16692 cm^{-1}).

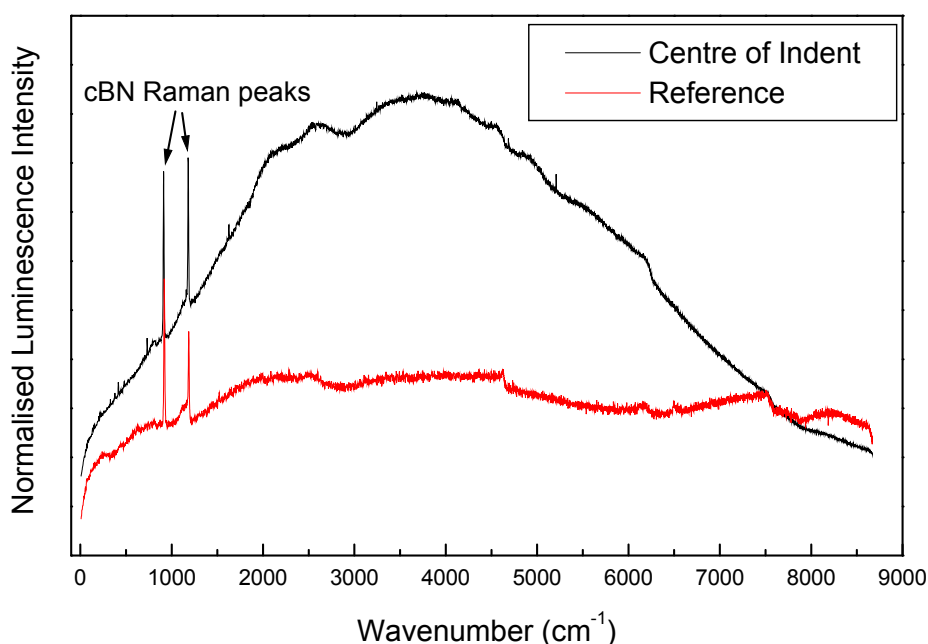


Figure 7.5: Normalised PL intensities, measured at 5 K, of a spot in the middle of the indentation (figure 7.1) and a reference spot measured well away from the indentation.

7.2 Indentations in PCBN samples

The PCBN samples were in the shape of small squares of approximate size $10 \times 10 \text{ mm}^2$. They contained approximately 95% cBN, with the balance made up of binder material. The samples were supplied with surfaces polished to a reflective finish. Indentations were made at room temperature using polycrystalline diamond conical indentors in the same way as described for the single cBN crystals. It was not necessary to mount the PCBN samples in any matrix, as the squares offered a large and stable enough platform for the indentation procedure. The indenter used had a $400 \mu\text{m}$ diameter tip, and required much larger loads than for single crystals in order to produce visible indents in the material. Loads typically varied between 2000 N and 3000 N. The indenters were supplied by Element Six (Pty) Ltd and at that stage of doing the PCBN indentations, only indenters with broad tips were available. As plastic deformation is possible in PCBN at room temperature (Brookes 1986), it is likely that the deformation brought about by the indenter had resulted in a residual stress field around the indent and Raman mapping was carried out to test this possibility.

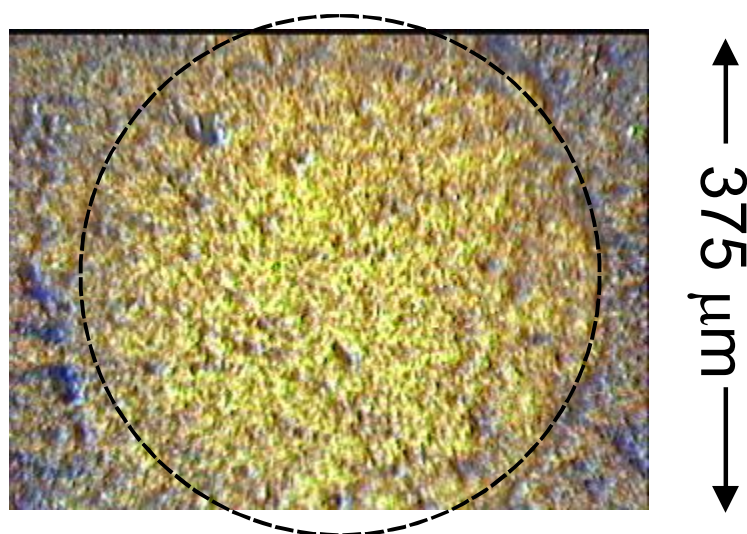


Figure 7.6: Micrograph of an indent in PCBN, made at 2600 N maximum load (estimated pressure $\sim 20 \text{ GPa}$). The broken line circle in the figure indicates the position of the indent on the surface of the sample.

7.2.1 Raman mapping

Raman spectra of 25 points across an indent were obtained in the shape of a 5×5 matrix, with the matrix measuring $500 \mu\text{m}$ on a side and the laser spot size being $1.5 \mu\text{m}$ diameter. The biggest

differences between the Raman spectra of single crystal and polycrystalline cubic boron nitride are the width and amplitude of the peaks, as illustrated in figure 2.11 in chapter 2. The spectra of polycrystalline samples show weaker intensity peaks that are significantly broader when compared to the single crystal spectra (typically $\sim 20 \text{ cm}^{-1}$ versus 6 cm^{-1}). This broadening is thought to be due to the deformation that takes place during the sintering process. The peaks are also situated on a sloping luminescence background that is much steeper and more intense than in the case of the single crystal samples. Here again only the TO peak was analysed in detail, mainly due to the frequent very weak intensity of the LO peak. For an indent made at a maximum load of 2600 N (micrograph in figure 7.6) the stresses present in the material were found to be quite variable and range from a maximum compressive stress of 1.0 GPa to tensile stresses of 0.8 GPa (figure 7.7).

No clear evidence of the presence of the indent was visible, as was observed in figure 7.3 for the case of single crystal cBN. Measurements of a similar map on a section of undeformed PCBN showed that the inherent surface stress fluctuations (as measured using the position of the TO Raman peak) vary from 0.7 GPa compressive to 0.4 GPa tensile. This indicated that the inherent stress fluctuations across the surface were of the same order as those introduced by the indentation process and it is thus difficult to “image” the indent via its residual stress map.

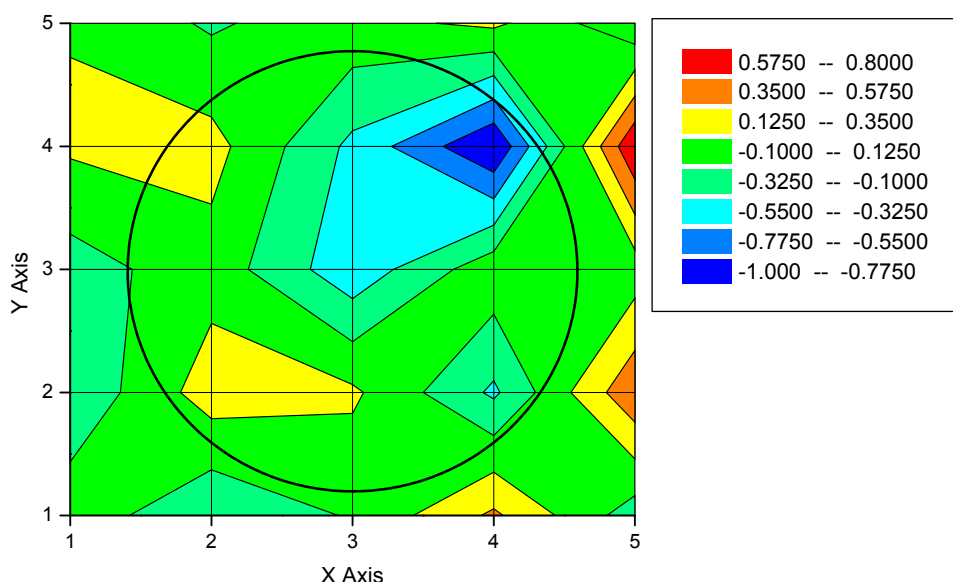


Figure 7.7: Stress contour map (units for values at top right is GPa) derived from the position of the Raman TO peak for the indent in figure 7.6. The circle is the position of the indentation relative to the grid of the 5×5 matrix.

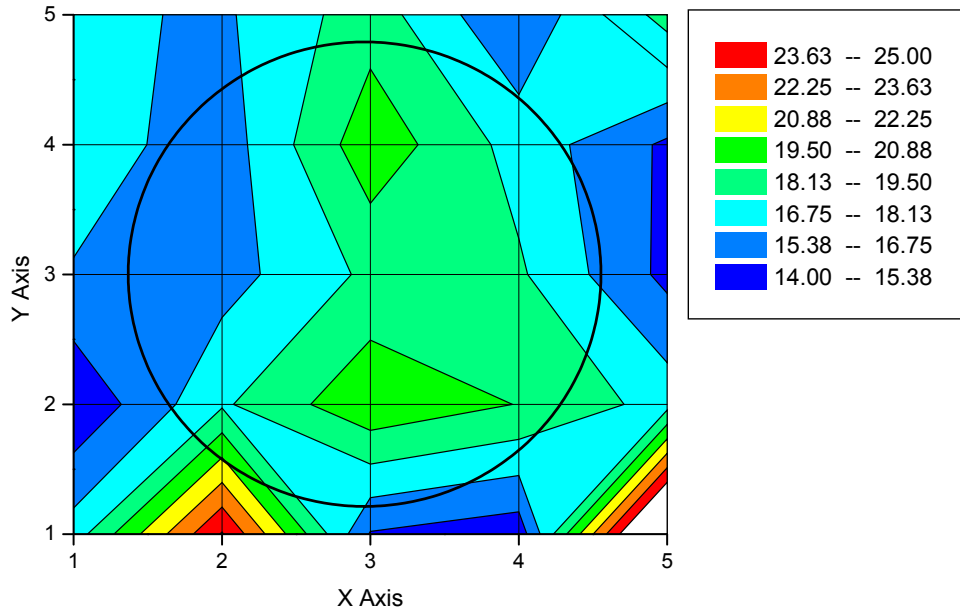


Figure 7.8: Contour map of FWHM of Raman TO peak for the indent in figure 7.6 (units for values at top right is cm^{-1}). The circle is the position of the indentation relative to the grid of the 5×5 matrix.

For the contour map of the FWHM of the Raman TO peak in figure 7.8 there is again very little evidence of a pattern, especially when compared to the case for the single-crystal indent in figure 7.4. Measurements of a similar map on a section of undeformed PCBN showed that the inherent TO Raman peak width fluctuations vary from 12.3 cm^{-1} to 19.5 cm^{-1} . This indicates that the inherent fluctuations in the degree of deformation across the surface as a result of the sintering manufacturing process are of the same order as those introduced by the indentation process. It is thus difficult to discriminate between deformation present before indentation and deformation brought about by the indentation.

7.2.2 PL mapping

PL spectra of the indented polycrystalline material show no visible evidence of ZPLs, either within the indented area or without (figure 7.9). Both inside and outside the indented area a broad peak centred at 4500 cm^{-1} is present. Spectra taken within the indented area show an additional shoulder in the spectrum at 2200 cm^{-1} . Bourne (1989) has shown that annealing of samples with clear ZPLs present above $1000 \text{ }^\circ\text{C}$ removes or heavily broadens and weakens the ZPLs. It is suggested that the feature at 4500 cm^{-1} is the B band observed by Bourne and that any PL active

defects that might have been present have been annealed out due to the high temperatures experienced during sintering.

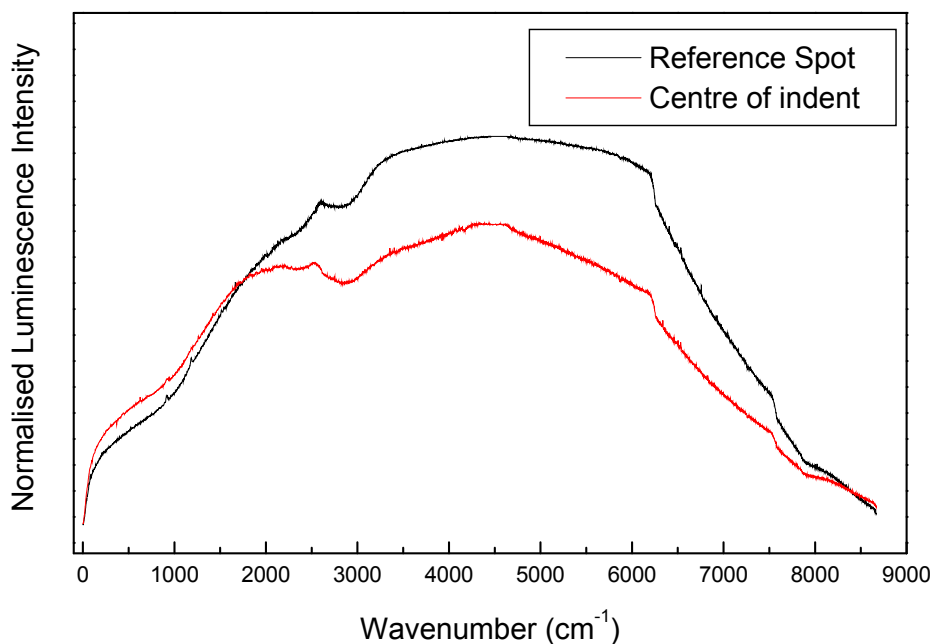


Figure 7.9: PL spectra of PCBN at 5 K. The reference spot is on the PCBN surface well removed from any indents. “Centre of indent” refers to the indent in figure 7.6.

7.3 PL spectroscopy of electron-irradiated cBN

Luminescence results for cBN appearing in the literature have been discussed in §2.2.5.2, and a short summary of the relevant references are given here. Cathodoluminescence (CL) studies (Tkachev *et al.* 1985b) of as-synthesised cBN showed two broad bands, a stronger feature centred on 3.1 eV and a weaker feature centred on 2.2 eV, as well as the vibronic spectra of three defect centres, labelled GC1, GC2 and GC3. GC1 was identified as vacancy-related, while GC2 was thought to be due to a vacancy complex. CL of 4.5 MeV electron-irradiated cBN (Zaitsev *et al.* 1986b) showed that irradiation introduced three vibronic defect centres, labelled RC1 (ZPL = 2.27 eV, ~546 nm), RC2 (ZPL = 2.15 eV, ~576 nm) and RC3 (ZPL = 1.99 eV, ~623 nm). These centres were different from the GC series, and thought to be intrinsic in nature as they were present in all samples. The RC defects were also thought to be vacancy related. Ion implantation (Zaitsev *et al.* 1987) with H⁺, He⁺, B⁺, S⁺, Ne⁺ and Se⁺ resulted in the introduction of the same RC series as found with electron irradiation. This supported the suggestion that the RC defects were intrinsic. It was also observed that all zero phonon lines (ZPLs) were doublets, and the widths varied with sample and irradiation conditions.

The first photoluminescence (PL) studies (Bourne 1989) on different types of cBN at 77 K showed that two broad bands centred on 1.96 eV (~633 nm) and 2.08 eV (~595 nm) were present in almost all samples. Several vibronic centres were observed, dependent on crystal type. Electron irradiation introduced the RC series observed earlier (Zaitsev *et al.* 1986b) with CL, but only the RC1 centre was observed in all samples. RC2 was present in most samples, and RC3 was only observed in about 50% of the cases.

In the present study, two types of cBN crystals were investigated. One type consists of small, synthetic (HPHT) crystals (<1 mm diameter), amber in colour, partly transparent and with no distinct morphology. The other type, also of HPHT origin, consists of crystals ~ 1 mm diameter, black-brown in colour, very opaque and with no distinct morphology. The black colour of these crystals has previously been shown to be due to excess boron in the lattice (Sachdev *et al.* 1997). It must be noted that most cBN crystals synthesised for industrial use have diameters significantly smaller than 1 mm.

7.3.1 Experimental details for PL spectroscopy of electron-irradiated cBN

Spectra were recorded with the Jobin-Yvon T64000 Raman spectrometer operated in single spectrograph mode with a 600 lines/mm grating and a CCD detector. Luminescence was excited with the 488 nm line of an argon ion laser. Samples were mounted in an Oxford Instruments continuous flow liquid helium microscope cryostat, and the photoluminescence of selected spots on the crystals acquired at 5 K with the microscope attachment. The laser beam diameter at the sample was ~1.5 μm . It was determined that the lower temperature was preferable to 77 K, as narrow lines with possible splitting were better resolved (see figure 4.3). Calibration was done via Hg and Kr lamp emission lines. Irradiation was performed with electrons at a nominal dose of 10^{17} electrons. cm^{-2} and energy of 1.9 MeV. The ZPL peak parameters were obtained from fitting the measured peak to a Voigt function. In order to be able to compare intensities of the spectra from different crystals, the intensities were normalised by dividing the intensity of the PL spectrum throughout the spectral range by the integrated intensity of the first order TO Raman peak, measured under identical excitation, collection and geometric conditions. This is in line with the practice followed for diamond (as discussed in §4.4.1) and is necessary as the intensity of PL spectra depend on several, often uncontrollable factors such as laser beam penetration depth, excitation volume and collection efficiency.

7.3.2 Results for PL spectroscopy of electron-irradiated cBN

Typical spectra measured for the black and amber cBN crystals are given in figure 7.10 and figure 7.11, respectively. ZPL peak parameters as extracted from peak fitting are given in Table 7.1 and Table 7.2.

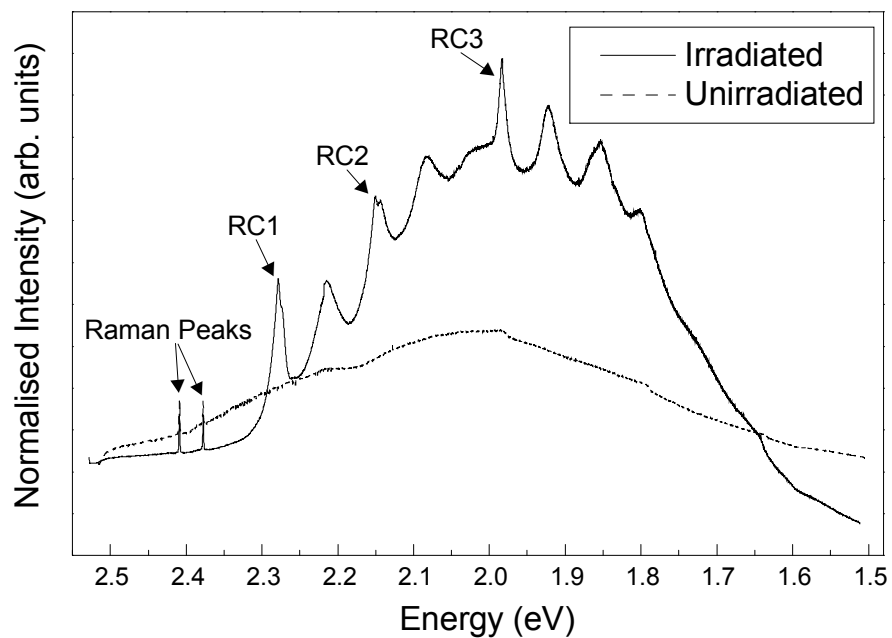


Fig. 7.10: PL spectra of unirradiated and irradiated black cBN crystals, acquired at 5 K.

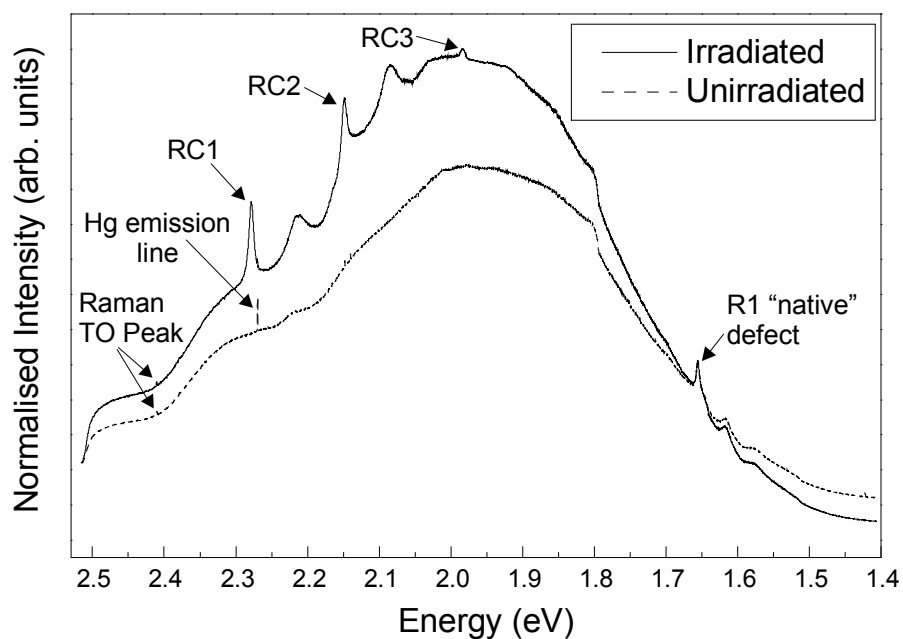


Fig. 7.11: PL spectra of unirradiated and irradiated amber cBN crystals, acquired at 5 K.

In both figures the unirradiated and the irradiated crystals show a broad band centred around 2 eV, with the normalised intensity higher for the irradiated crystal. Small crystals synthesised via spontaneous nucleation in the HPHT process are likely have high defect densities due to dislocations and possible uptake of flux precursor materials. Broad bands such as these occur when a number of broad defect peaks, associated with extended defects, overlap. There is also the indication that the irradiation process introduces additional defects into the lattice. The band around 2 eV has been attributed to stable neutral complexes (Bourne 1989).

Table 7.1 ZPL peak parameters for the RC defects in the black cBN crystals.

	Position (eV)	Splitting
RC1	2.28	Yes
RC2	2.15	Yes?
RC3	1.98	No

Table 7.2 ZPL peak parameters for the RC defects in the amber cBN crystals.

	Position (eV)	Splitting
RC1	2.28	Yes
RC2	2.15	Yes?
RC3	1.98	No

Electron irradiation introduces the RC series of peaks in both types of crystal investigated, as is clear from the position data in the tables. In the black crystals all three peaks are present, while in the amber crystals RC1 and RC2 predominate, with RC3 only weakly visible in some spectra. The RC1 defect has been attributed to the nitrogen vacancy in the cBN lattice (Bourne 1989), but no more detailed assignment has been made yet. The R1 defect in the amber crystals is present before and after irradiation, and has been linked to the presence of phosphorus in the lattice (Bourne 1989). This "native" defect peak is unsplit in all cases, and the ZPL width is unaffected by irradiation.

The ZPLs of RC1 and RC2 are observed to be split in some cases and the splitting is likely stress-induced (Zaitsev *et al.* 1987), but it is also possible that the RC centres are doublets that are strain-broadened in less perfect crystal regions. Although peak deconvolution using Origin 5.0 software indicates that the RC2 ZPL likely exhibits splitting, the case is somewhat problematic as there is significant overlap of the RC2 ZPL and the second phonon sideband of the RC1 line. Splitting is likely in cases where localised strain is oriented in a preferred direction, while the localised strain is likely to be more isotropic in nature or not oriented in the correct direction for unsplit peaks. Where splitting occurs it complicates the fitting of peaks and

subsequently line shape analysis is difficult. For the unsplit, symmetric peaks, the measured line shape of the ZPLs is Gaussian for both types of crystals. This engenders several possibilities. It is potentially the case that line-type defects dominate, as a prevailing Gaussian line shape is expected for crystals with line-type defects such as dislocations. It could also be due to a high concentration of point defects or even a combination of line-type defects and high concentrations of point defects (detailed discussion in §3.2.1). Both the presence of line-type defects and high concentrations of point defects would be consistent with the crystal quality, as discussed below.

The ZPL line widths and ZPL intensities of the RC centres in both types of sample vary from crystal to crystal and sample spot to sample spot, showing no obvious trends. As the line width is an indication of the strain-broadening present in the crystals, this implies an apparent random variation in localised strain in the crystals. It was observed that the peak widths for the ZPLs in the black crystals are generally larger than the corresponding widths for the amber crystals, indicating higher defect concentrations and associated strains in the black crystals. The intensity variations also point to an uneven distribution of the RC centres in the crystals.

It is clear from the above results that although the available cBN crystals fulfil their role in industrial applications very admirably, the current crystal quality in terms of distinct morphology and crystallinity is unlikely to be adequate for semiconductor applications. In the case of diamond it has been shown (Field 1992a) that lattice defects and impurities play a very important role in its optical, electrical and mechanical properties. It is very likely to be the same for cBN.

7.4 Raman spectroscopy of cBN as a function of temperature

The effect of temperature on the position of a Raman line was discussed in §3.1.6, and the discussion in this section will refer to this.

Before progressing, a note on the sequence of the work for this section is in order. The first set of measurements was done on a single, amber-coloured crystal of cBN (figure 7.12a), approximately 1 mm in diameter. This crystal was cooled to 4 K in an Oxford Instruments Microstat^{He} continuous flow liquid helium microscope cryostat (§4.5) for the low temperature measurements and then transferred to a Linkam TS1500 microscope furnace, operating under UHP argon, for the high temperature measurements. After the high temperature measurements, it was noticed that some surface degradation of the sample crystal had taken place (figure 7.12b). After data analysis, it was found that the low temperature data displayed some degree of scattering. As the Microstat^{He} is a vacuum cryostat it was possible that some localised heating of

the sample had taken place and/or that there was poor thermal equilibrium between the sample and the cold finger on which it was mounted. In order to test for this possibility a similar crystal (from the same synthesis batch) was mounted in an Oxford Instruments CF1204 exchange gas cryostat, itself mounted in the macro-chamber of the Jobin-Yvon spectrometer, for another set of low temperature measurements. The presence of He gas in the sample chamber of this cryostat ensures good thermal equilibrium of the sample and assists in making sure it remains uniformly cold during the measurements. The macrochamber also has a larger diameter incident laser beam due to the different focusing lens compared to the microscope. This has the effect of a relatively low laser power density at the sample. It was found that the measurements in the exchange gas cryostat gave more consistent results for especially the peak positions at low temperatures, so that these results were used in subsequent analyses.

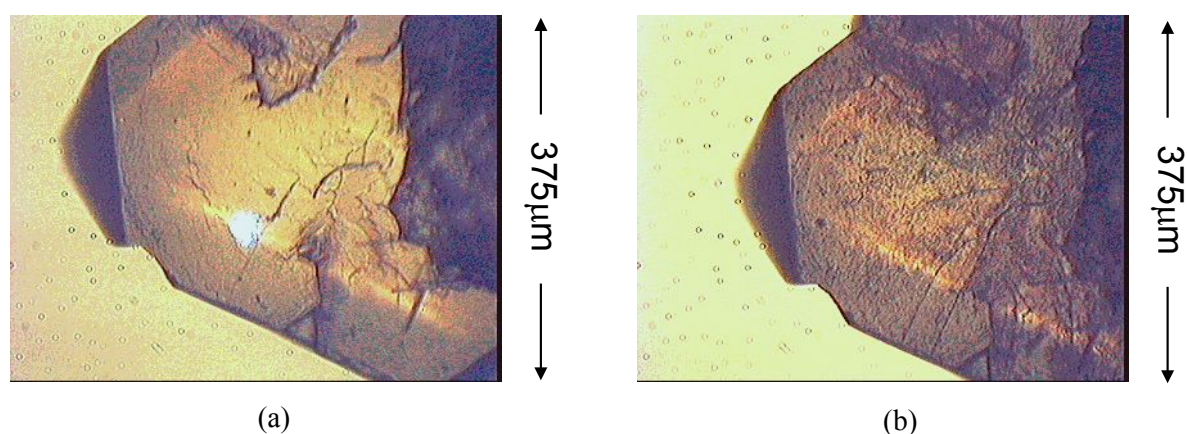


Figure 7.12: cBN crystal as mounted in the Linkam TS1500 microscope furnace and imaged under the Raman microscope; (a) before heating (the blue spot is from the laser beam) and (b) after heating to 1373 K.

Raman measurements in all cases were conducted with the Jobin-Yvon T64000 spectrograph operated in single spectrograph mode and with the 488 nm line of an argon ion laser as the excitation source. The CCD detector was used to record the dispersed light. The spectral line shapes were assumed to be Lorentzian in shape convoluted by a Gaussian instrument profile. The linewidths were determined by deconvoluting the instrumental function from the measured spectrum. This resulted in a small correction to the measured linewidths that were most significant at low temperature.

7.4.1 TO- and LO-mode position shifts

Figure 7.13 shows typical Raman spectra as measured at selected temperature. In the analyses, data for the Raman LO peak is only plotted up to 1173 K, as the peak is too weak at higher temperatures for meaningful fitting.

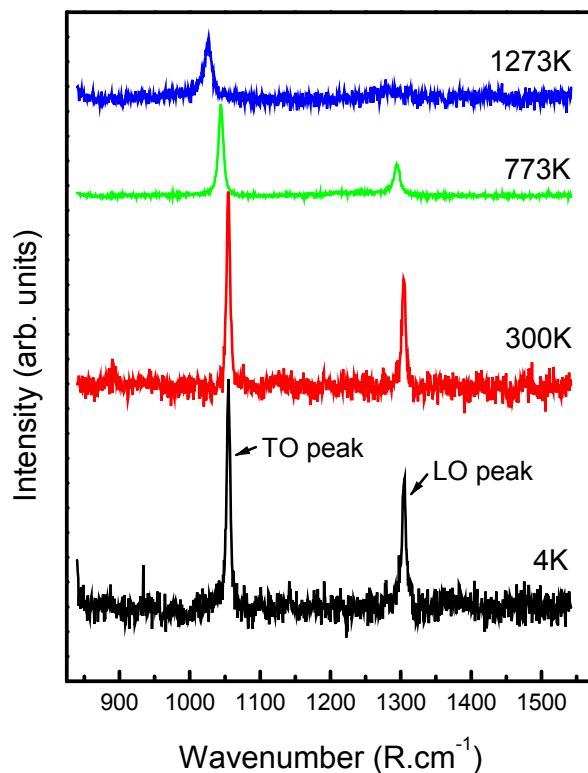


Figure 7.13: Typical Raman spectra of cBN at different temperatures. Note the shift of peak position and widening of the peaks with increasing temperature.

Figures 7.14 and 7.15 show the positions of the TO and LO peaks as a function of temperature. The solid lines are quadratic fits to the data, with temperature T in Kelvin. Error bars in the figures correspond to the peak fitting error, i.e. they give an indication of the uncertainty of the peak position. Where smaller than the symbols, the error bars have been omitted.

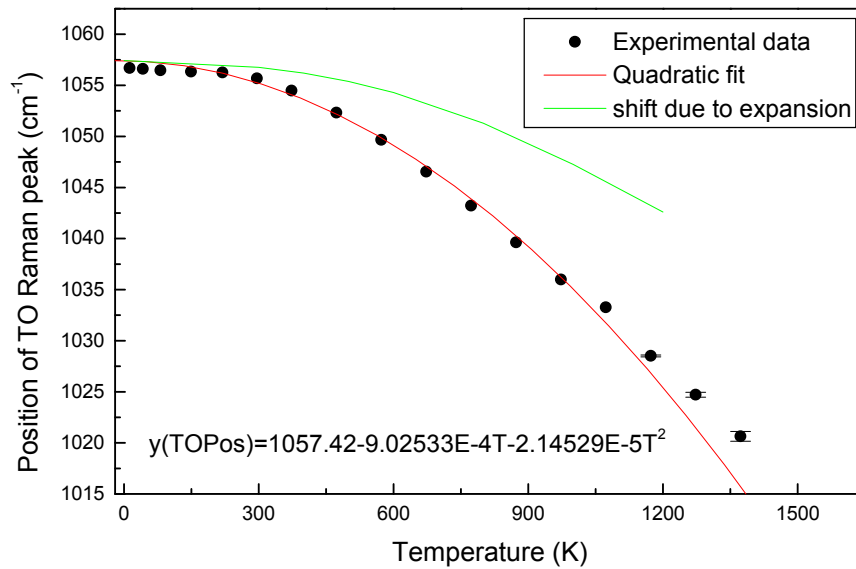


Figure 7.14: cBN Raman TO peak position as function of temperature. The solid circles are the measured data, the red line is a quadratic fit to this data and the green line is a calculation of the expected shift of the Raman TO line due to thermal expansion alone (see discussion in text).

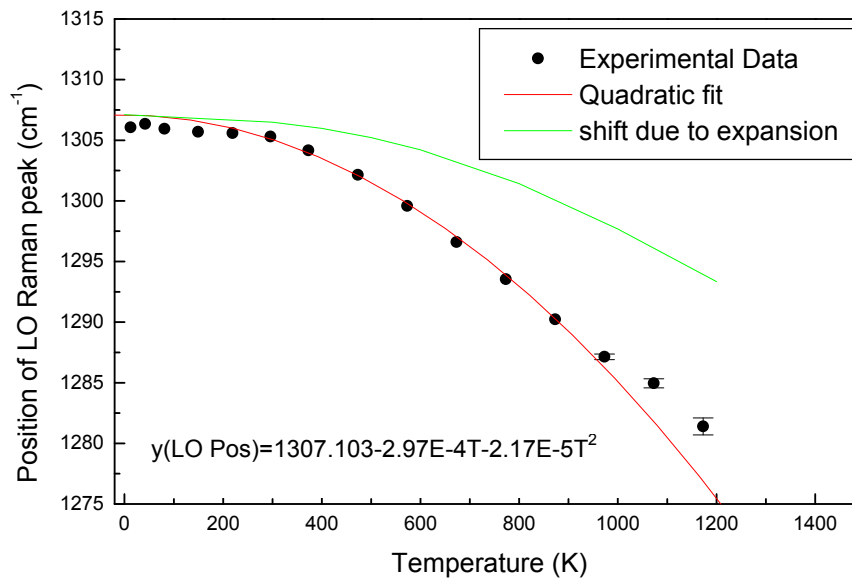


Figure 7.15: cBN Raman LO peak position as function of temperature. The solid circles are the measured data, the red line is a quadratic fit to this data and the green line is a calculation of the expected shift of the Raman LO line due to thermal expansion alone (see discussion in text).

Table 7.3: Fit parameters relevant to solid curves in figures 7.14 and 7.15. The constants refer to the equation $y(\text{Peak Pos}) = A + BT + CT^2$ (T in Kelvin).

	TO peak	LO peak
A=	1057.42 ± 0.48	1307.103 ± 0.57
B=	$-9.02533\text{E-}4$	$-2.97208\text{E-}4$
C=	$-2.14529\text{E-}5$	$-2.1703\text{E-}5$

Comparing the frequency values at zero temperature obtained in table 7.3 (values for A) with other published values, Herschen *et al.* (1993) report $\nu_{\text{TO}}(0) = 1060.6 \pm 1.4 \text{ cm}^{-1}$ and $\nu_{\text{LO}}(0) = 1307.6 \pm 1.2 \text{ cm}^{-1}$, while Datchi *et al.* (2004) report $\nu_{\text{TO}}(0) = 1058.3 \pm 0.1 \text{ cm}^{-1}$. The latter paper comments that the inclusion of low temperature Raman data, as is the case with our results, will likely result in a decrease of the zero temperature values. This is in fact observed for the TO frequency. Datchi *et al.* (2004) did not report on the LO frequency as this peak was hidden in their experiments by the diamond Raman line from the anvils in their diamond anvil cell.

Previous studies have differed as to whether the peak position changes linearly (Alvarenga *et al.* 1992) or quadratically (Herchen *et al.* 1993) with temperature. As can be seen from figure 7.14 and 7.15, our results clearly confirm a quadratic relationship. The quadratic relationship is also very similar to that shown by the Raman peak of diamond (Herchen *et al.* 1991 and Zouboulis *et al.* 1991). The Raman shift change in our data between room temperature and 1173 K is 2.6% for the TO peak and 1.8% for the LO peak, while it is 2.7% and 1.7% respectively for the data of Herchen *et al.* (1993). The change in the diamond Raman peak position over the same temperature interval is 1.7% (Herchen *et al.* 1991).

In the following, the approach used by Herchen *et al.* (1993), Datchi *et al.* (2004) and Goncharov *et al.* (2005) is used to estimate the anharmonic contribution to the Raman shift. If ν_G is taken to be the Raman shift due to thermal expansion alone (refer to §3.1.6), then mode Grüneisen parameters can be used to predict this volume dependence of the frequency shift. It can be written as (Postmus *et al.* 1968)

$$\nu_G(T) = \nu(0) \exp \left[-3\gamma \int_0^T \alpha dT \right] \quad (7.1)$$

where γ is the TO- or LO-mode Grüneisen parameter, $\nu(0)$ is the Raman shift at $T = 0 \text{ K}$ and α is the linear thermal expansion coefficient. The values for $\nu(0)$ for the two modes are obtained from Table 7.3 (i.e. the quadratic fits extrapolated to $T = 0 \text{ K}$). Literature values for α are somewhat scarce. References mostly quote the data of Slack *et al.* (1975) and Vel *et al.* (1991), which are

fairly similar. The data given in the Landoldt-Börnstein (2001) data series is also that from Slack *et al.* (1975) for the high temperature data. Data from x-ray diffraction studies at high temperature and high pressure reported by Datchi *et al.* (2007) compares favourably with that of Slack *et al.* (1975), but only attains 950 K at ambient pressure as the focus of the study was on the combination of high pressure and temperature. Experiments by Datchi *et al.* (2007) found that $\gamma_{\text{TO}} = 1.257 \pm 0.005$ and Aleksandrov *et al.* (1989) measured $\gamma_{\text{TO}} = 1.188 \pm 0.002$. The data from Chen *et al.* (2003) suggests that α decreases with increasing temperature and have not been taken into consideration in further calculations.

As Slack *et al.* (1975) provides the largest number of data points by a single author, a cubic spline fit to this data was used along with the values $\gamma_{\text{TO}} = 1.2$ and $\gamma_{\text{LO}} = 0.9$ for the Grüneisen parameters. These are smaller than the parameters chosen by Herchen *et al.* (1993), which were $\gamma_{\text{TO}} = 1.5$ and $\gamma_{\text{LO}} = 1.2$. These authors based their choice on the data by Sanjurjo *et al.* (1983), and as discussed in §2.2.5.1 the overly optimistic value of the bulk modulus in this paper implies slightly higher values for the cBN Grüneisen parameters. The predicted shifts of the Raman peak positions of the cBN TO and LO peaks due to thermal expansion alone evaluated in this way are given by the green lines in figures 7.14 and 7.15. As the data from Slack *et al.* (1975) only attains 1200 K, the green curves are not extrapolated beyond this point. Very clearly thermal expansion alone cannot account for the observed data and an anharmonic (or self-energy) contribution has to be included. This is especially necessary at higher temperatures where the difference between the observed data and the shift due to thermal expansion alone increases.

If ν_{obs} is defined as the observed Raman shift, the anharmonic or self-energy contribution to the shift can be written as

$$\Delta\nu_{\text{an}} = \nu_{\text{obs}} - \nu_G. \quad (7.2)$$

This anharmonic shift corresponds to the integral of the second term of equation 3.30. Figure 7.16 gives the anharmonic contribution to the Raman shift calculated from the difference between the thermal expansion contribution (ν_G) and the quadratic fits to the observed data. It can be seen that the anharmonic contribution is definitely non-linear and very similar for both the TO and LO modes. This is different from Herchen *et al.* (1993) on two accounts. Firstly, Herchen *et al.* (1993) found that $\Delta\nu_{\text{anh}}$ can be approximated as a straight line within experimental error. Secondly the magnitude of $\Delta\nu_{\text{anh}}$ for the LO mode is less than that for the TO mode in Herchen *et al.* (1993) by roughly half over most of the temperature range when compared to our data. Apart from the different experimental data, the biggest difference between the calculation of $\Delta\nu_{\text{anh}}$ in figure 7.16 and that in Herchen *et al.* (1993) is the choice of Grüneisen parameters (see the

discussion above). It is not immediately clear if this alone will account for the observed differences, but more accurate and higher-temperature thermal expansion data would assist in clarifying the issue.

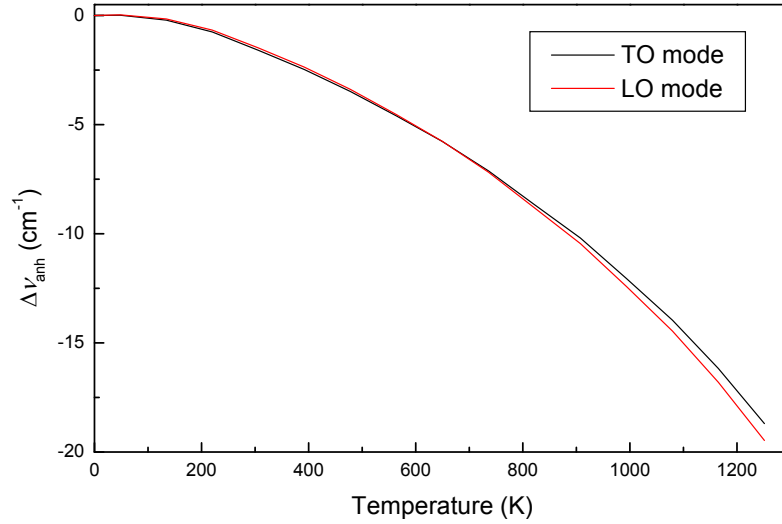


Figure 7.16: Variation of the anharmonic component of the Raman shift with temperature for the TO and LO modes of cBN.

Our results for the frequency shifts of the cBN Raman peaks with temperature thus compare very well with those of previous authors. Our measurements extend the data to low temperature. This does not change the primary conclusion that the shift of the peaks with temperature cannot be described by thermal expansion effects only, and that an anharmonic contribution is necessary to describe the observed data, especially at higher temperatures.

7.4.2 TO- and LO-mode linewidths

Figures 7.17 and 7.18 show the widths of the TO and LO peaks as a function of temperature. Solid lines are fits according to the 3-phonon (equation 3.32) and 3-and-4 phonon models (equation 3.33), respectively.

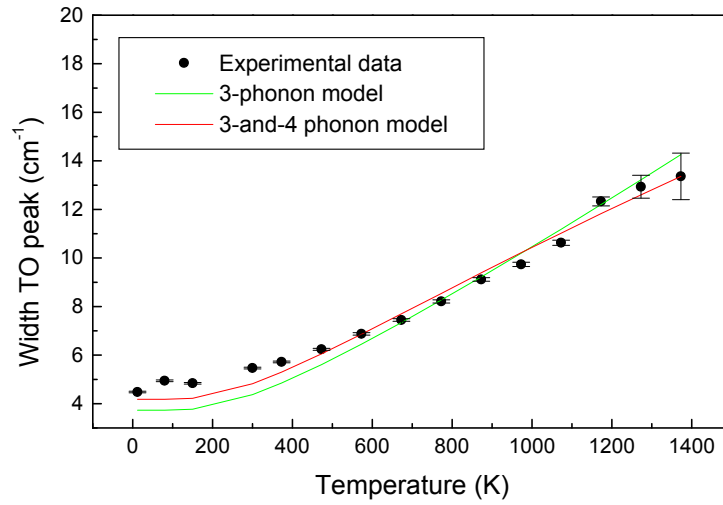


Figure 7.17: Width (FWHM) of TO Raman peak as a function of temperature. The coefficients A and B for the 3-and-4 phonon model (equation 3.33) are $A = 4.31 \text{ cm}^{-1}$ and $B = -0.129 \text{ cm}^{-1}$.

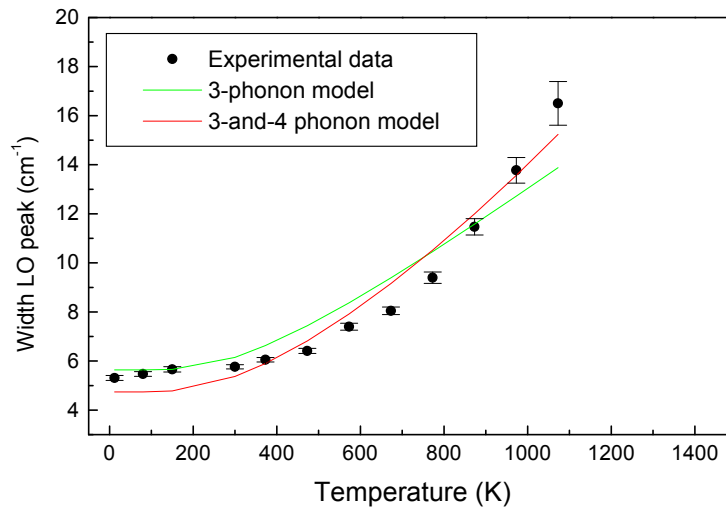


Figure 7.18: Width (FWHM) of LO Raman peak as a function of temperature. The coefficients A and B for the 3-and-4 phonon model (equation 3.33) are $A = 4.26 \text{ cm}^{-1}$ and $B = 0.483 \text{ cm}^{-1}$.

As can be seen in the above figures, the fit of the 3-and-4 phonon model is better than that of the 3-phonon only model, indicating the extension to four-phonon interactions is necessary to better account for the measured data. It is noted that at the highest temperatures measured for the LO peak in the present work there is some divergence between the data and the 3-and-4 phonon model. This demonstrates the need for higher order phonon interactions at these temperatures. Similar conclusions appear in the paper by Herschen *et al.* (1993).

7.5 Summary of results for cBN and PCBN

Raman spectroscopy was used to map the residual stresses and deformation associated with an indentation in a single crystal of cBN. The stress and deformation contours were clearly visualised by the Raman mapping, although the cracks associated with the indentation prevented the observation of similar detail as demonstrated for diamond (§5.1.1).

PL of defects introduced in electron-irradiated cBN crystals showed a range of ZPL peaks being introduced by the irradiation, and comparison of these peaks with literature shows that these are likely associated with intrinsic defects.

Raman and PL mapping of indentations in polycrystalline cBN did not show any clear residual stress, deformation patterns or introduction of defects. In the case of the Raman mapping this is likely due to the magnitude of the introduced stresses and deformation being comparable with that already existing in the PCBN. In the case of PL this may be due to the lack of diffusion of vacancies or other defects at the room temperature where the indentations were made.

The study of the effect of temperature on the Raman peaks of cBN showed clearly that thermal expansion alone is not sufficient to account for the shift of the peaks with temperature, and an anharmonic component must be included to more completely account for the experimentally observed data. The extension of Raman measurements to include spectra measured at liquid helium temperatures expanded the temperature range over which data has been reported, and its inclusion in the data set supports the inclusion of anharmonic effects.

Chapter 8: Conclusions and further work

In this thesis the optical spectroscopy techniques of Raman spectroscopy and photoluminescence (PL) spectroscopy have been applied to characterise two archetypal ultra-hard materials, these being diamond and cubic boron nitride (cBN). Appropriately used, these techniques are non-destructive methods for studying the stress and strain, degree of deformation and properties of luminescent defect centres in these materials.

Raman spectroscopy was the principal technique for the measurement of stress and degree of deformation in the crystal lattice, while PL spectroscopy played a strong complementary role in this regard through its ability to probe the luminescence defect centres in the crystal lattice.

8.1 Diamond-based materials

Studies were undertaken on single crystal synthetic type Ib diamond, as well as on the polycrystalline diamond (PCD) components of drillbits.

Raman spectroscopy of a plastic impression made at high temperature in single crystal diamond yielded contour maps of the residual stress distributions and degree of plastic deformation associated with these impressions, both on the surface of the diamond and along selected “slices” into the bulk of the diamond. This effectively resulted in a visualisation of the three-dimensional stress and deformation contours surrounding the impression. These contour maps were compared with predictions from elastic stress theory and a good correspondence was reported. Mapping of the PL due to nitrogen-vacancy defects associated with the impression yielded residual stress values in good agreement with Raman spectroscopy, and also illustrated the capability of PL to image defect centre distributions and plastic deformation in a material. These results were published in a paper in *Journal of Applied Physics* (Erasmus *et al.* 2011a).

Raman spectroscopy was applied to the study of residual stresses in the PCD layer that forms the working part of a drillbit. In prior work in our research group reviewed in § 6.1.3.1 and § 6.1.3.2 it was reported that the type of surface finishing applied to the PCD layer affected the magnitude of the residual compressive stress in the layer, with roughly lapped surfaces yielding

the largest residual compressive stress values and polished surfaces the smallest. It was also shown that the magnitude of the residual surface compressive stress decreases with increasing temperature. In the work presented in this thesis it was shown that repeated cycling of the toolbit to 600 °C has no influence on its stress state, but similar cycling to 800 °C leads to a permanent decrease in the residual surface compressive stress, implying a permanent degradation in the drillbit properties and thus its ability to behave as expected in a particular application environment. These results were published in a paper in the journal *Diamond and Related Materials* (Erasmus *et al.* 2011b).

8.1.1 Possible further work on diamond-based materials

In the Raman mapping of stress across the surface of the plastic impression, the focus was on the stress contours of the impression as a whole and how they related to the crystallographic structure of the single crystal. It would be interesting to focus on one of the arms of the rosette pattern to see if high spatial and spectral resolution Raman spectra can identify micron-sized areas of Raman peak splitting, indicating uni-axial stresses on a localised scale.

The extension of the PL maps to include 3D maps similar to those done with Raman spectroscopy would complement the existing Raman data and potentially image the detailed movement of dislocations during the deformation process in greater detail than that obtained via Raman spectroscopy.

The H3 defect was not readily apparent for the diamond used for the PL mapping, but impressions made on stones with higher nitrogen concentration has shown this defect to be present. It would be interesting to map the H3 defect in the volume surrounding an impression to compare with the 1.945 eV defect data and to find if any unique information can be obtained.

The studies by Daniel (2000) using the soft impressor technique have shown that the substitutional nitrogen concentration affects the hardness of diamond. It would be interesting to verify these results using optical spectroscopy by mapping stress and deformation contours of impressions made under similar conditions in diamonds with different substitutional nitrogen concentrations. It would also be possible to study the effect of substitutional boron on the mechanical properties of diamond by Raman mapping of plastic impressions in relevant diamond crystals.

8.2 cBN-based materials

Studies were undertaken on small (< 1 mm) cBN crystals, as well as polycrystalline cBN (PCBN).

Raman spectroscopy mapping of a room-temperature indentation in a single cBN crystal yielded a stress contour map as well as a deformation contour map associated with the indentation. The information obtained was not as detailed as in the case of diamond, due to the cracking associated with the room-temperature indentation, but nevertheless clearly illustrated the application of Raman mapping to cBN. This data was published in the journal *Diamond and Related Materials* (Erasmus *et al.* 2000).

PL mapping of the above-mentioned defect was also undertaken, but no clear ZPLs were visible in the low-temperature PL spectra. It was thus not possible to derive contour maps from PL as was the case with diamond. These results were also briefly discussed in Erasmus *et al.* (2000).

Both Raman and PL mapping of indentations in PCBN were attempted, but no clear contour maps could be obtained with either of these spectroscopy techniques. In the case of Raman mapping it appeared that the point-to-point fluctuations in residual surface stress and degree of plastic deformation present as a result of the sintering process undergone during synthesis were of the same order as the stresses introduced by the indentations, thus making it difficult to visualise the presence of the indentation via Raman mapping. In the case of PL spectroscopy the same constraint as for the single crystal work applied, namely the absence of clear ZPLs in the low-temperature spectra. The PCBN work was also briefly discussed in Erasmus *et al.* (2000).

PL spectroscopy of electron-irradiated single crystals of cBN was more successful, clearly showing a series of ZPLs associated with the irradiation damage in both black and amber-coloured cBN single crystals. Line shape analysis of several of these ZPL peaks showed a prevalence of line-type defects. These results were published in *physica status solidi (c)* (Erasmus *et al.* 2004).

Raman spectroscopy of cBN single crystals as a function of temperature was done over a wide temperature range from 4 K to 1373 K. The low temperature measurements extended the data previously reported in literature, as these data ranged from room to higher temperatures. It was concluded from the shift of Raman peak position with temperature that both linear expansion and anharmonic effects were required to adequately account for the observed data. This is in agreement with previously published findings. Both 3- and 4-phonon processes were required to

account for the observed linewidths as a function of temperature, again in agreement with literature.

8.2.1 Possible further work on cBN-based materials

The availability of good quality cBN single crystals of a size suitable for high temperature impressions made by means of the Soft Impressor Technique would greatly facilitate the Raman mapping of such impressions. Such detailed data would allow a proper comparison with both predictions from elastic stress theory and the results for diamond and highlight any potentially unique mechanical properties that cBN may have.

It would also be interesting to see if vacancy-related PL active defect centres form as in the case of diamond. Irradiation damage experiments show evidence for the presence of a stable and PL-active nitrogen vacancy or vacancy complexes, so there is potential for PL mapping of impressions in good quality crystals.

If dislocation movement alone during the impression process at higher temperature does not introduce PL-active defect centres, it may be necessary to introduce impurity atoms into the cBN lattice prior to the impression to facilitate the formation of stable PL-active defect complexes, analogous to the case of substitutional nitrogen in synthetic diamond.

References

- Ager J W, Veirs D K and Rosenblatt G M 1991 *Phys. Rev. B.* **43** 6491
- Ager J W and Drory D 1993 *Phys. Rev. B.* **48** 2601
- Akaishi M, Kanda H, Sato Y, Setaka N, Ohsawa T and Fukunaga O 1982 *J. Mat. Sci.* **17** 193
- Aleksandrov I V, Goncharov A F, Stishov S M and Yakovenko E V 1989 *JETP Lett.* **50** 127
- Alvarenga A D, Grimsditch M and Polian A 1992 *J. Appl. Phys.* **72** 1955
- Anastassakis E, Pinczuk A and Burstein E 1970 *Solid State Comm.* **8** 133
- Balkanski M, Wallis RF and Haro E 1983 *Phys. Rev. B* **28** 1928
- Baker J M 1998 *Diam. Relat.Mater.* **7** 1282
- Beard D R 1987 *An optical study of defects in diamond* (PhD Thesis: University of Reading)
- Bergman L and Nemanich R J 1995 *J. Appl. Phys.* **78** 6709
- Bernholc J, Kajihara S A, Wang C, Antonelli A and Davis R F 1992 *Mater. Sci. Eng.* **B11** 265
- Boppart H, van Straaton J and Silvera I F 1985 *Phys. Rev. B.* **32** 1423
- Borer W J, Mitra S S and Namjoshi D V 1971 *Solid State Comm.* **9** 1377
- Boteler J M and Gupta Y M 1993 *Phys. Rev. Lett.* **71** 3497
- Bourne R W 1989 *An Optical Study of Cubic Boron Nitride* (PhD Thesis: University of Reading)
- Boyd S R, Kiflawi I and Woods G S 1994 *Phil. Mag. B* **69** 1149
- Boyd S R, Kiflawi I and Woods G S 1995 *Phil. Mag. B* **72** 351
- Brafman O, Lengyel G, Mitra S S, Gielisse P J, Plendl J N and Mansur L C 1968 *Solid State Comm.* **6** 523
- Bridgman P W 1950 *Proc. Roy. Soc. London A* **203** 1
- Brookes C A 1979 in *The Properties of Diamond* ed. JE Field (London: Academic Press)
- Brookes C A 1986 *Inst. Phys. Conf. Ser. No.* **75**, 207
- Brookes C A, Hooper R M and Lambert W A 1983 *Phil. Mag.* **A47** 9
- Brookes C A, Brookes E J, Howes V R, Roberts S G and Waddington C P 1990 *J. Hard Mater.* **1** 3
- Brookes C A 1992a in *The Properties of Natural and Synthetic Diamond* ed. JE Field (London: Academic Press) p. 515

- Brookes E J 1992b *The Plasticity of Diamond* (PhD Thesis: The University of Hull)
- Brookes E J, Collins A T and Woods G S 1993 *J. Hard. Mater.* **4** 97
- Brookes E J, Comins J D, Daniel R D and Erasmus R M 2000 *Diam. Relat. Mater.* **9** 1115
- Brookes E J and Daniel R D 2001 in *Properties, Growth and Applications of Diamond* ed. MH Nazaré and AJ Neves (London: INSPEC, The Institution of Electrical Engineers) p. 142
- Brüesch P 1982 in *Phonons: Theory and Experiments I* (New York: Springer-Verlag)
- Brüesch P 1986 *Phonons: Theory and Experiments II* (Berlin Heidelberg: Springer-Verlag)
- Bundy F P and Wentorf R H 1963 *J. Chem. Phys.* **38** 1144
- Bundy F P 1980 *J. Geophys. Res. Solid Earth* **85** 6930
- Burenkov A F, Varychenko V S, Zaitsev A M, Komarov F F, Konoplyanik G G, Melnikov A A, Stelmakh V F and Tkachev V V 1989 *Phys. Stat. Sol. (a)* **115** 427
- Burns R C, Cvetkovic V, Dodge C N, Evans D J F, Rooney M T, Spear P M and Welbourn C M 1990 *J. Cryst. Growth* **104** 257
- Burns R C and Davies G J 1992 in *The Properties of Natural and Synthetic Diamond* ed. JE Field (London: Academic Press) p.395
- Campbell I H and Fauchet P M 1986 *Solid State Comm.* **58** 739
- Cardona M and Anastassakis E 1996 *Phys. Rev. B* **54** 14888
- Castineira J L P, Leite J R, Scolfaro L M R, Enderlein R, Alves J L A and Leite Alves H W 1998 *Mat. Sci. Eng. B* **51** 53
- Catledge S A and Vohra Y K 1995 *J. Appl. Phys.* **78** 7053
- Catledge S A, Vohra Y K, Ladi R and Rai G 1996 *Diam. Relat. Mater.* **5** 1159
- Chen J, Xu X, Yuan B, Deng J and Xing X 2003 *Acta Metallurgica Sinica* **39** 952
- Chrenko R M, Strong H M and Tuft R E 1971 *Phil. Mag.* **23** 313
- Chrenko R M, Tuft R E and Strong H M 1977 *Nature* **270** 141
- Clark C D, Collins A T and Woods G S 1992 in *The Properties of Natural and Synthetic Diamond* ed. JE Field (London: Academic Press) p.35
- Collins A T 1979 *Inst. Phys. Conf. Ser.* **46** 327
- Collins A T 1980 *J. Phys. C* **13** 2641
- Collins A T and Robertson S H 1985 *J. Mater. Sci. Lett.* **4** 681
- Collins A T 1991 *New Diamond Science and Technology MIRS Int. Conf. Proc.* 659
- Collins A T 1992 *Diam. Relat. Mater.* **1** 457
- Collins A T 1993 *Physica* **B185** 284
- Collins A T 1999 *Diam. Relat. Mater.* **8** 1455

- Comins J D, Erasmus R M, Mofokeng V, Martin Z 2001 *Proceedings of the Sixth Applied Diamond Conference / Second Frontier Carbon Technology Joint Conference (ADC/FCT 2001)* ed. Y Tzeng, K Miyoshi, M Yoshidawa, M Murakawa, Y Koga, K Kobashi and GAJ Amaratunga p376
- Corrigan F R and Bundy F P 1975 *J. Chem. Phys.* **63** 3812
- Crawford F S Jr 1968 *Waves: Berkeley Physics Course Vol 3* (New York: McGraw-Hill) p.376
- Daniel R D 2000 *The Influence of Nitrogen on the Plasticity of Diamond* (PhD Thesis: The University of Hull)
- Datchi F and Canny B 2004 *Phys. Rev. B* **69** 144106
- Datchi F, Dewaele A, Le Godec Y and Loubeyre P 2007 *Phys. Rev. B* **75** 214104
- Davey S T, Evans T and Robertson S H 1984 *J. Mater. Sci. Lett.* **3** 1090
- Davies G 1970 *J. Phys. C* **3** 2474
- Davies G 1971 *J. Phys. D* **4** 1340
- Davies G 1972 *J. Phys. C* **5** 2534
- Davies G 1976a *J. Phys. C* **9** L537
- Davies G, Nazaré M H and Hamer M F 1976b *Proc. R. Soc. Lond.* **A351** 245
- Davies G and Hamer M F 1976c *Proc. R. Soc. Lond.* **A348** 285
- Davies G 1979 *J. Phys. C: Solid State* **12** 2551
- Davies G, Lawson S C, Collins A T, Mainwood A and Sharp S J 1992 *Phys. Rev. B.* **46** 13157
- Davies G and Collins A T 1993 *Diam. Relat. Mater.* **2** 80
- Dekker A J 1970 *Solid State Physics* (London: MacMillan & Co) p.65 and p.160
- Demazeau G 1993 *Diam. Relat. Mater.* **2** 197
- Dodge C N 1986 *An optical study of sintered and black diamond* (PhD Thesis: University of Reading)
- Dyer H B and du Preez L 1965 *J. Chem. Phys.* **42** 1898
- Era K and Mishima O 1990 *Mat. Res. Soc. Symp. Proc.* **162** 555
- Erasmus R M, Comins J D and Fish M L 2000 *Diam. Relat. Mater.* **9** 600
- Erasmus R M and Comins J D 2004 *Phys. Stat. Sol. (c)* **1** 2269
- Erasmus R M, Daniel R D and Comins J D 2011a *J. Appl. Phys.* **109** 013527
- Erasmus R M, Comins J D, Mofokeng V and Martin Z 2011b *Diam. Relat. Mater.* **20** 907
- Eremets M I, Gauthier M, Polian A, Chervin J C, Besson J, Dubitskii G A and Semenova Y Y 1995 *Phys. Rev. B* **52** 8854

- Evans D A, McGlynn A G, Towlson B M, Gunn M, Jones D, Jenkins T E, Winter R and Poolton NRJ 2008 *J.Phys.: Condens. Matter* **20** 075233
- Evans T and Phaal C 1962 *Proc. R. Soc. Lond.* **A270** 538
- Evans T 1967 In *Science and Technology of Industrial Diamond* (J. Burls ed) pp 105-118
Industrial Diamond Information Bureau, London
- Evans T, Qi Z and Maguire J 1981 *J. Phys. C* **14** L379
- Evans T, Davey S T and Robertson S H 1984 *J. Mater. Sci.* **19** 2405
- Fahy S 1995 *Phys. Rev. B* **51** 12873
- Fahy S 1996 *Phys. Rev. B* **53** 11884 (E)
- Fahy S, Taylor C A and Clarke R 1997 *Phys. Rev. B* **56** 12573
- Field J E 1979 *The Properties of Diamond* ed. JE Field (London: Academic Press)
- Field J E 1991 *Surface and Coatings Technology* **47** 631
- Field J E 1992a in *The Properties of Natural and Synthetic Diamond* ed. JE Field (London: Academic Press) p. 667
- Field J E 1992b in *The Properties of Natural and Synthetic Diamond* ed. JE Field (London: Academic Press) p. 473
- Fish M L 1995 *Optical properties of synthetic diamond of different syntheis origin* (MSc Thesis: The Universtiy of the Witwatersrand)
- Fish M L and Comins J D 1997 *Mater. Sci. Forum* **239-241** 103
- Fish M L, Massler O, Reid J A, MacGregor R and Comins J D 1999 *Diam. Relat. Mater.* **8** 1511
- Frank F C, Lang A R, Evans D J F, Rooney M-L T, Spear P M and Welbourn C M 1990 *J. Cryst. Growth* **100** 354
- Gielisse P J, Mitra S S, Plendl J N, Griffis R D, Mansur L C, Marshall R and Pascoe E A 1967 *Phys. Rev.* **155** 1039
- Goncharov A F, Crowhurst J C, Dewhurst J K and Sharma S 2005 *Phys. Rev. B* **72** 100104(R)
- Goss J P, Coomer B J, Jones R, Fall C J, Latham C D, Briddon P R and Öberg S 2000 *J. Phys.: Condens. Matter* **12** 10257
- Goss J P, Coomer B J, Jones R and Fall C J 2003 *Phys. Rev. B* **67** 165208
- Griffith W P 1975 in *Infrared and Raman Spectroscopy of Lunar and Terrestrial Minerals* ed. C Karr (New York: Academic Press)
- Grimsditch M H, Anastassakis E and Cardona M 1978 *Phys Rev B* **18** 901
- Grimsditch M H, Zouboulis E S and Polian A 1994 *J. Appl. Phys.* **76** 832
- Gubanov V A, Lu Z W, Klein B M and Fong C Y 1996a *Phys. Rev. B* **53** 4377

- Gubanov V A, Hemstreet L A, Fong C Y and Klein B M 1996b *Appl. Phys. Lett.* **69** 227
- Gupta Y M, Horn P D and Yoo C S 1989 *Appl. Phys. Lett.* **55** 33
- Hall H T 1960 *Rev. Sci. Instrum.* **31** 125
- Haines J, Léger J M and Bocquillon G 2001 *Annu. Rev. Mater. Res.* **31** 1
- Hanfland M, Syassen K, Fahy S, Louie S G and Cohen M L 1985 *Phys. Rev. B* **31** 6896 (Rapid Comm.)
- Hanley P L, Kiflawi I and Lang A R 1977 *Phil. Trans. R. Soc.* **A284** 329
- Harris J W 1992 in *The Properties of Natural and Synthetic Diamond* ed. J E Field (London: Academic Press) p. 345
- Harris T K 1997 *The Mechanical Properties of Ultrahard Materials at Elevated Temperatures* (PhD Thesis: The University of Hull)
- Harris T K, Brookes E J and Daniel R D 2001 *Diam. Relat. Mater.* **10** 755
- Hart T R, Aggarwal R L and Lax B 1970 *Phys. Rev. B* **1** 638
- Henderson B 1972 *Defects in Crystalline Solids* (London: Edward Arnold)
- Herchen H and Cappelli M A 1991 *Phys. Rev. B* **43** 11740
- Herchen H and Cappelli M A 1993 *Phys. Rev. B* **47** 14193
- Hofsäss H, Ronning C, Griesmeier U and Gross M 1995 *Appl. Phys. Lett.* **67** 46
- Howard I A 1996 *Solid State Comm.* **99** 697
- Iakoubovskii K, Adriaenssens G J and Nesladek M 2000a *J. Phys.: Condens. Matter* **12** 189
- Iakoubovskii K, Adriaenssens G J 2000b *Phys. Stat. Sol. (a)* **181** 59
- Ichiki T and Yoshida T 1994 *Appl. Phys. Lett.* **64** 851
- Jobin-Yvon 1992 *T64000 System User Manual* Part. No. 31 087 018
- Kádas K, Kern G and Hafner J 1998 *Phys. Rev. B* **58** 15636
- Kaiser W and Bond W L 1959 *Phys. Rev.* **115** 857
- Keresztury G 2002 in *Handbook of Vibrational Spectroscopy, Volume 1: Theory and Instrumentation* ed. J M Chalmers and P R Griffiths (Chichester: John Wiley & Sons)
- Kern G 1998 *Clean and hydrogenated diamond and graphite surfaces* (PhD Thesis: Technische Universität Wien)
- Kern G, Kresse G and Hafner J 1999 *Phys. Rev. B* **59** 8551
- Kiflawi I, Mayer A E, Spear P M, van Wyk J A and Woods G S 1994 *Phil. Mag. B* **69** 1141
- Klein M V 1990 in *Dynamical Properties of Solids* ed. G K Horton and A A Maradudin (Amsterdam: North-Holland)
- Knittle E, Wentzcovitch R M, Jeanloz R and Cohen M L 1989 *Nature* **337** 349

- Landoldt-Börnstein, Zahlenwerte und Funktionen 2001 New Series Group III **41A1a** page
- Landsberg G and Mandelstam L 1928a *Naturwissenschaften* **16** 557
- Landsberg G and Mandelstam L 1928b *Z. Phys.* **50** 769
- Lang A R, Moore M and Walmsley J C 1992 in *The Properties of Natural and Synthetic Diamond* ed. JE Field (London: Academic Press) p. 215
- Larson G 1984 *The Far Side Gallery* (Andrews McMeel Publishing)
- Lin T P, Hood M, Cooper GA and Smith RH 1994 *J. Am. Ceram. Soc.* **77** 1562
- Linkam Scientific Instruments 1997 *Stage Reference Manual* Issue 2: 21-04-97
- Loubser J H N and van Wyk J A 1977 *Diamond Research* (London: Industrial Diamond Information Bureau) 16
- Loubser J H N and van Wyk J A 1981 *Diamond Conference Reading* (unpublished)
- Love A E H 1929 *Phil. Trans. Roy. Soc. London A* **228** 377
- Lukomskii A I, Shipilo V B, Shishonok E M and Anichenko N G 1987 *Phys. Stat. Sol. (a)* **102** K137
- Marcuse D 1980 *Principles of Quantum Electronics* (New York: Academic Press)
- Martin Z 1999 *Raman Studies into the Behaviour of Different Types of Deformation in Polycrystalline Diamond* (MA degree: University of Oxford)
- McCormick T L, Jackson W E and Nemanich R J 1994 *Mat. Res. Soc. Symp. Proc.* **349** 445
- Mishima O, Yamaoka S and Fukunaga O 1987 *J. Appl. Phys.* **61** 2822
- Mishima O 1990 *Mat. Res. Soc. Symp. Proc.* **162** 543
- Mita Y 1996 *Phys. Rev. B* **53** 11360
- Mitra S S, Brafman O, Daniels W B and Crawford R K 1969 *Phys. Rev.* **186** 942
- Mohammed K, Davies G and Collins A T 1982 *J. Phys. C: Solid State Phys.* **15** 2779
- Mohrbacher H, Van Acker K, Blanpain B, Van Houtte P and Celis J-P 1996 *J. Mater. Res.* **11** 1776
- Mossbrucker J and Grotjohn T A 1997 *J. Vac. Sci. Technol. A* **15** 1206
- Mosuang T E and Lowther J E 2002a *J. Phys. Chem. Solids* **63** 363
- Mosuang T E and Lowther J E 2002b *Phys. Rev. B* **66** 014112
- Nabarro F R N 1967 *Theory of Crystal Dislocations* (Oxford: Clarendon Press) chp 6
- Nassau K and Nassau J 1979 *J. Cryst. Growth* **46** 157
- Nemanich R J, Solin S A and Martin R M 1981 *Phys. Rev. B.* **23** 6348
- Newton M E, Campbell B A, Twitchen D J, Baker J M and Anthony T R 2002 *Diam. Relat. Mater.* **11** 618

- Notsu Y, Nakajima T and Kawai N 1977 *Mat. Res. Bull.* **12** 1079
- Novikov N V, Bondarenko V P, Kocherzhinskii Y A, Belyanika A V, Gerasimenko V K, Stolyarov E V and Tovstogan V M 1985 *Sverkhtverdye Materialy* **7** 17
- Nugent K W and Prawer S 1998 *Diam. Relat. Mater.* **7** 215
- Orth D L, Mashl R J and Skinner J L 1993 *J. Phys.: Condens. Matter* **5** 2533
- Oxford Instruments Limited 1988 *Instruction Manual for Continuous Flow Cryostat CF1204*
- Parsons B J 1977 *Proc. R. Soc. Lond.* **A352** 397
- Petrescu M I 2004 *Diam. Related. Mater.* **13** 1848
- Pipkin N J 1980 *J. Mat. Sci.* **15** 2651
- Prins J F, Derry T E and Sellschop J P F 1986 *Phys. Rev. B* **34** 8870
- Ponahlo J 1992 *J. Gemm.* **23** 3
- Postmus C, Ferraro J R and Mitra S S 1968 *Phys. Rev.* **174** 983
- Raman C V 1928 *Indian J. Phys.* **2** 387
- Raman C V and Krishnan K S 1928 *Nature* **121** 501
- Rammutla K E 2001 *Light scattering and computational studies on superionic compounds* (PhD thesis: University of the Witwatersrand, Johannesburg)
- Read W T 1953 *Dislocations in Crystals* (New York: McGraw-Hill) chp 6
- Richter H, Wang Z P and Ley L 1981 *Solid State Commun.* **39** 625
- Roberts S G 1988 *Phil. Mag. A* **58** 347
- Sachdev H, Haubner R, Nöth H and Lux B 1997 *Diam. Relat. Mater.* **6** 286
- Sanjurjo J A, Lopez-Cruz E, Vogl P and Cardona M 1983 *Phys. Rev. B* **28** 4579
- Satoh S, Nakashima T, Tsuzuji K and Yazu S 1990 *High Pressure Research* **5** 926
- Sawaoka A and Akashi T 1984 *Mat. Res. Soc. Symp. Proc.* **24** 365
- Sekkal W, Bouhafis B, Aourag H and Certier M 1998 *J. Phys.: Condens. Matter* **10** 4975
- Sellschop J P F 1992 in *The Properties of Natural and Synthetic Diamond* ed. JE Field (London: Academic Press) p. 81
- Sharma S K, Mao H K, Bell P M and Xu J A 1985 *J. Raman Spec.* **16** 350
- Shipilo V B, Rud A E, Leushkina G V, Kuzmin V S and Ugolev I I 1987 *Inorganic Materials* **23** 1751
- Shipilo V B, Shishonok E M, Zaitsev A M, Melnikov A A and Olekhovich A I 1988a *Phys. Stat. Sol. (a)* **108** 431
- Shipilo V B, Shishonok E M, Zaitsev A M, Melnikov A A and Olekhovich A I 1988b *J. Applied Spectroscopy* **49** 947

- Shipilo V B, Shishonok E M, Zaitsev A M, Anichenko N G and Unyarkha L S 1990 *Inorganic Materials* **26** 1404
- Shishonok E M, Shipilo V B, Lukomskii A I and Rapinchuk T V 1989 *Phys. Stat. Sol. (a)* **115** K237
- Shishonok E M and Steeds J W 2002 *Diam. Related. Mater.* **11** 1774
- Shishonok E M and Steeds J W 2004 *Phys. Solid State* **46** 1011
- Slack G A and Bartram S F 1975 *J. Appl. Phys.* **46** 89
- Sobolev E V, Lenskaya S V and Lisoivan V I 1968 *J. Struct. Chem.* **9** 917
- Solin S A and Ramdas A K 1970 *Phys. Rev. B.* **1** 1687
- Solozhenko V L 1988 *Dokl. Phys. Chem.* **301** 592
- Solozhenko V L, Chernyshev V V, Fetisov G V, Rybakov V B and Petrusha I A 1990 *J. Phys. Chem. Solids* **51** 1011
- Solozhenko V L 1994 *Diam. Relat. Mater.* **4** 1
- Solozhenko V L 1995 *J. Hard Mater.* **6** 51
- Stoneham AM 1969 *Rev. Mod. Phys.* **41** 82
- Strong H M 1989 *Am. J. Phys.* **57** 794
- Sumida N and Lang A R 1981 *Inst. Phys. Conf. Ser. No. 60: Section 6* 319
- Susa K, Kobayashi T and Taniguchi S 1974 *Mater. Res. Bull.* **9** 1443
- Tani E, Soma T, Sawaoka A and Saito S 1975 *Jpn. J. Appl. Phys.* **10** 1605
- Thorne A P 1988 *Spectrophysics* (2nd ed.) (London: Chapman and Hall)
- Tkachev V D, Shipilo V B and Zaitsev A M 1985a *Phys. Stat. Sol. (b)* **127** K65
- Tkachev V D, Shipilo V B and Zaitsev A M 1985b *Sov. Phys. Semicond.* **19** 491
- Uehara K and Yamaya S 1988 *Int. J. Refract. Met. Hard Mater.* **7** 219
- Van Camp P E, Van Doren V E and Devreese J T 1989 *Solid State Comm.* **71** 1055
- Van Camp P E, Van Doren V E and Devreese J T 1992 *Solid State Comm.* **84** 731
- Vel L, Demazeau G and Etourneau J 1991 *Mat. Sci. Eng. B* **10** 149
- Von Enkevort W J P and Lochs H G M 1988 *J. Appl. Phys.* **64** 434
- Wakatsuki M, Ichinose K and Aoki T 1972 *Mater. Res. Bull.* **7** 999
- Wakatsuki M 1984 *Materials science of the earth's interior* ed I Sunagawa (Tokyo: Terra Scientific Publishing Company)
- Walker J 1979 *Rep. Prog. Phys.* **42** 1605
- Watts R K 1977 *Point defects in crystals* (New York: John Wiley & Sons)
- Webb S W and Jackson W E 1995 *J. Mater. Res.* **10** 1700

- Wentorf R H 1957 *J. Chem. Phys.* **26** 956
- Wentorf R H 1959 *J. Phys. Chem.* **63** 1934
- Wentorf R H 1961 *Chem. Eng.* **68** 177
- Wentorf R H 1965 *Advances in chemical physics* **9** ed I Prigogine (New York: Interscience Publishers)
- Werninghaus T, Hahn J, Richter F and Zahn D R T 1997a *Appl. Phys. Lett.* **70** 958
- Werninghaus T, Friedrich M, Hahn J, Richter F and Zahn D R T 1997b *Diam. Relat. Mater.* **6** 612
- Whalley E, Lavergne A and Wong P 1976 *Rev. Sci. Instrum.* **47** 845
- Whiting E E 1968 *J. Quant. Spectrosc. Radiat. Transfer* **8** 1379
- Woods G S and Lang A R 1975 *J. Cryst. Growth* **28** 215
- Yamamoto N, Spence J C H and Fathy D 1984 *Phil. Mag. B* **49** 609
- Yazu S, Sumiya H and Degawa J 1986 *Eur. Patent* 0,220,462
- Zaitsev A M, Shipilo V B, Shishonok E M and Melnikov A A 1986a *Phys. Stat. Sol. (a)* **95** K29
- Zaitsev A M, Melnikov A A, Shipilo V B and Shishonok E M 1986b *Phys. Stat. Sol. (a)* **94** K125
- Zaitsev A M, Mel'nikov A A and Stel'makh V F 1987 *Sov. Phys. Semicond.* **21** 671
- Zaitsev A M, Ulyashin A G and Husein Ali Nur 1991 *Sverkhtverdye Materialy* **13** 18
- Zaitsev A M 1992 *Mat. Sci. Eng. B* **11** 179
- Zaitsev A M 2001 *Optical Properties of Diamond: A Data Handbook* (Berlin: Springer)
- Zhang W J, Jiang X and Matsumoto S 2001 *Appl. Phys. Lett.* **79** 4530
- Zouboulis E S and Grimsditch M 1991 *Phys. Rev. B* **43** 12490

Appendix: Copies of published papers

This appendix contains copies of the papers published from the research contained in this thesis.

In chronological order these papers are:

- 1) Erasmus R M, Comins J D and Fish M L 2000 *Diam. Relat. Mater.* **9** 600
- 2) Erasmus R M and Comins J D 2004 *Phys. Stat. Sol. (c)* **1** 2269
- 3) Erasmus R M, Daniel R D and Comins J D 2011 *J. Appl.Phys.* **109** 013527
- 4) Erasmus R M, Comins J D, Mofokeng V and Martin Z 2011 *Diam. Relat. Mater.* **20** 907

Raman and photoluminescence spectra of indented cubic boron nitride and polycrystalline cubic boron nitride

R.M. Erasmus^{a,*}, J.D. Comins^a, M.L. Fish^b

^a Department of Physics, University of the Witwatersrand, Private Bag 3, Johannesburg WITS, 2050, South Africa

^b De Beers Diamond Research Laboratory, PO Box 1770, Southdale, 2135, South Africa

Abstract

The use of Raman spectroscopy, and in particular Raman line shifts, to measure stress in diamond and nitrides such as gallium nitride (GaN), is well known. In both diamond and GaN the application is principally to study stresses in thin films and at the substrate–thin film interface. Stresses in polycrystalline diamond composites have also been measured by this method. Typically stresses of the order of GPa can be determined with a spatial resolution of a few micrometers. In this paper, Raman spectra of indentations on cubic boron nitride (cBN) crystals and polycrystalline cubic boron nitride (PcBN) composites are presented. Shifts of the cBN Raman lines from their unstressed positions quantify the residual stresses in the boron nitride due to the deformation brought about by the indentation. Making use of the measured coefficient of shift of $3.39 \text{ cm}^{-1}/\text{GPa}$ for the transverse optical Raman peak, these are of the order of 1 GPa. These measurements illustrate, for the first time, the use of Raman spectroscopy to study residual stresses in boron nitride. Plastic deformation is usually associated with the creation of vacancies. To investigate the possible presence of vacancy defects and vacancy-related defects, the indented boron nitride samples were also studied with photoluminescence spectroscopy. © 2000 Published by Elsevier Science S.A. All rights reserved.

Keywords: Carbides; Nitrides; Plastic deformation; Raman spectroscopy; Stress

1. Introduction

Cubic boron nitride (cBN) is well known in industrial applications due to its unique mechanical and physical properties [1]. In their working environment, tools made from cBN are subjected to various stresses and strains. Examples of such tools are grinding and polishing wheels, and shaped toolbits cut from sintered polycrystalline cubic boron nitride (PcBN) composites. The stresses and strains present in cBN tools play an important role in determining how these tools will perform in a particular application. For example, a tool with a surface under compressive stress will be better able to withstand repeated impacts than a surface under tensile stress. It is thus important from an applications point of view to be able to determine the nature and size of stresses present in such cBN tools. The presence of stresses (and strains) in a material manifests itself as a shift of the Raman lines(s) from their unstressed posi-

tions. In the case of diamond, stresses in both polycrystalline diamond (PCD) and thin diamond films have been measured via Raman spectroscopy [2–5].

The degree of strain-induced shift for the infrared absorption peaks of cBN has been calculated by Fahy [6,7] and Cardona and Anastassakis [8], and applied to cBN films by Fahy et al. [9]. The degree of strain-induced shift for the cBN transverse optical (TO) and longitudinal optical (LO) Raman lines has been measured in a diamond anvil cell by Sanjurjo et al. [10]. The reported stress dependence of the Raman lines was $(d\omega/dp)_{\text{TO}} = 3.39 \pm 0.08 \text{ cm}^{-1}/\text{GPa}$ and $(d\omega/dp)_{\text{LO}} = 3.45 \pm 0.07 \text{ cm}^{-1}/\text{GPa}$. In the literature, strain in cBN thin films has been measured via the radial curvature method [11] and infrared absorption methods [9]. X-ray diffraction techniques [12] have been applied to diamond coatings. The use of Raman spectroscopy to measure the residual stresses in cBN has not yet been reported, so far as we know. In this paper, the use of Raman spectroscopy to measure residual stresses in cBN and PcBN is illustrated.

The information of interest contained in the Raman spectra of cBN is the position of the Raman lines (in

* Corresponding author.

E-mail address: erasmus@physnet.phys.wits.ac.za (R.M. Erasmus)

cm^{-1}) and their full width at half maximum (FWHM). The positions of the unstressed TO and LO Raman lines for cBN are experimentally determined as $1054.7 \pm 0.6 \text{ cm}^{-1}$ and $1305 \pm 1 \text{ cm}^{-1}$ respectively [10]. The stress dependence coefficients of the Raman lines, which relate the shift of the lines to the stress giving rise to the shift, as measured by Sanjurjo et al. [10], compare well with the values calculated from

$$\frac{d\omega_i}{dp} = \gamma_i \frac{\omega_i}{B_0}, \quad (1)$$

where ω_i is the position of the unstressed Raman line, γ_i is the mode Grüneisen parameter associated with the particular lattice phonon, and B_0 is the bulk modulus of the material. Different values have been published for γ_i and B_0 , both experimental and calculated. Taking the values of ω_i as quoted above, $\gamma_{\text{TO}}=1.2$ and $\gamma_{\text{LO}}=0.9$ as calculated by Kern [13], and $B_0=369 \pm 14 \text{ GPa}$ as measured by Knittle et al. [14], $d\omega_{\text{TO}}/dp=3.43 \text{ cm}^{-1}/\text{GPa}$ and $d\omega_{\text{LO}}/dp=3.18 \text{ cm}^{-1}/\text{GPa}$ are obtained, in close agreement with the measured values. For the purposes of this paper, the measured values of $d\omega/dp$ in Ref. [10] are used.

The above stress-induced shifts of the Raman lines are applicable in the case of hydrostatic (isotropic) stresses in the cBN lattice. In the case of diamond thin films and PCD layers sintered on a tungsten carbide backing, a biaxial stress model [3] is often invoked due to the lattice and thermal mismatch between layer and substrate. In the presence of large stress values, a biaxial stress model gives rise to the splitting of the triply degenerate diamond Raman line into a singlet and a doublet [3,4]. For the cBN samples in this study, the application of a biaxial stress model to the results was unnecessary. The single cBN crystal is not constrained by a substrate, nor are the PcBN squares, as these are solid blocks of sintered cBN with no backing. The stress distribution in the cBN samples is thus assumed to be approximately hydrostatic.

The main mechanisms applicable to the broadening of the Raman linewidth are homogeneous broadening and broadening due to size effects of the crystal under study. The latter mechanism is due to phonon confinement in a small domain size and has been shown to give rise to a Raman peak shift to lower frequency and to an asymmetric line shape [15,16]. The theory of homogeneous spectral line shape predicts that the linewidth is inversely proportional to the phonon lifetime and that the line shape is expected to be Lorentzian. A discussion on the presence of broadening in the results is presented in a later paragraph.

Photoluminescence (PL) studies of cBN have previously been carried out by Bourne [17]. While zero phonon lines (ZPLs) were not reported in all types of

samples, virtually all samples exhibited two broad luminescence peaks centred at 4692 and 3692 Rcm^{-1} relative to the excitation frequency of 488.0 nm. These peaks were labelled band **A** and band **B** respectively. In some cases a shoulder was visible on the **B** band at 4492 Rcm^{-1} , with simultaneous shift of the centre of the band to 3392 Rcm^{-1} . It was suggested that band **B** was, in effect, a broad spectral feature with at least two components and with the intensity of the constituent components varying with sample and processing conditions.

Plastic deformation is associated with the creation of vacancies in the lattice via the mechanism of non-conservative dislocation slip. It is expected that these vacancies will give rise to vacancy-related PL active defect systems. In order to study these PL active defects introduced via plastic deformation, PL spectra of cBN crystals were measured before and after irradiation with electrons (nominal dose of $8 \times 10^{17} \text{ cm}^{-2}$ and energy of 1.9 MeV). Any PL defects appearing after irradiation are likely to be vacancy related, and can thus be compared with features measured in the spectra of plastically deformed crystals.

2. Experimental details

The cBN samples studied were in the form of small, faceted single crystals, or PcBN in the shape of small squares of $\sim 10 \text{ mm}$ side length. The single crystals varied in size from $\sim 360 \mu\text{m}$ diameter to $\sim 1 \text{ mm}$ diameter and in colour from dark yellow to black. The polycrystalline samples contained $\sim 95\%$ cBN, with the balance made up of binder material. The samples were supplied with surfaces polished to a reflective finish.

Raman and PL spectra were acquired with a Jobin-Yvon T64000 Raman spectrometer operated in single spectrograph mode with an 1800 grooves/mm grating and a CCD detector. The 488.0 nm line of a coherent argon ion laser was used as the excitation frequency. Spectra were acquired with a confocal micro-Raman attachment, where the laser beam was focused down to either a $25 \mu\text{m}$ diameter spot or a $10 \mu\text{m}$ diameter spot. A motorised X-Y microscope stage was used to obtain high resolution maps at specific frequencies of the samples under study.

The PL spectra were acquired with the samples mounted in a continuous flow liquid helium microscope cryostat. All PL spectra were measured at less than 10 K, as it was found that this gave the highest resolution of the peaks.

Indents were made with PCD conical indentors, the tip of which was ground to a fine point and then very lightly sanded down to a flat of the order of $100 \mu\text{m}$ diameter. The indentations were made by lowering the

tip into the sample at a fixed rate and then releasing the load when a predetermined value was reached.

As the exact position of the TO Raman peak is of importance in determining the nature and magnitude of stressed measured, the spectrograph was carefully calibrated before each set of acquisitions on the 1056.94 Rcm^{-1} laser plasma line. During acquisition, this laser line was removed by means of an interference filter in order to prevent it distorting the position and shape of the cBN TO Raman peak.

3. Results and discussion

The work on single crystal samples will be discussed first, followed by the results for the polycrystalline samples. The indentations on the single crystals were technically difficult to make, since the samples were very small and the indentation could not always be centred on the sample as desired. Raman spectra were acquired as described in the previous section and Fig. 1a is a typical example of such a spectrum. The peak positions and FWHM of our data are in good agreement with the Raman data on one of the samples of cBN measured by Sachdev et al. [19]. Our Raman spectrum is of better quality and does not exhibit the extra peaks attributed

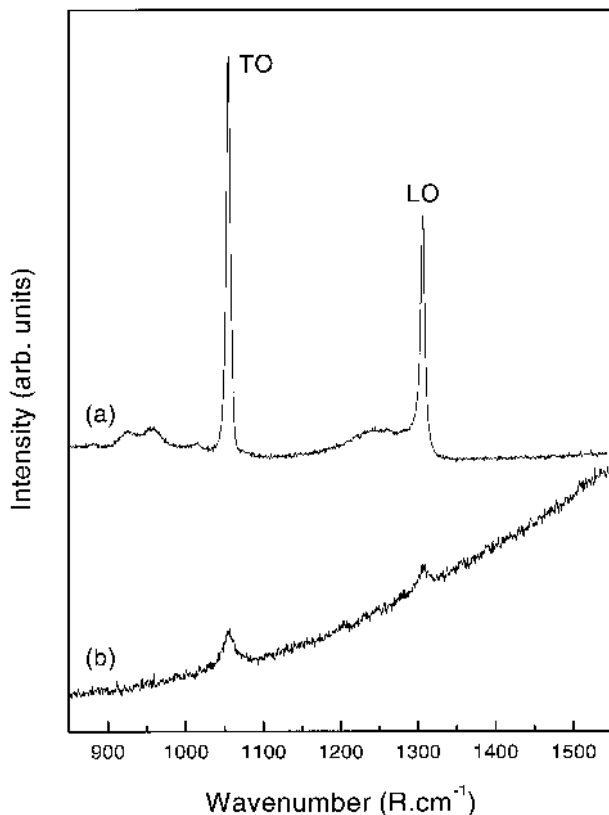


Fig. 1. Typical Raman spectra measured on: (a) a single crystal of cBN; (b) a PcBN composite.

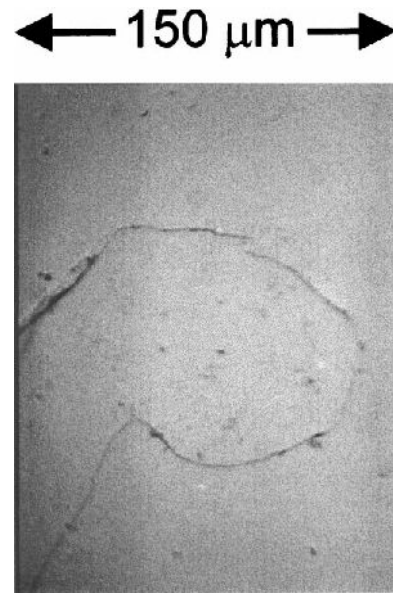


Fig. 2. Micrograph of an indent in a cBN crystal, made at 30 N maximum load. The indenter tip diameter was $100 \mu\text{m}$.

to excessive boron in the crystal lattice, possibly indicating a difference in crystal provenance. The TO peak was fitted to a Lorentz line shape, which yielded the position and FWHM of the peak. The Lorentz line shape was a good fit to the experimental data, with no asymmetry visible in the peak. This indicates that the dominant broadening mechanism at work is that of phonon lifetime broadening. The TO peak was used in preference to the LO peak since the latter was frequently less intense and, for some samples, there was a broad feature present in the lower frequency side of the peak which complicated background subtraction and introduced uncertainty in the width measurement of the peak. Fig. 2 is a micrograph of an indent made in a black cBN crystal at a maximum load of 30 N. The circular indent is clearly visible with cracking around its circumference and two cracks radiating away from the indent. The leftmost crack runs to the edge of the crystal.

The Raman spectrum of 49 points across the indent was obtained in the shape of a 7×7 matrix, with a $25 \mu\text{m}$ step size between the points and the grid centred on the indent. A $10 \mu\text{m}$ diameter laser spot size was used. The position of the TO Raman peak and the FWHM of the same peak across the indent are plotted as contour maps in Figs. 3 and 4 respectively. It can be seen from Fig. 3 that there are clear contour lines indicating the presence of the indent. The peak position is shifted to higher frequencies in the vicinity of the centre of the indent, as well as in the region of the crack feature at the top of Fig. 2. At these positions the stresses are compressive and approximately 0.3 GPa in magnitude. Away from the centre of the indent, the peak has been shifted less, but still to higher frequencies indicating that compressive stresses are present. The

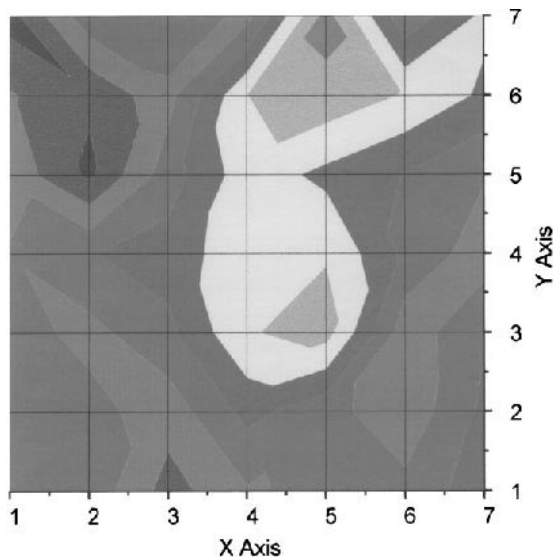


Fig. 3. Contour plot of the TO Raman peak position across the indent in Fig. 1. The biggest shift in peak position to higher frequencies is visible in the centre of the plot and towards the top (lighter areas).

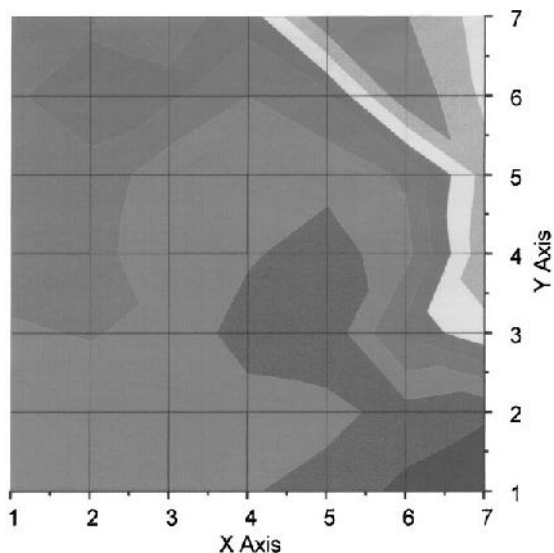


Fig. 4. Contour map of the FWHM of the TO Raman line across the indent in Fig. 1. The biggest values are at the top right of the plot and the gradient runs down towards the centre and lower right.

lowest value stress is 0.07 GPa. This contour map very clearly illustrates the effect of the indent on the cBN crystal surface. In Fig. 4, the crack feature at the top of Fig. 2 is again clearly visible as the region with the biggest FWHM (8.3 to 8.7 cm^{-1}). The FWHM decreases towards the centre of the contour map, where a clear suggestion of the presence of the indent is visible. The FWHM at the centre varies around 5.5 cm^{-1} . This is somewhat unexpected, as deformation of the cBN would likely lead to an increase in FWHM. This result is not yet understood.

Neither of the PL spectra of points measured within

and without the indent show any evidence of sharp ZPLs. The normalised luminescence intensity is observed to be substantially more at the centre of the indent. Two broad features are visible, with a shoulder peak centred on 2600 Rcm^{-1} and a very broad hump centred around 5000 Rcm^{-1} .

Indentations in the polycrystalline samples required loads an order of magnitude larger than for single crystals in order to produce visible indents in the material. Loads typically varied between 2000 and 3000 N. As plastic deformation is possible in PcBN at room temperature [18], it is likely that the deformation brought about by the indenter has resulted in a residual stress field around the indent. Raman spectra of 25 points across an indent were obtained in the shape of a 5×5 matrix, with the matrix measuring $500\text{ }\mu\text{m}$ on a side and the laser spot size being $25\text{ }\mu\text{m}$ in diameter. The biggest differences between the Raman spectra of single crystal and PcBN are the width and amplitude of the peaks, as illustrated in Fig. 1b. The spectra of polycrystalline samples show weaker intensity peaks which are significantly broader when compared to the single crystal spectra (typically 15 cm^{-1} versus 6 cm^{-1}). This broadening is thought to be due to the deformation which takes place during the sintering process. The peaks are also situated on a sloping luminescence background which is much steeper and more intense than in the case of the single crystal samples. Here again only the TO peak was analysed in detail, mainly due to the frequent very weak intensity of the LO peak. For an indent made at a maximum load of 2600 N the stresses present in the material were found to be quite variable and range from a compressive stress of 1.3 GPa inside the indent to tensile stresses of 0.4 GPa in the vicinity of the indent. No clear evidence of the presence of the indent was visible, as was the case in Fig. 3, possibly indicating that the inherent stress fluctuations across the surface were of the same order as those introduced by the indentation process. There is a suggestion of a pattern in the contour plot of FWHM and the peak widths are slightly wider in the centre, but it is difficult to make a clear conclusion. This widening of the peak within the indented area would conform to the expectation that the indentation process would bring about additional deformation.

PL spectra of the indented polycrystalline material show no visible evidence of ZPLs, either within the indented area or without. Both inside and outside the indented area a broad peak centred at 4500 Rcm^{-1} is present. Spectra taken within the indented area show an additional shoulder in the spectrum at 2200 Rcm^{-1} . Bourne [17] has shown that annealing samples with clear ZPLs present above 1000°C removes, or heavily broadens and weakens, the ZPLs. It is suggested that the feature at 4500 Rcm^{-1} is the \underline{B} band observed by Bourne and that any PL active defects which might

have been present have been annealed out due to the high temperatures experienced during sintering.

4. Conclusions

In this paper it has been clearly illustrated that Raman spectroscopy is a viable technique for characterising stresses in cBN. It has been shown that a compressive stress field is present around an indent in a single cBN crystal, with stresses ranging from 0.07 to 0.3 GPa. The FWHM is narrower in the centre of the indent than outside, which is unexpected and not yet understood. Stress measurement on PcBN revealed substantial stress fluctuations from point to point, and the presence of indents was not clearly manifested as a stress field associated with the indent. No clear evidence of vacancy formation during indentation has been obtained via photoluminescence.

Acknowledgements

The authors thank De Beers Industrial Diamond Division for providing the samples used in this study and for the valuable advice and assistance rendered. We thank Craig Vucinovich for his assistance with the

indentations. RME thanks the National Research Foundation of South Africa for financial support.

References

- [1] L. Vel, G. Demazeau, J. Etourneau, *Mater. Sci. Eng. B* 10 (1991) 149.
- [2] S.A. Catledge, Y.K. Vohra, R. Ladi, G. Rai, *Diamond Relat. Mater.* 5 (1996) 1159.
- [3] J.W. Ager III., M.D. Drory, *Phys. Rev. B* 48 (1993) 2601.
- [4] S.A. Catledge, Y.K. Vohra, *J. Appl. Phys.* 78 (1995) 7053.
- [5] L. Bergman, R.J. Nemanich, *J. Appl. Phys.* 78 (1995) 6709.
- [6] S. Fahy, *Phys. Rev. B* 51 (1995) 12 873.
- [7] S. Fahy, *Phys. Rev. B* 53 (1996) 11 884 (E).
- [8] M. Cardona, E. Anastassakis, *Phys. Rev. B* 54 (1996) 14 888.
- [9] S. Fahy, C.A. Taylor II., R. Clarke, *Phys. Rev. B* 56 (1997) 12 573.
- [10] J.A. Sanjurjo, E. López-Cruz, P. Vogl, M. Cardona, *Phys. Rev. B* 28 (1983) 4579.
- [11] S. Ilias, V. Stambouli, J. Pascallon, D. Bouchier, G. Nouet, *Diamond Relat. Mater.* 7 (1998) 391.
- [12] H. Mohrbacher, K. Van Acker, B. Blanpain, P. Van Houtte, J.P. Celis, *J. Mat. Res.* 11 (1996) 1776.
- [13] G. Kern, Clean and hydrogenated diamond and graphite surfaces, PhD Thesis, Technische Universität Wien, 1998, p. 147.
- [14] E. Knittle, R.M. Wentzovitch, R. Jeanloz, M.L. Cohen, *Nature* 337 (1989) 349.
- [15] R.J. Nemanich, S.A. Solin, R.M. Martin, *Phys. Rev. B* 23 (1981) 6348.
- [16] T. Werninghaus, J. Hahn, F. Richter, D.R.T. Zahn, *Appl. Phys. Lett.* 70 (1997) 958.
- [17] R.W. Bourne, PhD Thesis, University of Reading, 1989.
- [18] C.A. Brookes, *Inst. Phys. Conf. Ser.* 75 (1986) 207.
- [19] H. Sachdev, R. Haubner, H. Nöth, B. Lux, *Diamond Relat. Mater.* 6 (1997) 286.

Photoluminescence spectroscopy of electron-irradiation induced defects in cubic boron nitride (cBN)

R. M. Erasmus* and J. D. Comins

Raman and Luminescence Laboratory, School of Physics, University of the Witwatersrand, Johannesburg, Private Bag 3, WITS, 2050, South Africa

Received 26 February 2004, revised 13 May 2004, accepted 13 May 2004

Published online 28 June 2004

PACS 61.80.Fe, 71.55.Eq, 78.55.Cr, 81.40.Wx

Cubic boron nitride is an ultra-hard material that is widely used in industrial applications where its specific mechanical properties make it the material of choice. Compared to diamond, which has similar applications, relatively little is known about the defects in cBN, their structure, electronic properties and their possible effects on the mechanical properties. We present results of photoluminescence spectroscopy at low temperature (<10 K) of two types of cBN irradiated at ambient temperature with 1.9 MeV electrons. All the samples were small (<1 mm diameter) single crystals of cBN. Three defect centres (with narrow lines at 2.28 eV, 2.15 eV and 1.98 eV) are introduced in both the amber-coloured and black-brown coloured samples by the irradiation. The amber coloured sample also shows a defect centre (at 1.65 eV) that is present before and after irradiation. Line shape analysis of the zero phonon lines of all three irradiation-induced centres shows that the lines are predominantly Gaussian in character, suggesting that line-type defects such as dislocations are a prevalent characteristic of these crystals.

© 2004 WILEY-VCH Verlag GmbH & Co. KGaA, Weinheim

1 Introduction Cubic boron nitride (cBN) is a synthetic material, isostructural with diamond, and first synthesised under high pressure and temperature (HPHT) conditions from hexagonal boron nitride by Wentorf [1]. It is the second hardest material after diamond, with high thermal conductivity and a high resistance to oxidation [2]; thus its main applications are industrial processes such as cutting, grinding and polishing. It has promising potential as a wide bandgap semiconductor for optical and electrical applications, but after initial pilot studies of a p–n junction and UV light emission [3, 4] further progress has been slow.

Cathodoluminescence (CL) studies [5] of as-synthesised cBN showed two broad bands, a stronger feature centred on 3.1 eV and a weaker feature centred on 2.2 eV, as well as the vibronic spectra of three defect centres, labelled GC1, GC2 and GC3. GC1 was identified as vacancy-related, while GC2 was thought to be due to a vacancy complex.

CL of electron-irradiated (4.5 MeV) cBN [6] showed that irradiation introduced three vibronic defect centres, labelled RC1 (ZPL = 2.27 eV, 546.2 nm), RC2 (ZPL = 2.15 eV, 576.7 nm) and RC3 (ZPL = 1.99 eV, 623.1 nm). These centres were different to the GC series, and thought to be intrinsic in nature as they were present in all samples. The RC defects were also thought to be vacancy related. Ion implantation [7] with H^+ , He^+ , B^+ , S^+ , Ne^+ and Se^+ resulted in the introduction of the same RC series as found with electron irradiation. This supported the suggestion that the RC defects were intrinsic. It was also observed that all zero phonon lines (ZPLs) were doublets, and the widths varied with sample and irradiation conditions.

* Corresponding author: e-mail: erasmusr@physics.wits.ac.za, Phone: +27 11 717 6859, Fax: +27 11 717 6879

The first photoluminescence (PL) studies [8] of cBN at 77 K on different types of cBN showed that two broad bands centred on 1.96 eV (633.2 nm) and 2.08 eV (595.5 nm) were present in almost all samples. Several vibronic centres were observed, dependent on crystal type. Electron irradiation introduced the RC series observed earlier [6] with CL, but only the RC1 centre was observed in all samples. RC2 was present in most samples, and RC3 was only observed in about 50% of the cases.

A basic understanding of crystal structure and defects are necessary to realise applications, as has been demonstrated for diamond. This paper reports on a PL characterisation of the larger cBN crystals currently commercially available.

2 Theory The zero phonon line (ZPL) associated with a PL-active defect centre yields several useful parameters, namely the position of the line, the Full Width at Half Maximum (FWHM), the normalised intensity and the line shape. In real crystals at low temperatures the PL line shape is determined almost entirely by the crystal strain inhomogeneities. The inhomogeneous broadening is at least 1000 times greater than the homogeneous broadening [9] and in general the principle mechanism of inhomogeneous broadening at low temperatures is the strain broadening that arises from the presence of dislocation-type defects and point defects in the crystal. A comprehensive review of the theory of inhomogeneous strain broadening in crystals was presented by Stoneham [10]. The main results can be summarised as follows:

- for a symmetric lattice, in which the lattice sites accommodate at random the optical centres and defects, the line shape is expected to be symmetric;
- when the strain in the crystal arises solely from uniformly distributed point defects, the luminescence line shape is expected to be Lorentzian;
- when the sources of strain in the crystal are uniformly distributed dislocations (line-type defects) the line shape is expected to be Gaussian;
- in the case when both types of defects are present in the crystal, the resulting line is the convoluted line shape of the Gaussian and the Lorentzian, known as the Voigt profile. The relative linewidths of the Gaussian component and the Lorentzian component in the Voigt profile reflect which defect is the dominant stress source in the crystal.

3 Experimental detail Two types of cBN crystals were investigated. One type consists of small, synthetic (HPHT) crystals (<1 mm diameter), amber in colour, partly transparent and with no distinct morphology. The other type, also of HPHT origin, consists of crystals ~ 1 mm diameter, black-brown in colour, very opaque and with no distinct morphology. The black colour of these crystals has previously been shown to be due to excess boron in the lattice [11]. The HPHT process for cBN often involves spontaneous nucleation of crystals followed by rapid growth. Crystal quality can be poor due to high densities of dislocations and uptake of impurities. It must be noted that most cBN crystals synthesised for industrial use have diameters significantly smaller than 1 mm.

Spectra were recorded with a Jobin-Yvon T64000 Raman spectrometer operated in single spectrograph mode with a 600 lines/mm grating and a CCD detector. Luminescence was excited with the 488 nm line of an argon ion laser. Samples were mounted in an Oxford Instruments continuous flow liquid helium microscope cryostat, and the photoluminescence of selected spots on the crystals acquired at 5 K with the microscope attachment. The laser beam diameter at the sample was ~1 μm . It was determined that the lower temperature was preferable to 77 K, as narrow lines with possible splitting were better resolved. Calibration was done via Hg and Kr lamp emission lines. Irradiation was performed with electrons at a nominal dose of 10^{18} electrons. cm^{-2} and energy of 1.9 MeV. The ZPL peak parameters were obtained from fitting the measured peak to a Voigt function.

In order to be able to compare intensities of the spectra from different crystals, the intensities were normalised by dividing the intensity of the PL spectrum throughout the spectral range by the integrated intensity of the first order TO Raman peak, measured under identical excitation, collection and geometric conditions. This is in line with the practice followed for diamond [12, 13] and is necessary as the intensity of PL spectra depend on several, often uncontrollable factors such as laser beam penetration depth, excitation volume and collection efficiency.

4 Results and discussion Typical spectra measured for the black cBN crystals and amber cBN crystals are given in Fig. 1 and Fig. 2, respectively. ZPL peak parameters as extracted from peak fitting are given in Table 1 and Table 2.

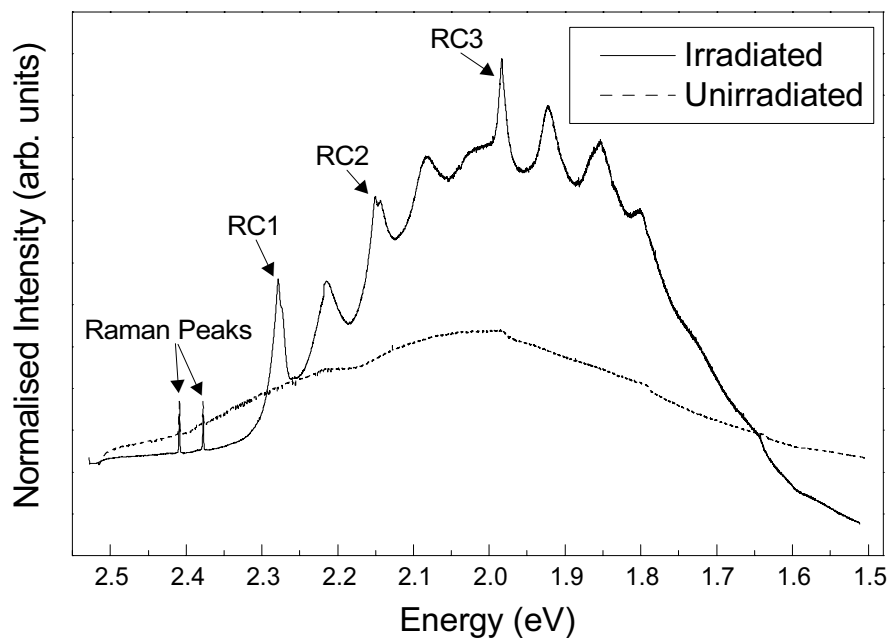


Fig. 1 PL spectra of unirradiated and irradiated black cBN crystals.

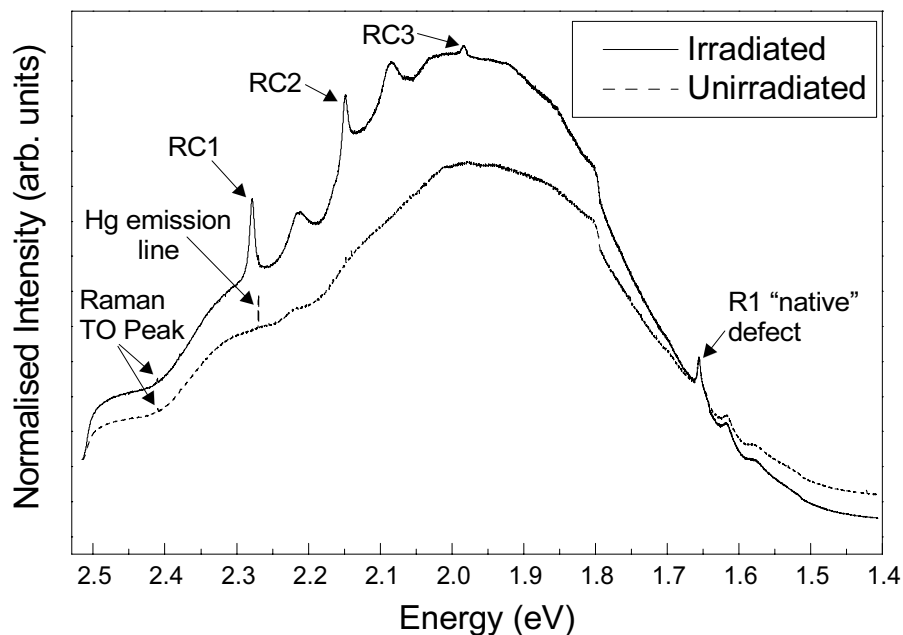


Fig. 2 PL spectra of unirradiated and irradiated amber cBN crystals.

In both figures the unirradiated and the irradiated crystals show a broad band centred around 2 eV, with the normalised intensity higher for the irradiated crystal. Small crystals synthesised via spontaneous nucleation in the HPHT process are likely have high defect densities due to dislocations and possible uptake of flux precursor materials. Broad bands such as these occur when a number of broad defect peaks, associated with extended defects, overlap. There is also the indication that the irradiation process introduces additional defects into the lattice. The band around 2 eV has been attributed to stable neutral complexes [8].

Table 1 ZPL peak parameters for the RC defects in the black cBN crystals.

	Position (eV)	Splitting
RC1	2.28	Yes
RC2	2.15	Yes?
RC3	1.98	No

Table 2 ZPL peak parameters for the RC defects in the amber cBN crystals.

	Position (eV)	Splitting
RC1	2.28	Yes
RC2	2.15	Yes?
RC3	1.98	No

Electron irradiation produces individual point defects [14], and introduces the RC series of peaks in both types of crystal investigated, as is clear from the position data in the tables. In the black crystals all three peaks are present, while in the amber crystals RC1 and RC2 predominate, with RC3 only weakly visible in some spectra. The RC1 defect has been attributed to the nitrogen vacancy in the cBN lattice and RC2 and RC3 associated with vacancy complexes [8], but no more detailed assignments have been made yet. The R1 defect in the amber crystals is present before and after irradiation, and has been linked to the presence of phosphorus in the lattice [8]. This "native" defect peak is unsplit in all cases, and the ZPL width is unaffected by irradiation.

The ZPLs of RC1 and RC2 are observed to be split in some cases and the splitting is likely stress-induced [7], but it is also possible that the RC centres are doublets that are strain-broadened in less perfect crystal regions. Although peak deconvolution using Origin 5.0 software indicates that the RC2 ZPL likely exhibits splitting, the case is somewhat problematic as there is significant overlap of the RC2 ZPL and the second phonon sideband of the RC1 line. Splitting is likely in cases where localised strain is oriented in a preferred direction, while the localised strain is likely to be more isotropic in nature or not oriented in the correct direction for unsplit peaks.

Where splitting occurs it complicates the fitting of peaks and subsequently line shape analysis is difficult. For the unsplit, symmetric peaks, the measured line shape of the ZPLs is Gaussian for both types of crystals. In the presence of point defects and line defects, the longer range strain field (proportional to $1/r$) associated with line-type defects already present would dominate the $1/r^2$ strain fields associated with point defects introduced by the irradiation. The lineshape analysis thus indicates that the dominant defect type in these crystals is line-type defects such as dislocations.

The ZPL line widths and ZPL intensities of the RC centres in both types of sample vary from crystal to crystal and sample spot to sample spot, showing no obvious trends. As the line width is an indication of the strain broadening present in the crystals, this implies an apparent random variation in localised strain in the crystals. It was observed that the peak widths for the ZPLs in the black crystals are generally larger than the corresponding widths for the amber crystals, indicating higher defect concentrations and

associated strains in the black crystals. The intensity variations also point to an uneven distribution of the RC centres in the crystals.

In diamond it has been shown [13] that the growth morphology and growth process plays a large role in determining the type of defects occurring in the material. We suggest that the RC series of defects are growth-related defects that change charge state upon irradiation and then become active in photoluminescence. In this way the RC defect centres can still accommodate vacancies, as suggested in the literature, but it would also explain the different proportions of centres in different materials, e.g. in the case of the RC3 defect in this paper. The much reduced presence of RC3 in the amber crystals relative to the black crystals could also be due to the different RC centres being due to vacancies trapped at different impurity centres, but this would require the vacancies to be mobile during or after introduction. This is unlikely, as vacancies in diamond are only mobile at high temperature (~900K) and it is reasonable to expect a similar high temperature for cBN.

It is clear from the above results that although the available cBN crystals fulfil their role in industrial applications very admirably, the current crystal quality in terms of distinct morphology and crystallinity is unlikely to be adequate for semiconductor applications. In the case of diamond it has been shown (e.g. [15]) that lattice defects and impurities play a very important role in its optical, electrical and mechanical properties. It is very likely to be the same for cBN.

Acknowledgements The authors would like to thank the National Research Foundation of South Africa for financial assistance and Dr Simon Lawson of DTC, Maidenhead, UK, for the electron irradiation.

References

- [1] R. H. Wentorf, Jr., *J. Chem. Phys.* **26**, 956 (1957).
- [2] L. Vel, G. Demazeau, and J. Etourneau, *Mater. Sci. Eng. B* **10**, 149 (1991).
- [3] O. Mishima, J. Tanaka, S. Yamaoka, and O. Fukunaga, *Science* **238**, 181 (1987).
- [4] O. Mishima, K. Era, J. Tanaka, and S. Yamaoka, *Appl. Phys. Lett.* **53**, 53 (1988).
- [5] V. D. Tkachev, V. B. Shipilo, and A. M. Zaitsev, *Sov. Phys. Semicond.* **19**, 491 (1985).
- [6] A. M. Zaitsev, A. A. Melnikov, V. B. Shipilo, and E. M. Shishonok, *phys. stat. sol. (a)* **94**, K125 (1986).
- [7] A. M. Zaitsev, A. A. Melnikov, and V. F. Stel'makh, *Sov. Phys. Semicond.* **21**, 671 (1987).
- [8] R. W. Bourne, Ph.D Thesis, University of Reading, 1989.
- [9] G. Davies, *J. Phys. C* **3**, 2474 (1970).
- [10] A. M. Stoneham, *Rev. Mod. Phys.* **41**, 82 (1969).
- [11] H. Sachdev, R. Haubner, H. Nöth, and B. Lux, *Diam. Relat. Mater.* **6**, 286 (1997).
- [12] T. Evans, S. T. Davey, and S. H. Robertson, *J. Mater. Sci.* **19**, 2405 (1984).
- [13] M. L. Fish, M.Sc Thesis, University of the Witwatersrand (1995).
- [14] J. Walker, *Rep. Prog. Phys.* **42**, 1605 (1979).
- [15] J. E. Field (ed.), *The Properties of Natural and Synthetic Diamond* (Academic Press, London, 1992).

Three-dimensional mapping of stresses in plastically deformed diamond using micro-Raman and photoluminescence spectroscopy

R. M. Erasmus,^{1,2,3,a)} R. D. Daniel,⁴ and J. D. Comins^{1,2,3}

¹*Raman and Luminescence Laboratory, School of Physics, University of the Witwatersrand, Johannesburg, Wits 2050, South Africa*

²*DST/NRF Centre of Excellence in Strong Materials, University of the Witwatersrand, Johannesburg, Wits 2050, South Africa*

³*Materials Physics Research Institute, School of Physics, University of the Witwatersrand, Johannesburg, Wits 2050, South Africa*

⁴*School of Engineering, University of Hull, Cottingham Road, Hull, HU6 7RX, United Kingdom*

(Received 20 September 2010; accepted 24 November 2010; published online 14 January 2011)

The extreme mechanical properties of diamond have made it the material of choice for many industrial applications, ranging from cutting and grinding to wire-drawing dies. A detailed knowledge of its mechanical properties, also at high temperature, is thus of importance. Micro-Raman and photoluminescence (PL) spectroscopy were used to map the three-dimensional (3D) stress distribution surrounding a plastic impression made in a synthetic, type Ib single crystal diamond. The impression was created on a (100) face of the crystal with an Si_3N_4 impressor at 1400 °C using the so-called soft impressor technique. The diamond Raman peak was mapped at room temperature at the surface and at fixed intervals of 10 μm below the surface using a motorised X-Y stage. The depth (Z)-resolution was limited to 10 μm by means of a confocal pinhole. Using data from the Raman peak position, a 3D map of the stress contours surrounding the impression was generated, while the Raman width data yielded a map of the plastic deformation volume. The surface stress map shows a cross-shaped rosette pattern that corresponds very closely with micrographs imaging the pile-up on the surface due to dislocation movement. The “arms” of the pattern are in compression (~ 1.5 GPa), while the center of the impression is in tension (~ 1 GPa). The deformation map shows a radially symmetric area of deformation centered on the impression, with the maximum degree of deformation at the center. The stress contours compare favorably with the resolved shear stress contours calculated for diamond. PL intensity maps of the zero phonon line (ZPL) associated with the $[\text{N}-\text{V}]^-$ defect center at 1.945 eV provide images of the extent of vacancy formation and movement during the impression process. Data concerning the position and width of the ZPL correspond well with the Raman results. © 2011 American Institute of Physics. [doi:10.1063/1.3531548]

I. INTRODUCTION

Nondestructive evaluation of the mechanical properties of ultrahard materials is an important topic in applied physics. Of this class of materials, diamond is the quintessential example with an ever-expanding range of industrial applications. It is readily available, and in addition to its ultrahardness, other well-known physical properties include high radiation hardness, high thermal conductivity and promising electronic properties.¹

Diamond's hardness makes it very brittle, a characteristic which often limits the study of its mechanical properties to those where brittle behavior dominates. The development of the soft impressor technique by Brookes *et al.*^{2,3} and its application to diamond has largely overcome this limitation and has enabled many studies of the plastic properties of diamond. Briefly, the technique permits the controlled plastic deformation of ultrahard covalent materials at high tempera-

tures; it allows the introduction of limited levels of strain such that tensile stresses that cause brittle failure are not attained. Plastic deformation in the form of multiple intersecting slip, without fracture, occurs at temperatures $< 0.3 T_m$, where T_m is the melting point of the material. Resolved shear stresses (RSSs) exceed those required for dislocation initiation and multiplication and pressure is controlled by selection of an appropriate impressor material. In the case of diamond, temperatures in the range 800–1400 °C are used.

Efforts over several years have been made to model the response of diamond to different types of indentors. In the present paper the model by Roberts⁴ is compared with our experimental results. This model is based on elastic deformation and elastic force fields and can make certain predictions regarding the distribution of applied force within the diamond and the resultant deformation. Although some assumptions of initial elastic behavior break down once plastic deformation takes place, it has been found that the model has been quite useful in predicting the behavior of diamond.

^{a)}Electronic mail: rudolph.erasmus@wits.ac.za.

In the present paper, micro-Raman spectroscopy is used to map the nature and magnitude of the stress and the degree of plastic deformation associated with an impression made in type Ib diamond at high temperature. These results are compared with predicted stress contours derived from the above-mentioned model. Photoluminescence (PL) spectroscopy of the zero phonon line (ZPL) of the $[N-V]^-$ defect center at 1.945 eV allows for the visualization of the vacancy creation and movement during the impression process.

II. EXPERIMENTAL METHODS

For the purposes of the present paper, an impression is defined as a plastic deformation made in diamond at high temperature where no brittle fracture has occurred, while an indentation is considered to be a deformation where brittle fracture has taken place.

Impressions were made using a Si_3N_4 impressor on a $\{001\}$ face of a synthetic high pressure high temperature type Ib diamond with a mean contact pressure of 3.1 GPa within a vacuum furnace held at a temperature of 1400 °C. Nitrogen is present in the diamond as a substitutional impurity at the 500 ppm level. The diamond slip system is: $\{111\}\langle 110\rangle$; applied stress is thus resolved onto $\{111\}$ planes in $\langle 110\rangle$ directions.⁵

Raman spectra were acquired at ambient pressure and temperature using the micro-Raman attachment of a Jobin-Yvon T64000 Raman spectrometer operated in single spectrograph mode. The excitation source was the 514.5 nm line of an argon ion laser and the backscattered light was dispersed onto the liquid nitrogen-cooled charge-coupled device detector by an 1800 grooves/mm grating. The confocal pinhole was selected to give a specific Z-depth sampling thickness (exact details are given in the results section). A computer-controlled motorized X-Y stage in conjunction with manual Z-movement was used to map the spectral features within the three-dimensional (3D) volume of the impression.

The position and width of the diamond Raman peak was extracted by fitting a Lorentzian function to the data using ORIGIN software. The stress at any given mapping point was calculated using the equation

$$\Delta\nu = \nu - \nu_0 = \alpha\sigma, \quad (1)$$

where ν is the diamond Raman peak position as measured, ν_0 is the peak position of a stress-free reference diamond, α is the piezo-Raman coefficient, and σ is the stress at the point in question. The value of α used was $1.9 \text{ cm}^{-1}/\text{GPa}$.⁶

The full width at half maximum (FWHM) of the diamond Raman peak can be used as a convenient ranking indicator of the degree of plastic deformation. Since the peak linewidth broadens due to homogeneous (lifetime) broadening, the FWHM is sensitive to “crystal disorder,” and hence is an indicator of the degree of plastic deformation.

The PL spectra were acquired at 77 K using an Oxford Instrument Microstat^{He} microscope cryostat mounted on the microscope stage of the Jobin-Yvon T64000 spectrometer. The 514.5 nm line of an argon ion laser was used for the PL studies reported here, with a 600 lines/mm grating to dis-

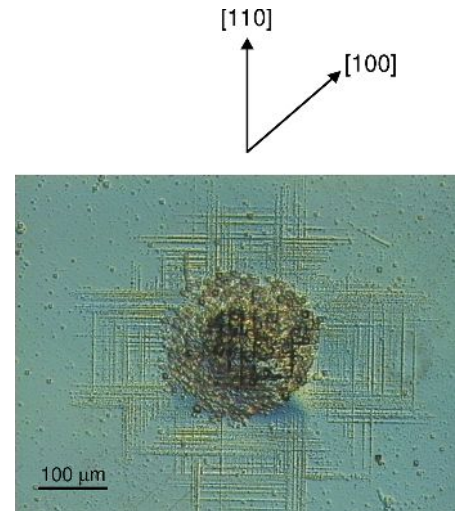


FIG. 1. (Color online) Optical micrograph of an impression on a single crystal synthetic diamond.

perse the light. The ZPL peak was fitted to a Voigt lineshape and the intensity of the ZPL at each point was normalized by the area under the Raman peak acquired under the same measurement conditions.⁷ The grid for the maps is the same as that shown in Figs. 2 and 3 for the Raman measurements.

III. RESULTS

The results are presented in three parts: the first covers Raman results for surface two-dimensional (2D) mapping of the impression, the second contains Raman results for sections through the impression and the third contains PL results for surface mapping of the impression.

A. 2D Raman mapping

Figure 1 is a typical optical micrograph of an impression on single crystal synthetic diamond. The circular dark center corresponds to the area of contact of the impressor and the cross-shaped pattern visible around its extremities is the so-called rosette.^{3,5} The horizontal and vertical lines are dislocations which have run out on the surface during the impression process and have been etched to make them visible. It can be seen by referring to the indicators of crystallographic orientation at the top of Fig. 1 that the rosette shape is determined by the crystallographic plane used for the indentation and the slip system of diamond. For the impression in question, the diameter is $223 \mu\text{m}$. Interferometric images show that the rosette pattern is associated with small areas of pile-up on the surface of the diamond.⁸

The grid in Figs. 2 and 3 below is a 10×10 matrix, measuring $900 \times 900 \mu\text{m}^2$. Figure 2 shows a 2D contour plot of the surface stress associated with the impression, as determined from the position of the diamond Raman peak using Eq. (1). The black circle corresponds to the physical area of the impression on the surface of the diamond. The confocal pinhole was set at 2 mm to create a laser beam with a focal barrel of $50 \mu\text{m}$ in order to sample a section of the diamond of this thickness, while the laser beam diameter at

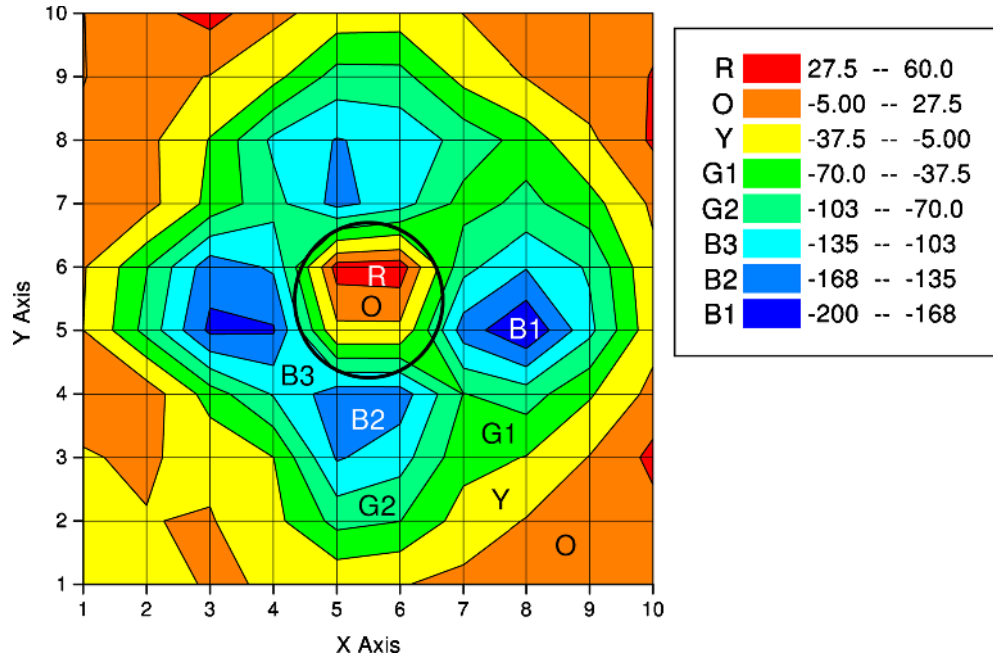


FIG. 2. (Color online) 2D contour map of surface stress associated with the impression, calculated from the Raman peak position of diamond. The black circle corresponds to the physical area of the impression, its diameter being $223 \mu\text{m}$. The physical dimensions of the map are $900 \times 900 \mu\text{m}^2$. The units for the values in the table at the top right are MPa.

the surface was $\sim 1.5 \mu\text{m}$. The entrance slit width was $20 \mu\text{m}$, which gave a band pass of 0.45 cm^{-1} with the 1800 grooves/mm grating used.

The orange (O) shading in Fig. 2 corresponds to an essentially zero (stress-free) value, while red (R) shading corresponds to tensile stress (having positive stress values). The progression of colors from yellow (Y) through green (G) to blue (B) corresponds to increasing compressive stress (increasing negative stress values), with the maximum compressive stress of $\sim 200 \text{ MPa}$ in the dark blue (B1) shaded regions.

In the case of Fig. 3, which provides a 2D contour map of FWHM of the diamond Raman peak across the impression and its surrounds, the blue color (B2) corresponds to a “background” value for the FWHM of 2.0 to 2.1 cm^{-1} and the maximum peak width [red (R)] corresponds to 2.6 to 2.7 cm^{-1} . The peak width thus increases by $\sim 30\%$ in the center of the impression. There is a near radially symmetric pattern associated with the impression on the surface.

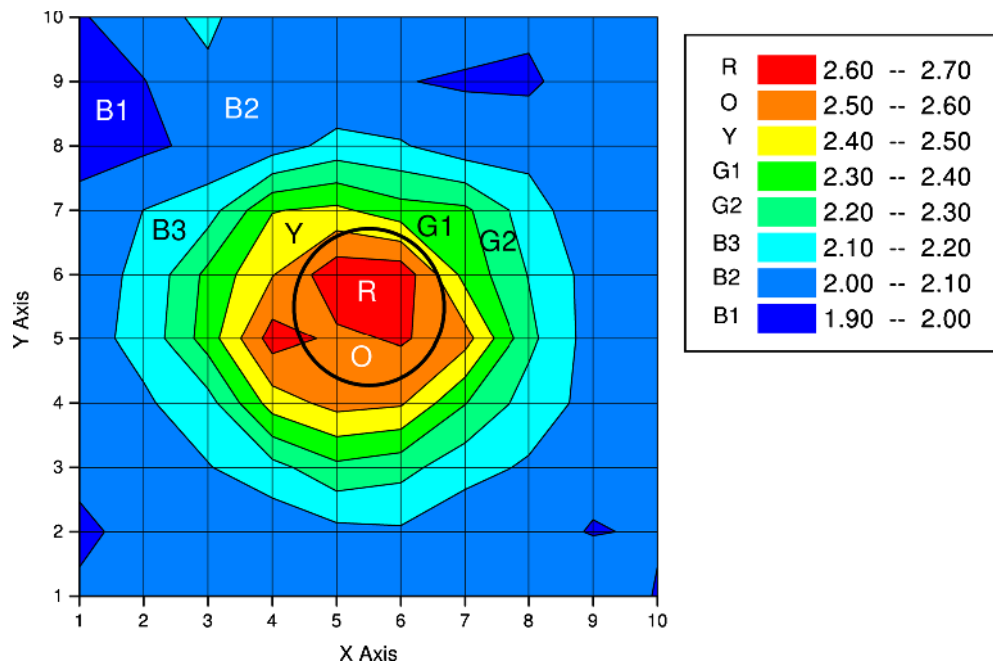


FIG. 3. (Color online) 2D contour map of FWHM of the diamond Raman peak across the impression and its surrounds. The black circle corresponds to the physical area of the impression, diameter being $223 \mu\text{m}$. The physical dimensions of the map are $900 \times 900 \mu\text{m}^2$. The units for the values in the table at the top right are cm^{-1} .

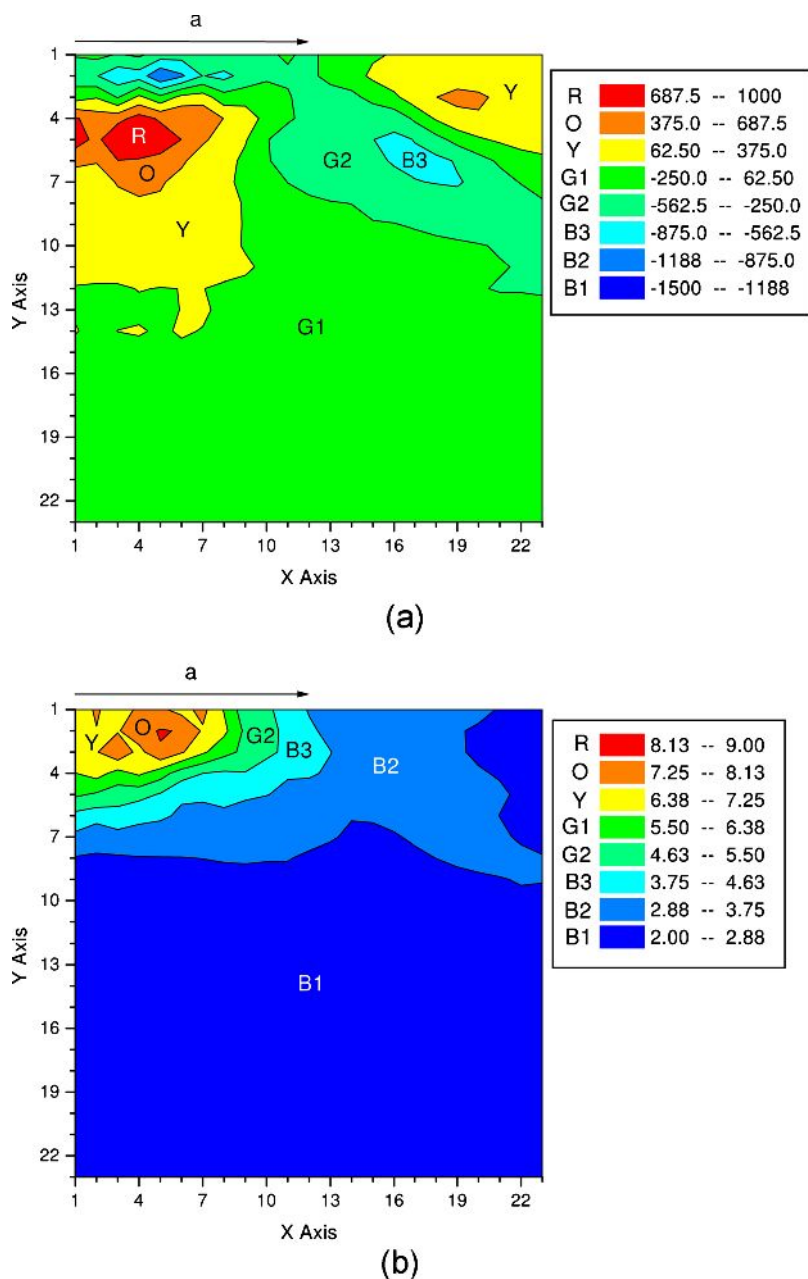


FIG. 4. (Color online) (a): Stress contour map of slice mapped into the diamond along the [100] direction. The center of the impression is at top left and the radius of the impression is “ $a=110\ \mu\text{m}$.” The color coding of the different regions of the map and the values in MPa of the respective stresses are given in the accompanying table. Negative values indicate compressive stress and positive values indicate tensile stress. (b) Contour map of the FWHM of the diamond Raman peak within the slice mapped into the diamond along the [100] direction. The center of the impression is at top left and the radius of the impression is $a=110\ \mu\text{m}$. The color coding of the respective regions and the values in cm^{-1} of the FWHM in each region are presented in the accompanying table.

B. Raman mapping of 3D sections

3D sections were obtained by selecting (100) and (110) crystallographic planes within the diamond and focusing the laser beam at appropriately chosen depths from the diamond surface along these planes to create effectively vertical “slices” within the bulk sample. Changes in the Raman peak position and peak width were mapped along these sections.

The center of the impression is at the origin of the arrow “a” in Figs. 4 and 5. This arrow represents the radius of the circular impression on the surface of the diamond. Each map is thus of dimension $2a$ on a side. The mapping grid size is 23×23 points, with $10\ \mu\text{m}$ intervals. A $50\times$ ultralong working distance objective was used with a $0.1\ \text{mm}$ pinhole, resulting in the laser beam focal barrel being $10\ \mu\text{m}$ and corresponding to the thickness of the diamond being sampled in the Z-direction for a particular focal position of the microscope.

Compressive stress is indicated by negative stress values and its color range [green (G1) (minimum) to blue (B1) (maximum)], while tensile stress is indicated by positive stress values and its color range [yellow (Y) minimum to red (R) (maximum)]. The degree of deformation is depicted by a range for colors: the blue color (B1) corresponds to a “background” value for the FWHM of 2.00 to $2.88\ \text{cm}^{-1}$ and the maximum peak width (red, R) corresponds to a peak width of 8.13 to $9.00\ \text{cm}^{-1}$.

The stress and degree of deformation maps for the (100) slice are shown in Figs. 4(a) and 4(b), respectively, and are located between two arms of the rosette pattern associated with the impression.

For the (100) slice, the largest compressive stress values and the greatest degree of plastic deformation are associated with the volume of diamond immediately below the contact area of the impressor. The greatest magnitude of tensile

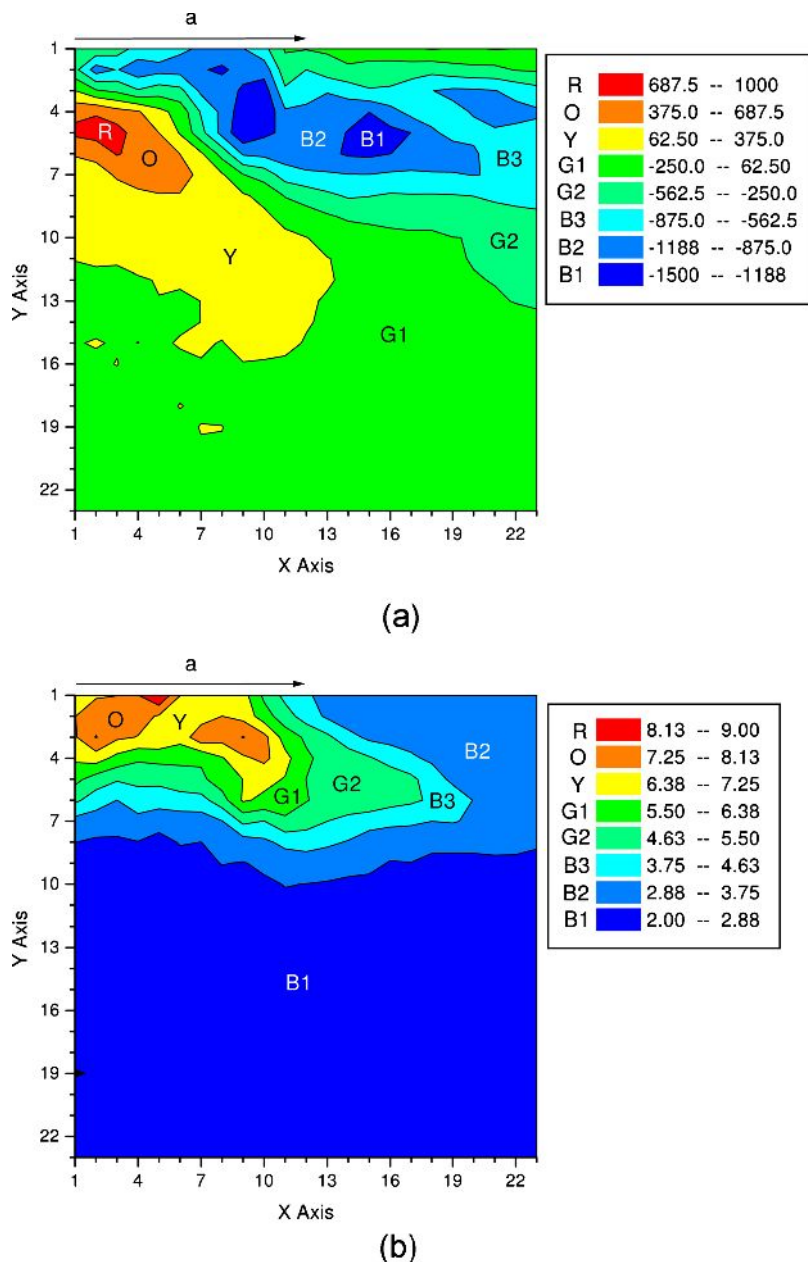


FIG. 5. (Color online) (a) Stress contour map of slice mapped into the diamond along the $[110]$ direction. The center of the impression is at top left and the radius of the impression is $a=110 \mu\text{m}$. The color coding of the different regions of the map and the values in MPa of the respective stresses are given in the accompanying table. Negative values indicate compressive stress and positive values indicate tensile stress. (b) Contour map of the FWHM of the diamond Raman peak within the slice mapped into the diamond along the $[110]$ direction. The center of the impression is at top left and the radius of the impression is $a=110 \mu\text{m}$. The color coding of the respective regions and the values in cm^{-1} of the FWHM in each region are presented in the accompanying table.

stress is also located immediately below the contact area of the impressor but at a depth of approximately $50 \mu\text{m}$.

The maps for the (110) slice shown in Figs. 5(a) and 5(b) clearly illustrate the presence of the arm of the rosette in the $[110]$ direction by the presence of an extended region of compressive stress. As shown in Fig. 5(a) the maximum compressive stress in the arm (-1490 MPa) is associated with a volume located approximately $50 \mu\text{m}$ below the surface of the diamond. The volume associated with the greatest magnitude of tensile stress is located immediately below the contact area of the impressor, also at a depth of approximately $50 \mu\text{m}$.

The degree of deformation mapped in Fig. 5(b) from the data on the FWHM of the Raman peak clearly shows that the maximum deformation is associated with the volume immediately below the contact area of the impressor.

The respective magnitudes of the tensile stress measured for the (100) slice (maximum of 990 MPa) and the (110)

slice (maximum of 830 MPa) slices agree well, and the respective degrees of deformation are also in good agreement (maximum widths of 8.2 and 9.0 cm^{-1} for (100) and (110) slices).

It is important to note that the magnitudes of the stresses and degrees of deformation measured in Figs. 2 and 3 are different from those reported in Figs. 4 and 5 as different volumes of diamond were sampled in the two cases due to different confocal parameters being used. In the case of the 2D surface maps, the laser beam focal barrel and hence the thickness of the slice sampled was $50 \mu\text{m}$, while for the 3D maps within the diamond this value was $10 \mu\text{m}$. For the thicker slice, the stresses and deformation was averaged over a larger volume, thus leading to lower values than for the thinner slice. Thus, knowledge of the confocal parameters is important in the correct interpretation of the respective contour maps.

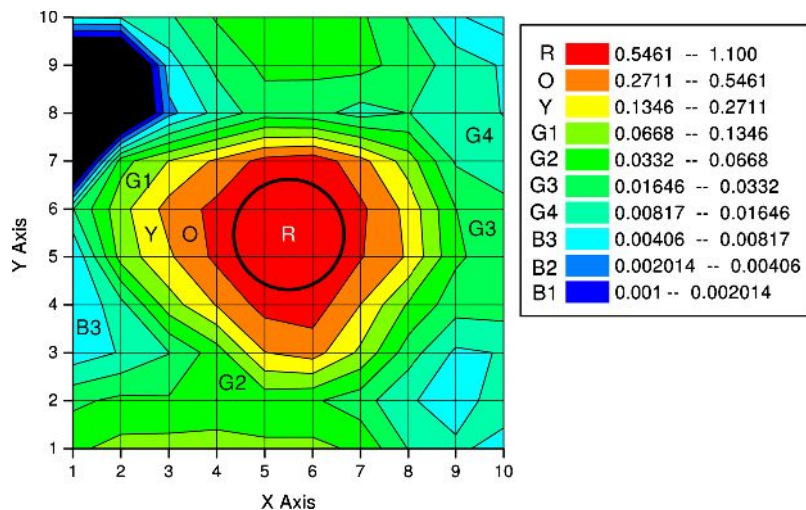


FIG. 6. (Color online) Normalized intensity map of ZPL of the 1.945 eV defect $[N-V]^-$. Note the log scale. The black circle represents the contact area of the impressor.

In order to check if the different slip systems that are operative for two orthogonal arms result in different stress and width contour maps, slices into the diamond were mapped along the $[110]$ and $[\bar{1}10]$ directions of the impression. The results, available in the online supplementary material,¹⁴ indicate that deformation along orthogonal rosette arms give rise to qualitatively very similar residual stress contours and deformation profiles.

It is also noted that whereas the degree of plastic deformation as indicated by the linewidth extends approximately $75 \mu\text{m}$ from the surface of the diamond, the tensile stress field extends to approximately $150 \mu\text{m}$ from the surface. It follows that the extent of the plastic deformation is less than that of the tensile stress field.

C. 2D PL maps

The data for the 1.945 eV defect $[N-V]^-$ is presented here.

The intensity of the ZPL associated with the $[N-V]^-$ center at 1.945 eV normalized relative to the area of the diamond Raman peak as described in Sec. II is given in Fig. 6. Note that the intensity is plotted on a logarithmic scale to emphasize the very strong growth of the intensity of the defect over the background level. The black area represents a surface area where the ZPL was not detected. This figure illustrates the very clear association of the negative charge state of the $[N-V]$ defect with the impression in the diamond. The impression under discussion was made at 1400°C , which is substantially above the temperature ($\sim 600^\circ\text{C}$) where the vacancy in diamond becomes mobile. Nonconservative slip of dislocations during the impression process generates vacancies, which are then free to diffuse and bind with substitutional nitrogen, which is the dominant form of nitrogen in synthetic type Ib diamond. This gives rise to the $[N-V]^-$ defects observed here. The intensity gradient highlights the fact that most of the vacancy generation takes place in the immediate vicinity of the impression. A comparison of the maps of Figs. 3 and 6 shows the similar extent of the surface contours for the degree of deformation determined from the Raman FWHM and the extent of vacancy formation from the ZPL intensity of the 1.945 eV defect.

Although these two maps result from different physical mechanisms (Raman line broadening and PL-active defect concentration), they contribute to a consistent picture of the processes that take place during the formation of an impression. The good correlation of the contours implies that most of the plastic deformation is confined to the immediate vicinity of the impression and that vacancies formed during the impression process are quickly trapped after their formation.

Figure 7 maps the position of the ZPL of the 1.945 eV defect across the impression. There are clearly two lobes (left and right of the impression in the figure) as well as a much weaker two-lobe pattern at right angles to the strong pair. In relation to Fig. 7, the electric field of the incoming laser beam is linearly polarized in the $[110]$ direction (i.e., parallel to the x -axis), this being the stress axis associated with the two left-right lobes. These ZPL intensity lobes will thus be greater intensity than the pair at right angles, the difference being the direct result of the polarization of the exciting light.

Davies and Hamer⁹ investigated the effect of strain on the optical properties of the 1.945 eV defect. Shifting and splitting of the ZPL was reported for various uniaxial stress configurations, chiefly for absorption rather than luminescence of the defect. Comparison with the calculations for splitting under uniaxial stress in the case of PL (Ref. 10) shows that although the intensity ratios of the components differ between absorption and luminescence, the rate of shift in the ZPL components for the case of $[110]$ stress and electric field parallel to this stress (as in Fig. 7) is the same for absorption and luminescence. It is thus possible to use the data of Davies and Hamer to calculate the stress in the two left-right lobes in Fig. 7.

Although the uniaxial stress data in Ref. 9 shows a splitting of the ZPL for the stated relative orientation of stress axis and exciting light, there is no clear evidence for peak splitting in the PL spectra measured in the present work. The majority of peaks are symmetrical without any sidebands. In the few cases where a shoulder may be present, it is weak and difficult to deconvolute from the major peak. It is suggested that there are two reasons for this observation. For the stress axis—exciting light geometry applicable here, the ZPL splits into a major and minor component, with the major

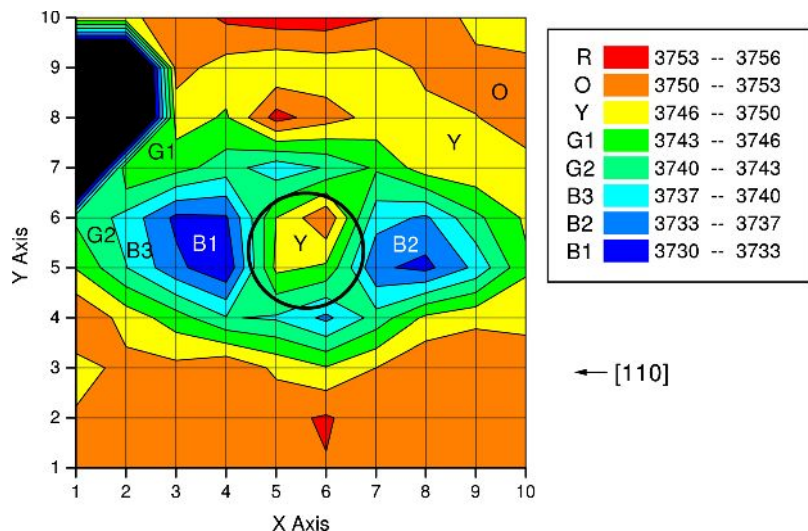


FIG. 7. (Color online) Map of the position of the ZPL of the 1.945 eV defect. The units of the scale are relative wavenumbers (compared with 514.5 nm). The black circle represents the contact area of the impressor.

component expected to be ~ 3 times more intense. The confocal parameters are also such that an approximate $50 \mu\text{m}$ thickness of diamond is being sampled. This averaging effect coupled with the difference in intensity ratios between the components of the peak leads to only a single component of the ZPL in fact being observed. For the two left-right lobes mentioned earlier in this paragraph, the ZPL peak position is shifted downwards by $\sim 20 \text{ cm}^{-1}$, which converts to an energy difference of $\sim 2 \text{ meV}$. According to Davies and Hamer this shift is due to a stress of just greater than 200 MPa. This value is in good agreement with that measured via Raman spectroscopy.

For ZPLs a larger linewidth is associated with a larger degree of deformation due to inhomogeneous line broadening.¹¹ The deformation of the diamond due to the impression is clearly mapped via the linewidth of the ZPL in Fig. 8(a) and is clearly centered on the contact area of the impressor. It corresponds well with the deformation mapped via the Raman linewidth in Fig. 3. Comparison of the change in the values of the width (units in wavenumbers) in Figs. 3 and 8(a) shows that the ZPL width is a more sensitive indicator for local deformation. The Raman linewidth changes by approximately a third between the bulk (undeformed) value and the center of the impression, while the ZPL Voigt width more than doubles when comparing the width of ZPLs from defects present in undeformed diamond with those in the center of the impression.

In Fig. 8(b), the Gaussian component of the linewidth is mapped and it is clear that this makes the major contribution. This implies that the majority of defects giving rise to the 1.945 eV luminescence are at or near line-type defects.¹¹ This is not unexpected, as the dislocation movement during the deformation process is expected to give rise to line-type defects.

IV. DISCUSSION

The most suitable model at present for indentation hardness is that suggested by Roberts⁴ who modeled the whole of the slip pattern over an area of $2a \times 2a$, where a is the contact area radius. This includes the areas directly beneath and adjacent to the contact point. Roberts used extended stress

fields produced by a circular contact in an elastically isotropic material, making use of the approach in Ref. 12 to predict the likely slip patterns and their associated stresses. This allowed complete 3D patterns of the relevant slip planes to be visualized together with the RSSs on them.

To model the magnitude of the RSSs which control plastic deformation in the bulk of a crystal, the crystallographic plane of the indented surface and the active slip systems must be identified. For this discussion, a (001) surface and $\{111\}\langle 110 \rangle$ slip systems are considered, the nomenclature indicating that the applied stress resulting in slip is resolved onto $\{111\}$ planes in the $\langle 110 \rangle$ directions. Figures 9(a) and 9(b) (Refs. 2 and 5) are maps showing the highest RSSs and the slip systems which are associated with those stresses on a (100) plane and a (110) plane, respectively, where both of these planes represent sections which pass through the center of a circular contact area and are normal to the indented surface. For each of the (100) and (110) sections, the 12 possible slip systems in diamond cubic crystals are identified and numbered on the respective slip plane pyramids shown in Figs. 9(a) and 9(b). In each of these pyramids, the respective apices "C" are assumed to be below the indented (001) plane. A further convention used here is that a bar over the slip system number indicates that material under that slip plane is sheared downwards while a number without the bar corresponds to material above the slip plane being sheared downwards; in other words, negative and positive slip, respectively. The actual slip systems subjected to the highest RSS in various regions beneath the contact area are shown in rectangular boxes between the solid lines, e.g., the numbers 9,12 in a box indicate that slip systems 9 and 12 are operative. The dashed lines indicate contours of constant RSS, and the number next to each contour indicates the percentage of P_m that is experienced along the contour, where P_m is the stress applied by the impressor over a circular contact area of radius a .

For Fig. 9(a), i.e., on the (100) section or slice, the RSS values immediately below the surface are relatively low. The maximum shear stress is about $0.316P_m$ where this lies in a region where slip systems 9 and 12 are those most likely to be activated. This region is $\sim 0.58a$ beneath the center and

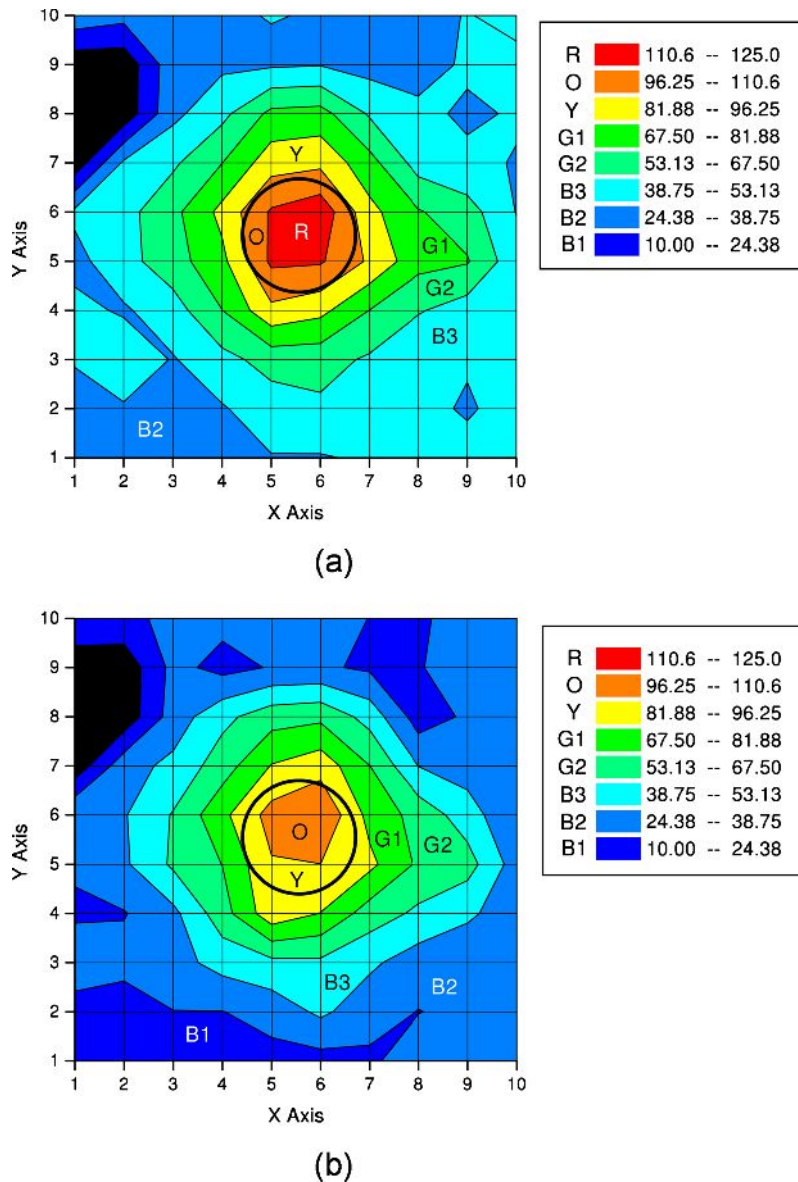


FIG. 8. (Color online) (a) Voigt linewidth of the 1.945 eV ZPL. Units in the table at the top right are wave numbers. (b) Gaussian component of the width of the 1.945 eV ZPL. Units in the table at the top right are wave numbers.

$\sim 0.54a$ from the center line of the impression. For Fig. 9(b), i.e., on the (110) section or slice, the maximum shear stress is $0.30P_m$ and this region is $\sim 0.52a$ beneath the center of the impression and $\sim 0.5a$ from the center line of the impression. Thus, the zone of maximum RSS is roughly toroidal in shape (doughnut-shaped).

In Figs. 9(a) and 9(b), the volume of maximum tensile stress corresponds fairly closely with the volume of diamond that would experience the maximum RSS during the impression process (broken line contours of 30% of the mean applied pressure P_m). The volume of maximum tensile stress for the (100) slice also appears to be slightly larger than that for the (110) slice, which corresponds to the 30% contour being larger for the (100) slice. The maps in Figs. 4(a) and 5(a) thus show a close correspondence with the RSS contours in Figs. 9(a) and 9(b), respectively.

In order to further discuss the relationship(s) between the experimental and model contours in Figs. 4, 5, and 9, it is necessary to include a description of the process by which the soft impressor technique creates strain and plastic deformation. Dislocation movement plays an important part.

The deformation process by which a conical soft impressor creates a circular impression in diamond can be split into three parts, the first being the initiation and multiplication of dislocations. The second part is the mechanism by which they fill the highly stressed volume beneath the impressor and the third part involves the mechanism by which further dislocation initiation and subsequent movement manifests itself as the visible rosette formation with its accompanying pile-up. These three parts are discussed in the following paragraphs.

Part 1. When a diamond crystal is subjected to stress, the crystal will slip on the plane most favorably oriented to allow dislocations to move. Thus dislocations are created and begin to move at a fixed level of RSS but restricted to certain planes and directions. For diamond the applied stress is resolved onto {111} planes in the $\langle 110 \rangle$ directions. The critical RSS (CRSS) is the resolved stress required to create and move a dislocation onto the surface. During the impression process, one can imagine a dislocation is initiated at a discrete point under the contact area and expands under the

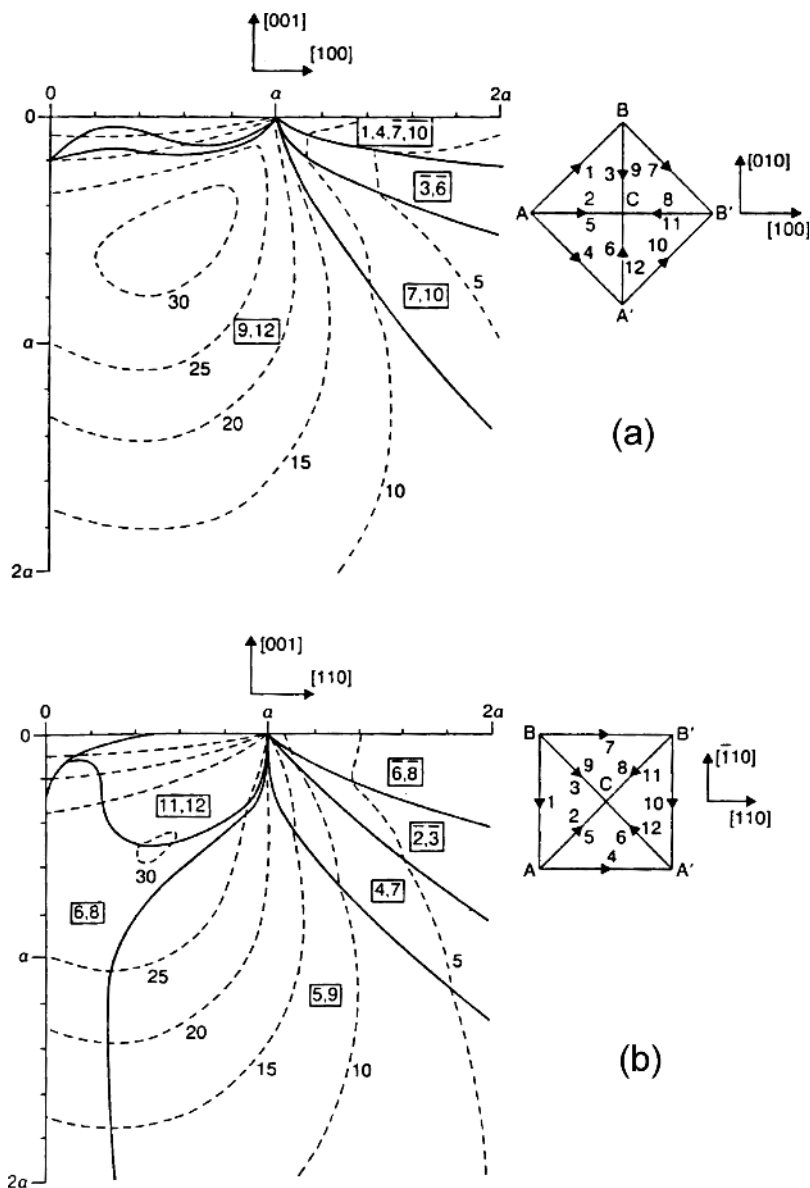


FIG. 9. (a) Modeled contours (broken lines) of RSS on the most stressed slip systems for contact on the (001) surface and for a section normal to the surface and along the [100] direction (from Refs. 2 and 5). (b) Modeled contours (broken lines) of RSS on the most stressed slip systems for contact on the (001) surface and a section normal to the surface and along the [110] direction (from Refs. 2 and 5). The values indicated are percentages of the stress P_m applied by the impressor over a circular contact area of radius a . Solid lines divide regions where different slip systems are the most highly stressed. The slip system labeling is shown in the inserts, where the apices “C” of the pyramids of {111} slip planes (viewed from above the contact surface) are below the plane of the paper. A bar over the slip system number indicates that material under that slip plane is sheared downwards (negative slip) while no bar corresponds to material above the slip plane being sheared downwards (positive slip).

applied stress until it reaches the surface. At the same time the dislocation propagates into the bulk until it reaches a point where the RSS acting on it is insufficient to sustain dislocation movement.

Part 2. Increasing the pressure by a small amount will increase the volume around the initial point of highest shear stress in which the RSS is sufficient to initiate dislocations. This leads to further dislocation production with each able to expand on their respective slip planes under the applied shear stress. Figure 10 shows the Roberts model for a (110) cross section, where the dark shading indicates the area in which the RSS is high enough to initiate dislocations. The lighter shading indicates the limit of the area in which the RSS is sufficient to cause dislocation loop expansion.

A dislocated volume is thus created, the level of strain is increased and work hardening is possible. If a cross section were taken of an impression where a significant volume had been allowed to dislocate, then the resultant dislocation structure might look similar to that shown in Fig. 11. As the

slip system of diamond creates two points of maximum RSS, the dislocation structure is that of two overlapping structures, these being roughly identical in shape.

The picture in reality is more complicated, as the initiated dislocations are not confined to those slip systems that

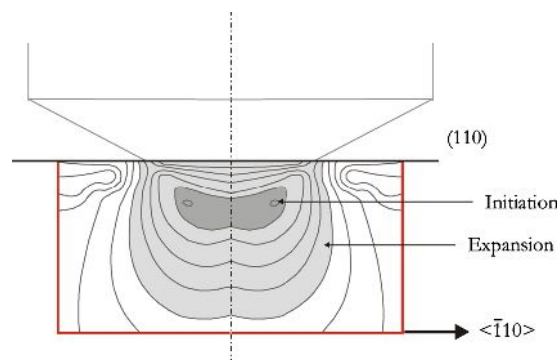


FIG. 10. (Color online) Roberts model of a (110) plane or slice showing the area of dislocation initiation (dark shading) and the subsequent limit of dislocation loop expansion (light shading).

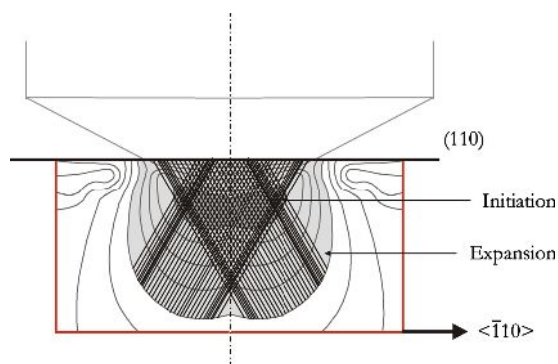


FIG. 11. (Color online) Roberts model of a (110) plane or slice showing the likely resultant dislocation structure of an impression before the onset of reversed plasticity.

intersect the surface or those that are perpendicular to the (110) plane—slip on all of the $\{111\}\langle 110 \rangle$ slip systems is possible. Nevertheless the principle remains the same.

Part 3. In general, rosette patterns are formed at certain higher pressures and temperatures. The CRSS at temperatures above 1300 °C (i.e., when it is relatively independent of temperature) is between 0.32 and 1.3 GPa.¹³ The impression in question was made at 1400 °C and the mean contact pressure was 3.07 GPa. This implies the CRSS was comfortably achieved during its formation (30% of 3.07 GPa = 920 MPa). Brookes¹³ also showed that the resultant RSSs in the range quoted above were sufficient to initiate dislocations from inside the contact area, but not outside. The dislocations thus form and start to move beneath the contact area. The geometry of the slip plane with respect to the surface means that dislocations emerge outside the contact area. A cross section of an impression at the point where rosette formation just begins is shown in Fig. 12.

It has to be kept in mind that once the first dislocation is produced, the ideal shear stress distribution, as shown by the Roberts model, is altered. As more dislocations are produced, the volume in which dislocation initiation is possible is increased, as the stress field of each dislocation will distort the elastic stress field. Significant dislocation activity leading to rosette pattern formation further complicates the picture. When all these factors are taken into account, it can be seen that the dislocation structure beneath an impression becomes increasingly chaotic. Ideally the stress field model should be

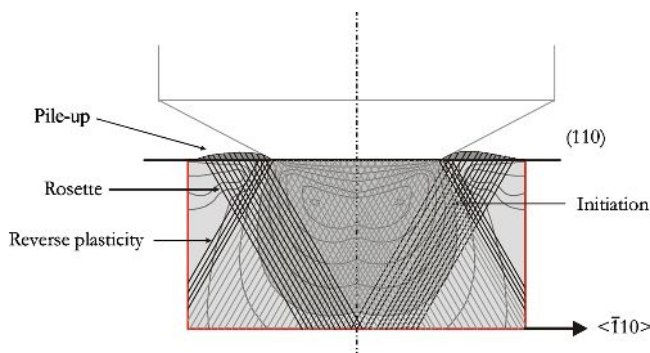


FIG. 12. (Color online) Roberts model for a (110) plane or slice showing the likely resultant dislocation structure of an impression just after the onset of rosette formation.

elastic-plastic, including the stresses from effects generated at the surface plus stresses from other defects present within the plastic zone. The basic elastic stress field calculations remain valid, however, when considering the whole of the deformed region as the extent of the deformed volume is similar to that predicted.

From the description given above the process resulting in the measured contours can be visualized. The first dislocation nucleation takes place in the volume of maximum RSS (30% broken line contour). As the impression process continues, dislocations multiply and move to fill the volume under impressor contact area. Material is thus “moving away” from the volume where the dislocations movement originates. At the end of the deformation process, this volume is thus “deficient” in material with the result that it is in tension. Although it would be expected that some relaxation of shear stress were to take place due to plastic deformation, the results show that most of the shear stress is “locked in” on cooling. A 0.316 fraction [maximum shear stress is $0.316P_m$, Fig. 11(a)] of 3.07 GPa = 970 MPa, close to the measured maximum stress of 990 MPa for the (100) slice in the vicinity of the 30% contour. A 0.3 fraction (30% contour toroid in Fig. 11) of 3.07 GPa = 920 MPa, comparable with the measured maximum for the (110) slice in an equivalent position of 830 MPa. The calculated RSS contours for the (100) slice encompass a larger volume than those for the (110) slice and this is reflected to a certain degree in the measured contours as well.

As noted previously, the extent of deformation for both the slice directions as measured by the Raman linewidth appears to be shallower than the range of the stress contours. This would be accounted for by the CRSS initially being exceeded closer to the surface, whereas deeper into the crystal no dislocation movement took place, but there is a residual stress gradient between the deformed and undeformed volumes. These residual stress gradients are to a certain extent locked in by the irreversible nature of the plastic deformation.

It is also observed that the volume where dislocation movement has produced maximum plastic deformation corresponds closely with the volume of maximum tensile stress. Dislocation initiation and movement starts from that volume of diamond where the CRSS is attained first. It is thus to be expected that the largest degree of deformation would correspond with the volume where the movement initiated. This volume is also “most deficient” of diamond (as per the argument above), resulting in it also being the volume of maximum tensile stress.

It is noted that the good correspondence of the measured contours and the Roberts model is further reason to use the latter in spite of the breakdown of the original elastic stress field assumptions of the model in reality. The “extra” material being displaced from under the impression propagates along the slip planes to form pile-up, and due to the slip system of diamond, this extra material ends up in the arms of the rosette and with the arms being in compression. The compressive stress contours associated with the arms of the rosette pattern are not reflected in the calculated RSS contours of the Roberts model. This is due to the contours being

related to the applied pressure from the impressor being projected onto the slip system of diamond, whereas the arms of the rosette pattern are wholly the result of the plastic deformation taking place at high temperature. In this aspect the Roberts model is inadequate in predicting the experimental observations.

V. CONCLUSIONS

The present work reports an investigation of plastic impressions in single crystal, synthetic type Ib diamond by micro-Raman and PL spectroscopy. Maps of the residual stresses were produced from the position of the Raman peak, while the degree plastic deformation was mapped via the Raman peak width. Raman contour maps clearly distinguished between the tensile central area of the impression and the compressive stress in the arms of the rosette pattern. These contour maps were also constructed for slices into the bulk of the diamond crystal, making comparisons between the experimental contours and contours modeled from elastic stress field theory possible. A good correspondence was found between the results and the predictions from the model, although some disagreements exist which can be attributed to the breakdown of the assumptions associated with the elastic stress fields. PL spectroscopy maps of the ZPL of the 1.945 eV defect ($[N-V]^-$ structure) yielded results qualitatively and quantitatively (for stress values) in good agreement with those from the Raman measurements.

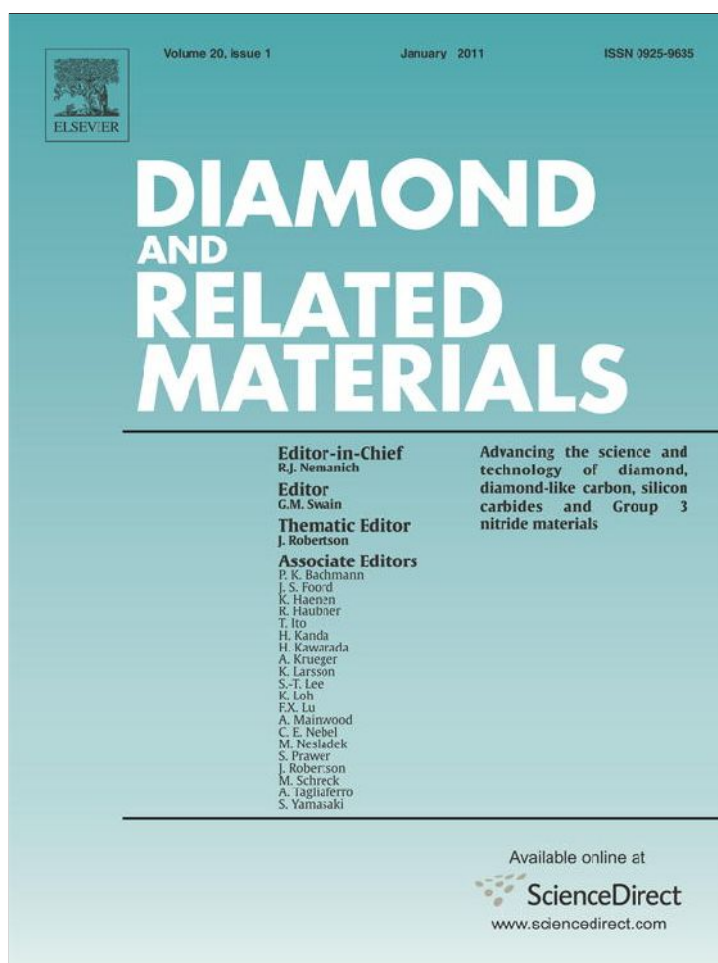
Optical spectroscopy was thus successfully applied to the nondestructive characterization of the mechanical prop-

erties of single crystal diamond, demonstrating the value of these techniques in the exploration of industrially relevant ultrahard materials.

ACKNOWLEDGMENTS

The authors wish to thank Dr E. J. Brookes for making the plastic impressions analyzed in this paper. Financial support from the National Research Foundation of South Africa under Grant No 2053306 and the DST/NRF Centre of Excellence in Strong Materials hosted by the University of the Witwatersrand is also gratefully acknowledged.

- ¹J. E. Field, in *The Properties of Natural and Synthetic Diamond*, edited by J. E. Field (Academic, London, 1992), p. 667.
- ²C. A. Brookes, E. J. Brookes, V. R. Howes, S. G. Roberts, and C. P. Waddington, *J. Hard Mater.* **1**, 3 (1990).
- ³E. J. Brookes, A. T. Collins, and G. S. Woods, *J. Hard Mater.* **4**, 97 (1993).
- ⁴S. G. Roberts, *Philos. Mag. A* **58**, 347 (1988).
- ⁵C. A. Brookes, in *The Properties of Natural and Synthetic Diamond*, edited by J. E. Field (Academic, London, 1992), p. 515.
- ⁶L. Bergman and R. J. Nemanich, *J. Appl. Phys.* **78**, 6709 (1995).
- ⁷T. Evans, S. T. Davey, and S. H. Robertson, *J. Mater. Sci.* **19**, 2405 (1984); M. L. Fish, Optical properties of synthetic diamond of different synthesis origin, M.Sc. thesis, University of the Witwatersrand, 1995.
- ⁸E. J. Brookes, J. D. Comins, R. D. Daniel, and R. M. Erasmus, *Diamond Relat. Mater.* **9**, 1115 (2000).
- ⁹G. Davies and M. F. Hamer, *Proc. R. Soc. London, Ser. A* **348**, 285 (1976).
- ¹⁰K. Mohammed, G. Davies, and A. T. Collins, *J. Phys. C* **15**, 2779 (1982).
- ¹¹A. M. Stoneham, *Rev. Mod. Phys.* **41**, 82 (1969).
- ¹²A. E. H. Love, *Philos. Trans. R. Soc. London, Ser. A* **228**, 377 (1929).
- ¹³E. J. Brookes, The plasticity of diamond, Ph.D. thesis, The University of Hull, 1992.
- ¹⁴See supplementary material at <http://dx.doi.org/10.1063/1.3531548> for maps comparing stress and width contours along $[110]$ and $[\bar{1}10]$ directions, i.e. along orthogonal rosette arms.



(This is a sample cover image for this issue. The actual cover is not yet available at this time.)

This article appeared in a journal published by Elsevier. The attached copy is furnished to the author for internal non-commercial research and education use, including for instruction at the authors institution and sharing with colleagues.

Other uses, including reproduction and distribution, or selling or licensing copies, or posting to personal, institutional or third party websites are prohibited.

In most cases authors are permitted to post their version of the article (e.g. in Word or Tex form) to their personal website or institutional repository. Authors requiring further information regarding Elsevier's archiving and manuscript policies are encouraged to visit:

<http://www.elsevier.com/copyright>



Application of Raman spectroscopy to determine stress in polycrystalline diamond tools as a function of tool geometry and temperature

R.M. Erasmus^{a,b,c,*}, J.D. Comins^{a,b,c}, V. Mofokeng^b, Z. Martin^{c,d}

^a DST/NRF Centre of Excellence in Strong Materials, Physics Building, University of the Witwatersrand, Johannesburg, WITS 2050, South Africa

^b Materials Physics Research Institute, School of Physics, University of the Witwatersrand, Johannesburg, WITS 2050, South Africa

^c Raman and Luminescence Laboratory, School of Physics, University of the Witwatersrand, Johannesburg, WITS 2050, South Africa

^d Department of Materials, University of Oxford, Parks Road, Oxford, OX1 3PH, United Kingdom

ARTICLE INFO

Article history:

Received 20 September 2010

Received in revised form 1 March 2011

Accepted 14 March 2011

Available online xxxx

Keywords:

Polycrystalline diamond (PCD)

Tool-bits

Raman spectroscopy

Stress

Temperature

ABSTRACT

Polycrystalline diamond (PCD) tools commonly consist of a PCD layer sintered onto a cobalt-tungsten carbide (Co-WC) substrate. These tools are used in diverse applications and both the magnitude and distribution of the stresses in the PCD layer affect tool behavior. These stresses in sample drill-bits were investigated by means of micro-Raman spectroscopy in which the properties of the diamond Raman peak reveal both the nature of the stress present (compressive or tensile) and its magnitude. It was found that the surface preparation techniques influenced the average stress present in the PCD surface layer which was in compression in all cases investigated. The largest stresses were encountered in the roughly lapped sample (1.4 GPa) with the stress values decreasing for fine lapping (0.8 GPa) and polishing (0.1 GPa). Small areas with low tensile stresses were found in some polished samples. Measurements of stress as a function of temperature for roughly lapped sample drill-bits indicated a linear trend of decreasing stress values with increasing temperature, although the stress remained compressive. Cyclic annealing of a sample drill-bit to 600 °C shows that the tool properties are retained after 5 cycles, while similar cycling to 800 °C resulting in a permanent degradation of the tool properties.

© 2011 Elsevier B.V. All rights reserved.

1. Introduction

The applications of diamond, apart from its role as gemstone, are quite diverse [1]. Currently synthetic diamond is mainly exploited for its ultra-hardness property in cutting, grinding and polishing. The very property that contributes to its desirability as an industrial ceramic also leads to it being extremely brittle. The solution to this problem is to make use of sintered polycrystalline diamond (PCD), frequently with cobalt (Co) as a sintering agent. This combines the hardness properties with increased toughness, which translates to better wear and fracture resistance under extreme loading conditions [2]. Polycrystalline diamond (PCD) tools commonly consist of a PCD layer sintered onto a cobalt-tungsten carbide (Co-WC) substrate. These tools are used in diverse applications such as drilling for oil exploration, machining of hard metal alloys and the cutting and finishing of wood chipboard.

In the applications of PCD tools, the environment is often quite hostile, and can include circumstances such as high temperature and the presence of abrasive liquids. Certain demands are placed on the tool by the end-user in terms of cost and life expectancy. The stress

state of the surface of a PCD tool is important in its use. A compressive stress state opposes the formation and propagation of median cracks under impact loads, as well as the propagation of micro-cracks already present in the PCD. A tensile stress state, on the other hand, is conducive to crack formation and propagation. It is thus clear that the stress state of the surface of a PCD tool is of interest to both manufacturer and end-user.

Raman spectroscopy has been used quite widely in the measurement of stress in thin diamond films (see e.g. Refs. [3–7]), but has been less frequently applied to PCD tools [8]. Mohrbacher et al. [9] compare X-ray diffraction and micro-Raman spectroscopy as techniques to measure residual stress in diamond coatings. In the case of thin diamond films, stresses at the diamond/substrate interface and within the diamond films have been analyzed. Residual compressive stresses up to 7.1 GPa have been measured in thin films without de-lamination occurring [4,5]. These stresses have been attributed to the difference in the thermal expansion coefficients between the diamond film and the substrate [4], as well as to the high density of microcrystalline defects in the films [3]. Different facets of isolated crystals of CVD diamond have been shown to have different types of residual stress depending on the dominant growth sector [7]. In Ref. [6] a correlation was found between the degree of sp^2 bonding present in diamond films and the magnitude of residual compressive stress. The work on PCD tools [8] showed that micro-Raman spectroscopy can be applied

* Corresponding author at: School of Physics, University of the Witwatersrand, Private Bag 3, WITS 2050, South Africa. Tel.: +27 11 7176859; fax: +27 11 7176879. E-mail address: rudolph.erasmus@wits.ac.za (R.M. Erasmus).

to the measurement of residual stress in PCD cutting tools with reasonable accuracy. The same paper also illustrated that the stress distribution in the PCD layer is not necessarily hydrostatic, and a bi-axial stress model was found to be more appropriate.

2. Theory

In Raman scattering, the sample under study is illuminated with a laser beam with photons at a specific frequency. A small proportion of these photons interact with the optic modes of lattice phonons in the sample material and are scattered inelastically. These scattered photons have a frequency shifted from the incident photons by the frequency of the mode which is characteristic of the sample material. Diamond has a single, triply degenerate Raman peak at 1332.5 Rcm^{-1} [10] (units are in wavenumbers relative to the incident laser beam wavenumber). The frequency and linewidth of the Raman peak thus convey information on the nature and structure of the material under study.

In an ideal crystal, the sample would be stress free and the Raman peak would be measured at its theoretical position. As soon as the crystal is subjected to stresses, be it externally imposed or due to internal imperfections, the frequency of the lattice phonons is subtly affected and thus also the frequency of the Raman peak. In this way, careful measurements of the shift of the Raman peak relative to its unstressed frequency can yield information on the stresses present in the sample. Compressive stress results in a shift of the peak to higher frequencies, and tensile stress to lower frequencies. In order to convert a degree of shift to a stress quantity, use is made of the coefficient of stress-induced shift as follows:

$$\nu_s - \nu_r = \alpha \sigma \quad (1)$$

where ν_r is the position of the stress-free Raman line, ν_s is the measured frequency of the Raman line, σ is the stress present (in GPa) and α is the coefficient of stress-induced frequency shift.

The value of α has been determined under hydrostatic conditions in diamond anvil cells by several authors, and the average value of these measurements is $2.88 \pm 0.17 \text{ cm}^{-1}/\text{GPa}$ [8]. For a PCD layer on a Co-WC substrate, it is, however, more reasonable to assume a bi-axial stress model [4]. With this assumption, and following the derivation of Ref. [9], the value of α for the bi-axial model is $1.92 \pm 0.11 \text{ cm}^{-1}/\text{GPa}$, in agreement with Ref. [6]. This value of α was used for the calculations in this paper.

The Raman linewidth broadening is mainly attributable to two mechanisms, these being homogeneous (lifetime) broadening and broadening due to the size effect of the crystal. In the case of homogeneous broadening, the Full Width at Half Maximum (FWHM) of the diamond Raman peak is inversely proportional to the phonon lifetime. Since the phonon lifetime is shortened by scatter at grain boundaries and defect sites, the FWHM can be used as a convenient ranking indicator of the degree of "crystal disorder" and hence as an indicator of the degree of plastic deformation.

In the case of broadening due to phonon confinement in a small domain size, the FWHM gets broader, the Raman peak shifts to lower wavenumbers and the line shape becomes asymmetric towards lower wavenumbers as the domain size decreases. In our data, the Raman peak is highly symmetric, so the phonon confinement effect is not considered, as was the case for the data in Refs. [3] and [6].

3. Experimental details

The samples used in this work were commercial cylindrical drill-bits manufactured by Element Six (Pty) Ltd., of dimensions approximately 17 mm in length and 19 mm in diameter, consisting of a Co-WC substrate with a PCD layer sintered onto the circular face of the substrate. The diamond used was HPHT-synthesized synthetic grit

(type Ib) with nitrogen as substitutional impurity present in excess of 500 ppm. Synthesis conditions for PCD generally involve applied pressures of 5 to 10 GPa, sintering temperatures of 1300 °C to 1800 °C and sintering times of 5 to 60 min. The average grain size was 10 μm . During the synthesis process, liquid phase sintering facilitated by molten Co takes place, resulting in an extended diamond structure with considerable direct diamond to diamond bonding and cobalt at the grain boundaries (see e.g. Refs. [11,12]).

The PCD layer was 0.6 to 1 mm thick, depending on the processing. Three different batches of samples were examined, each with a different surface preparation. All three batches were synthesized using the same synthesis conditions, so that the samples had nominally the same PCD structure and properties. The first batch had roughly lapped surfaces, the second had finely lapped surfaces and the third had surfaces polished to a mirror finish. During rough lapping grit sizes of 20 to 40 μm are typically employed, and for fine lapping the sizes range from 6 to 15 μm . These are usually suspended in an organic alcohol such as iso-propanol. The final polishing step (3rd batch of samples) took place on a scaife, where the polishing was done dry on a resin-bonded diamond wheel with air-cooling.

Room temperature Raman spectra were acquired with a Jobin-Yvon T64000 Raman spectrometer operated in single spectrograph mode with an 1800 grooves/mm grating and a CCD detector. The 514.5 nm line of an argon ion laser was used as the excitation wavelength. Spectra were acquired with a confocal micro-Raman attachment, where the laser beam was focused to a 50 μm diameter spot. A motorized X-Y microscope stage was also available and used to obtain high spatial resolution measurements. Certain samples were measured in the macro chamber of the spectrometer, where the diameter of the spot size was $\sim 300 \mu\text{m}$. The PCD layer was nearly opaque, thus limiting the penetration depth of the laser to several tens of microns.

As discussed in the Results section, large variations in stress occur from point to point on the surface of the PCD. As the main interest of our investigation is the macroscopic stress state of the PCD, the spot sizes given above were used to provide some degree of averaging of stresses during the measurement process. Although stress variations and degrees of deformation within individual grains are undoubtedly also of interest, these aspects are not addressed in this paper.

High temperature measurements were made *in situ* with a custom-built furnace, fitted into the macro chamber of the spectrometer. The furnace was mounted on an X-Y-Z adjustable stage with micrometer adjustments. Prior to heating the furnace was evacuated to a high vacuum, and backfilled with low pressure argon gas to promote a uniform temperature of the sample. High temperature measurements were only performed on the samples with roughly lapped surfaces, as their spectra had the best signal-to-noise ratios.

For the room temperature measurements utilizing the motorized X-Y stage, data points were acquired as follows: two traverses, separated by a distance of 500 μm , were made across the diameter of each sample, with the measurement points in each traverse spaced 1000 μm apart. Another similar pair of traverses was also acquired at right angles to the first set. At each measurement point a Raman spectrum was acquired, thus yielding a spectral map in the shape of a cross across the surface of the sample. For the high temperature measurements performed in the furnace, only a single line of measurement points spaced at 2000 μm intervals was used.

The diamond Raman peak position was determined by fitting a Voigt function to the corresponding data. Certain samples, especially those with a polished surface, were found to have very weak diamond peaks at certain points. In these cases, or where the peak was not detectable, data points are missing on the corresponding graphs.

As the exact frequency of the diamond Raman peak is important in determining the nature and magnitude of stresses measured, the spectrograph was very carefully calibrated before each set of acquisitions. For this work, the 546.074 nm line of a Hg discharge

lamp was used as the calibration standard. As a reference for the frequency of the diamond Raman peak in an unstressed sample, measurements were conducted on a type IIa diamond used as a standard [3].

The diamond Raman peak shifts in frequency during changes of temperature as discussed in Ref. [13]. These data were used to compensate for the frequency shift due to changing temperature before calculating the residual stresses in the PCD during the heating experiments.

4. Results

The effect of surface processing on the surface compressive stress in the PCD layer of the drill-bit samples is illustrated in Fig. 1. Two traverses are shown for a representative sample of each of the different surface finishes. Although large variations in stress occur from point to point, there is a definite trend showing a lowering of the average compressive stress with the successive surface processing stages. Similar conclusions are drawn from results on other sets of representative samples. The surface compressive stress averaged over the two traverses for each of the respective samples shown in Fig. 1 is as follows: for the roughly lapped samples it is 1.4 GPa, for the finely lapped samples 0.8 GPa and for the polished samples 0.1 GPa.

As is illustrated by Fig. 1, there are no obvious stress distributions over the diameter of the samples and the variations in the magnitude of the stress are large over relatively short distances. The stress measurements were repeated for the roughly lapped samples with a larger diameter laser spot, i.e. 100 μm instead of 50 μm in an attempt to obtain an average over a larger number of grains with a single measurement. These results were very similar to those presented in Fig. 1 and suggest that there is a random distribution of fluctuating stress values across the surface of the sample.

The effects of temperature on the surface compressive stress in the PCD layer of the drill-bit samples are illustrated in Figs. 2 and 3. In Fig. 2, the average surface compressive stresses for two roughly lapped samples (A and D) are reported. It is observed that the average surface compressive stress decreases linearly with increasing temperature. In the limited number of experiments conducted it appears that on cooling to room temperature, the surface compressive stress recovers to a value that is slightly less than the room temperature starting value. The error bars on the measured values represent the standard deviation of the stress values. It can be seen that the standard deviation decreases with increasing temperature, especially for sample D, and again recovers to previous values on cooling.

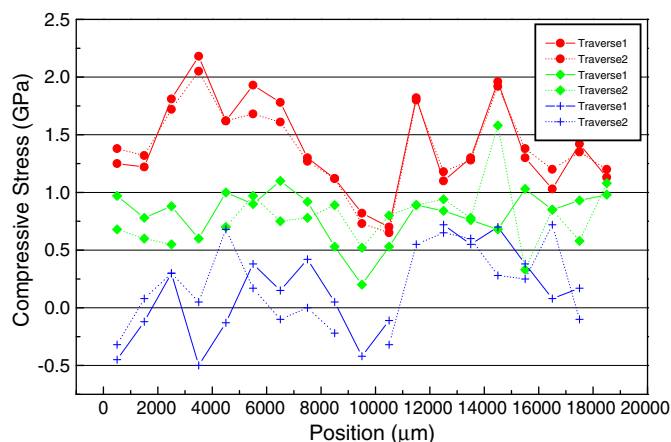


Fig. 1. Compressive stress as a function of surface finish across the diameter of three different drill-bit samples. Circles (●) correspond to a roughly lapped sample, diamonds (◆) to a finely lapped sample and the crosses (+) correspond to a polished surface. Two traverses were made for each sample.

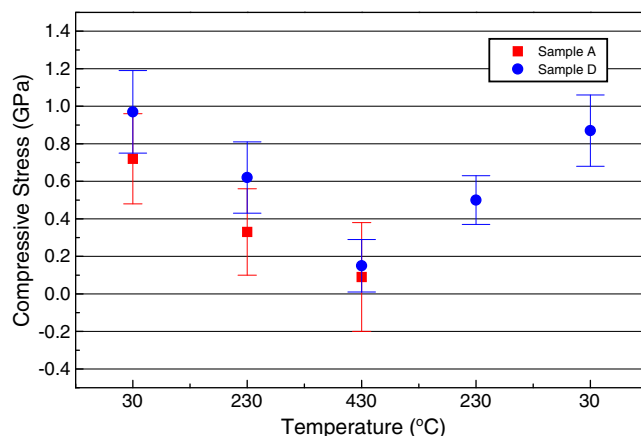


Fig. 2. Change of average surface compressive stress in the PCD layer with temperature for two roughly lapped drill-bit samples. The error bars correspond to the standard deviation of the variations across the surface.

In order to investigate the apparent linear trend in stress relaxation upon heating, and the influence of higher temperatures, a different drill-bit was measured to 620 °C. These results are illustrated in Fig. 3. It can be seen that the initial room temperature compressive stress value is higher than the average value extracted from the data of Fig. 1 for the roughly lapped sample, but comparable to the higher values measured in Fig. 1. On heating, the compressive stress values decrease in a similar way to those observed in Fig. 2. The standard deviation of the measurements decreases with increasing temperature to a larger degree than for the results reported in Fig. 2.

In order to investigate the effect that repeated cycling to a specific temperature would have on the tool-bit properties, several points (n = 10 to 11) were measured across the surface of the PCD layer, using the X–Y–Z micrometer-driven mounting stage of the furnace to move the sample. The surface stress state was measured at room temperature (21 °C) prior to annealing and after each annealing cycle for 5 cycles. During each heating cycle, the sample was heated at 15 °C/min to the set temperature, held at the set temperature for 30 min, and then cooled at 15 °C/min back to room temperature. In practice the furnace cooled at the set rate to ~200 °C, below which the cooling rate decreased substantially. This did not affect the results, as the temperatures where changes were expected to happen, were substantially above this temperature.

Results for 5 annealing cycles to 600 °C in an argon atmosphere are plotted in Fig. 4. It is clear that the surface compressive stress as measured at room temperature remains unchanged at approximately

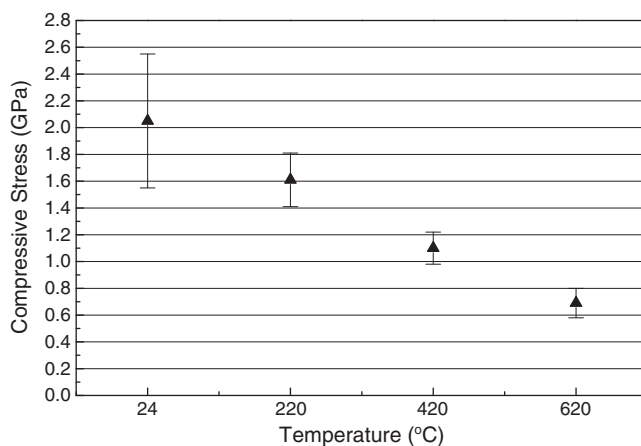


Fig. 3. Change of average surface compressive stress in the PCD layer with temperature for a different drill-bit. The error bars correspond to the standard deviation of the variations across the surface.

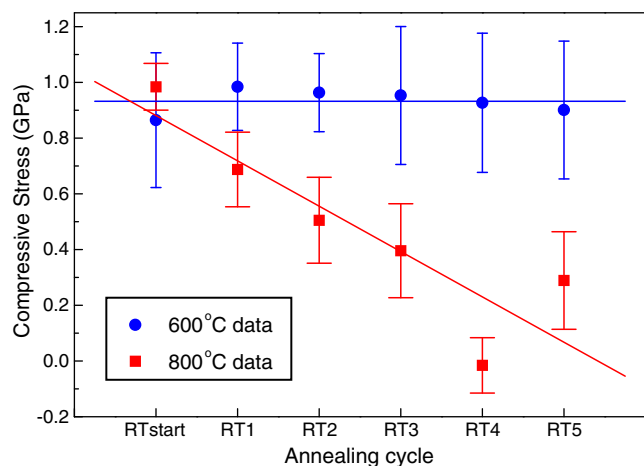


Fig. 4. Surface stress state for the PCD layer of a tool-bit as measured at room temperature after each of 5 cycles to 600 °C and 5 cycles to 800 °C. The solid lines are linear fits to the data to illustrate the trends. The data in the figure represent the average stress value across the surface, and the error bars represent one standard deviation in the data.

0.9 GPa under these temperature and annealing conditions, indicating that the tool retains its properties. The data for the FWHM of the diamond Raman peak follows a similar trend, i.e. the FWHM remains unchanged at around 12.5 cm^{-1} with cycling to 600 °C (Fig. 5).

Results for 5 annealing cycles to 800 °C in vacuum of a different tool-bit from the same manufacturing batch are also plotted in Fig. 4. Here it is clear that the annealing temperature and cycling is affecting the surface compressive stress, with the magnitude of the stress decreasing from 0.9 GPa to considerably lower values with increasing cycling. The tool-bit properties are thus being modified permanently. The FWHM in this case remains unchanged at around 12.2 cm^{-1} with cycling (Fig. 5). Although substantially larger than the FWHM for single crystal diamond, these values are consistent with those reported by other authors [3,6] for polycrystalline diamond. The large width is ascribed to both the micro-defects that form due to fracture during the pressure ramp of the synthesis cycle, as well as the plastic deformation that takes place during sintering.

As mentioned earlier, a surface compressive stress state in the PCD layer is desirable, as it would act to prevent the formation and slow the propagation of cracks in application, thus effectively acting as a toughening mechanism. It is clear from our results that the higher

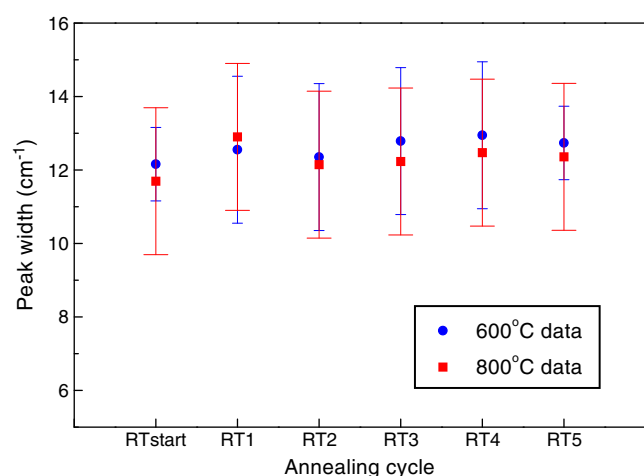


Fig. 5. FWHM of the PCD layer of a tool-bit as measured at room temperature after each of 5 cycles to 600 °C and 5 cycles to 800 °C. The data in the figure represent the average width value across the surface, and the error bars represent one standard deviation in the data.

annealing temperature thus has a negative effect on the tool-bit properties.

5. Discussion

If it is assumed that the PCD layer on the Co-WC substrate can be treated as a thin film, it is reasonable to expect a compressive stress in the diamond layer and a tensile stress in the substrate induced by the differential thermal contraction between the PCD and substrate during cooling from the sintering temperature [14]. If it is further assumed that the stresses are transmitted uniformly through the diamond layer, then the induced compressive stress can be calculated to be between 1.5 GPa and 2.7 GPa. These values are comparable to the actual values measured in this work.

When investigating the effect of temperature on compressive stress, it is clear that a reversible mechanism must be considered to account for the largest observed changes, with an irreversible mechanism possibly contributing to a lesser degree. A plausible reversible mechanism is the differential thermal expansion between the PCD layer and the substrate. Upon heating the differential expansion decreases, leading to a relaxation in the measured stress, with an increase in stress upon returning to room temperature. The apparent linear relationship between temperature and compressive stress also supports the suggestion that differential thermal expansion is the dominant mechanism at work during heating and cooling. The temperature data thus also suggests that the assumption that the PCD layer acts as a thin film is valid.

The effect that the differential thermal expansion has on the stress experienced by the PCD layer on heating can also be used to explain the observed decrease of the standard deviation in the measured stress values with increasing temperature in Figs. 2 and 3. As the compressive stress experienced by the PCD layer relaxes with increasing temperature, the most stressed grains would tend to relax more than less-stressed grains, thereby leading to a decrease in the standard deviation of the average stress value. On cooling this effect is reversible, leading to the standard deviation increasing again.

The lapping process is known to introduce a compressive surface layer, primarily due to the plastic deformation of the surface that occurs when chips are formed (see e.g. Ref. [15]). The observed surface compressive stress for the lapped samples is in agreement with this.

The polishing process can be considered to be a combination of chipping and plastic flow taking place on a very small scale. Frictional processes play a large role in the material removal, with the result that local hot spots are formed on the diamond surface. These hot spots allow for the plastic flow of diamond and subsequent decrease in localized residual stresses. If the annealing process is sufficiently localized, it can result in small areas of tensile stress developing.

Several possible mechanisms exist that can account for the observed trends in surface stress state with annealing temperature. The temperatures for cyclic annealing were chosen to assist in discriminating between mechanisms. Cobalt undergoes a phase transition from hcp to fcc around 420 °C. It is thus anticipated that annealing at 600 °C would indicate any effect that this process has on the surface stress state. The data shows that the surface stress state remains essentially unchanged during annealing to 600 °C, showing that the cobalt phase transition does not affect the surface stress state. Cobalt-catalyzed graphitization of diamond has an onset temperature of around 750 °C at ambient pressure, and thus annealing to 800 °C would show if this mechanism affects the surface stress state. Our data suggests strongly that this mechanism is mainly responsible for the change in surface stress state. It is noted that PCD heated to 1000 °C shows clear evidence of graphitic carbon in the Raman spectra measured on the surface of the PCD.

The results for the FWHM data indicate that no annealing of the diamond material in the PCD layer is taking place, as the FWHM is

unchanged with repeated cycling for both temperatures. This suggests that the stress relieving mechanism is not due to a change in the diamond grains, e.g. possible dislocation movement, but due to changes in the diamond-matrix boundaries. This supports the role of a mechanism such as the cobalt-catalyzed graphitization mentioned in the previous paragraph.

The constituent diamond for the PCD layer in the above tool-bits is Type Ib. It has been shown that the Brittle–Ductile Transition Temperature (BDTT) for single crystal Type Ib diamond is 750 °C [16] suggesting that this might influence the peak width data in Fig. 5. Due to limited thermal stability of diamond-cobalt materials around 800 °C flow stress data for these materials are inconclusive, but flow stress studies on diamond/ β -SiC aggregates have shown that in the range of 800 °C to 1250 °C time dependent plastic deformation does not occur [17]. This indicates that for polycrystalline diamond materials the BDTT is at a higher value than for single crystal diamond. The absence of a change in the Raman peak width data with repeated cycling thus suggests that the BDTT has not been reached yet for the tool-bits considered in this study. Processes in the cobalt matrix and/or graphitization of the diamond are thus the most likely mechanisms to account for the observed reduction in compressive stress.

In conclusion it can be stated that a PCD tool is a complex material, involving several variables in its manufacture and use. The present work has provided new information on the surface stress state in the PCD layer on tool-bits, this being of value to manufacturers and end users of these products. It is suggested that use be made of Finite Element Modeling to investigate stress distributions from a complementary, theoretical point of view.

Acknowledgments

This work has been supported by the National Research Foundation of South Africa under Grant Number 2053306, the University of the Witwatersrand, Johannesburg, and the DST/NRF Centre of Excellence in Strong Materials.

References

- [1] M. Seal, in: J.E. Field (Ed.), *The Properties of Natural and Synthetic Diamond*, Academic Press, London, 1992, pp. 607–636.
- [2] R.H. Wentorf, R.C. DeVries, F.P. Bundy, *Science* 208 (1980) 873–880.
- [3] J.W. Ager III, D.K. Veirs, G.M. Rosenblatt, *Phys. Rev. B* 43 (1991) 6491–6499.
- [4] J.W. Ager III, M.D. Drory, *Phys. Rev. B* 48 (1993) 2601–2607.
- [5] S.A. Catledge, Y.K. Vohra, *J. Appl. Phys.* 78 (1995) 7053–7058.
- [6] L. Bergman, R.J. Nemanich, *J. Appl. Phys.* 78 (1995) 6709–6719.
- [7] K.W. Nugent, S. Praver, *Diam. Relat. Mater.* 7 (1998) 215–221.
- [8] S.A. Catledge, Y.K. Vohra, R. Ladi, G. Rai, *Diam. Relat. Mater.* 5 (1996) 1159–1165.
- [9] H. Mohrbacher, K. Van Acker, B. Blanpain, P. Van Houtte, J.-P. Celis, *J. Mat. Res.* 11 (1996) 1776–1782.
- [10] Y. Sato, M. Kamo, in: J.E. Field (Ed.), *The Properties of Natural and Synthetic Diamond*, Academic Press, London, 1992, p. 428.
- [11] T. Evans, S.T. Davey, S.H. Robertson, *J. Mat. Sci.* 19 (1984) 2405–2414.
- [12] K. Uehara, S. Yamaya, *Int. J. Refract. Met. Hard Mater.* 7 (1988) 219–223.
- [13] H. Herschen, M.A. Cappelli, *Phys. Rev. B* 43 (1991) 11740–11744.
- [14] T.P. Lin, M. Hood, G.A. Cooper, R.H. Smith, *J. Am. Ceram. Soc.* 77 (1994) 1562–1568.
- [15] D.W. Richerson, Marcel Dekker, Inc, New York, 1982, pp. 260–273.
- [16] C.A. Brookes, E.J. Brookes, V.R. Howes, S.G. Roberts, C.P. Waddington, *J. Hard Mater.* 1 (1990) 3–24.
- [17] T.K. Harris, E.J. Brookes, R.D. Daniel, *Diam. Relat. Mater.* 10 (2001) 755–759.